ANNEX I: Articles accepted by PhD commision

Paper A:	Ru Complexes That Can Catalytically Oxidize Water to Molecular Dioxygen
Paper B:	Synthesis, Structure and Reactivity of New Tetranuclear Ru-Hbpp Based Water Oxidation Catalysts
Paper C:	A Ru-Hbpp-Based Water-Oxidation Catalyst Anchored on Rutile TiO_2

Paper A: Ru Complexes That Can Catalytically Oxidize Water to Molecular Dioxygen

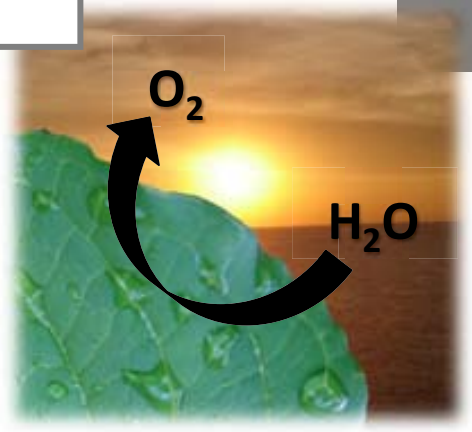

Paper B: Synthesis, Structure and Reactivity of New Tetranuclear Ru-Hbpp Based Water Oxidation Catalysts

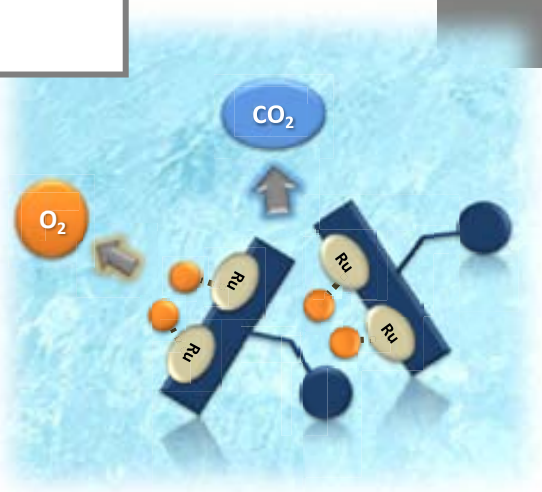

Paper C: A Ru-Hbpp-Based Water-Oxidation Catalyst Anchored on Rutile TiO_2

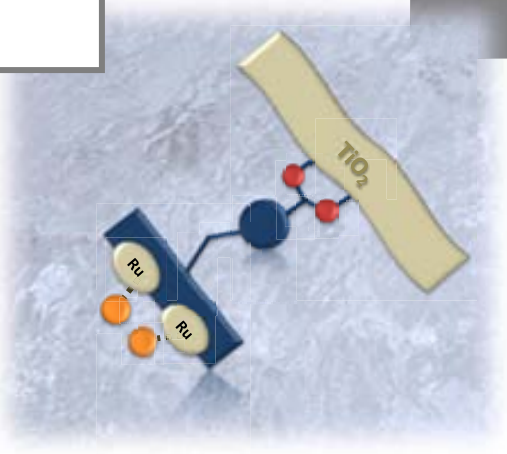

ANNEX II: Additional articles

Paper D:	Ru-Hbpp-Based Water-oxidation Catalysts anchored on FTO-TiO_2
Paper E:	Synthesis, Characterization and Linkage Isomerism in Mono- and Dinuclear Ruthenium Complexes Containing the New Pyrazole Based ligand Hpbl

Paper D: Ru-Hbpp-Based Water-oxidation Catalysts anchored on FTO-TiO_2

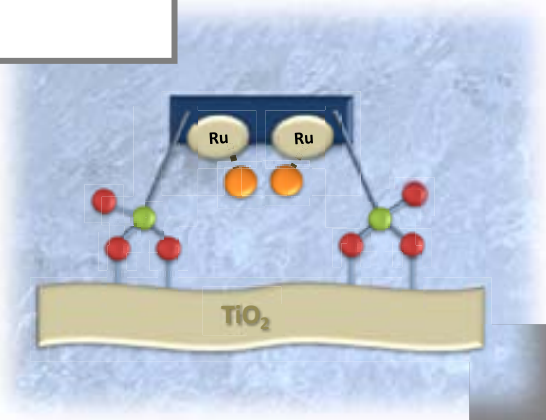

Ru-Hbpp-Based Water-oxidation Catalysts Anchored on FTO-TiO_2

Laia Francàs,[a] Xavier Sala,[a] Jordi Benet-Buchholz,[b] Lluís Escriche[*,a] and Antoni Llobet*[*,a,b]*

[a]Departament de Química, Universitat Autònoma de Barcelona, Cerdanyola del Vallès, E-08193 Barcelona, Spain and [b]Institute of Chemical Research of Catalonia (ICIQ), Av. Països Catalans 16, E-43007 Tarragona, Spain

lluis.escriche@uab.cat, allobet@iciq.es

Abstract

The ligand trpy-P_e (Phosphonic acid, P-[2,2':6',2"-terpyridin]-4'-yl-diethyl ester) has been used to synthesize a family of ruthenium compounds with formulas **$[Ru^{III}Cl_3(trpy\text{-}P_e)]$** (**1**), **$[Ru^{II}_2(L\text{-}L)(bpp)(trpy\text{-}P_e)_2]^{n+}$** (L-L= μ-Cl and n = 2 in **2^{2+}**; L-L= μ-Ac and n = 2 in **3^{2+}**; L-L = $(H_2O)_2$ and n = 3 in **6^{3+}**) and **$[Ru^{II}_2(\mu\text{-}Br)(bpp)(trpy\text{-}P_a]\cdot 2MeOH$** (**4**). These complexes have been characterized in solution by 1D and 2D ^{1}H NMR spectroscopy, UV-Vis spectroscopy and electrochemical techniques. The complexes **4** and **$[Ru^{II}_2(\mu\text{-}Cl)(bpp\text{-}R_a)(trpy)_2]^{2+}$** (**$12^{2+}$**) (Hbpp-$R_a$ = 4-((3,5-di(pyridine-2-yl)-1H-pyrazol-4-yl)methyl)benzoic acid) have been anchored onto TiO_2-anatase coated FTO films. Upon heterogenization, the electrochemical properties of compounds **$[Ru^{II}_2(H_2O)_2(bpp)(trpy\text{-}P_a)_2]$** (**$5^{3+}$**) and **$[Ru^{II}_2(H_2O)_2(bpp\text{-}R_a)(trpy)_2]^{3+}$** (**$13^{3+}$**) were significantly modified with respect to their homogeneous equivalents, which had direct implication in their activity as water oxidation catalysts.

Introduction

Nowadays, huge scientific efforts are focused on the study of the water oxidation process (WO).[1] The main reasons for the worldwide interest on this process are: its biological relevance in natural photosynthesis; and their key role in the design of artificial systems potentially able to convert solar energy into a useful and storable chemical fuel.[2] The WO reaction is a thermodynamically unfavorable process and its mechanism is extremely complex because involves the simultaneous removal of 4 electrons and 4 protons from two water molecules and the formation of an O-O bond. A quite large number of WO catalysts has been reported in the last few years,[3] most of them belonging to the Ru-aqua/Ru-oxo kind of systems[4], which were extensively studied by Meyer's group during the 80s and 90s.[5] Its intrinsic properties, such as the capacity of reaching several oxidation states in a narrow potential range, make them excellent candidates redox catalysis. However there are several problems related with the use of these complexes. Their initial form needs to be oxidized to an upper oxidation state in order to obtain the catalytically active species. Usually this activation is carried out by adding a chemical oxidant such as Ce(IV), which is neither environmentally friendly nor atom-economic. In addition, and as consequence of the high reactivity of the active oxidized species, one of the well-known deactivation pathways is the catalyst-catalyst intermolecular oxidation, which generates non-active species or/and CO_2 as catalyst degradation product.[6] One interesting strategy to overcome this hurdle is the immobilization of the catalyst onto a conductive solid support, thus allowing its electrochemical activation through bulk electrolysis.[6b] Following this strategy, the Meyer's group recently anchored mononuclear active WO catalysts onto FTO-TiO_2 and ITO-TiO_2 surfaces, thus presenting improved catalytic results when comparing these hybrid materials with their homogeneous counterparts.[7]

Chart 1. Ligands employed in this work.

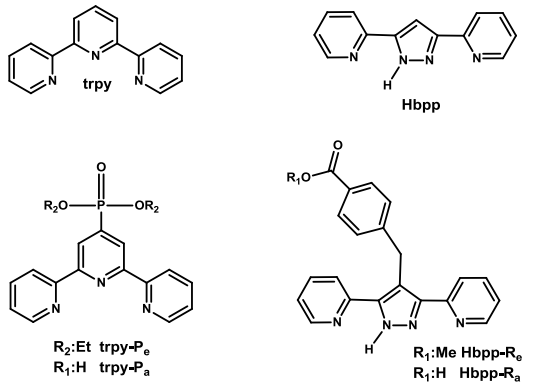

Earlier in 2004 our research group reported a highly efficient catalytic system for WO based on two [Ru(trpy)]-subunits linked by the rigid Hbpp bridge (chart 1).[8] Later on, the O-O bond formation mechanism of this dinuclear catalyst was elucidated as an intramolecular pathway.[9] The next step in our project to develop new and efficient WO catalysts was the anchoring of these dinuclear ruthenium complexes onto conducting solid supports for its electrochemical activation. This will aid the introduction of these WO systems in more complex devices for the overall splitting of water from sunlight. Our first approach in this direction was the electro-polymerization of a pyrrole-modified Ru-Hbpp system onto different conducting electrodes (VCE and FTO).[6b] Despite the observed increase on the system robustness when compared with its homogeneous counterpart, the oxidation of the polypyrrole backbone during the catalytic process ends up with the catalyst deactivation. However, this study confirms the feasibility of the solid-state approach, which is able to improve considerably the activity of its homogenous homolog. Moreover, this system can act as a WO catalyst through electroactivation at 1.17 V vs. SSCE. In order to anchor this catalyst to more rugged, all inorganic solid support such as TiO_2, the Hbpp ligand was modified introducing reactive functional groups in its molecular framework. Therefore, the acid-containing Hbpp-R_a ligand (Chart 1) was prepared and its corresponding Ru complex anchored onto TiO_2 rutile nanoparticles.[10] This chemically activated complex generated both O_2 and CO_2, the later due to the intermolecular ligand oxidation starting at the benzylic position of the ligand. To improve these results our group have envisaged two strategies; (a) the replacement of Ce(IV), an indiscriminate chemical oxidant which could promote the ligand degradation, by an electric potential properly applied and (b) the combination of the original Hbpp ligand with phosphonate-containing terpyriridine ligands as anchoring groups (trpy-P_e in Chart 1). Some studies on this field have demonstrated the more rugged character of the phosphonate group with regards to the carboxylate one as well as its stronger bonding to TiO_2.[11] Both approaches are presented and compared in the present work, together with other important factors to take into account like the number of anchoring groups present in the catalyst and their distance to the catalytic active site.[12]

Experimental Section.

Materials. The trpy-P_e ligand was obtained from HetCat company and $RuCl_3 \cdot 3H_2O$ from Alfa Aesar. All the other reagents were purchased at Sigma-Aldrich Chemical Co and were used without further purification. Reagent grade organic solvents were obtained from SDS.

Preparations. The 3,5-bis(2-pyridyl)pirazole ligand (Hbpp)[13] was prepared as described in the literature. All synthetic manipulations were routinely performed under nitrogen atmosphere using Schlenck and vacuum line techniques.

$[Ru^{III}Cl_3(trpy\text{-}P_e)] \cdot 0.5H_2O$ (1). A sample of 212 mg (0.813 mmol) of $RuCl_3 \cdot 3H_2O$ and 300 mg of trpy-P_e were added to a schlenck charged with 30 mL of dry methanol. The mixture was heated at reflux temperature and vigorously stirred for 3 h and a reddish precipitate appeared. The reaction mixture was cooled down at 0ºC to enforce complete precipitation and the resulting solid was filtered, washed with cold methanol, and dried with diethyl ether. Yield: 380 mg (81%). ESI-MS (MeOH): *m/z*= 597.0 ($[M+Na^+]^+$). UV-vis (CH_2Cl_2) [λ_{max}, nm (ε, M^{-1} cm^{-1})]: 277 (18581), 285 (17347), 318 (15546), 327 (16388), 340 (9015), 408 (5066), 424 (5534), 500 (2732), 566 (1162). Elemental analysis calcd. (%) for ($C_{19}H_{21}Cl_3N_3O_{3.5}PRu$): C, 38.96; H, 3.61; N, 7.17. found: C, 38.68; H, 3.47; N, 7.08.

$[Ru^{II}_2(\mu\text{-}Cl)(bpp)(trpy\text{-}P_e)_2](PF_6)_2$ [2]$(PF_6)_2$. A sample of 0.300 g (0.519 mmol) of **1** and 66 mg (1.56 mmol) of LiCl were dissolved in 30 mL of dried MeOH containing 144 µL (1.038 mmol) of NEt_3. The mixture was stirred at RT for 20 minutes and then 15 mL of dried MeOH containing 57.6 mg (0.2595 mmol) of Hbpp and 1.16 mL (0.2595 mmol) of 0.223 M MeONa were added. The resulting solution was heated at reflux temperature under stirring for 4 h and then stirred in the presence of a 100 W tungsten lamp for 12 h. The resulting solution was filtered and 1 mL of a saturated aqueous NH_4PF_6 solution and 3 mL of water were added. The volume was reduced on a rotary evaporator until a precipitate appeared and the resulting mixture was cooled down at 5 ºC for 24h. The solid precipitated was filtered on a frit, washed with cold water (3 x 5 mL) and diethyl ether (3 x 5 mL) and dried under vacuum. Yield: 315 mg (82%). ^{1}H NMR (400

MHz, acetone-d_6, ppm) δ=8.79 (d, $4H_{51}$, $^3J_{51\text{-}P}$=13.22 Hz), 8.76 (ddd, $4H_{44}$, $^3J_{44\text{-}49}$=8.15 Hz, $^4J_{44\text{-}48}$=1.130 Hz, $^5J_{44\text{-}47}$=0.65 Hz), 8.55 (s, $1H_{14}$), 8.42 (ddd, $4H_{47}$, $^3J_{47\text{-}48}$=5.50 Hz, $^4J_{47\text{-}49}$=1.50 Hz, $^5J_{47\text{-}44}$=0.65 Hz), 8.29 (ddd, $2H_{11}$, $^3J_{11\text{-}12}$=8.20 Hz, $^4J_{11\text{-}7}$=1.50 Hz, $^5J_{11\text{-}8}$=0.80 Hz), 7.99 (ddd, $4H_{49}$, $^3J_{49\text{-}44}$=8.15 Hz, $^4J_{49\text{-}48}$=7.75 Hz, $^5J_{49\text{-}47}$=1.50 Hz), 7.84 (ddd, $2H_{12}$, $^3J_{12\text{-}11}$=8.30 Hz, $^4J_{12\text{-}7}$=7.62 Hz, $^5J_{12\text{-}8}$=1.45 Hz), 7.68 (ddd, $4H_{48}$, $^3J_{48\text{-}49}$=7.75 Hz, $^4J_{48\text{-}47}$=5.50 Hz, $5J_{48\text{-}44}$=1.30 Hz), 7.44 (ddd, $2H_8$, $^3J_{8\text{-}7}$=5.82 Hz, $^4J_{8\text{-}12}$=1.45 Hz, $^5J_{8\text{-}11}$=0.8 Hz), 6.79 (ddd, $2H_7$, $^3J_{7\text{-}12}$=7.62 Hz, $^4J_{7\text{-}8}$=5.82 Hz, $^5J_{7\text{-}11}$=1.50 Hz), 4.27 (ddq, $4H_{24\text{ o }25}$, $^2J_{24\text{-}25}$=10.33 Hz, $^3J_{24\text{-}P}$=8.36 Hz, $^3J_{24\text{-}26}$=7.02 Hz), 4.24 (ddq, $4H_{24\text{ o }25}$, $^2J_{25\text{-}24}$=10.33 Hz, $^3J_{25\text{-}P}$=8.36 Hz, $^3J_{25\text{-}26}$=7.02 Hz), 1.35 (td, $12H_{26}$, $^3J_{26\text{-}24,25}$=7.02 Hz, $^4J_{26\text{-}P}$=0.57 Hz). ^{13}C {^1H} NMR (100.6 MHz, acetone-d_6, ppm) δ=160.10 ($C_{52,}$ $^1J_{52\text{-}P}$=14.7Hz), 159.73 (C_{45}), 159.71 (C_{50}), 154.36 (C_{10}), 154.98 (C_8), 154.29 (C_{47}), 149.46 (C_{13}), 138.25 (C_{49}), 138.18 (C_{12}), 128.67 (C_{48}), 125.19 (C_{44}), 124.59 ($C_{51,}$ $^2J_{51\text{-}P}$=10.12Hz), 123.24 (C_7), 121.57 (C_{11}), 104.39 (C_{14}), 63.73 ($C_{9,}$ $^2J_{9\text{-}P}$=5.60Hz), 16.69 ($C_{26,}$ $^3J_{26\text{-}P}$=6.00Hz). ^{31}P {^1H} NMR (400 MHz, acetone-d_6, ppm). δ= 14.71. ESI-MS (MeOH): *m/z*= 599.0 ($[M\text{-}2PF_6^-]^{2+}$). UV-vis (CH_2Cl_2) [λ_{max}, nm (ε, M^{-1} cm^{-1})]: 278 (62612), 321 (61368), 378 (27544), 486 (18957), 516 (18105). NMR assignment uses the same labelling scheme as Figure 2.

$[Ru^{II}_2(\mu\text{-}O_2CMe)(bpp)(trpy\text{-}P_e)_2](PF_6)_2\cdot 5H_2O$ [3]$(PF_6)_2$. A sample of 0.050 g (0.0336 mmol) of **[2]$(PF_6)_2$** and 22 mg (0.164 mmol) of sodium acetate were dissolved in 10 mL of acetone:water (3:1) and heated at reflux temperature under stirring overnight. The resulting mixture was filtered and 1 mL of a saturated aqueous NH_4PF_6 solution was added to the filtrate. Upon reducing the volume in a rotary evaporator (c.a. 4 mL) a solid came out, which was filtered, washed with cold water and diethyl ether and dried under the vacumm. Yield: 36 mg (71%). ^1H NMR (400 MHz, acetone-d_6, ppm) δ= 8.86 (d, $4H_{51}$, $^3J_{51\text{-}P}$=13.23 Hz), 8.84 (ddd, $4H_{44}$, $^3J_{44\text{-}49}$=8.16 Hz, $^4J_{44\text{-}48}$=1.28 Hz, $^5J_{44\text{-}47}$=0.70 Hz), 8.59 (s, $1H_{14}$), 8.47 (ddd, $4H_{47}$, $^3J_{47\text{-}48}$=5.50 Hz, $^4J_{47\text{-}49}$=1.50 Hz, $^5J_{47\text{-}44}$=0.80 Hz), 8.23 (ddd, $2H_{11}$, $^3J_{11\text{-}12}$=8.06 Hz, $^4J_{11\text{-}7}$=1.45 Hz, $^5J_{11\text{-}8}$=0.80 Hz), 8.07 (ddd, $4H_{49}$, $^3J_{49\text{-}44}$=8.16 Hz, $^4J_{49\text{-}48}$=7.65 Hz, $^5J_{49\text{-}47}$=1.50 Hz), 7.77 (ddd, $2H_{12}$, $^3J_{12\text{-}11}$=8.06 Hz, $^4J_{12\text{-}7}$=7.45 Hz, $^5J_{12\text{-}8}$=1.41 Hz), 7.58 (ddd, $4H_{48}$, $^3J_{48\text{-}49}$=7.65 Hz, $^4J_{48\text{-}47}$=5.50 Hz, $5J_{48\text{-}44}$=1.28 Hz), 7.38 (ddd, $2H_8$, $^3J_{8\text{-}7}$=5.79 Hz, $^4J_{8\text{-}12}$=1.41 Hz, $^5J_{8\text{-}11}$=0.80 Hz), 6.81 (ddd, $2H_7$, $^3J_{7\text{-}12}$=7.45 Hz, $^4J_{7\text{-}8}$=5.79 Hz, $^5J_{7\text{-}11}$=1.45 Hz), 4.32 (ddq, $4H_{24\text{ o }25}$, $^2J_{24\text{-}25}$=10.42 Hz, $^3J_{24\text{-}P}$=8.59 Hz, $^3J_{24\text{-}26}$=7.03 Hz), 4.30 (ddq, $4H_{24\text{ o }25}$, $^2J_{25\text{-}24}$=10.42 Hz, $^3J_{25\text{-}P}$=8.59 Hz, $^3J_{25\text{-}26}$=7.03 Hz), 1.39 (td, $12H_{26}$, $^3J_{26\text{-}24,25}$=7.03 Hz, $^4J_{26\text{-}P}$=0.44 Hz), 0.38 (s, 3H acetate). ^{13}C {^1H} NMR (100.6 MHz, acetone-d_6, ppm) δ=192.81 (C, CO acetate), 161.53 ($C_{52,}$ $^1J_{52\text{-}P}$=14.7 Hz), 160.07 (C_{45}), 160.05 (C_{50}), 156.96 (C_{10}), 154.48 (C_{47}), 153.87 (C_8), 152.82 (C_{13}), 138.50 (C_{49}), 137.29 (C_{12}), 128.74 (C_{48}), 125.20 (C_{44}), 124.75 ($C_{51,}$ $^2J_{51\text{-}P}$=9.95 Hz), 123.31 (C_7), 120.71 (C_{11}), 104.98 (C_{14}), 63.81 ($C_{9,}$ $^2J_{9\text{-}P}$=5.62 Hz), 26.12 (C, Me acetate), 16.74 ($C_{26,}$ $^3J_{26\text{-}P}$=5.65 Hz). ^{31}P {^1H} NMR (400 MHz, acetone-d_6, ppm). δ= 14.93. ESI-MS (MeOH): *m/z*= 611 ($[M\text{-}2PF_6^-]^{2+}$). UV-vis (CH_2Cl_2) [λ_{max}, nm (ε, M^{-1} cm^{-1})]: 280 (62612), 323 (642489), 371 (30163), 505 (17141), 548 (15088). Elemental analysis calcd (%) for ($C_{53}H_{62}F_{12}N_{10}O_{13}P_4Ru_2$): C, 39.73; H, 3.99; N, 8.74. found: C, 39.66; H, 3.70; N, 8.45. NMR assignment uses the same labelling scheme as Figure 2.

$[Ru^{II}_2(\mu\text{-}Br)(bpp)(trpy\text{-}P_a)]\cdot 2MeOH$ (4). A sample of 20 mg of complex **[2]$(PF_6)_2$** was dissolved in 5 mL of dry CH_2Cl_2 and then 0.40 mL TMSBr were slowly added and stirred at room temperature for 60 h. Then the volatiles were removed under reduced pressure and the residual brown solid was dissolved in MeOH and stirred at room temperature for 24 h. This process was repeated again and after removing the solvents the solid was redissolved in a mixture of MeOH/H_2O, a drop of saturated aqueous NH_4PF_6 solution was added and the volume was reduced until a precipitated appeared. This solid was filtered off, washed with diethyl ether and vacuum dried. Yield: 11 mg (69%). ^1H NMR (400 MHz, MeOD-d_4, ppm). δ=8.74 (d, $4H_{51}$, $^3J_{51\text{-}P}$=12.40 Hz), 8.45 (ddd, $4H_{44}$, $^3J_{44\text{-}49}$=8.10 Hz, $^4J_{44\text{-}48}$=1.30 Hz, $^5J_{44\text{-}47}$=0.65 Hz), 8.35 (s, $1H_{14}$), 8.20 (ddd, $4H_{47}$, $^3J_{47\text{-}48}$=5.55 Hz, $^4J_{47\text{-}49}$=1.60 Hz, $^5J_{47\text{-}44}$=0.65 Hz), 8.16 (ddd, $2H_{11}$, $^3J_{11\text{-}12}$=8.08 Hz, $^4J_{11\text{-}7}$=1.45 Hz, $^5J_{11\text{-}8}$=0.72 Hz), 7.88 (ddd, $4H_{49}$, $^3J_{49\text{-}44}$=8.10 Hz, $^4J_{49\text{-}48}$=7.60 Hz, $^5J_{49\text{-}47}$=1.60 Hz), 7.74 (ddd, $2H_{12}$, $^3J_{12\text{-}11}$=8.08 Hz, $^4J_{12\text{-}7}$=7.50 Hz, $^5J_{12\text{-}8}$=1.40 Hz), 7.46 (ddd, $4H_{48}$, $^3J_{48\text{-}49}$=7.60 Hz, $^4J_{48\text{-}47}$=5.55 Hz, $^5J_{48\text{-}44}$=1.30 Hz), 7.16 (ddd, $2H_8$, $^3J_{8\text{-}7}$=5.80 Hz, $^4J_{8\text{-}12}$=1.40 Hz, $^5J_{8\text{-}11}$=0.72 Hz), 6.76 (ddd, $2H_7$, $^3J_{7\text{-}12}$=7.50 Hz, $^4J_{7\text{-}8}$=5.82 Hz, $^5J_{7\text{-}11}$=1.45 Hz). ^{13}C {^1H} NMR (100.6 MHz, MeOD-d_4, ppm) δ= 160.41 (C_{45}), 159.81 (C_{10}), 159.54 (d, $C_{50,}$ $^1J_{C\text{-}P}$=13.50 Hz),

154.53 (C_{47}), 153.70 (C_8), 150.80 (C_{13}), 138.32 (C_{49}), 137.97 (C_{12}), 128.40 (C_{48}), 124.74 (C_{44}), 124.36 (d, $C_{51,}$ $^2J_{C-P}$=9.46 Hz), 123.55 (C_7), 121.71 (C_{11}). ^{31}P {^1H} NMR (400 MHz, MeOD-d_4, ppm). δ= 8.38. ESI-MS (MeOH): m/z=1151 ([M-2MeOH+Na]$^+$). UV-vis (MeOH) [λ_{max}, nm (ε, M^{-1} cm^{-1})]: 270 (45998), 310 (39009), 370 (19038), 470 (13233), 490 (14278).

$[Ru^{II}_2(H_2O)_2(bpp)(trpy\text{-}P_e)]^{3+}$ (5^{3+}). This complex is prepared by hydrolysis of the compound **[3]$(PF_6)_2$** in acidic aqueous media. Even though the NMR experiments, obtained by dissolving **[3]$(PF_6)_2$** in acidic media, show the presence of pure **5^{3+}**, we could not isolate a characterizable solid, presumably due to the replacement of the aqua ligands by the anions present in the solution during the precipitation, which gives a mixture of compounds as a final product. ^1H NMR (400 MHz, D_2O, acetone-d_6 and CF_3SO_3D, ppm). δ=8.66 (d, $4H_{51}$, $^3J_{51\text{-}P}$=13.22 Hz), 8.49 (d, $4H_{47}$, $^3J_{47\text{-}48}$=8.00 Hz), 8.15 (bb, $4H_{44}$), 8.10 (s, $1H_{14}$), 7.95 (bb, $2H_8$), 7.92 (t, $4H_{48}$, $^3J_{48\text{-}47,49}$=8.00 Hz), 7.59 (t, $2H_7$, $^3J_{7\text{-}8,12}$=7.00 Hz), 7.45 (bb, $4H_{49}$), 6.95 (bb, $2H_{11}$), 6.67 (bb, $2H_{12}$), 4.26 (q, $8H_{25\text{-}24}$, $^3J_{25\text{-}26}$=7.50 Hz), 1.32 (t, $12H_{26}$). UV-vis (0.1 M of CF_3COOH aqueous solution at pH=1) [λ_{max}, nm (ε, M^{-1} cm^{-1})]: 270 (58149), 320 (58326), 350 (26338), 480 (16961), 510 (16185).

FTO-TiO_2-**$[Ru^{II}_2(\mu\text{-}Br)(bpp)(trpy\text{-}P_a)_2]$** (FTO-$TiO_2$–**4**). On clean FTO films TiO_2 paste, was spread uniformly. Then the films were heated for 10 min at 100ºC in order to reduce the surface irregularities. The films were calcinated following the appropriated temperature ramps (see Figure S32). The anchoring process was carried out by soaking the films into a methanol solution containing the complex **4** during 48 h. The coated films were rinsed with methanol and air dried.

FTO-TiO_2-**$[Ru^{II}_2(H_2O)_2(bpp)(trpy\text{-}P_a)_2]$** (FTO-$TiO_2$ –**5^{2+}**). To obtain the FTO-TiO_2-**5^{2+}**, FTO-TiO_2–**4** was soaked into 0.1 M triflic acid aqueous solution for 24 h, rinsed with methanol and air dried.

Instrumentation and Measurements: UV-Vis spectroscopy was performed by a HP8453 spectrometer using 1 cm quartz cells provided by the Chemical Analysis Service of the Universitat Autonòma de Barcelona (CAS-UAB). NMR spectroscopy was performed on a Bruker DPX 400 MHz in SeRMN UAB. Samples were run in acetone-d_6 or MeOD-d_4 with internal references (residual signals and/or tetramethylsilane or DSS respectively). In ^{31}P {^1H} NMR experiments a capillary of phosphoric acid was used as internal reference. Elemental analyses were performed using a Carlo Erba CHMS EA-1108 instrument provided by the CAS-UAB. ESI-MS experiments were carried out on a HP298s GC-MS system from the CAS-UAB. CV experiments were performed with a PAR283 potentiostat using a three-electrode cell. A glassy carbon disk (3 mm diameter) was used as working electrode, platinum wire was used as auxiliary electrode, and a saturated sodium calomel electrode (SSCE) was used as the reference electrode. When the catalysts were supported onto FTO-TiO_2 surface the film was used as working electrode. For solutions of complexes in organic solvents, nBu_4NPF_6 was used as supporting electrolyte to yield a solution with 0.1 M ionic strength. All $E_{1/2}$ values reported here were estimated from cyclic voltammetry as the average of the oxidative and reductive peak potentials ($E_{p,a}$+$E_{p,c}$)/2 and are referred to the SSCE reference electrode. The concentration of the species was approximately 1 mM.

Online manometric measurements were carried out on a Testo 521 differential pressure manometer with an operating range of 1–100 hPa and accuracy within 0.5% of the measurement, coupled to thermostated reaction vessels for dynamic monitoring of the headspace pressure above each reaction. The secondary ports of the manometers were connected to thermostatically controlled reaction vessels that contained the same solvents and headspace volumes as the sample vials. Online monitoring of the gas evolution was performed on a Pfeiffer Oministar GSD 301C mass spectrometer. Typically, 16.04 mL degassed vials containing a suspension of the catalysts in 0.1 M triflic acid (1.5 mL) were connected to the apparatus capillary tubing. Subsequently, the previously degassed solution of Ce(IV) (0.5 mL) at pH=1 (triflic acid, 100 equiv) was introduced using a Hamilton gas-tight syringe and the reaction was dynamically monitored. A response ratio of 1:2 was observed when injecting equal concentrations of O_2 and CO_2, respectively, and thus was used for the calculation of their relative concentrations. Electrocatalytic experiments were performed always using pH = 1 solution prepared with

Scheme 1. Schematic complex synthesis

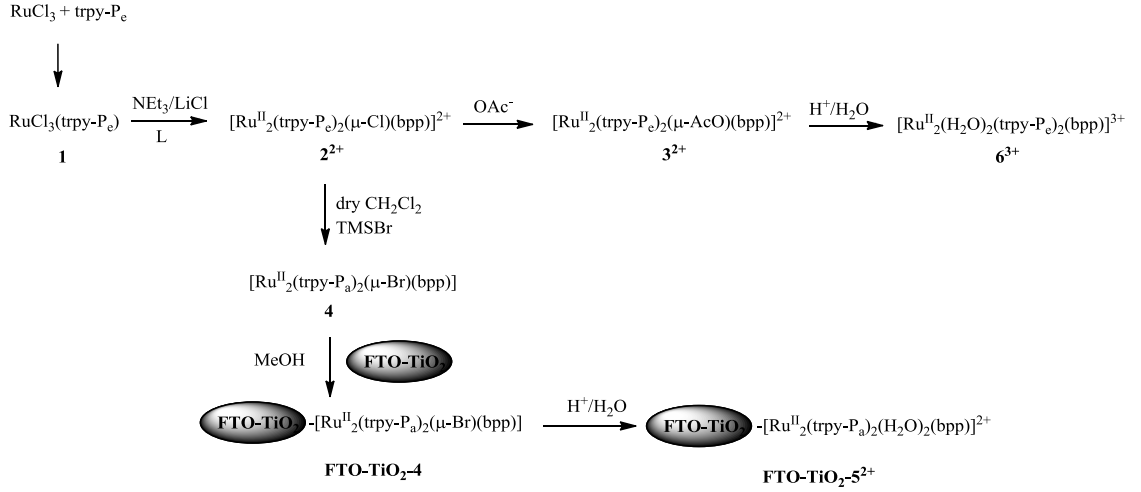

triflic acid in Mili-Q water. All the controlled potential electrolysis (CPE), electrocatalysis and CVs before and after the catalytic process of the anchored compounds were performed in a two compartment/three electrode cell using a Bio-Logic potentiostat/galvanostat and EC-Lab software. Sensitized FTO-TiO_2-$\mathbf{5}^{2+}$ or FTO-TiO_2-$\mathbf{13}^{2+}$ (see Table 2 for complex numbering) films connected to a tin wire were used as working electrode, platinum grid as auxiliary and SSCE as the reference electrode. The O_2 concentration of the headspace of the compartment containing the working electrode was monitored with a Clark's fast-response oxygen micro-electrode needle sensor (OX-N, 40 mm needle length, 1.1 mm diameter, 90% response time <10 s) commercialized by Unisense A/S.

X-ray Crystal Structure Determination. Crystals of **1** were obtained by the slow diffusion of diethyl ether into an acetone complex solution. Crystals of **4** were obtained as brown blocks by dissolving the complex in methanol at room temperature allowing the solvent to slowly evaporate. The measured crystals were prepared under inert conditions immersed in perfluoropolyether as protecting oil for manipulation.

Data collection: were made on a Bruker-Nonius diffractometer equipped with an APPEX 2 4K CCD area detector, a FR591 rotating anode with MoK_α radiation, 200 multilayer Montel mirrors as monochromator and a Kryoflex low temperature device (T = -173 °C). Full-sphere data collection was used with ω and φ scans. *Programs used:* Data collection APEX-2 v2009.1-0, data reduction Bruker Saint V7/.60A and absorption correction TWINABS [14], due to the measured crystal was a twin.

Structure Solution and Refinement: For crystals of **1** and **4** SHELXS [15] was used. The collected data for both crystals were processed with TWINABS taking in account overlapping reflections. The crystal **4** data parameters are listed in Table 2 and the crystal **1** data parameters are listed in Figure S6 and its structure is shown in Figure S7. Two crystals with a ratio of 68:32 formed Crystal **1** and its asymmetric unit contains one molecule of the complex. A half molecule of the complex and three and half molecules of methanol make up the asymmetric unit of crystal **4**. This corresponds to seven molecules of methanol for each molecule of complex. One of the methanol molecules is disordered in two positions (50:50) located around a twofold axis. The main molecule is also located on the twofold rotation axis showing C2 symmetry in crystal packing.

Results and Discussion

Synthesis of complexes

The ester form of the trpy-P_a ligand (ligand trpy-P_e, Chart 1) was used to synthesize the ruthenium complexes due to the lower coordination capacity of the ester group, thus minimizing the generation of undesired compounds. Furthermore, working with the ester derivate instead of the phosphoric acid allows a simpler workup procedure because of its higher solubility in organic solvents. The followed synthetic strategy is depicted in Scheme 1. The preparation of the Ru(III) precursor consists on the direct reaction between $RuCl_3 \cdot 3H_2O$ and trpy-P_e. The preparation of the dinuclear chloro-

bridged complex **[2](PF$_6$)$_2$** involves the direct reaction of [RuCl$_3$(trpy-P$_e$)], **1**, with the Hbpp ligand (previously deprotonated by MeONa) in the presence of NEt$_3$ as reducing agent and the overnight irradiation overnight with a tungsten lamp. Under an excess of acetate the chloro bridging ligand can be easily replaced by an acetato bridge forming complex **[3](PF$_6$)$_2$** that, later on, is hydrolyzed to the desired aqua complex (**6**$^{3+}$) under acidic conditions. The hydrolysis of the phosphonate group to obtain the phosphoric acid derivate (**4**) is carried out under strictly anhydrous conditions using the chloro-bridged derivate **[2](PF$_6$)$_2$** as starting material. The reaction proceeds *via* substitution of the ethyl groups for TMSBr followed by the hydrolysis with methanol to lead the desired phosphoric acid derivative **4**. During the hydrolysis, the chloro bridge is replaced by a bromo bridging group, and the complex precipitates in its neutral form presenting only one protonated oxygen. This is confirmed by the crystal structure (Figure 1), the mass spectrum (Figure S22) and the redox titration of the resulting complex (Figure S13).

Characterization of the Ru complexes

The complexes presented in the present work were thoroughly characterized in solution by the usual spectroscopic (UV-vis, MS and NMR) and electrochemical (CV) techniques, and in the solid state by means of X-ray diffraction analysis.

For complex **4** suitable crystals for X-ray diffraction analysis were obtained by slow evaporation of a MeOH solution. Its crystallographic data are listed in Table 1 and a view of its molecular structure is depicted in Figure 1. The structure shows the two ruthenium centers with a distorted octahedral coordination and double bridged by the bpp$^-$ and the bromo ligands that occupy three of the four merdional coordination positions. The fourth position is occupied by the tridentate trpy ligand, which is situated perpendicular to the bpp$^-$. The added phosphoric group originates a distortion in the planarity of the terpyridine group, being the angle between the two trpy ligands of 47º instead of the 66º found for the non-substituted Cl-bridge complex **[Ru^{II}$_2$(μ-Cl)(bpp)(trpy)$_2$](PF$_6$)$_2$** [**7**](PF$_6$)$_2$.[8] This angle diminution could be caused by the hydrogen bonds established between the two phosphoric groups and a methanol molecule, which is situated in-between (Figure 1b). As expected, the phosphoric moiety attached to the central pyridine of terpyridine is not involved in the first coordination sphere of ruthenium. The metal-ligand bond distances are typical and similar to the values obtained for related ruthenium complexes.[6,8]

Table 1. Crystallographic Data for Complex **4**

Empirical formula	C_{50} H_{59} Br N_{10} O_{13} P_2 Ru_2
Formula Weight	1352.06
Temperature, K	100(2)
Wavelength, Å	0.71073
Crystal system	Monoclinic
Space group	I2/a
a, Å	17.5058(13)
α , deg	90.00
b, Å	13.7662(9)
β , deg	101.695(4)
c, Å	24.003(2)
γ , deg	90.00
Vol., Å^3	5664.3(8)
Z	4
ρ (g/cm^3)	1.585
R [I>2 σ (I)]^a	0.0770
wR	0.1717

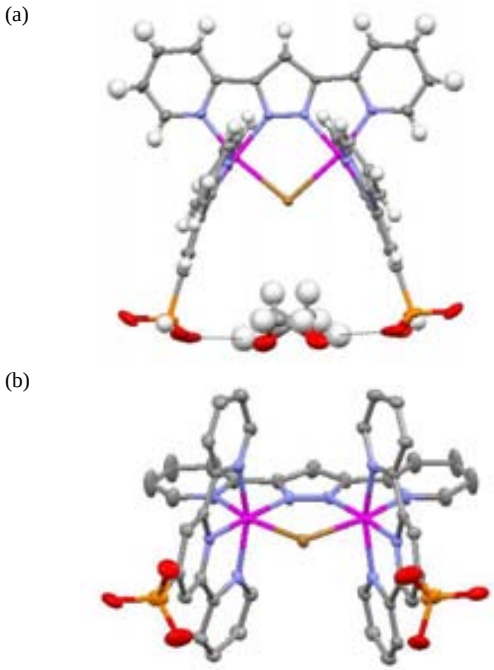

Figure 1. Mercury™ ellipsoid plot (50% probability) for complex **4**. (a) Upper view showing the contact of a methanol molecule and the two phosphonate groups. (b) Frontal view, the hydrogen atoms are not shown. Color codes: Ru, pink; Br, Yellow; N, blue; O, red; H, white; P, orange; C, grey.

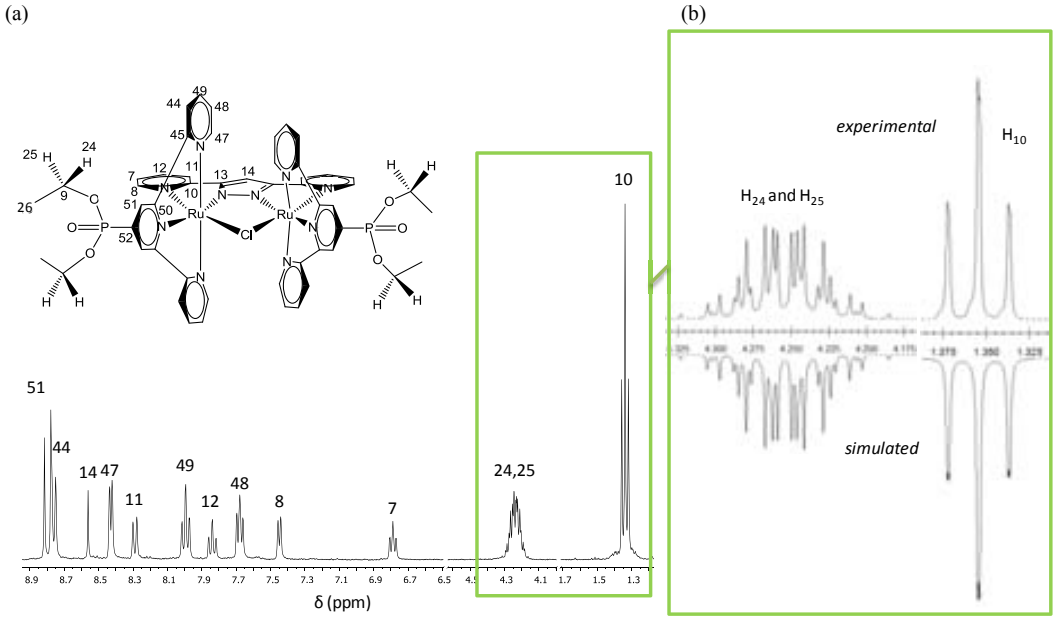

Figure 2. (a) Drawn structure with atom labelling scheme and ^{1}H-NMR (acetone-d_6) for complex **[2](PF$_6$)$_2$**. (b) Comparison of the experimental and the simulated spectrum of the ethyl fragment.

Complexes $\mathbf{2}^{2+}$, $\mathbf{3}^{2+}$, $\mathbf{6}^{3+}$ and **4** were characterized in solution by 1D and 2D NMR spectroscopy (Figure 2, Experimental Section and Figures S1-S4). All the resonances observed in the spectra could be unambiguously assigned based on their integrals, symmetry and multiplicity. In complexes $\mathbf{2}^{2+}$ and $\mathbf{3}^{2+}$, the CH_2 groups of the ethyl chains in the phosphonate moieties presents a diastereotopic behaviour caused by their restricted rotation. This fact combined with the coupling to the CH_3 protons and the phosphorous atoms, makes them to appear as a complex multiplet. Simulations using the gNMR[16] software (Figure 2b) proved that the signals can be interpreted as two ddq and allowed to calculate the coupling constants and the chemical shift for these protons, which were 4.240 and 4.268 ppm for $\mathbf{2}^{2+}$, and 4.297 and 4.320 ppm for $\mathbf{3}^{2+}$. The chloro bridged dinuclear complex $\mathbf{2}^{2+}$ displays a C_{2v} symmetry in solution, with one symmetry plane containing the bpp$^-$ ligand as well as the two Ru centers, the Cl$^-$ bridging ligand and the central N of the trpy moieties. This plane bisects the trpy ligands and is perpendicular to a second symmetry plane that bisects the bridging bpp$^-$ and interconverts the two terpyridines. However, the acetato $\mathbf{3}^{2+}$ and diaqua $\mathbf{6}^{3+}$ complexes present a reduced C_2 symmetry. In order to accommodate the acetato bridge or the diaqua monodentate ligand, the pseudo-octahedral geometry of the Ru metal centers has to be further distorted. Furthermore, in solution and at room temperature these two complexes present dynamic behaviour and, consequently, an apparent C_{2v} symmetry is observed in NMR. Consequently, the external pyridyls of the trpy ligand (that move together with the corresponding metal center) appear as magnetically equivalent at room temperature.[17,9] In the NMR spectrum of complex **4** is important to note the absence of aliphatic signals, which confirms the successful completion of the hydrolysis process. The chemical shifts in the ^{31}P $\{^1$H$\}$ NMR spectra were the expected for this kind of phosphorous atom (See Figures S1-S4).[18]

The UV-vis spectral features for complexes **1-4** and $\mathbf{6}^{3+}$ in CH_2Cl_2, MeOH or pH=1 aqueous solution are listed in the experimental section. As general trend three main regions can be distinguished: one between 200 and 350 nm, in which very intense absorptions are observed due to intra-ligand π-π* transitions; [19] the second between 350 and 550 nm, in which mainly broad unsymmetrical Ru(dπ)-trpy/bpp(π*) metal-to-ligand charge transfer (MLCT) bands are observed;[20] and finally the third above 550 nm in which d-d transitions appear. Comparing the spectra of the trpy-P$_e$ containing complexes with the ones reported for the non-phosphonated analogs, a 15 nm red shift of the MLCT bands can be observed.

Cyclic voltammetry (CV) experiments were carried out to evaluate the electrochemical

Table 2. Redox properties and numbering for the complexes described in the present work and for related Ru-Hbpp complexes for comparative purposes.[a] ($E_{1/2}$ in V and ΔE in mV)

		IV,III-III,III		III,II-II,II		III,III-III,II	
		$E_{1/2}$	ΔE	$E_{1/2}$	ΔE	$E_{1/2}$	ΔE
$[Ru^{II}_2(\mu\text{-Cl})(bpp)(trpy)_2]^{2+}$	7^{2+}			0.71	76	1.12	83
$[Ru^{II}_2(\mu\text{-Cl})(bpp)(trpy\text{-}P_e)_2]^{2+}$	2^{2+}			0.84	41	1.19	53
$[Ru^{II}_2(\mu\text{-Cl})(bpp\text{-}R_e)(trpy)_2]^{2+}$	10^{2+}			0.79	52	1.19	58
FTO-TiO_2-$[Ru^{II}_2(\mu\text{-Br})(bpp)(trpy\text{-}P_a)_2]$	FTO-TiO_2-4			0.76	250	1.19	210
FTO-TiO_2-$[Ru^{II}_2(\mu\text{-Cl})(bpp\text{-}R_a)(trpy)_2]^{2+}$	FTO-TiO_2- 12^+			0.73	88	1.20	92
$[Ru^{II}_2(\mu\text{-AcO})(bpp)(trpy)_2]^{2+}$	8^{2+}			0.73	86	1.05	86
$[Ru^{II}_2(\mu\text{-AcO})(bpp)(trpy\text{-}P_e)_2]^{2+}$	3^{2+}			0.85	31	1.12	45
$[Ru^{II}_2(\mu\text{-AcO})(bpp\text{-}R_e)(trpy)_2]^{2+}$	11^{2+}			0.78	93	1.13	90
$[RuCl_3(trpy\text{-}P_e)]$	1			0.16	57		
$[RuCl_3(trpy)]$	14			0.03	50		
$[Ru^{II}_2(H_2O)_2(bpp)(trpy)_2]^{3+}$	9^{3+}	0.88	110	0.65	64	0.59	64
$[Ru^{II}_2(H_2O)_2(bpp)(trpy\text{-}P_e)_2]^{3+}$	6^{3+}	0.95	90	0.70	86	0.66	31
$[Ru^{II}_2(H_2O)_2(bpp\text{-}R_a)(trpy)_2]^{3+}$	13^{3+}	0.98	88	0.66	70	0.61	74
FTO-TiO_2- $[Ru^{II}_2(H_2O)_2(bpp)(trpy\text{-}P_a)_2]$	FTO-TiO_2-5^{2+}	0.97	87	0.63	94	0.60	40
FTO-TiO_2- $[Ru^{II}_2(H_2O)_2(bpp\text{-}R_a)(trpy)_2]^{2+}$	FTO-TiO_2-13^{2+}	1.14	70	0.93	50	0.61	70

[a] Chloro and acetato bridged complexes are recorded using CH_2Cl_2 as solvent whereas the aqua complexes are reported in aqueous solution at pH = 1.0 (0.1 M triflic acid).

properties of the whole set of complexes (Table 2). Complex **1** shows only one quasi-reversible wave at $E_{1/2}$ = 0.16 V vs. SSCE, which is associated to the oxidation of Ru(II) to Ru(III). Comparing the electrochemistry of complex **1** with the reported for the corresponding non-phosphonated analogue, $[RuCl_3(trpy)]$ (**14**), a 120 mV shift to higher potentials is observed. This tendency is also observed in the Ru(II,III/II,II) waves of complexes $\mathbf{2}^{2+}$ and $\mathbf{3}^{2+}$. These complexes present two chemically reversible and electrochemically quasi-reversible redox processes. For complex $\mathbf{2}^{2+}$**,** the first wave appears at $E_{1/2}$= 0.85 V vs. SSCE and is assigned to the formation of the mixed valence species Ru(II,III/II,II) whereas the second one at $E_{1/2}$ = 1.19 V vs. SSCE, involves the removal of a second electron associated with the Ru(II,III/III,III) redox process. The second redox couple is not significantly affected by the presence of the phosphonate group. The 340 mV difference observed between the Ru(II,III/II,II) and Ru(III,III/II,III) redox processes is indicative of the relatively strong electronic coupling between the metal centers through the bridging ligands.[21] To characterize complex $\mathbf{6}^{3+}$, which contains two aqua ligands, the electrochemical experiments were performed at pH = 1.0 in a 0.1 M triflic acid aqueous solution. The redox behaviour observed (Figure 6) is radically different from the previously described for complexes $\mathbf{2}^{2+}$ and $\mathbf{3}^{2+}$ because of the proton transfer can be coupled to the electron transfer. In this case, three redox processes are observed in the CV which are assigned by comparison with the voltammogram recorded for the parent non-phosphonated Ru-Hbpp complex under the same experimental conditions.[9] The first redox couple at $E_{1/2}$ = 0.66 V involves only electron transfer (ET) and is assigned to the process,

$$Ru^{II}H_2O\text{-}Ru^{II}H_2O - 1e^- \rightarrow Ru^{II}H_2O\text{-}Ru^{III}H_2O \quad (1);$$

the second one at $E_{1/2}$ = 0.70 V also involves a proton transfer and is assigned to the process

$$Ru^{II}H_2O\text{-}Ru^{III}H_2O - 1e^- - 1H^+ \rightarrow Ru^{III}H_2O\text{-}Ru^{III}OH \quad (2);$$

and the third and last wave observed at $E_{1/2}$ = 0.95 V generates an oxo group and is assigned to the process

$$Ru^{III}H_2O\text{-}Ru^{III}OH - 1e^- - 1H^+ \rightarrow Ru^{III}OH_2\text{-}Ru^{IV}O \quad (3).$$

There is another redox process not observed in the CV because its potential lies out of the solvent window. This process involves again the simultaneous removal of electrons and protons to generate the bis-dioxido species $Ru^{IV}O\text{-}Ru^{IV}O$, where the formation of the oxido groups allows the easy access to higher oxidation states for complex $\mathbf{6}^{3+}$ *via* their σ- and π-donor capacity.[22] These $Ru^{IV}O\text{-}Ru^{IV}O$ species are the responsible for the generation of molecular oxygen.

Attachment of Ru catalysts onto FTO-TiO_2

Complex **4** was anchored onto conducting FTO-TiO_2 electrodes by soaking the transparent films into a methanolic solution of the complex. This process is found to be strongly dependent on the initial complex concentration (Figure 3). The initial anchoring rate and the final amount of anchored complex show a lineal dependence on the initial concentration of **4** (Figure 3b and S24). Quantification of the anchored complex was achieved by means of UV-vis spectrophotometric experiments (see Figure S26).

In the present work, the previously described anchoring process for complex $[Ru^{II}_2(\mu\text{-Cl})(bpp\text{-}Ra)(trpy)_2]^{2+}$ (**12^{2+}**) onto FTO-TiO_2 has been improved[10] by changing the solvent from acetonitrile to methanol, thus avoiding the possible substitution of the chloro bridge for two acetonitrile molecules but increasing the anchoring time. The same procedure has also been used in the preparation of the FTO-TiO_2-**4** hybrid material.

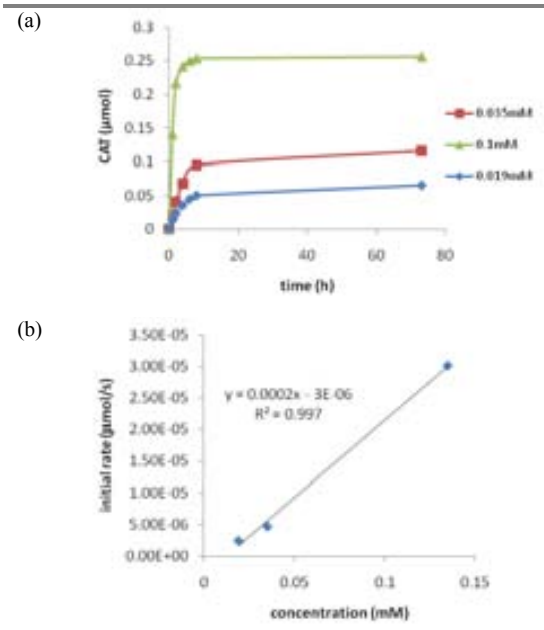

Figure 3. (a) Anchoring evolution profile of complex **4** at three different catalyst concentrations. (b) Initial anchoring rate of complex **4** with regards to its initial concentration in solution.

The anchored halogen-bridge species FTO-TiO_2-**4** and FTO-TiO_2-**12^{2+}** were spectroscopically and electrochemically characterized. In the UV-vis spectra a band appearing at 460 nm, attributed to MLCT, confirms the attachment of the complexes to the FTO-TiO_2 surface (Figure 4b). From an electrochemical point of view, these new heterogeneous materials present similar potentials to those found for the complex **7^{2+}** and slightly lower than their homogeneous analogs **2^{2+}** and $[Ru^{II}_2(\mu\text{-Cl})(bpp\text{-}R_e)(trpy)_2]^{2+}$ (**10^{2+}**) (Figure 5).

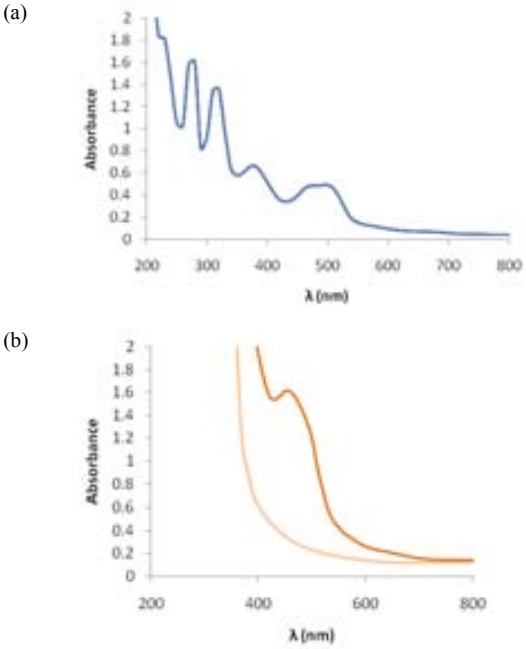

Figure 4. UV-Vis spectroscopy of (a) complex **4** in MeOH, (b) FTO-TiO_2 (light orange) and FTO-TiO_2-**4** (dark orange).

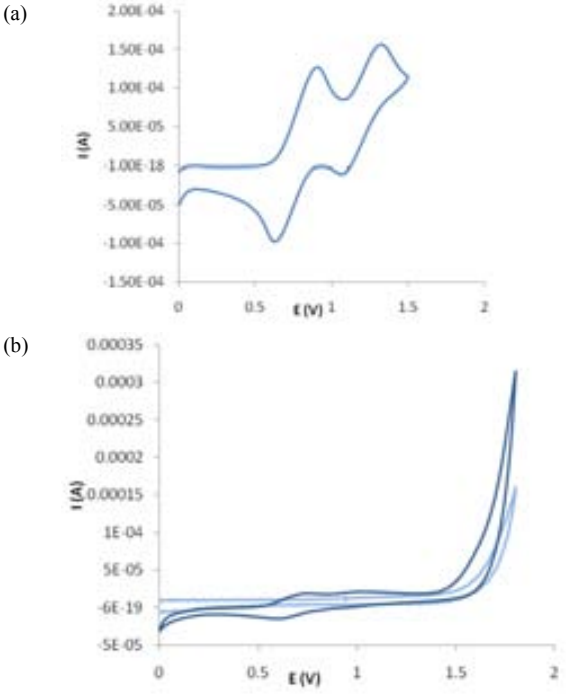

Figure 5. Cyclic voltammograms: (a) FTO-TiO_2-**4** in CH_2Cl_2, scanning anodically at a scan rate of 100 mV/s, (b) FTO-TiO_2-**5^{2+}** at pH=1 in 0.1M triflic acid scanning anodically at a scan rate of 50 mV/s, dark blue, the **FTO-TiO_2** blank, light blue.

The anchored aqua-complexes FTO-TiO_2-$\mathbf{5}^{2+}$ and FTO-TiO_2-$\mathbf{13}^{2+}$ are obtained by soaking the FTO-TiO_2-**4** and FTO-TiO_2-$\mathbf{12}^{+}$ in 0.1 M triflic acid aqueous solution at pH=1 during 24 h. This process allows the replacement of the halogen bridging ligand (Br^- or Cl^-) for two water molecules.

The cyclic voltammograms of FTO-TiO_2-$\mathbf{5}^{2+}$ show a quite different behaviour than its homogeneous counterpart, complex $\mathbf{6}^{3+}$ (Figure 6). The electrocatalytic WO current, clearly observed for complex $\mathbf{6}^{3+}$ with an onset potential of 1.3 V, is not observed for the FTO-TiO_2-$\mathbf{5}^{2+}$ modified films despite scanning up to the same potential values (Figure 6). Moreover, a small shift of this electrocatalytic current can be observed in Figure 4b. The electrochemical studies of the anchored complex FTO-TiO_2-$\mathbf{13}^{2+}$ also show a displacement to upper potentials of the electrocatalytic wave (Figure 7a). These experimental evidences indicate that the anchoring process has modified the catalytic properties of the complexes.

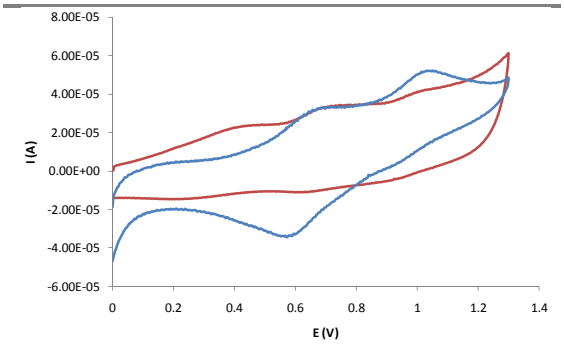

Figure 6. Cyclic voltammograms for complex $\mathbf{6}^{3+}$ (red) and the anchored complex FTO-TiO_2-$\mathbf{5}^{2+}$ (blue).

Water oxidation

Complexes $\mathbf{6}^{3+}$ and $[Ru^{II}_2(H_2O)_2(bpp\text{-}Bz)(trpy)_2]^{3+}$ (corresponding to the homogeneous counterparts of FTO-TiO_2-$\mathbf{5}^{2+}$ and FTO-TiO_2-$\mathbf{13}^{2+}$ respectively) have been tested as water oxidation catalysts, using Ce(IV) as sacrificial oxidant, to insure that the chemical modifications introduced in the ligand have not altered their catalytic performance. Their activities were monitored by manometric techniques together with on-line mass spectrometry. Complex $\mathbf{6}^{3+}$ presents an activity similar to $[Ru^{II}_2(H_2O)_2(bpp)(trpy)_2]^{3+}$ ($\mathbf{9}^{3+}$) (Figure S27), noticing that the additional phosphonate groups have not altered its original behaviour. On the other hand, the additional benzyl moiety present in complex $[Ru^{II}_2(H_2O)_2(bpp\text{-}Bz)(trpy)_2]^{3+}$ cause a clear decrease of its O_2 generation capacity which can be attributed to the observed co-evolution of O_2 and CO_2.[6]

As mentioned before, even though compounds $\mathbf{6}^{3+}$ and $\mathbf{13}^{3+}$ present a WO electrocatalytic wave in solution at 1.3 V vs. SSCE, for the hybrid materials FTO-TiO_2-$\mathbf{5}^{2+}$ and FTO-TiO_2-$\mathbf{13}^{2+}$ one must scan up to 1.6 V in order to observe the incipient beginning of a similar oxidative process. Therefore, potentials of 1.6 and 1.7 V were chosen to perform CPE of the FTO-TiO_2-$\mathbf{5}^{2+}$ and FTO-TiO_2-$\mathbf{13}^{2+}$ modified electrodes, respectively. The catalytic reaction has been carried out in an electrochemical teflon cell (Scheme 2) formed by two different compartments (A and C) separated by a nafion membrane (B). The water oxidation takes place in compartment A whereas the proton reduction occurs in compartment B (Scheme 2).

Scheme 2. Electrochemical cell (left, schematic drawing; right, picture of the real device) formed by: compartment A, where water oxidation takes place; Compartment C, where the proton reduction takes place; Membrane C is a Nafion membrane which is permeable to the proton exchange. 1, Clark electrode; 2, working electrode FTO-TiO_2-catalyst; 3, platinum electrode acting as a counter electrode; 4, SSCE as a reference electrode.

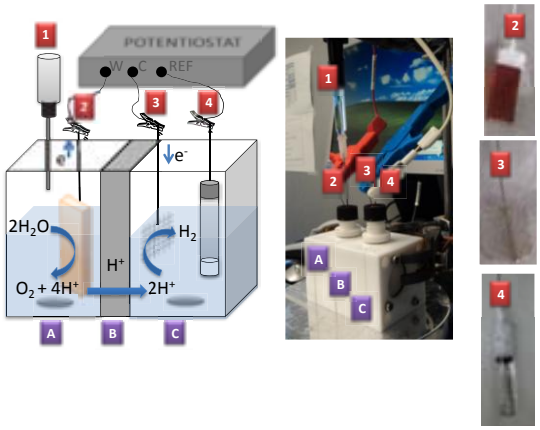

The FTO-TiO_2-$\mathbf{13}^{2+}$ electrode was used as catalyst in the above mentioned electrochemical cell applying a 1.7 V potential during 6 h. Online O_2 measurement on the headspace of the cell compartment using a Clark electrode (1 in Scheme 2) revealed that no oxygen was evolved. The UV-vis analysis of the acidic solution in the anodic cell compartment at the end of the experiment presented an absorption spectra corresponding to a species closely related to $\mathbf{13}^{3+}$, (see Figure S31a). In Figure 7a and 7b the cyclic voltammograms of the FTO-TiO_2-$\mathbf{13}^{2+}$ electrode

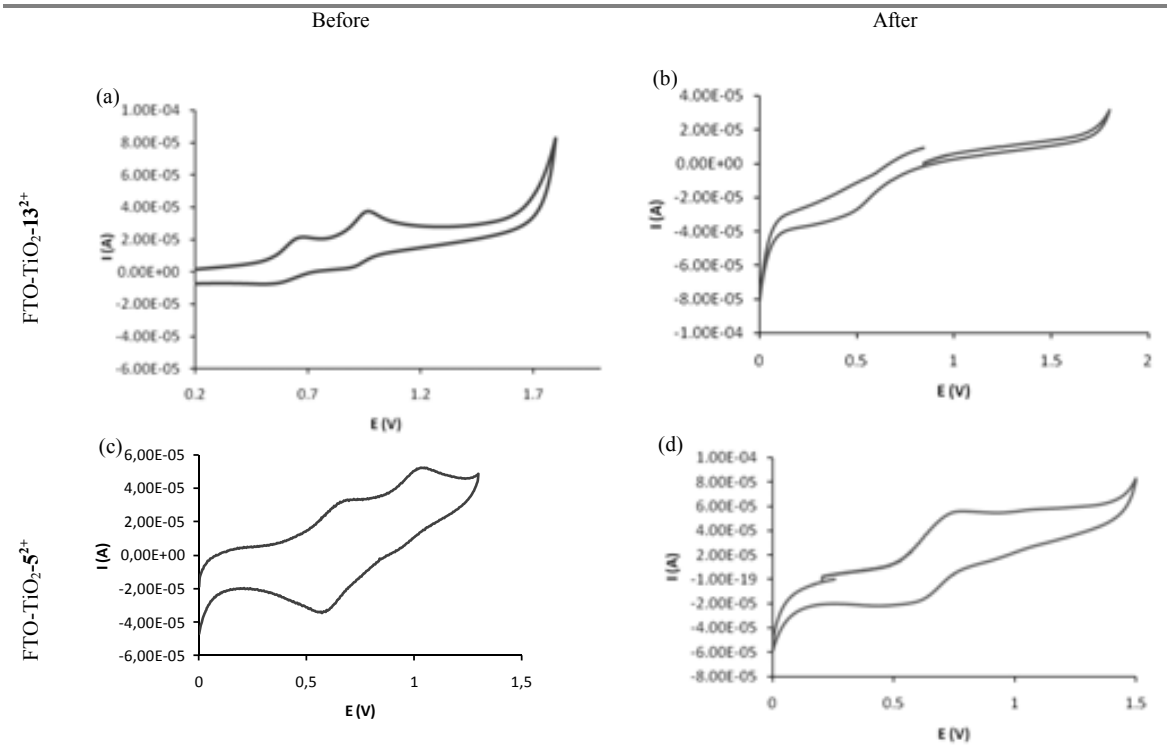

Figure 7. Cyclic voltammograms performed to the anchored catalysts FTO-TiO_2-$\mathbf{5}^{2+}$ and FTO-TiO_2-$\mathbf{13}^{2+}$ before and after the catalytic process.

before and after the controlled potential electrolysis (CPE) are shown. Their comparison reveals an important decrease of the dinuclear ruthenium compound anchored on the surface of the electrode. Additionally, new redox active species were detected. All this data indicates that most of the current was employed in undesired processes which promotes the leaching of the catalyst, reactions involving the decomposition of the anchored catalyst and energy dissipation in the form of heat.

Likewise, the results using FTO-TiO_2-$\mathbf{5}^{2+}$ as electrode showed that when a 1.6 V potential was applied during 6 h no oxygen was generated. However, in this case the leaching process was negligible, as can be observed by comparing the CV before and after CPE (Figures 7c and 7d). The major part of the current could be associated to the blank activity.

In order to evaluate the oxidative capacity towards organic substrates and to gain further insight in the catalytic behaviour of the FTO-TiO_2-$\mathbf{13}^{2+}$ and FTO-TiO_2-$\mathbf{5}^{2+}$ supports**,** the cyclic voltammograms from 0 to 2 V vs SSCE of both anchored complexes were performed in ethanol

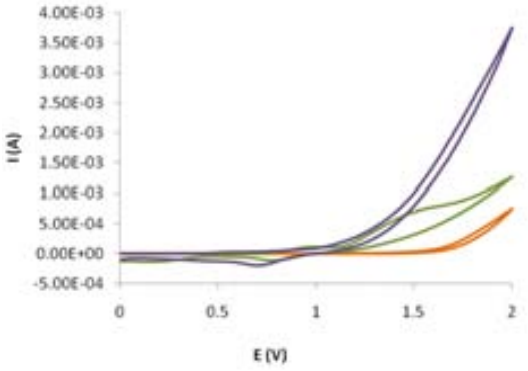

Figure 8. Cyclic voltammograms in EtOH scanning anodically at a scan rate of 20 mV/s: FTO-TiO_2 (orange); FTO-TiO_2-$\mathbf{5}^{2+}$ (green); FTO-TiO_2-$\mathbf{13}^{2+}$ (purple).

as solvent and substrate. To carry out this evaluation the blank (FTO-TiO_2 film as working electrode) electrocatalytic ethanol oxidation wave was compared with the electrocatalytic wave generated when the modified electrodes were employed (FTO-TiO_2-$\mathbf{13}^{2+}$ and FTO-TiO_2-$\mathbf{5}^{2+}$, Figure 8). In both cases an electrocatalytical wave is observed, indicating that both are able to oxidize ethanol. The intensity of this ethanol electrocatalytic wave is higher when FTO-TiO_2-$\mathbf{13}^{2+}$ is used as working electrode, than when FTO-TiO_2-$\mathbf{5}^{2+}$ is used. This difference can be a

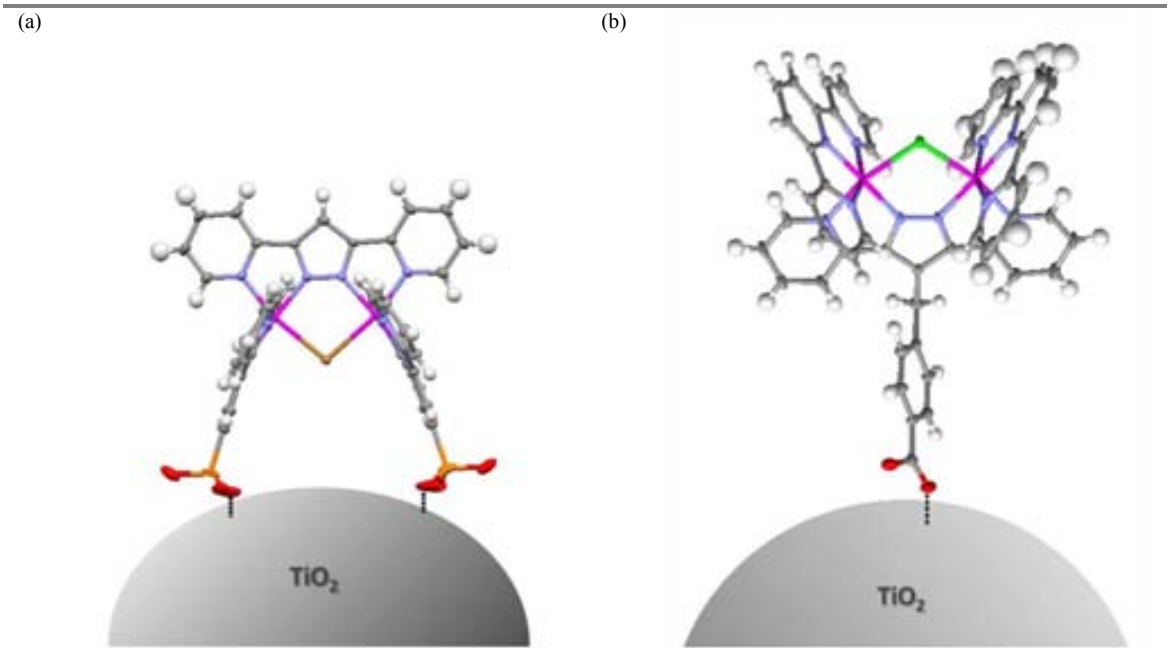

Figure 9. Schematic representation of the active sites orientation in (a) FTO-TiO_2-**4** and (b) FTO-TiO_2-$\mathbf{12}^{2+}$.

consequence of the different orientation of their active sites (Figure 9).

Among the different reasons which can originate the upper shift of the electrocatalytic WO wave observed after the anchoring of compounds $\mathbf{6}^{3+}$ and $\mathbf{13}^{3+}$ onto the solid supports, three key factors should be considered: a) the aqueous phase composition, including potentially coordinating anions b) the interaction between the catalyst and the semiconductor surface and c) the nature of the cavity formed upon the anchoring process.

As has been previously reported for other water oxidation catalysts in homogeneous phase, the anions present in solution could participate in an anation process.[23] Likewise, the interaction of oxygen atoms from TiO_2 with the Ru centers would block the active sites, increasing the potential needed for the activation of the catalytic process.

Alternatively, since we are dealing with a thermodynamic rather than kinetic phenomenon, a hydrophobic nature of the resulting cavity would explain the properties observed in the case of FTO-TiO_2-$\mathbf{5}^{3+}$ (Figure 9). Hence, such a kind of cavity would not favor the access of the H_3O^+ ions to the active catalytic sites, thus being a plausible explanation for the observed redox properties.

As can be observed in Figure 9 the active sites of the modified electrode FTO-TiO_2-$\mathbf{13}^{3+}$ are oriented far from the TiO_2 surface. This

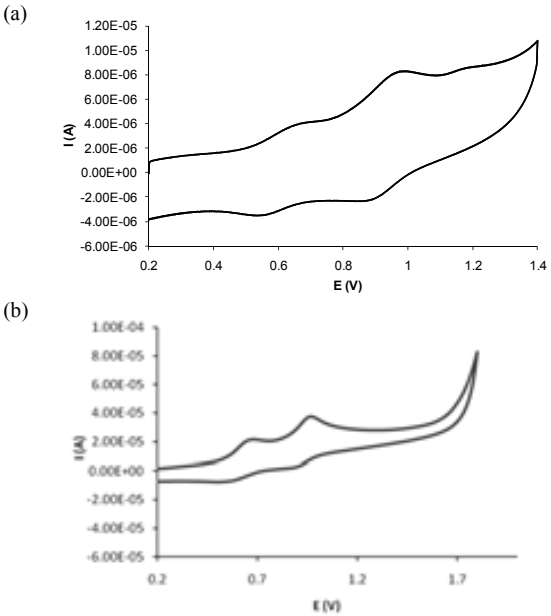

Figure 10. CV of FTO-TiO_2-$\mathbf{13}^{3+}$ anchored using the process which consist in (a) soaking the FTO-TiO_2 films into acetonitrile complex solution during 24 h, and (b) soaking the FTO-TiO_2 films into methanol complex solution during 48 h.

disposition could prevent the formation of the above-mentioned hydrophobic cavity. This fact is in agreement with the nature of the electrocatalytic wave observed when the CV of this hybrid material is performed in ethanol, showing higher electrocatalytic currents than when the FTO-TiO_2-$\mathbf{5}^{2+}$ is employed. Nevertheless, the benzylic ligand moiety could confer enough flexibility to the anchored complex to allow the interaction of the Ru active sites with the O atoms of the TiO_2 surfaces. The

latter, together with the observed oxidative catalyst degradation and subsequent leaching process, could explain the lack of oxygen evolution during CPE when employing this modified electrode. The interaction between the active sites and TiO_2, which seems to be hampering the catalytic activity, could be caused by the prolonged anchoring time needed with the new MeOH anchoring process. Figure 10 shows the CV of FTO-TiO_2-$\mathbf{13}^{2+}$ using the two different anchoring methods: the first one consists on soaking the FTO-TiO_2 films into an acetonitrile solution of the complex during 24 h and the second one performed by soaking the FTO-TiO_2 films into a methanolic solution of the complex during 48 h. As can be observed, in the first case (Figure 10a) the CV is similar to that recorded for its homogenous counterpart. However, for the second one (Figure 10b) the CV only presents two electrochemical waves. The disappearance of several electron transfers in the CV could be indicative of the blocking of the active sites in the later case, thus explaining the observed loose in activity.

Conclusions

In order to face a modular approach for the construction of a real device for artificial photosynthesis, accurate understanding of the limitations and implications of the anchoring of water oxidation catalysts onto semiconductor surfaces such as FTO-TiO_2 is needed. To this end, we have synthesized and thoroughly characterised a family of dinuclear complexes with two phosphonate terpyridines. This new complexes has been anchored onto FTO-TiO_2 [FTO-TiO_2-**4** and FTO-TiO_2-$\mathbf{5}^{2+}$], changing their electrochemical properties to the extent that they are no longer active as water oxidation catalysts. These results have been compared with the ones obtain for the modified electrode FTO-TiO_2-$\mathbf{13}^{2+}$, which is neither active for the oxidation of water.

Furthermore, the presented results demonstrate that the nature and position of the anchoring groups have important influence on the properties of the final hybrid materials and on their catalytic activity. From the experimental data we can conclude that the phosphonate-modified trpy (complex $\mathbf{5}^{3+}$) is a much more robust ligand than its carboxylate-modified Hbpp counterpart (complex $\mathbf{13}^{3+}$). This is clear from the leaching analysis of their corresponding complexes: negligible for the FTO-TiO_2-$\mathbf{5}^{2+}$ and important for the FTO-TiO_2-$\mathbf{13}^{2+}$ one. The lack of catalytic activity in FTO-TiO_2-$\mathbf{5}^{2+}$ could be caused by the hydrophobic cavity formed between the actives sites and TiO_2. On the other hand, when FTO-TiO_2-$\mathbf{13}^{2+}$ is used as working electrode, the non-observed oxygen evolution could be the result of the interaction between the terminal O from TiO_2 and the catalyst active sites (caused by the prolonged anchoring time) together with the ease of its de-anchoring process.

Therefore, the present work constitutes an example of how the heterogenization of a catalyst can result in a material with dramatically modified properties. This work shows that catalyst heterogenization is not a straightforward matter. Thus, more research is urgently needed to understand the additional requirements that a water oxidation catalyst should fulfill to be electrocatalytically employed supported onto conductive surfaces. Appropriate combinations of solid supports, linking functional groups and WO catalysts are currently being tested in our laboratory in order to get active and rugged heterogenous systems.

The application of these modified electrodes as electrocatalysts for organics substrates is also currently being evaluated.[24]

Acknowledgements

Support form SOLAR-H2 (EU 212508) and MEC (CTQ2010-21497 and Consolider Ingenio 2010 CSD2006-0003) are gratefully acknowledged. LF is grateful for the award of doctoral grant from UAB.

References

[1] (a) Hou, H. J. *J. Integr. Plant Biol.* **2010**, *52*, 704-711 and all the reference therein. (b) Hurst, J. K. *Science.* **2010**, *328*, 315-316. (c) Sanderson, K. *Nature.* **2008**, *452*, 400-402.

[2] (a) McConnell, I.; Li, G.; Brudvig, G. W. *Chem. Biol.* **2010**, *17*, 434-447. (b) McDaniel, N. D.; Bernhard, S. *Dalton Trans.* **2010**. (c) Magnuson, A.; Anderlund, M.; Johansson, O.; Lindblad, P.; Lomoth, R.; Polivka, T.; Ott, S.; Stensjö, K.; Styring, S.; Sundström, V.; Hammarström, L. *Acc. Chem. Res.* **2009**, *42*, 1899-1909. (d) Gust, D.; Moore, T. A.; Moore, A. L. *Acc. Chem. Res.* **2009**, *42*, 1890-1898. (e) Herrero, C.; Lassallekaiser, B.; Leibl, W.; Rutherford, A.; Aukauloo, A. *Coord. Chem. Rev.* **2008**, *252*, 456-468. (f) Balzani, V.; Credi, A.; Venturi, M. *ChemSusChem.* **2008**, *1*, 26-58. (g) Armaroli, N.; Balzani, V. *Angew. Chem. Int. Ed.* **2007**, *46*, 52-66.

[3](a) Yamazaki, H.; Shouji, A.; Kajita, M.; Yagi, M. *Coord. Chem. Rev.* **2010**, *254*, 2483-2491. (b) Romero, I.; Rodríguez, M.; Sens, C.; Mola, J.; Rao Kollipara, M.; Francàs, L.; Mas-Marza, E.; Escriche, L.; Llobet, A. *Inorg. Chem.* **2008**, *47*, 1824-1834.

[4] Llobet, A. *Nature Chem.* **2010**, *2*, 804-805. And all the reference therein.
[5] Meyer, T. J.; Huynh, M. H. V. *Inorg. Chem.* **2003**, *42*, 8140-8160.
[6] (a) Francàs, L.; Sala, X.; Escudero-Adán, E.; Benet-Buchholz, J.; Escriche, L.; Llobet, A. *Inorg. Chem.* **2011**, *50*, 2771-2781. (b) Mola, J.; Mas-Marza, E.; Sala, X.; Romero, I.; Rodríguez, M.; Viñas, C.; Parella, T.; Llobet, A. *Angew. Chem. Int. Ed.* **2008**, *47*, 5830-5832.
[7] (a) Chen, Z.; Concepcion, J. J.; Jurss, J. W.; Meyer, T. J. *J. Am. Chem. Soc.* **2009**, *131*, 15580-15581. (b) Concepcion, J.; Jurss, J.; Hoertz, P.; Meyer, T. *Angew. Chem. Int. Ed.* **2009**, 48, 9473-9476.
[8] Sens, C.; Romero, I.; Rodríguez, M.; Llobet, A.; Parella, T.; Benet-Buchholz, J. *J. Am. Chem. Soc.* **2004**, *126*, 7798-7799.
[9] (a) Bozoglian, F.; Romain, S.; Ertem, M. Z.; Todorova, T. K.; Sens, C.; Mola, J.; Rodríguez, M.; Romero, I.; Benet-Buchholz, J.; Fontrodona, X.; Cramer, C. J.; Gagliardi, L.; Llobet, A. *J. Am. Chem. Soc.* **2009**, *131*, 15176-15187. (b) Romain, S.; Bozoglian, F.; Sala, X.; Llobet, A. *J. Am. Chem. Soc.* **2009**, *131*, 2768-2769.
[10] Francàs, L.; Sala, X.; Benet-Buchholz, J.; Escriche, L.; Llobet, A. *ChemSusChem.* **2009**, *2*, 321-329.
[11] (a) Bae, E.; Choi, W. *J. Phys. Chem. B.* **2006**, *110*, 14792-14799. (b) Park, H.; Bae, E.; Lee, J.; Park, J.; Choi, W. *J. Phys. Chem. B.* **2006**, *110*, 8740-8749. (c) Bae, E.; Choi, W.; Park, J.; Shin, H. S.; Kim, S. B.; Lee, J. S. *J. Phys. Chem. B.* **2004**, *108*, 14093-14101.
[12] (a) Hirva, P.; Haukka, M. *Langmuir.* **2010**, *26*, 17075-17081. (b) Johansson, E. M. J.; Plogmaker, S.; Walle, L. E.; Schölin, R.; Borg, A.; Sandell, A.; Rensmo, H. *J. Phys. Chem. C.* **2010**, *14*, 15015-15020. (c) Abrahamsson, M.; Johansson, P. G.; Ardo, S.; Kopecky, A.; Galoppini, E.; Meyer, G. J. *J. Phys. Chem. Lett.* **2010**, *1*, 1725-1728. (d) Sahin, C.; Dittrich, T.; Varlikli, C.; Icli, S.; Lux-Steiner, M. *Sol. Energ. Mat. Sol. C.* **2010**, *94*, 686-690. (e) Liu, F.; Cardolaccia, T.; Hornstein, B. J.; Schoonover, J. R.; Meyer, T. J. *J. Am. Chem. Soc.* **2007**, *129*, 2446-2447. (f) Myahkostupov, M.; Piotrowiak, P.; Wang, D.; Galoppini, E. *J. Phys. Chem. C.* **2007**, *111*, 2827-2829. (g) Kilså, K.; Mayo, E. I.; Brunschwig, B. S.; Gray, H. B.; Lewis, N. S.; Winkler, J. R. *J. Phys. Chem. B.* **2004**, *108*, 15640-15651.
[13] Teixidor, F.; Garcia, R.; Pons, J.; Casabó, J. *Polyhedron.* **1988**, *7*, 43.
[14] TWINABS Version 2008/4 Bruker AXS Blessing, Acta Cryst. (**1995**) A51 33-38.
[15] Sheldrick, G.M. *Acta Cryst.* **2008** A64, 112-122.
[16] P.H.M. Butzelaar, g NMR-version 4.0, IvorySoft, Cherwell Scientific Oxford, UK, **1997**.
[17] Planas, N.; Christian, G. J.; Mas-Marzà, E.; Sala, X.; Fontrodona, X.; Maseras, F.; Llobet, A. *Chem. Eur. J.* **2010**, *16*, 7965-7968.
[18] (a) Houarner-Rassin, C.; Chaignon, F.; She, C.; Stockwell, D.; Blart, E.; Buvat, P.; Lian, T.; Odobel, F. *J. Photochem. Photobiol. A: Chem.* **2007**, *192*, 56-65. (b) Gallagher, L. A.; Serron, S. A.; Wen, X.; Hornstein, B. J.; Dattelbaum, D. M.; Schoonover, J. R.; Meyer, T. J. *Inorg. Chem.* **2005**, *44*, 2089-2097.
[19] (a) Hu, Y.-Z.; Xiang, Q.; Thummel, R. P. *Inorg. Chem.* **2002**, *41*, 3423. (b) Brown, D.; Muranjan, S.; Jang, Y.; Thummel, R. *Org. Lett.* **2002**, *4*, 1253. (c) Wu, F.; Thummel, R. P. *Inorg. Chim. Acta.* **2002**, *327*, 26. (d) Juris, A.; Prodi, L.; Harriman, A.; Ziessel, R.; Hissler, M.; El-Ghayoury, A.; Wu, F.; Riesgo, E. C.; Thummel, R. P. *Inorg. Chem.* **2000**, *39*, 3590. (e) Wu, F.; Riesgo, E. C.; Thummel, R. P.; Juris, A.; Hissler, M.; El-Ghayoury, A.; Ziessel, R. *Tet. Lett.* **1999**, *40*, 7311.
[20] (a) Rodríguez, M.; Romero, I.; Llobet, A.; Deronzier, A.; Biner, M.; Parella, T.; Stoeckli-Evans, H. *Inorg. Chem.* **2001**, *40*, 4150. (b) Barkawi, K.; Llobet, A.; Meyer, T. J. *J. Am. Chem. Soc.* **1988**, *110*, 7751. (c) Llobet, A. *Inorg. Chim. Acta.* **1994**, *221*, 125-131.
[21] Röser, Stephan. *Mono- and Dinuclear Ruthenium Complexes: Synthesis, Characterization and their Impact in Oxidation Reactions*. Tarragona: Universitat Rovira i Virgili, ICIQ, **2011**.
[22] Liu, F.; Concepcion, J. J.; Jurss, J. W.; Cardolaccia, T.; Templeton, J. L.; Meyer, T. J. *Inorg. Chem.* **2008**; *47*; 1727.
[23] (a) Concepcion, J. J.; Jurss, J. W.; Templeton, J. L.; Meyer, T. J. *Proc.Natl. Acad. Sci.* **2008**, *105*, 17632-17635. (b) Liu, F.; Concepcion, J. J.; Jurss, J. W.; Cardolaccia, T.; Templeton, J. L.; Meyer, T. J. *Inorg. Chem.* **2008**, *47*, 1727-1752. (c) Ottenwaelder, X.; Rudd, D. J.; Corbett, M. C.; Hodgson, K. O.; Hedman, B.; Stack, T. D. P. *J. Am. Chem. Soc.* **2006**, *128*, 9268-9269.
[24] (a) Gagliardi, C. J.; Jurss, J. W.; Thorp, H. H.; Meyer, T. J. *Inorg. Chem.* **2011**, *50*, 2076-2078. (b) Drew, K.; Girishkumar, G.; Vinodgopal, K.; Kamat, P. V. *J. Phys. Chem. B.* **2005**, *109*, 11851-11857. (c) Gallagher, L. A.; Serron, S. A.; Wen, X.; Hornstein, B. J.; Dattelbaum, D. M.; Schoonover, J. R.; Meyer, T. J. *Inorg. Chem.* **2005**, *44*, 2089-2097. (d) Gallagher, L. A.; Meyer, T. J. *J. Am. Chem. Soc.* **2001**, *123*, 5308-5312.

SUPPLEMENTARY INFORMATION FOR:

Ru-Hbpp-Based Water-oxidation Catalysts anchored on FTO-TiO_2

Laia Francas,[a] Xavi Sala,[a] Jordi Benet-Buchholz,[b] Antoni Llobet*[a,b] and Lluis Escriche*[a]

[a]Departament de Química, Universitat Autònoma de Barcelona, Cerdanyola del Vallès, E-08193 Barcelona, Spain and [b]Catalan Institute of Chemical Research (ICIQ), Av. Països Catalans 16, E-43007 Tarragona, Spain

lluis.escriche@uab.cat, allobet@iciq.es

Figure S1. 1D and 2D NMR spectra (400 MHz, 298 K, acetone-d^6) for complex $\mathbf{2}^{2+}$: (a) ^{1}H-NMR, (b) COSY, (c) ^{13}C{^{1}H}-NMR, (d) HSQC NMR, (e) aromatic zone HSQC NMR (f) aromatic zone HMBC NMR (g) ^{31}P {^{1}H} NMR (h) HMBC-P NMR.

(a)

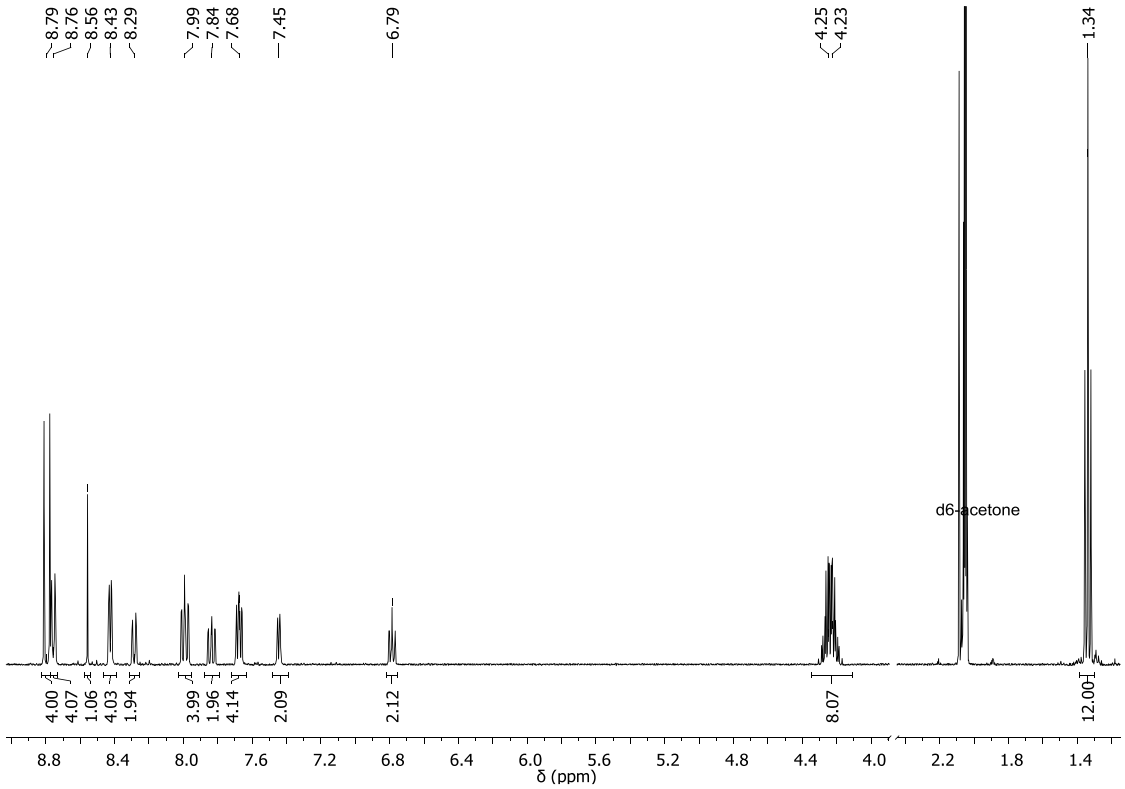

(b)

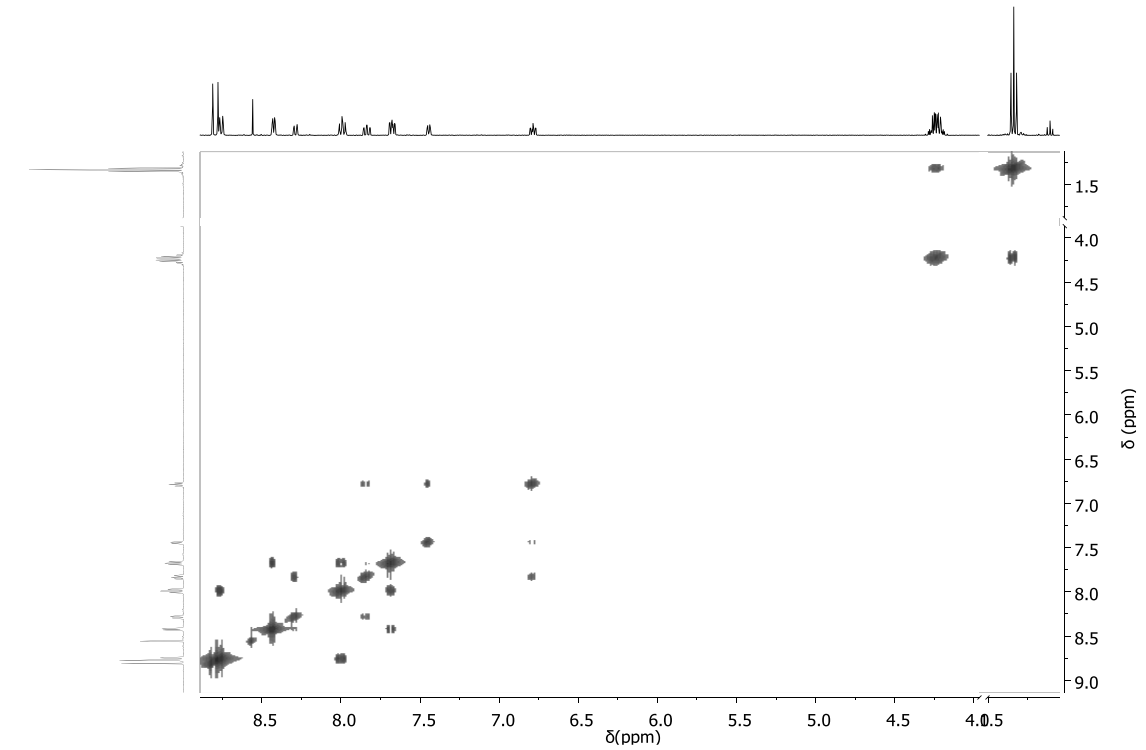

(c)

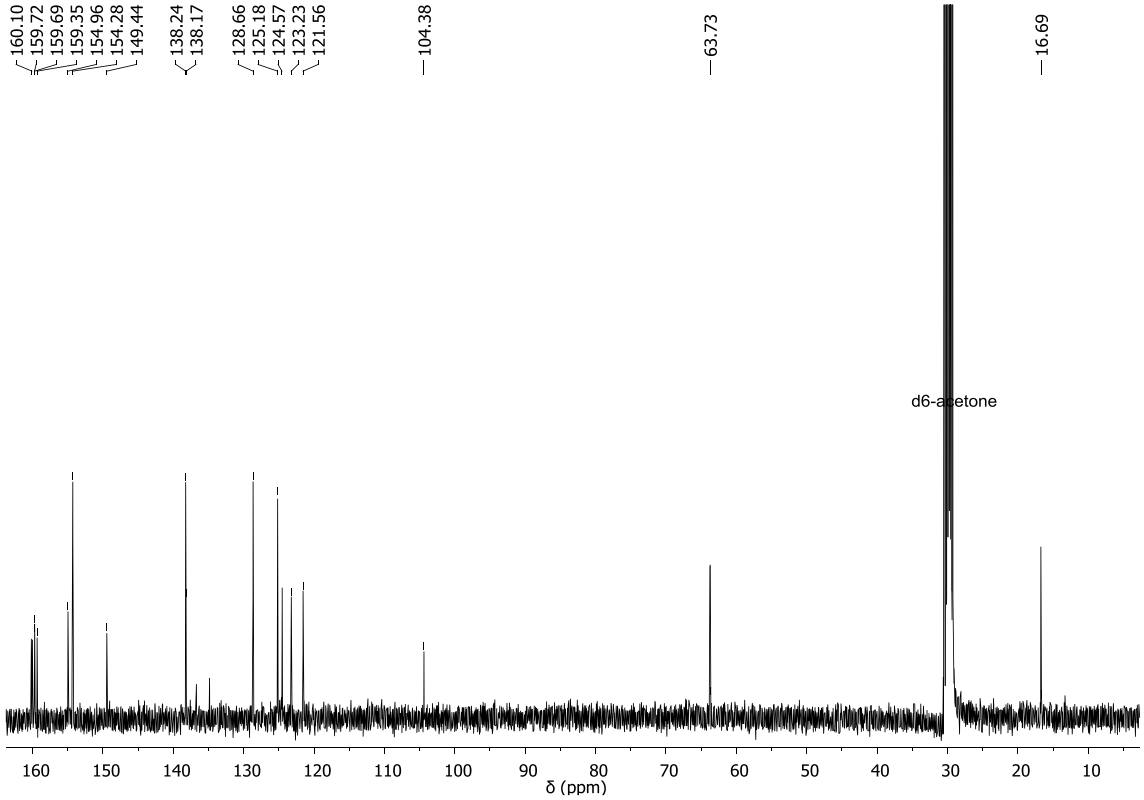
160.10
159.72
159.69
159.35
154.96
154.28
149.44
138.24
138.17
128.66
125.18
124.57
123.23
121.56
104.38
63.73
16.69
d6-acetone
160
150
140
130
120
110
100
90
80
70
60
50
40
30
20
10
δ (ppm)

(d)

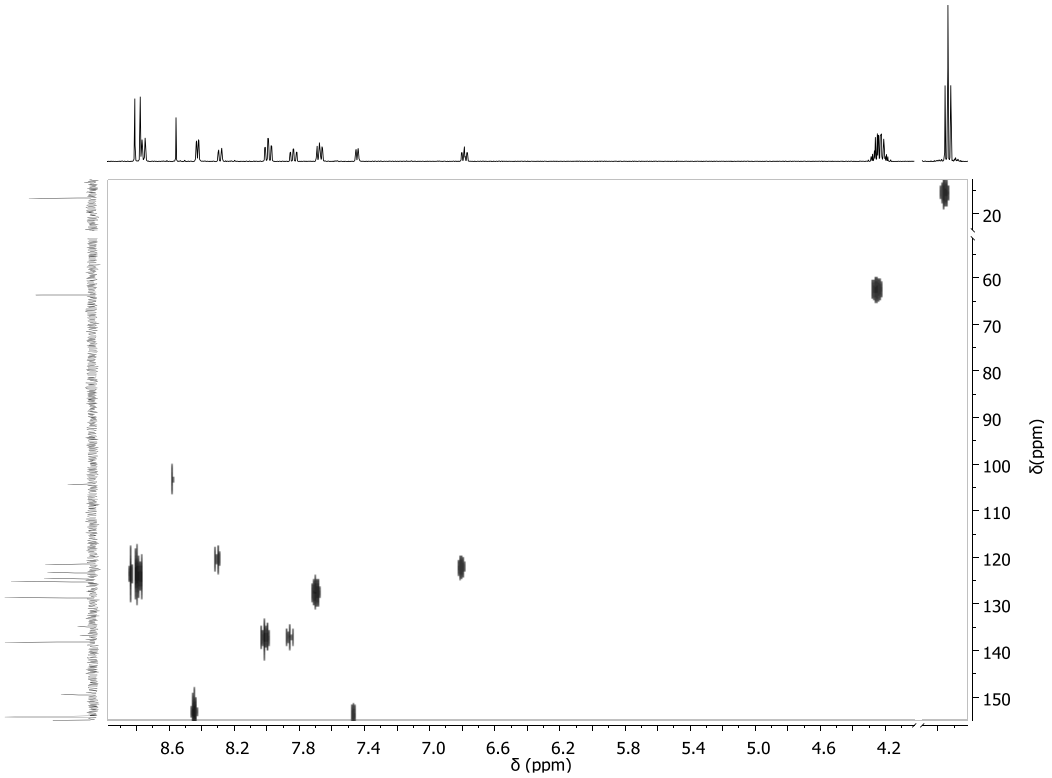
8.6
8.2
7.8
7.4
7.0
6.6
6.2
5.8
5.4
5.0
4.6
4.2
δ (ppm)
20
60
70
80
90
100
110
120
130
140
150
δ(ppm)

(e)

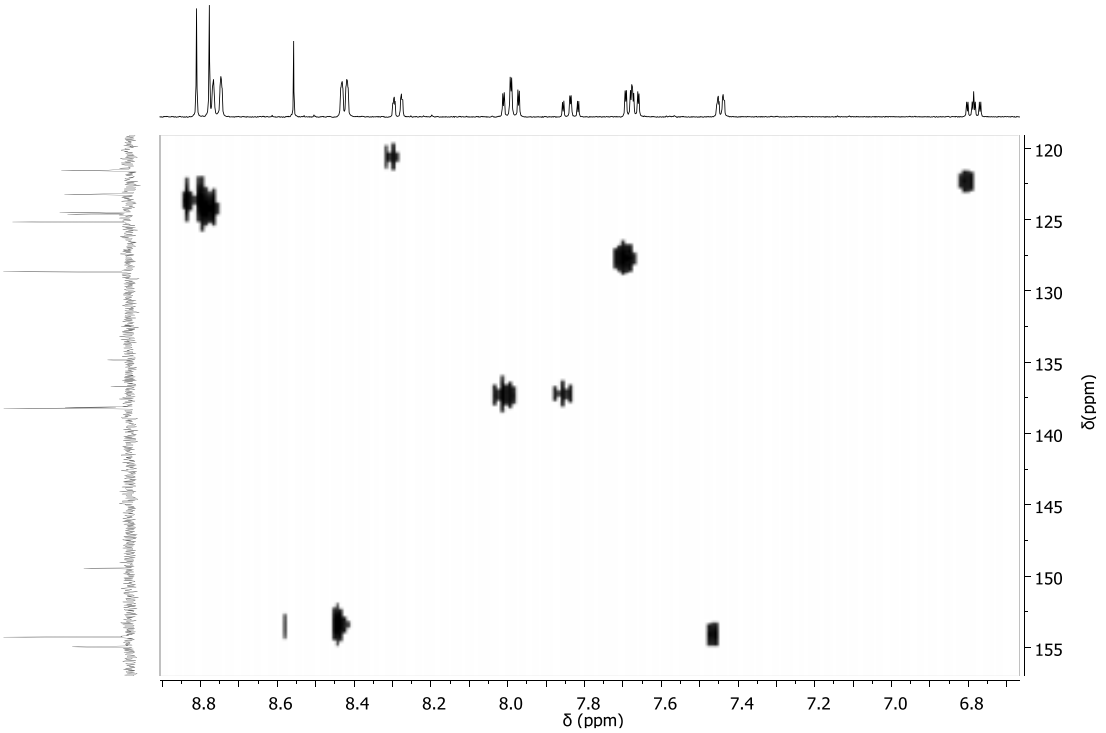
120
125
130
135
140
145
150
155
δ(ppm)
8.8
8.6
8.4
8.2
8.0
7.8
7.6
7.4
7.2
7.0
6.8
δ (ppm)

(f)

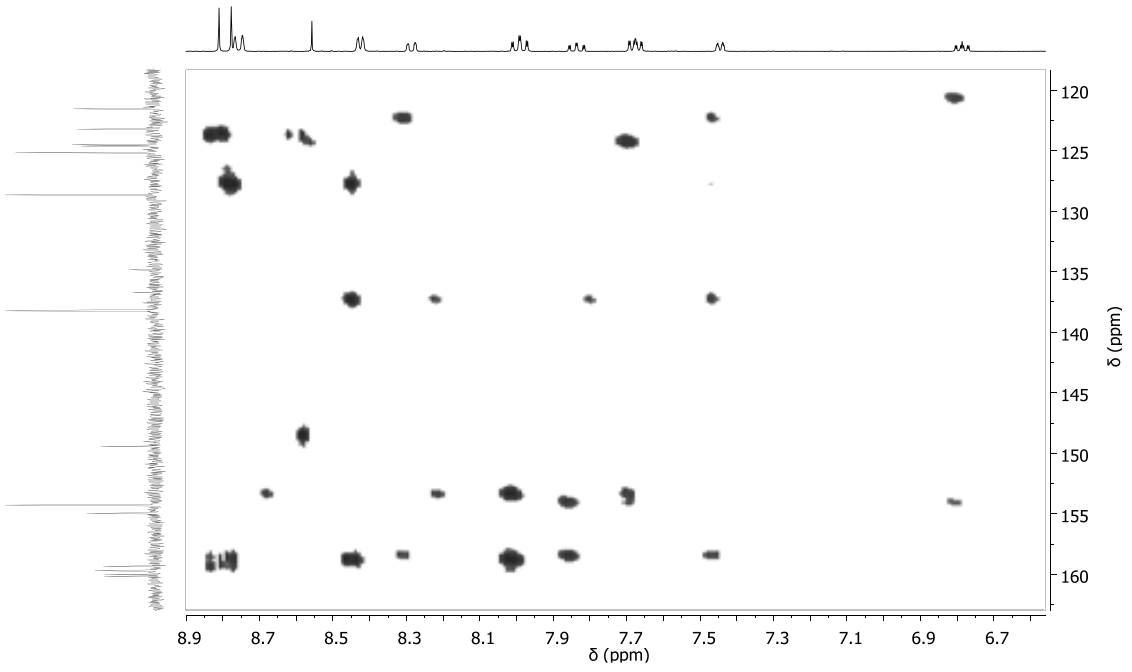
120
125
130
135
140
145
150
155
160
δ (ppm)
8.9
8.7
8.5
8.3
8.1
7.9
7.7
7.5
7.3
7.1
6.9
6.7
δ (ppm)

(g)

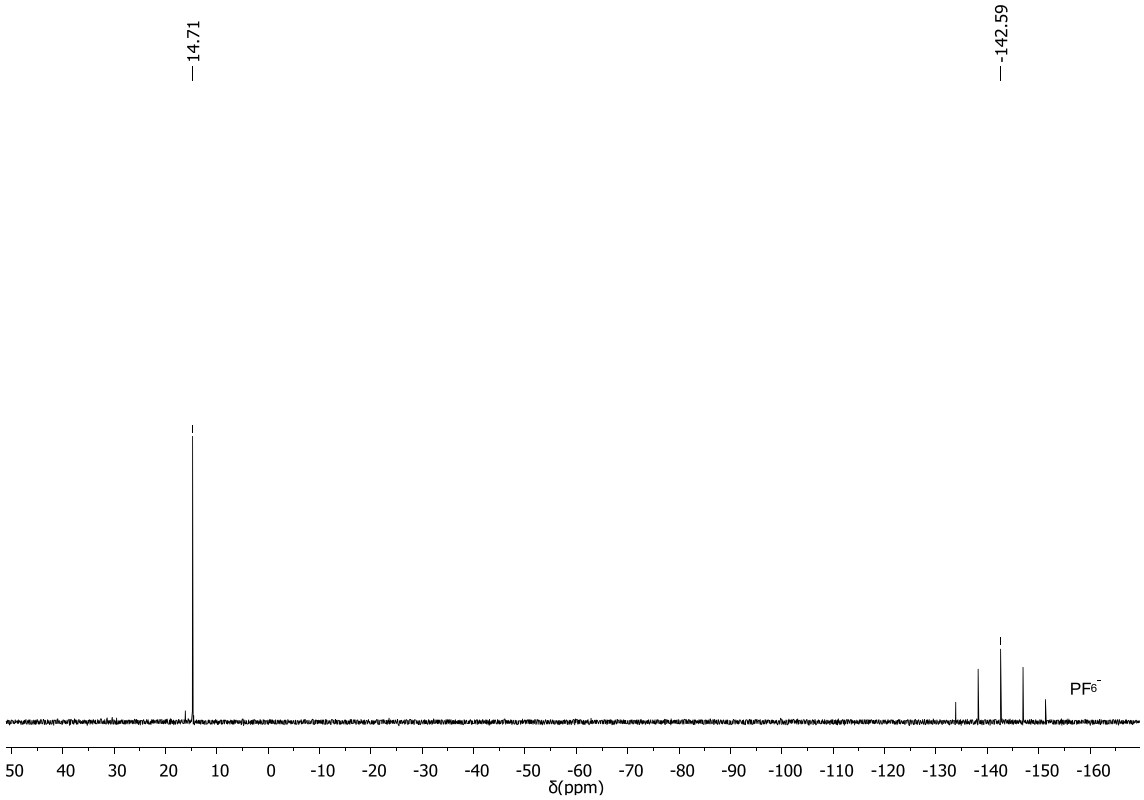
14.71
-142.59
PF6-
50 40 30 20 10 0 -10 -20 -30 -40 -50 -60 -70 -80 -90 -100 -110 -120 -130 -140 -150 -160
δ(ppm)

(h)

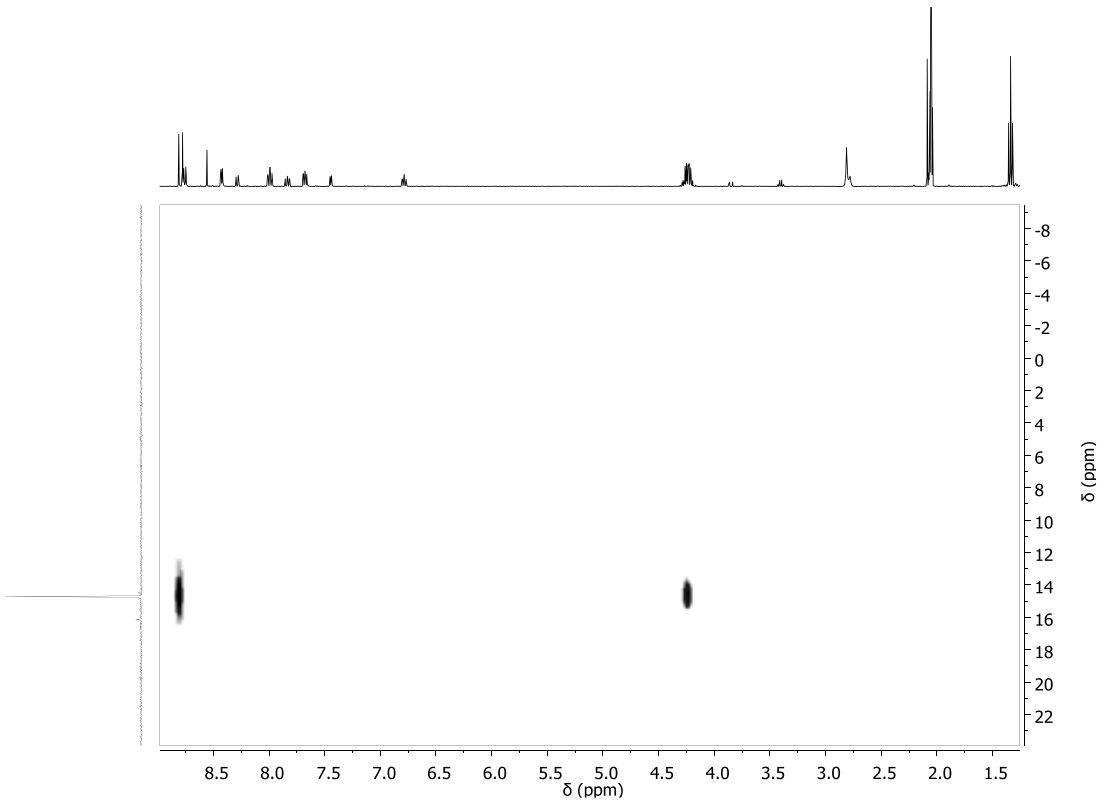
-8 -6 -4 -2 0 2 4 6 8 10 12 14 16 18 20 22
δ (ppm)
8.5 8.0 7.5 7.0 6.5 6.0 5.5 5.0 4.5 4.0 3.5 3.0 2.5 2.0 1.5
δ (ppm)

Figure S2. 1D and 2D NMR spectra (400 MHz, 298 K, acetone-d^6) for complex $\mathbf{3}^{2+}$: (a) ^{1}H-NMR, (b) COSY, (c) ^{13}C{^{1}H}-NMR, (d) HSQC NMR, (e) HMBC NMR (f) aromatic zone HMBC NMR (g) ^{31}P {^{1}H} NMR (h) HMBC-P NMR.

(a)

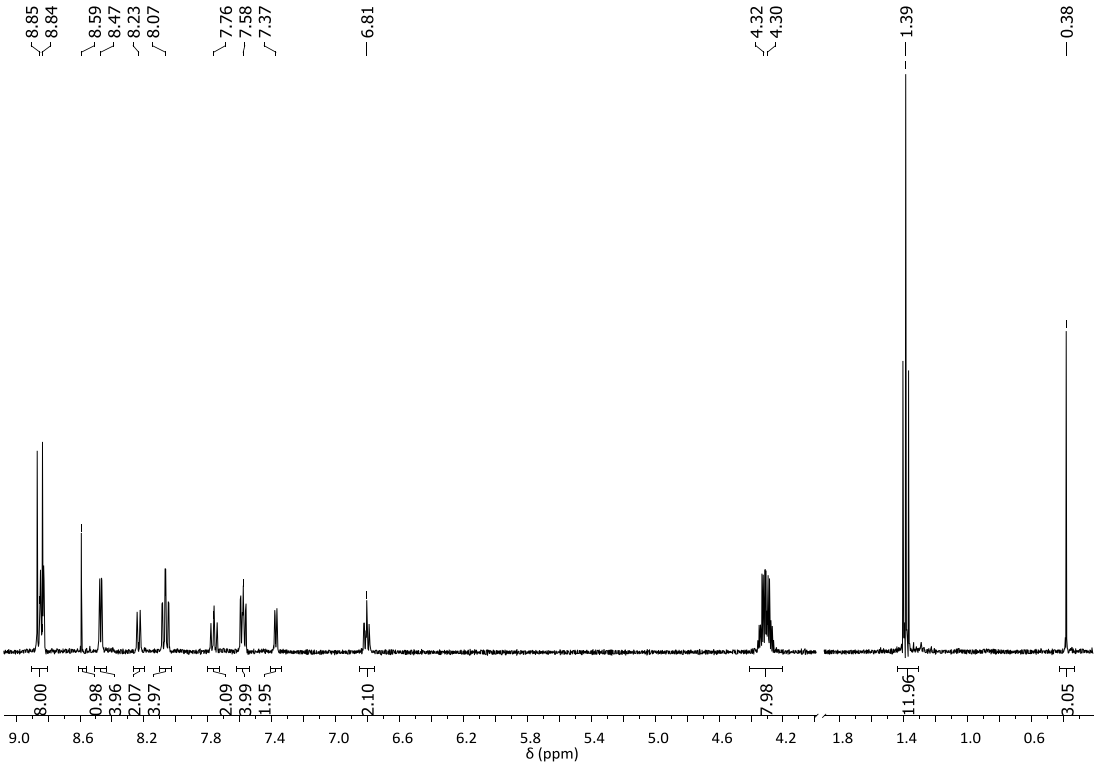

(b)

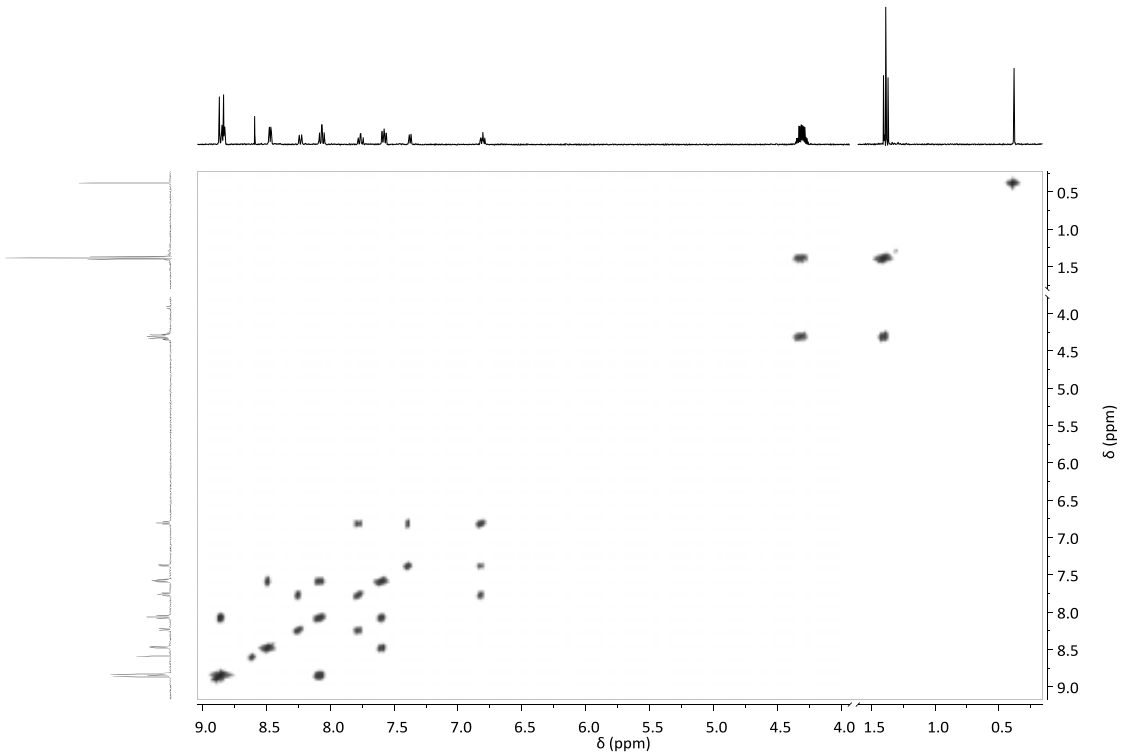

(c)

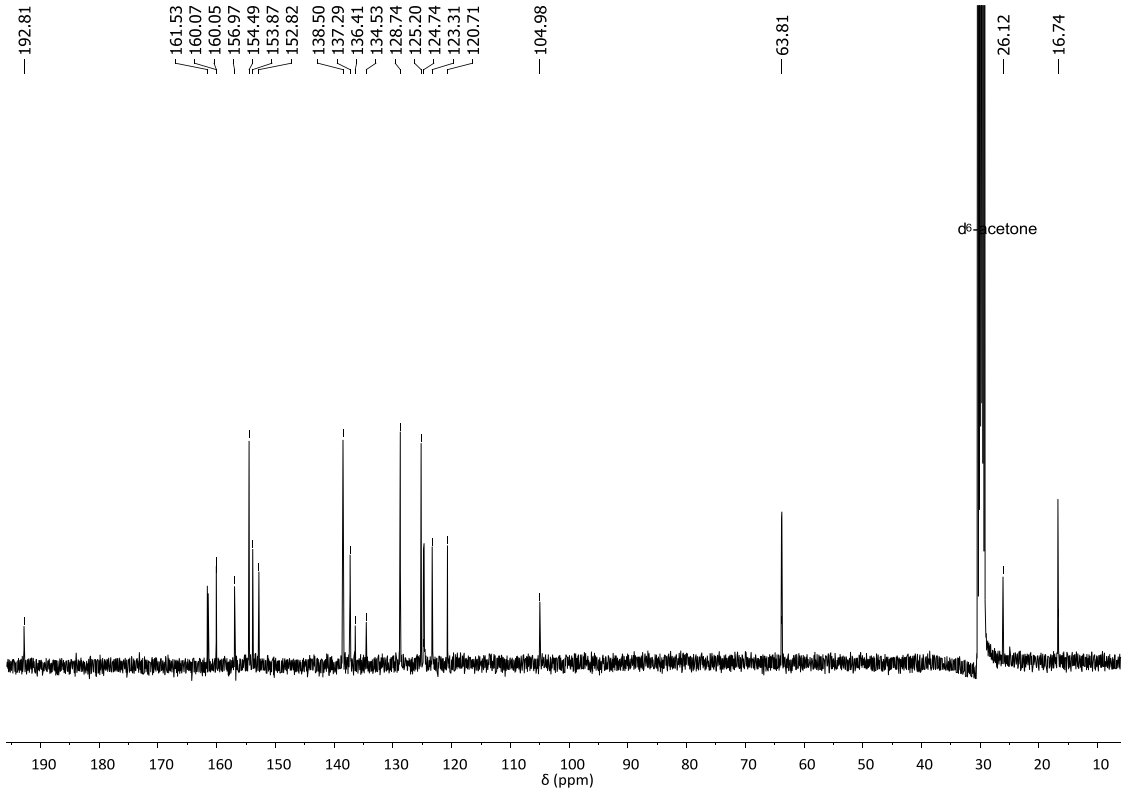
192.81
161.53
160.07
160.05
156.97
154.49
153.87
152.82
138.50
137.29
136.41
134.53
128.74
125.20
124.74
123.31
120.71
104.98
63.81
26.12
16.74
d6-acetone
190 180 170 160 150 140 130 120 110 100 90 80 70 60 50 40 30 20 10
δ (ppm)

(d)

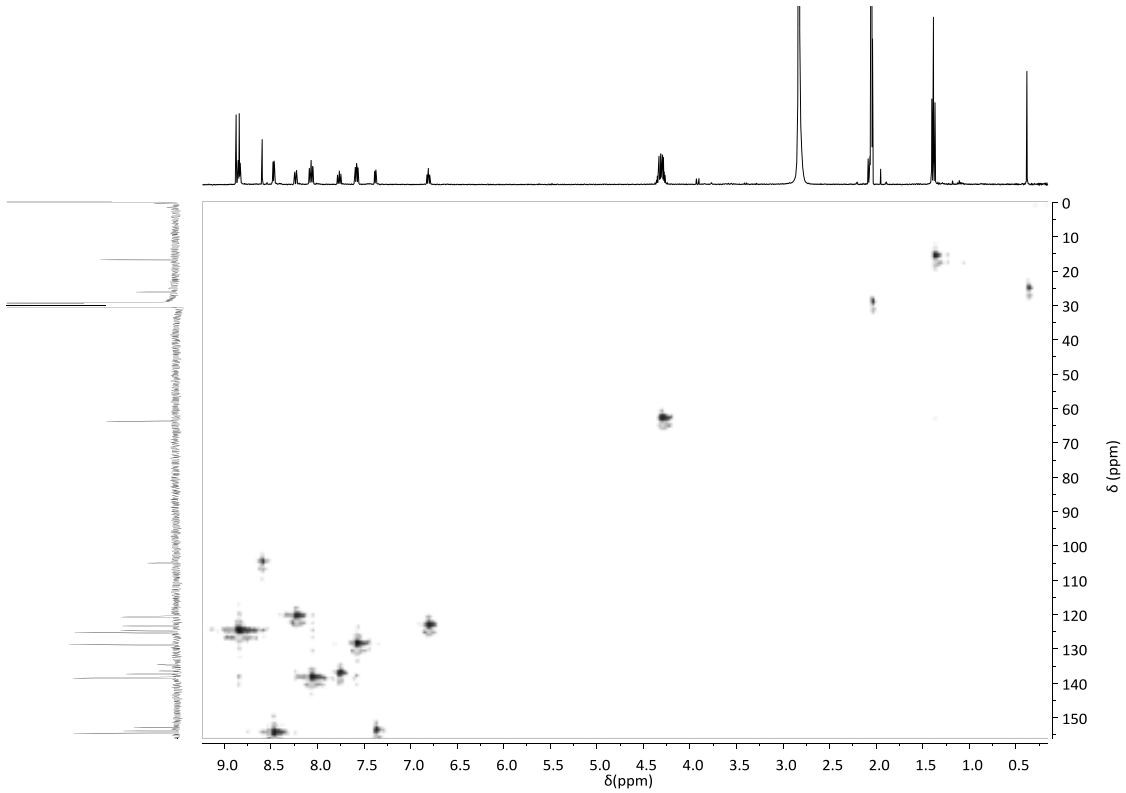
0 10 20 30 40 50 60 70 80 90 100 110 120 130 140 150
δ (ppm)
9.0 8.5 8.0 7.5 7.0 6.5 6.0 5.5 5.0 4.5 4.0 3.5 3.0 2.5 2.0 1.5 1.0 0.5
δ(ppm)

(e)

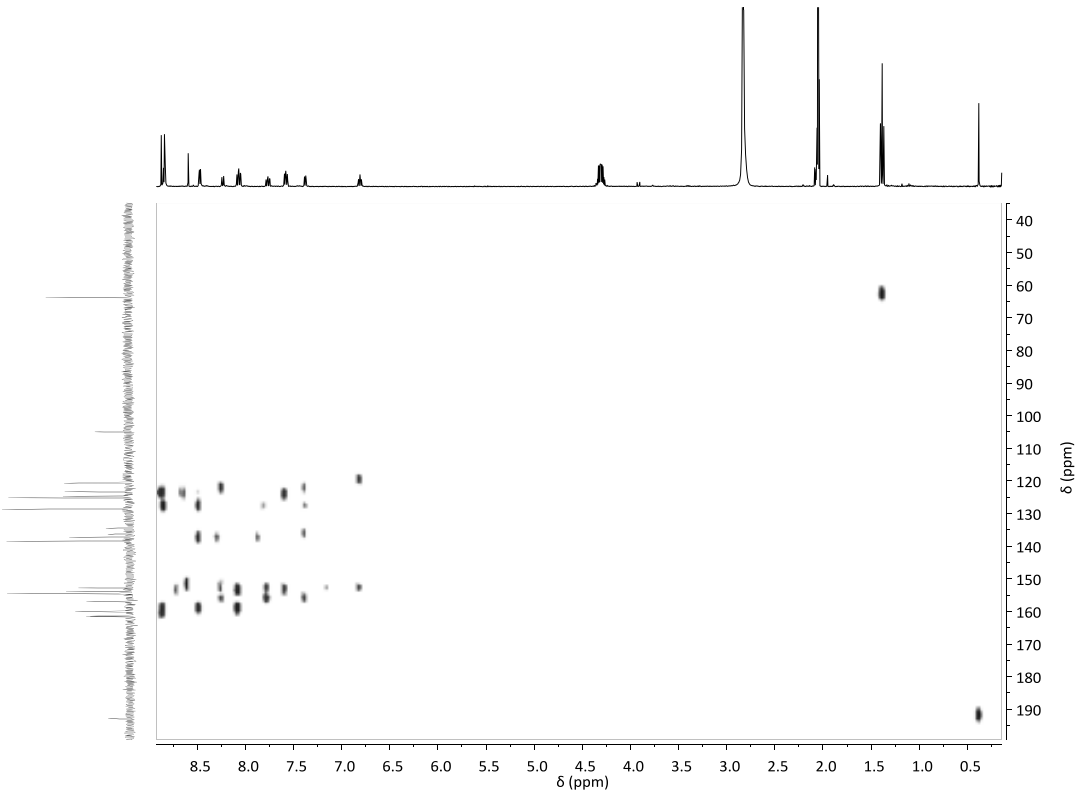
40
50
60
70
80
90
100
110
120
130
140
150
160
170
180
190
δ (ppm)
8.5
8.0
7.5
7.0
6.5
6.0
5.5
5.0
4.5
4.0
3.5
3.0
2.5
2.0
1.5
1.0
0.5
δ (ppm)

(f)

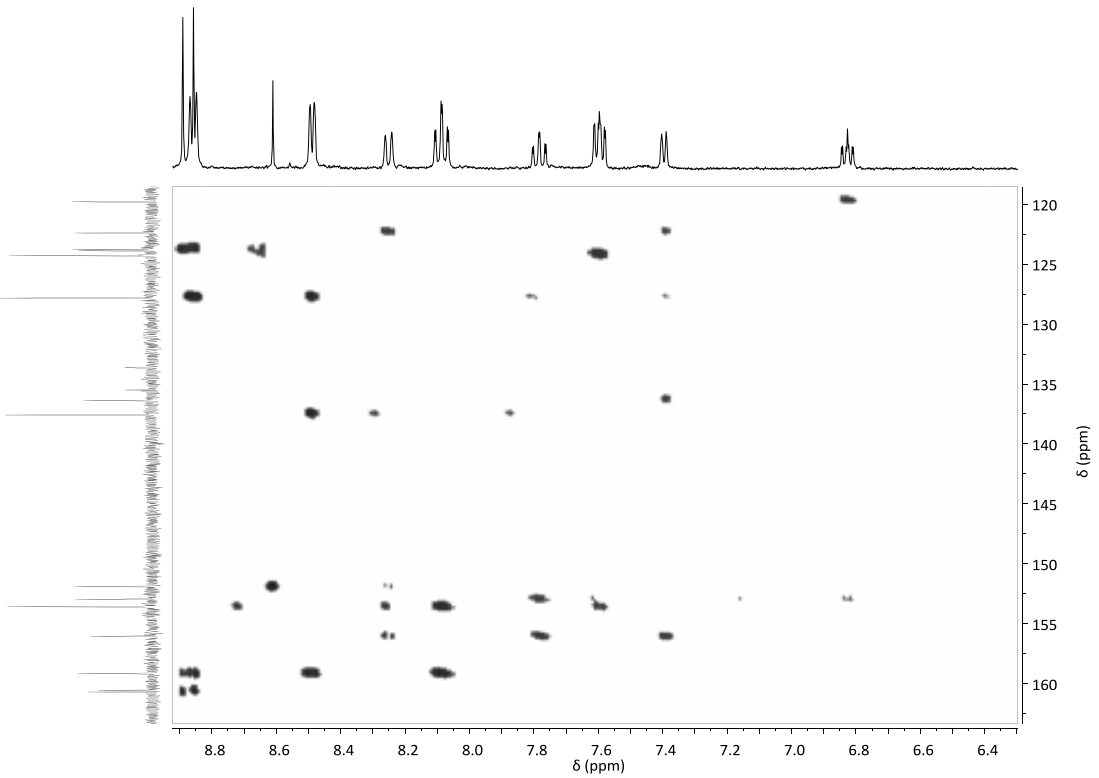
120
125
130
135
140
145
150
155
160
δ (ppm)
8.8
8.6
8.4
8.2
8.0
7.8
7.6
7.4
7.2
7.0
6.8
6.6
6.4
δ (ppm)

(g)

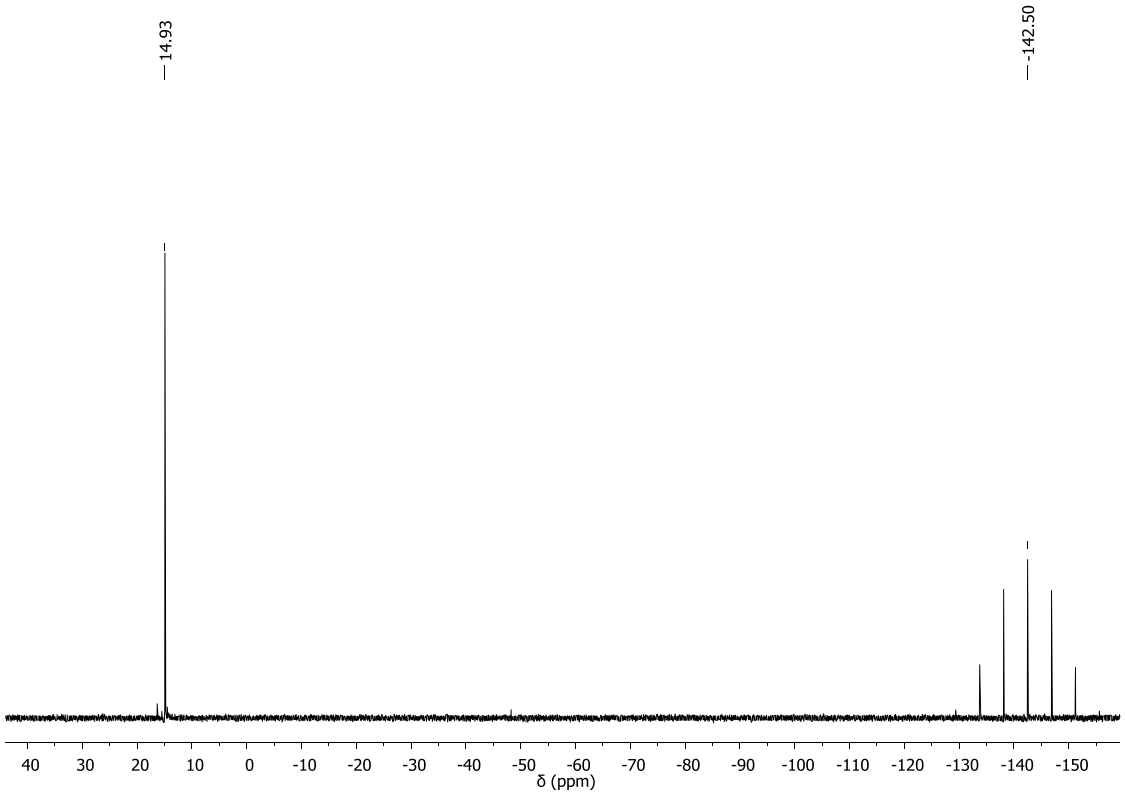
14.93
-142.50
40 30 20 10 0 -10 -20 -30 -40 -50 -60 -70 -80 -90 -100 -110 -120 -130 -140 -150
δ (ppm)

(h)

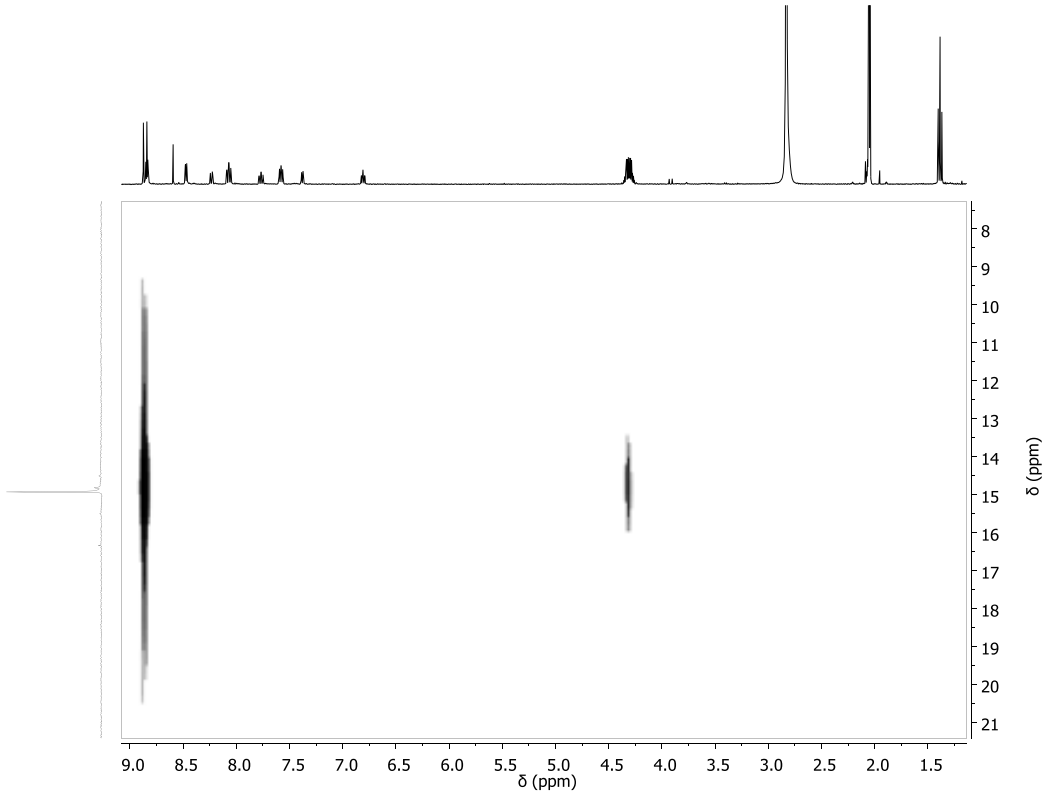
8 9 10 11 12 13 14 15 16 17 18 19 20 21
δ (ppm)
9.0 8.5 8.0 7.5 7.0 6.5 6.0 5.5 5.0 4.5 4.0 3.5 3.0 2.5 2.0 1.5
δ (ppm)

Figure S3. 1D and 2D NMR spectra (400 MHz, 298 K, MeOD-d^4) for complex **4**: (a) ^{1}H-NMR, (b) COSY, (c) $^{13}C\{^1H\}$-NMR, (d) HSQC NMR, (e) HMBC NMR (f) aromatic zone HMBC NMR (g) $^{31}P\ \{^1H\}$ NMR (h) HMBC-P NMR.

(a)

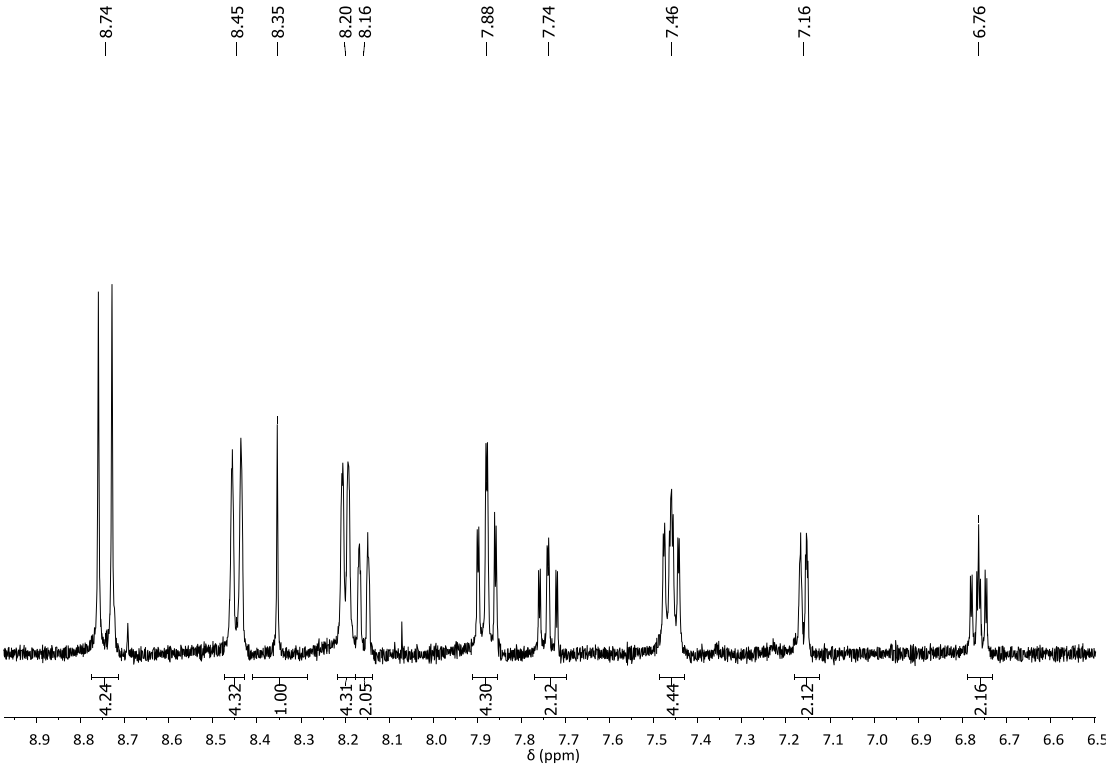

(b)

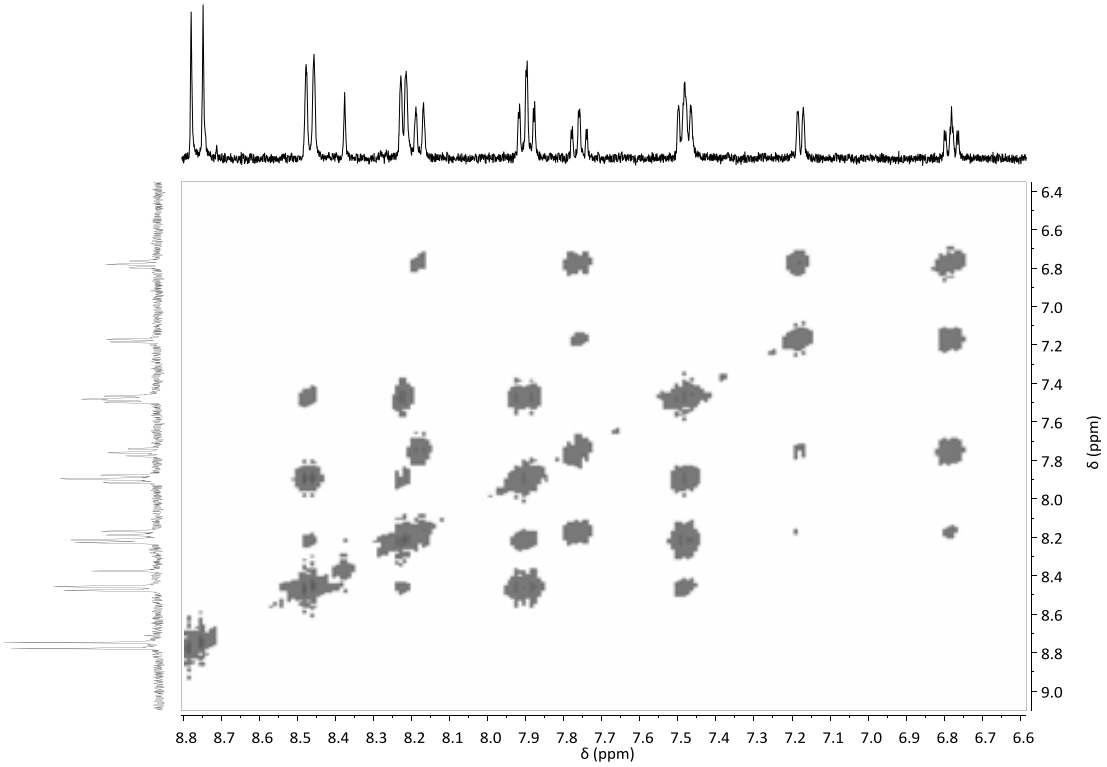

(c)

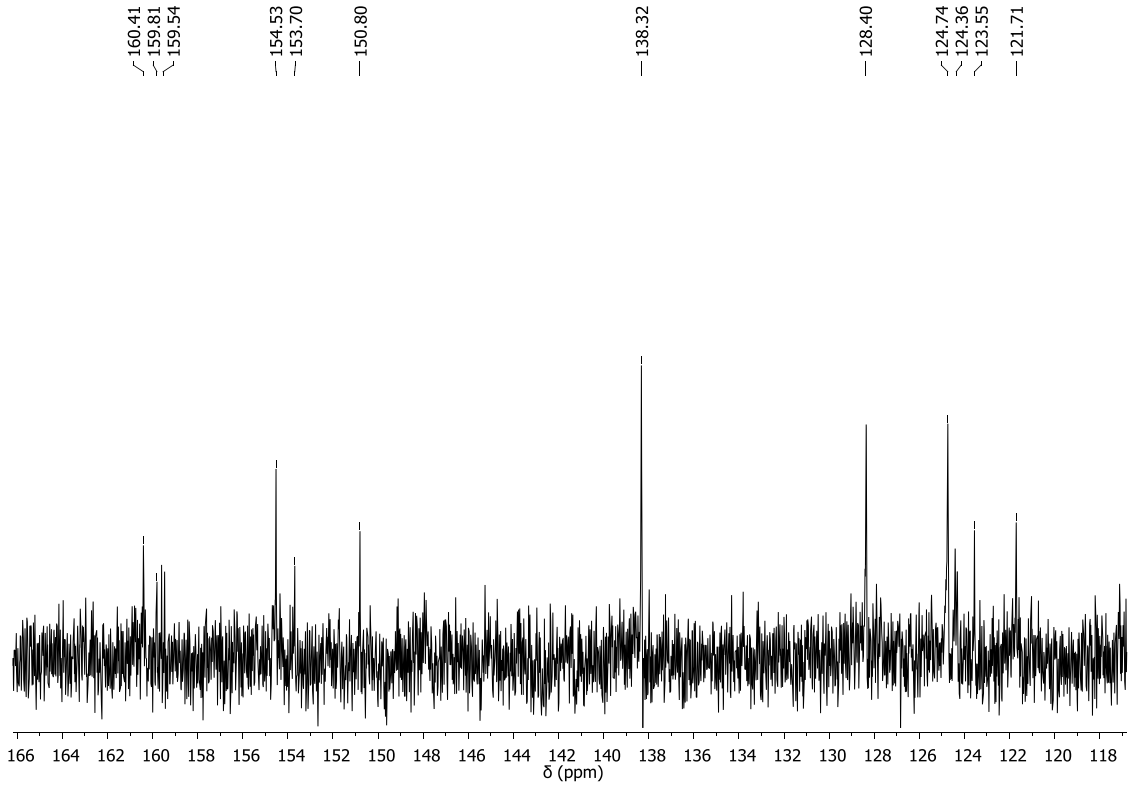
160.41
159.81
159.54
154.53
153.70
150.80
138.32
128.40
124.74
124.36
123.55
121.71
166 164 162 160 158 156 154 152 150 148 146 144 142 140 138 136 134 132 130 128 126 124 122 120 118
δ (ppm)

(d)

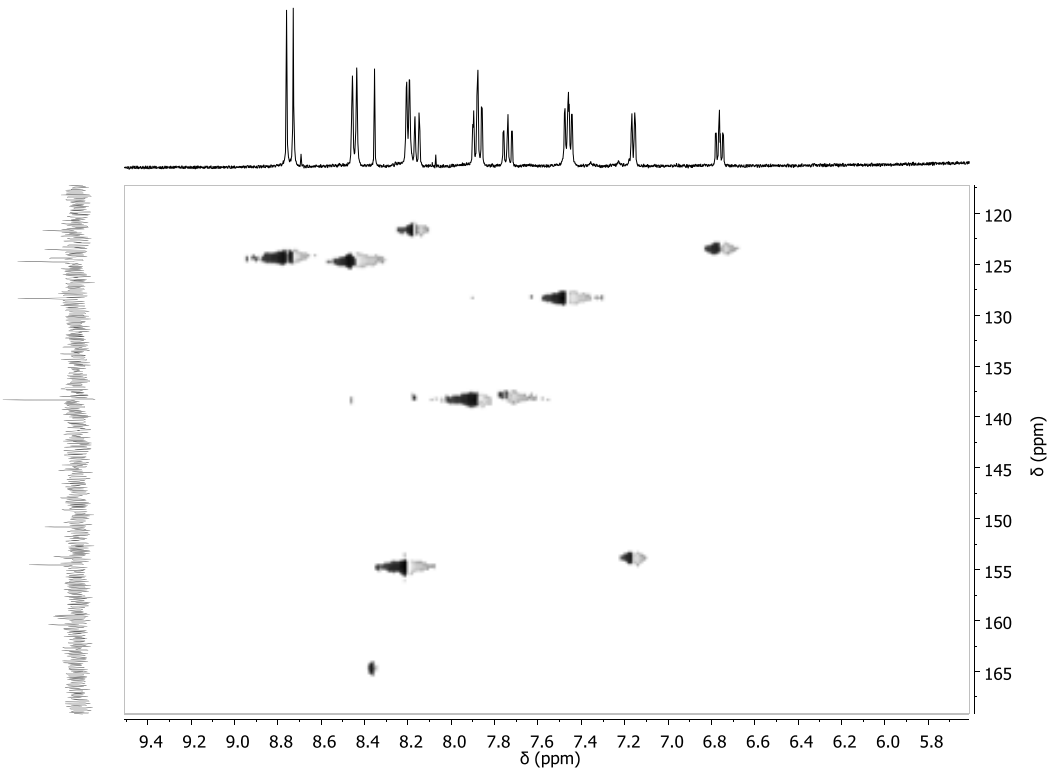
120
125
130
135
140
145
150
155
160
165
δ (ppm)
9.4 9.2 9.0 8.8 8.6 8.4 8.2 8.0 7.8 7.6 7.4 7.2 7.0 6.8 6.6 6.4 6.2 6.0 5.8
δ (ppm)

(e)

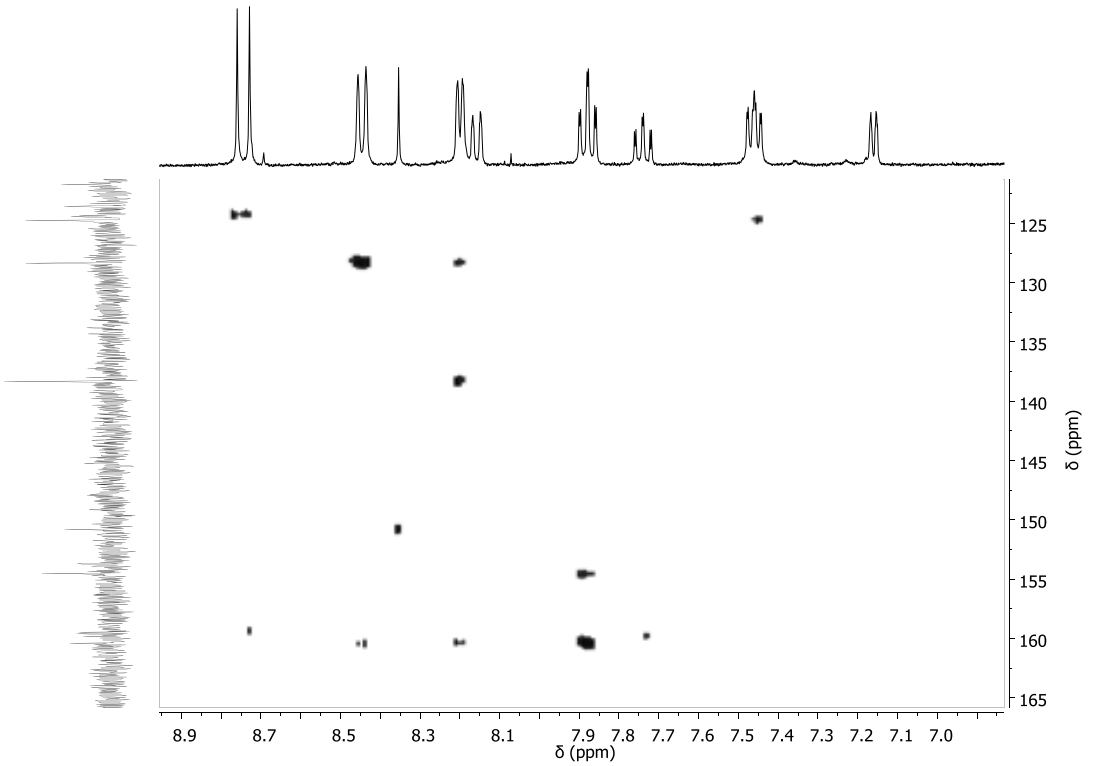
125
130
135
140
145
150
155
160
165
δ (ppm)
8.9
8.7
8.5
8.3
8.1
7.9
7.8
7.7
7.6
7.5
7.4
7.3
7.2
7.1
7.0
δ (ppm)

(f)

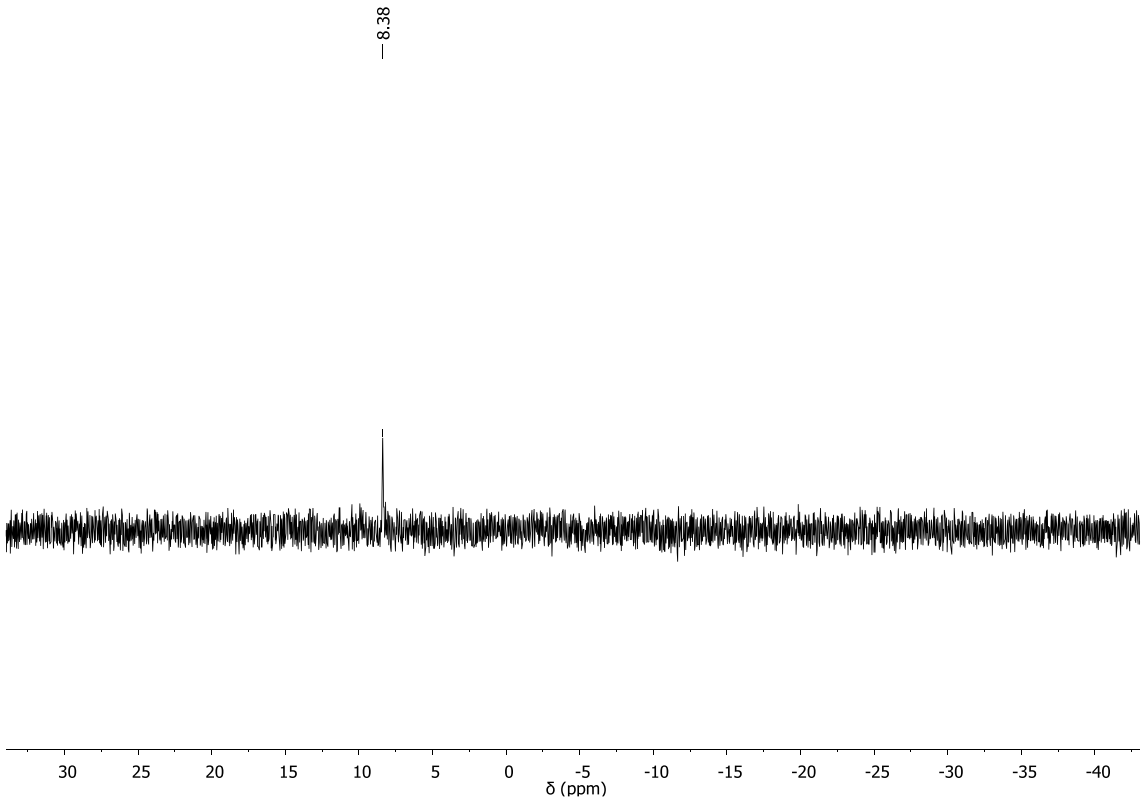
8.38
30
25
20
15
10
5
0
-5
-10
-15
-20
-25
-30
-35
-40
δ (ppm)

(g)

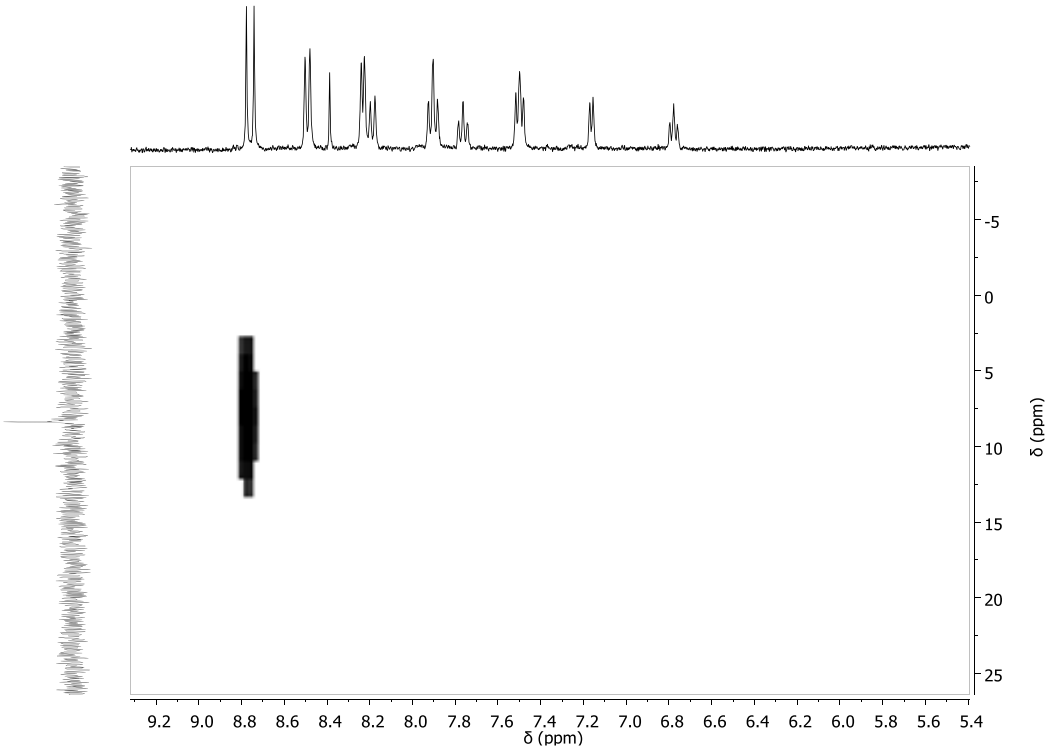

Figure S4. 1D and 2D NMR spectra (400 MHz, 298 K, acetone-d_6 and CD_3COOD in D_2O) for complex $\mathbf{6}^{3+}$: (a) ^{1}H-NMR, (b) COSY, (c) ^{31}P $\{^1H\}$ NMR (d) HMBC-P NMR.

(a)

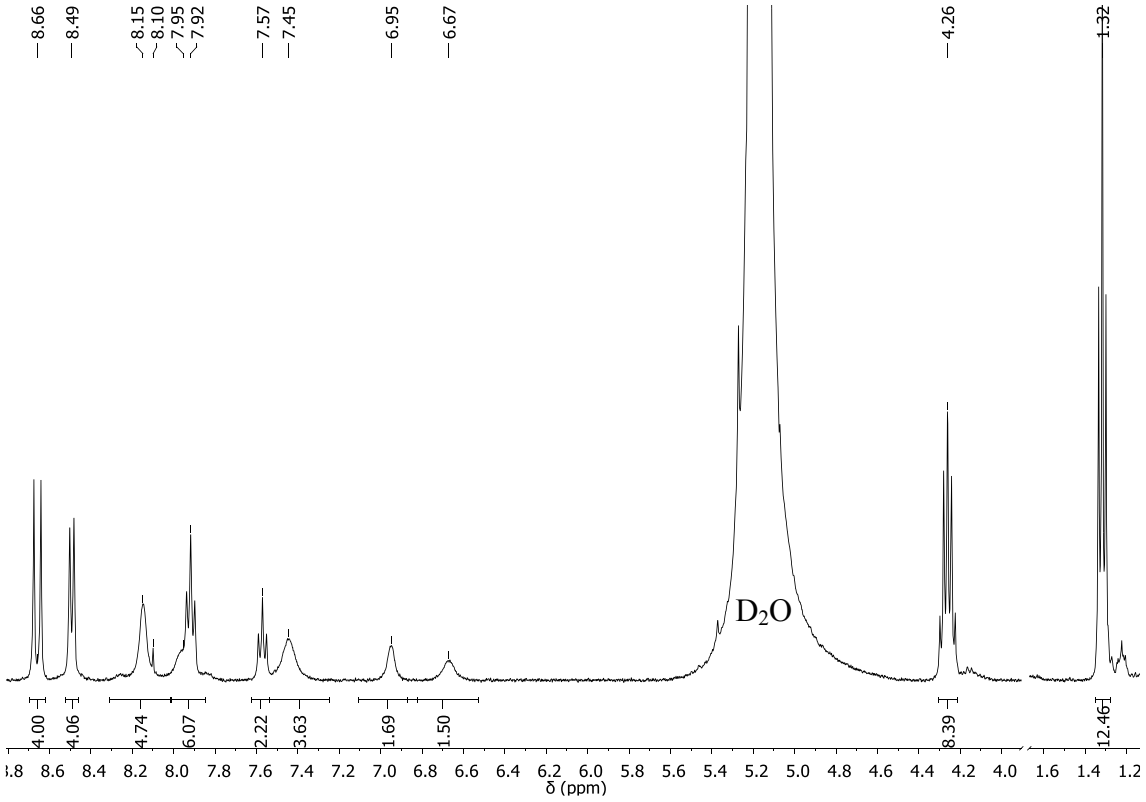

(b)

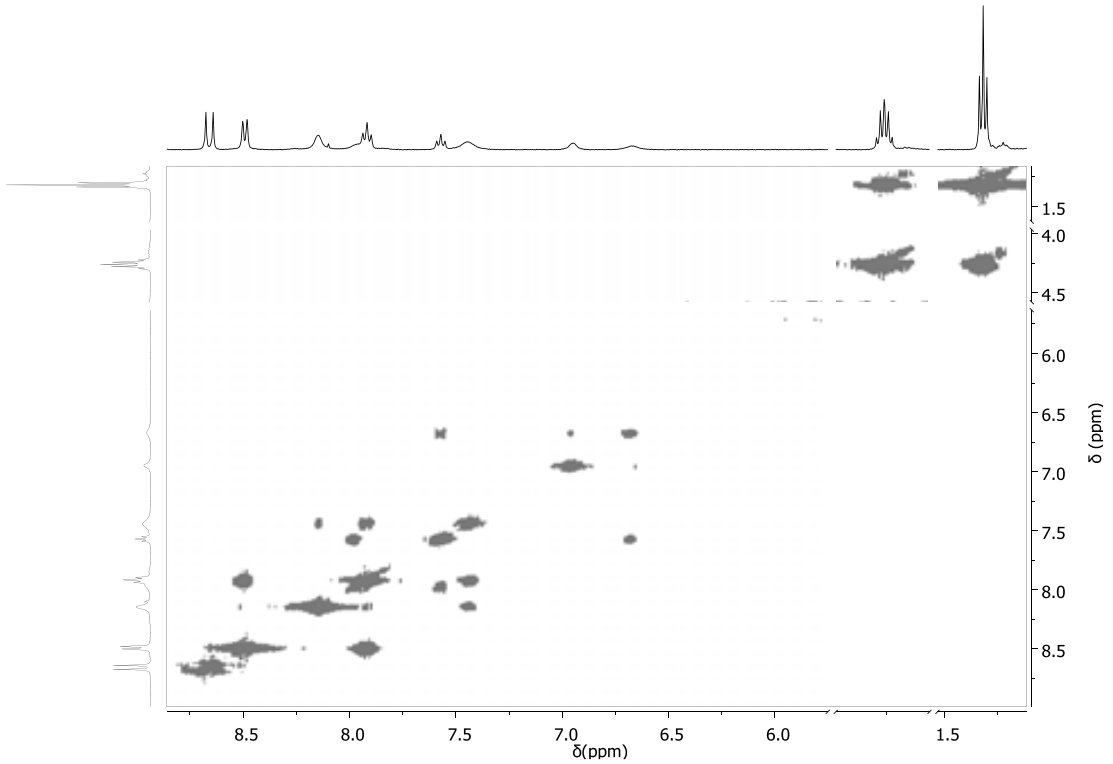

Figure S5: The comparison of the experimental and the simulated spectrum of the ethyl fragment for complex $\mathbf{3}^{2+}$.

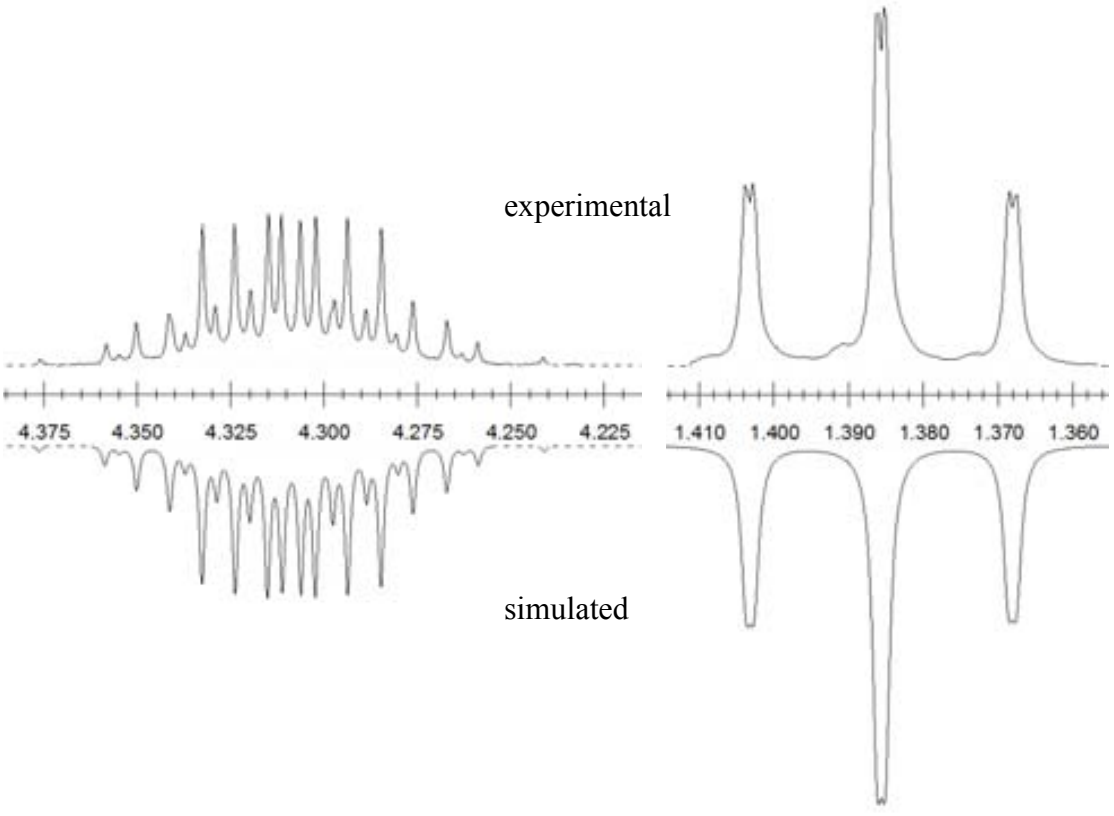

Figure S6: . Crystallographic Data for Complex **1**

Empirical formula	C19 H20 Cl3 N3 O3 P Ru
Formula Weight	576.77
Temperature, K	300(2)
Wavelength, Å	0.71073
Crystal system	Triclinic
Space group	P-1
a, Å	8.4544(6)
α, deg	63.748(4)
b, Å	11.7711(8)
β, deg	83.479(5)
c, Å	12.6435(9)
γ, deg	70.329(4)
Vol., $Å^3$	1061.69(13)
Z	2
ρ(g/cm^3)	1.804
R [$I>2\sigma(I)$]$^{\alpha}$	0.0549
wR	0.1283

$$R = \sum[F_0 - F_c]/\sum F_0 \qquad \mathrm{wR} = \left[\sum\left(w(F_0^2 - F_c^2)^2\right)/\sum(wF_0^4)\right]^{1/2}$$

Figure S7: Two Ortep views (50% probability) of the complex **1**.

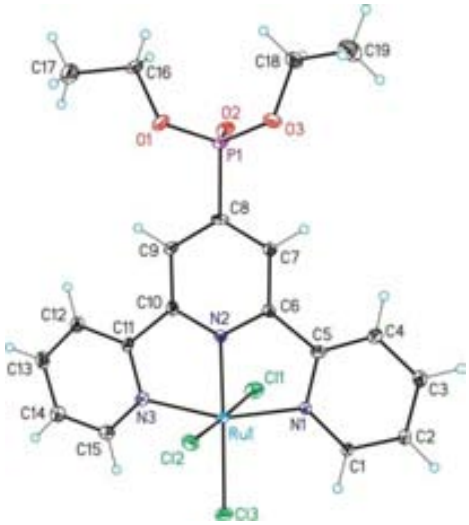

Figure S8: Cyclic voltammogram of complex **1** in CH_2Cl_2 at scan rate of 100 mV/s vs SSCE using carbon electrode.

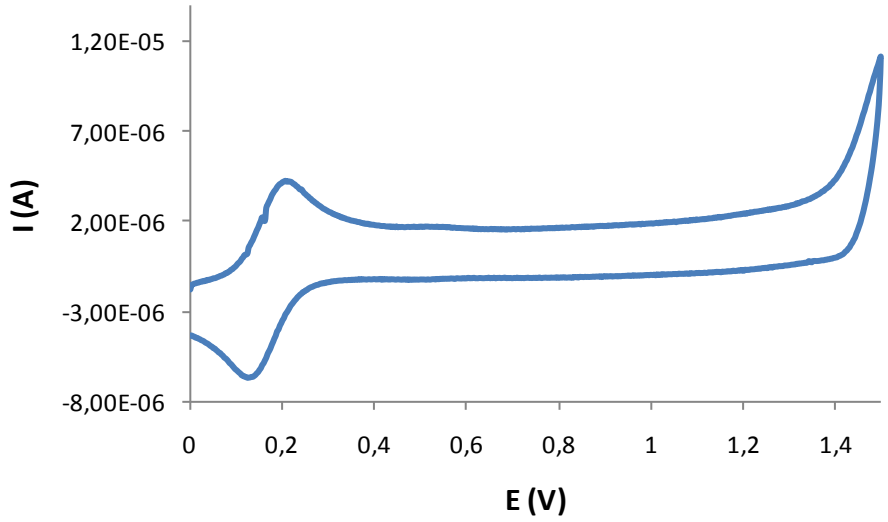

Figure S9: Cyclic voltammogram of complex $\mathbf{2}^{2+}$ in CH_2Cl_2 at scan rate of 300 mV/s vs SSCE using carbon electrode.

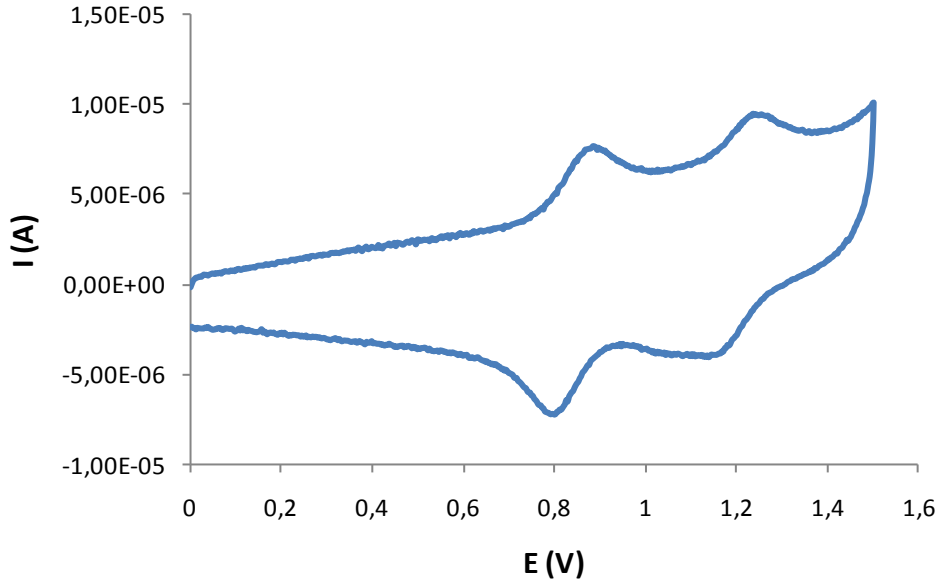

Figure S10: Cyclic voltammogram of complex $\mathbf{3}^{2+}$ in CH_2Cl_2 at scan rate of 100 mV/s vs SSCE using carbon electrode.

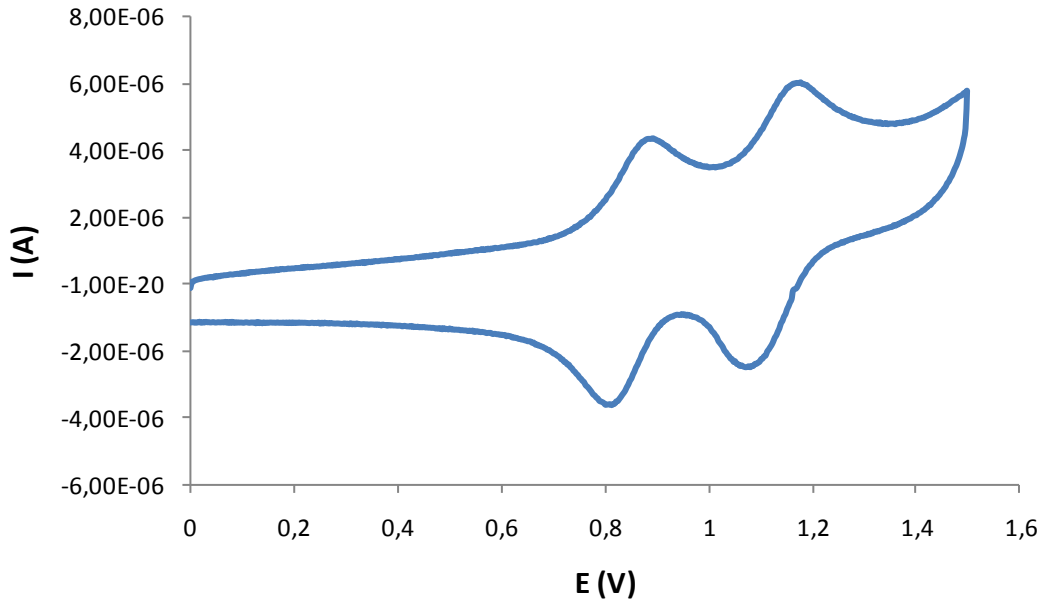

Figure S11: Cyclic voltammogram of complex **4** in MeOH at scan rate of 100 mV/s vs SSCE using carbon electrode.

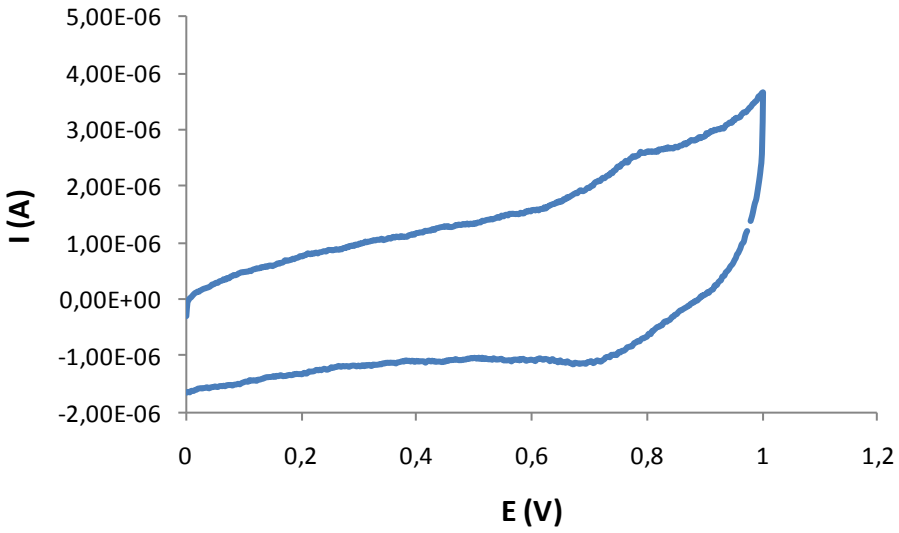

Figure S12: Cyclic voltammogram of complex $\mathbf{6}^{3+}$ in aqueous solution 0.1 M CF_3COOH at scan rate of 100 mV/s.

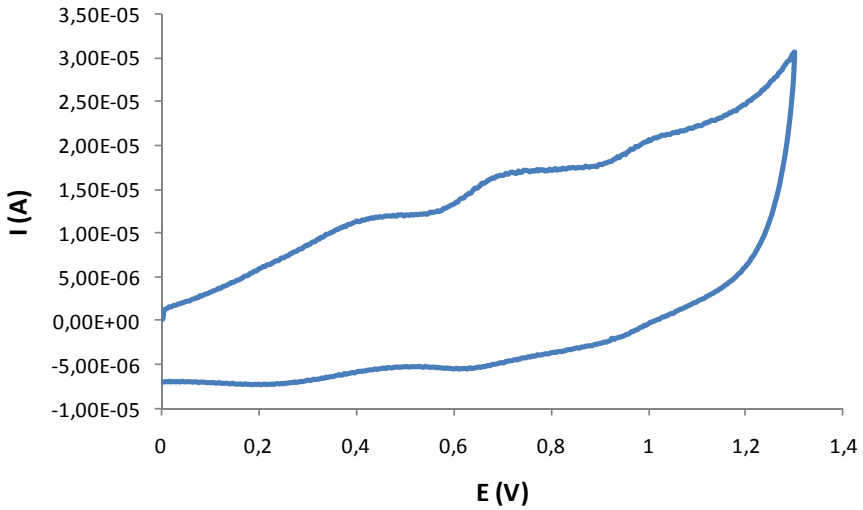

Figure S13: Redox titration of complex **4** in aqueous solution 0.1 M triflic acid with the additions of 5 µL 0.55 mM cerium (IV) solution to determine the molecular weight. (a) UV-Vis spectroscopy experiments. (b) the absorbance at 250 nm during the titration. (c) calculations.

(a)

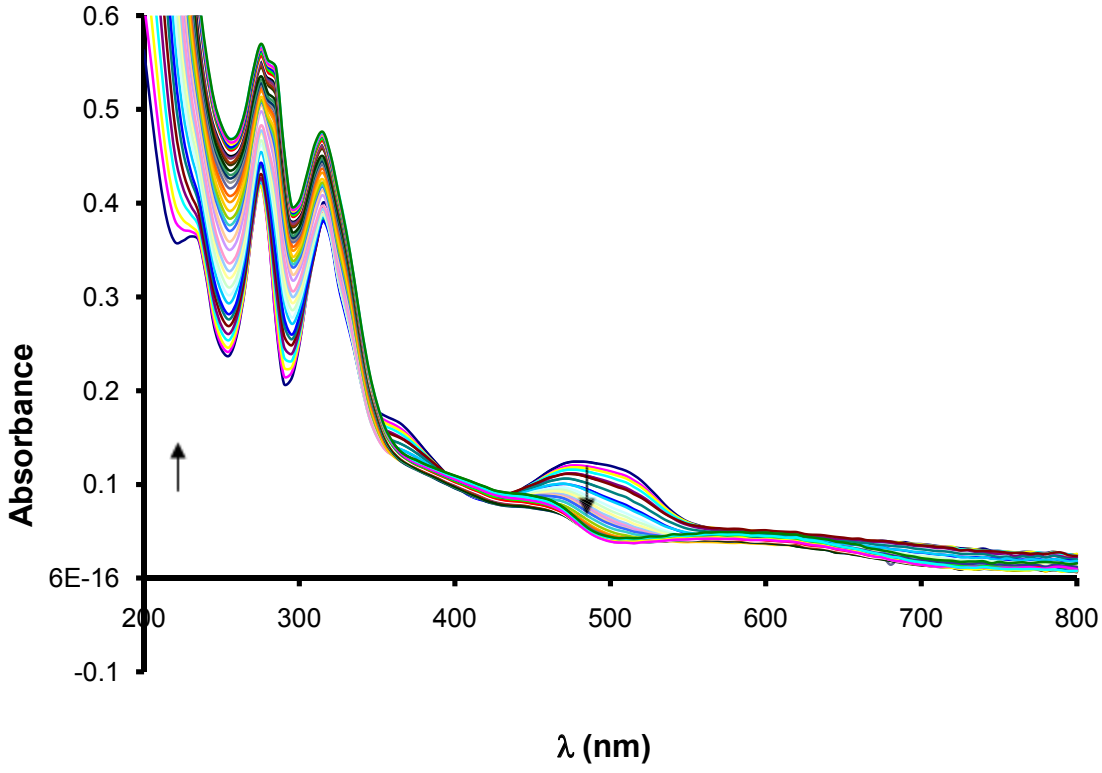

(b)

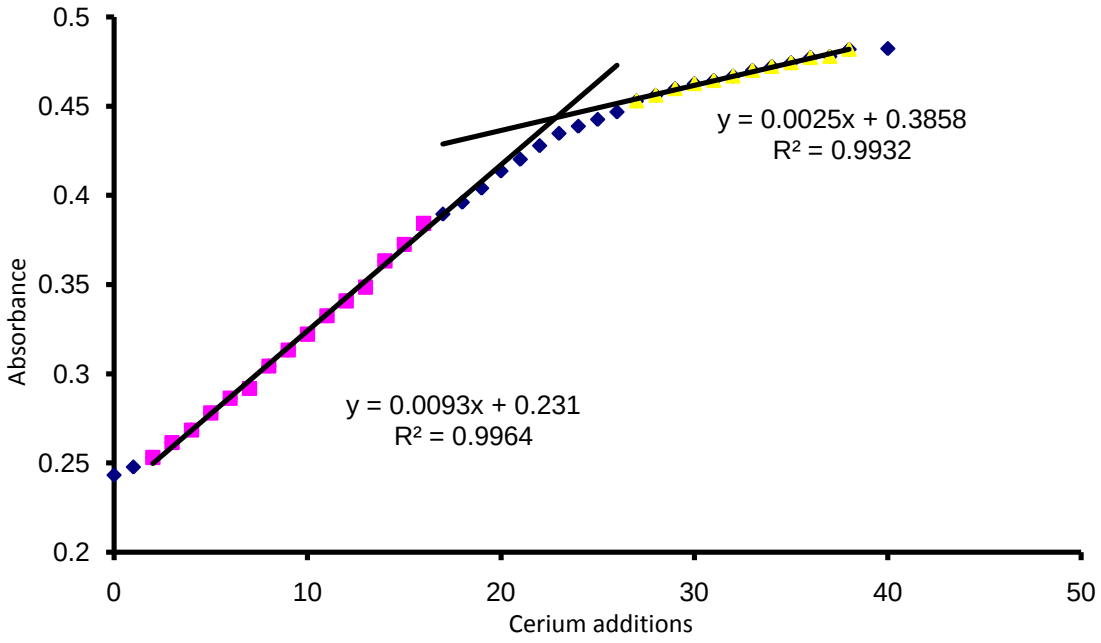

(c) the intersection point of both regression lines corresponds with the addition of one equivalent of Cerium (IV). In this example is 22.76 Ce(IV) additions, which corresponds $6.25 \cdot 10^{-5}$ mmol of Ce (IV) and $6.25 \cdot 10^{-5}$ mmol of complex 4.

The initial complex weight was: 0,07464 mg

Then PM= mg/mmol ⟶ **PM= 1993 g/mol**

Figure S14: UV-Vis spectroscopy of complex **1** in CH_2Cl_2.

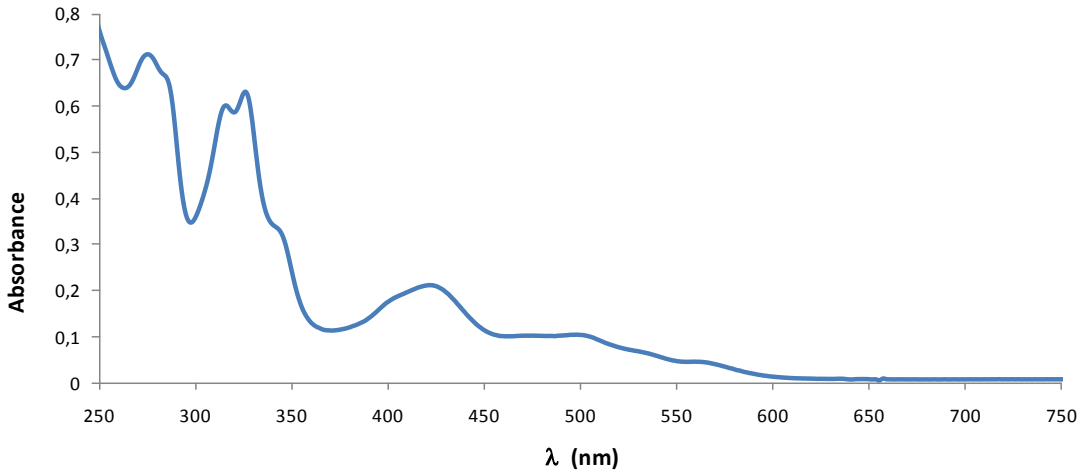

Figure S15: UV-Vis spectroscopy of complex $\mathbf{2}^{2+}$ in CH_2Cl_2.

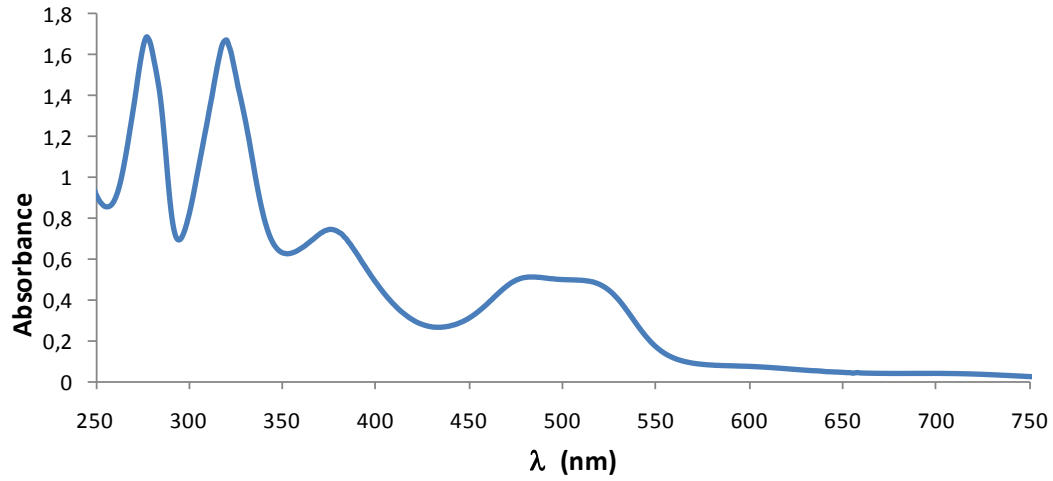

Figure S16: UV-Vis spectroscopy of complex $\mathbf{3}^{2+}$ in CH_2Cl_2.

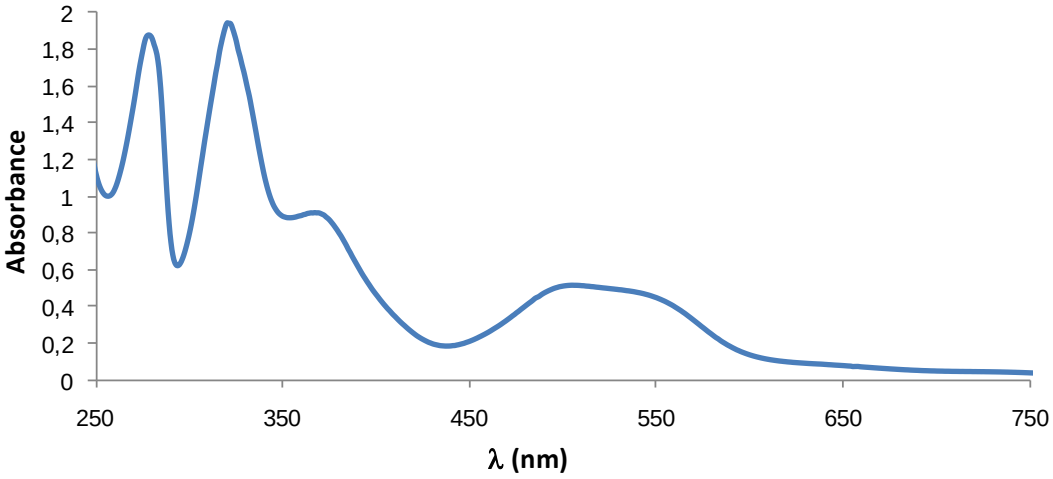

Figure S17: UV-Vis spectroscopy of complex **4** in MeOH.

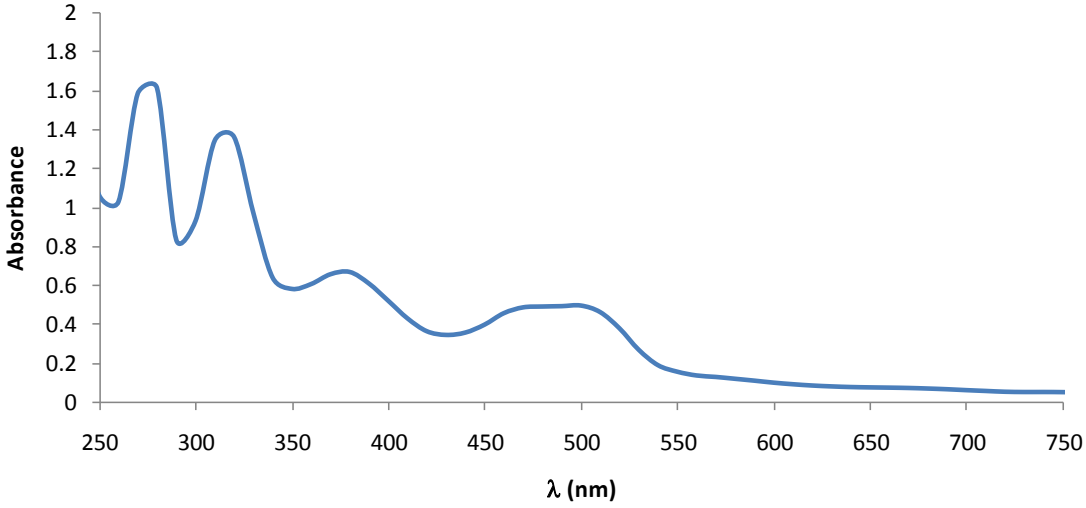

Figure S18: UV-Vis spectroscopy of complex $\mathbf{6}^{3+}$ in aqueous solution 0.1 M CF_3COOH.

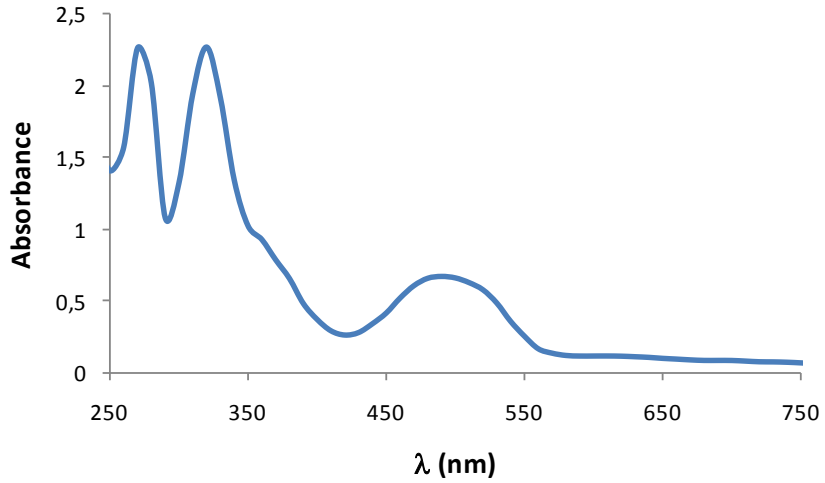

Figure S19: MS-ESI spectra of complex **1** in MeOH.

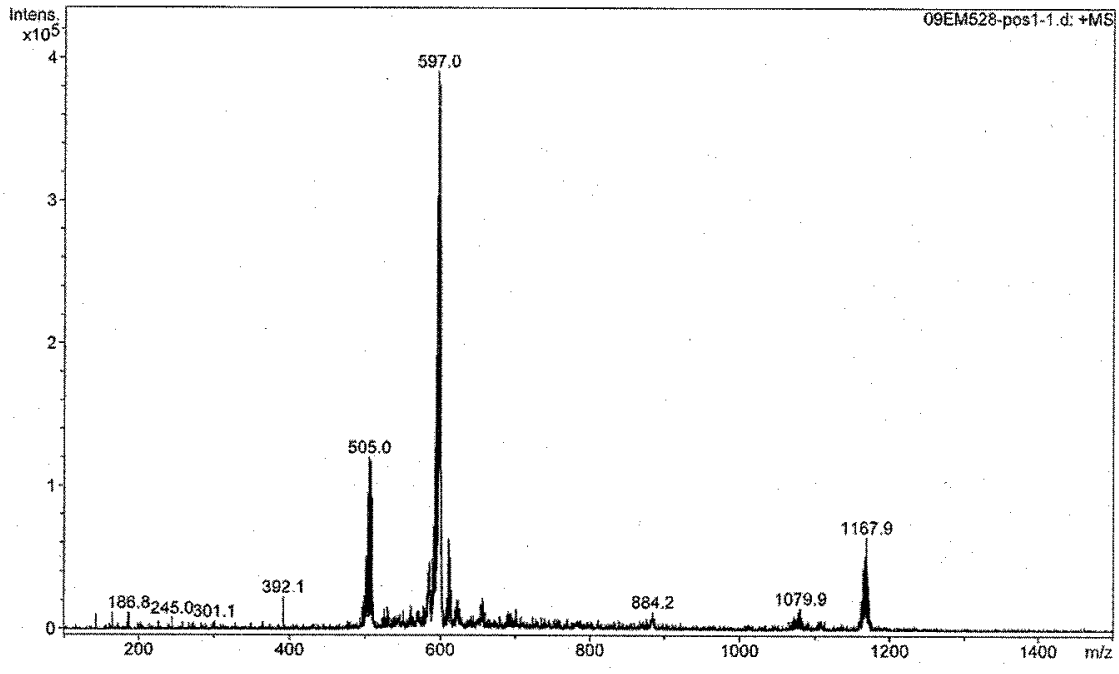

#	m/z	I	I %	#	m/z	I	I %	#	m/z	I	I %	#	m/z	I	I %
19	529.0	15650	4.0	34	585.5	34371	8.8	49	598.0	269674	69.0	64	611.9	28809	7.4
20	531.0	12579	3.2	35	586.0	44701	11.4	50	598.6	276243	70.7	65	612.9	50088	12.8
21	550.7	12942	3.3	36	586.6	19279	4.9	51	599.0	380976	97.5	66	613.9	21308	5.5
22	560.9	16193	4.1	37	587.1	27446	7.0	52	599.5	197647	50.6	67	614.9	27241	7.0
23	570.6	13175	3.4	38	588.0	23192	5.9	53	600.0	272406	69.7	68	618.8	14060	3.6
24	577.0	16229	4.2	39	589.0	49320	12.6	54	600.5	108350	27.7	69	619.9	12158	3.1
25	579.0	14932	3.8	40	590.0	42761	10.9	55	601.0	106895	27.4	70	620.9	16022	4.1
26	580.9	13012	3.3	41	591.0	72101	18.5	56	601.5	37927	9.7	71	622.0	20296	5.2
27	582.0	22415	5.7	42	592.0	115268	29.5	57	602.0	29815	7.6	72	622.9	13261	3.4
28	582.5	24929	6.4	43	593.0	138747	35.5	58	602.6	18428	4.7	73	623.9	20586	5.3
29	583.0	18370	4.7	44	594.0	192057	49.2	59	605.0	13365	3.4	74	624.9	13598	3.5
30	583.6	27773	7.1	45	595.0	302770	77.5	60	607.9	14933	3.8	75	625.9	14628	3.7
31	584.1	40472	10.4	46	596.0	191475	49.0	61	608.9	22121	5.7	76	654.1	17427	4.5
32	584.5	43028	11.0	47	597.0	390565	100.0	62	609.9	45910	11.8	77	655.0	13782	3.5
33	585.1	46619	11.9	48	597.6	186173	47.7	63	610.9	63468	16.3	78	656.2	21728	5.6

Figure S20: MS-ESI spectra of complex [**2**]**(PF$_6$)$_2$**in MeOH.

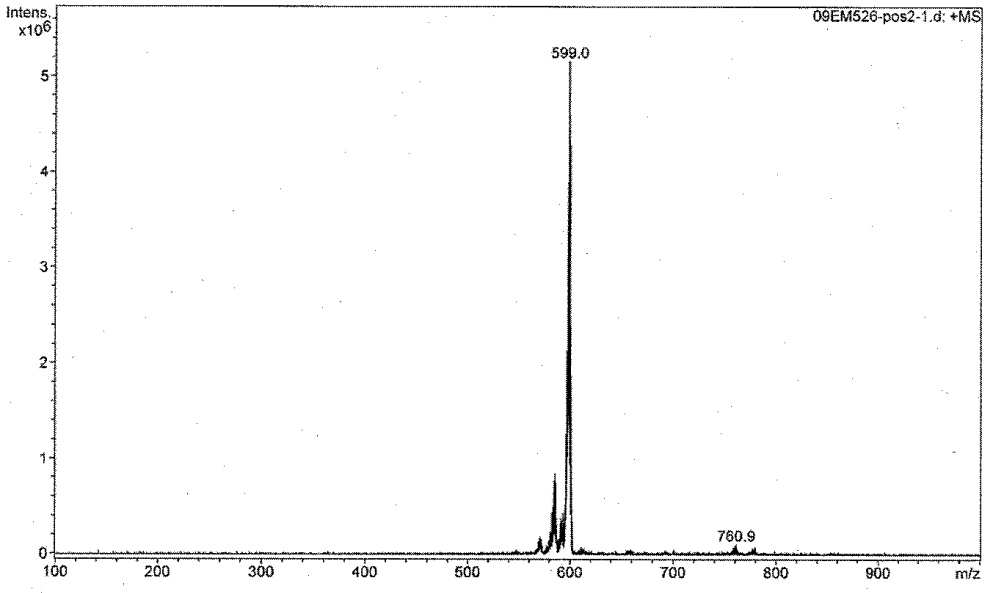

#	m/z	I	A %
1	569.0	129086	1.7
2	569.4	116817	2.0
3	570.0	165192	2.3
4	570.5	163443	3.3
5	570.9	182648	3.5
6	571.4	134286	3.3
7	572.0	158498	3.0
8	572.5	100955	1.8
9	572.9	81667	1.0
10	577.1	65112	1.1
11	577.5	92707	1.4
12	578.0	72258	1.4
13	578.6	75030	1.2
14	579.0	130348	2.5
15	579.5	130312	2.6
16	580.0	155019	3.3
17	580.5	229124	3.6
18	581.0	218285	4.4
19	581.5	230604	4.3
20	582.0	435285	7.8
21	582.5	374922	7.1
22	583.0	447171	8.9
23	583.5	489446	10.4
24	584.0	658901	13.6
25	584.5	767203	17.8
26	585.0	842106	16.0
27	585.5	732189	14.0
28	586.0	750744	14.1
29	586.5	371641	7.2
30	587.0	300956	6.7
31	587.5	133481	3.0
32	587.6	139503	3.0
33	588.0	138166	2.4
34	588.6	127156	2.2
35	588.9	150309	3.1
36	589.4	171385	2.9
37	589.9	162203	3.8
38	590.5	311446	6.5
39	591.0	380633	7.2
40	591.5	355459	7.1
41	592.0	273205	7.2
42	592.5	252693	4.2
43	593.0	437976	9.2
44	593.4	267795	4.9
45	594.0	224684	4.3
46	594.5	378167	9.2
47	595.0	441949	9.2
48	595.5	636286	14.4
49	596.0	1268201	28.9
50	596.5	1193014	24.8
51	597.0	2130329	51.4
52	597.5	3022206	64.1
53	598.0	3891217	80.5
54	598.5	4845443	88.8
55	599.0	5155141	100.0
56	599.5	4146573	79.9
57	599.9	4275506	77.6
58	600.4	2384598	41.4
59	600.9	1873856	36.3
60	601.4	732951	13.8
61	601.9	347574	5.7
62	602.5	165887	2.4
63	602.8	53503	1.2
64	656.2	40208	1.1
65	658.1	41462	1.0
66	659.1	49666	1.0
67	700.3	51224	1.0
68	758.0	68200	1.2
69	758.9	64552	1.4
70	759.9	85259	1.9
71	760.4	73842	1.0
72	760.9	101759	1.0
73	778.8	60105	1.0
74	779.4	68192	1.1

Figure S21: MS-ESI spectra of complex [**3**]$(PF_6)_2$ in MeOH.

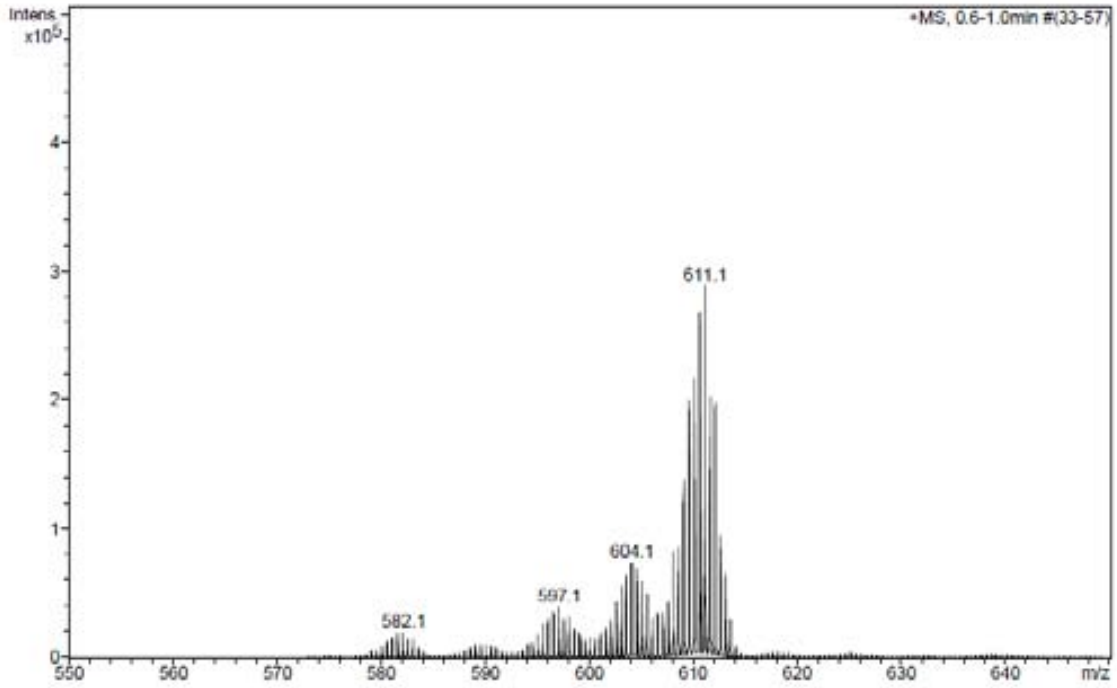

#	m/z	I	I %
1	217.1	104969	36.3
2	218.2	55538	19.2
3	234.2	32938	11.4
4	246.3	20369	7.0
5	261.1	65121	22.5
6	274.3	20886	7.2
7	580.6	13948	4.8
8	581.1	15678	5.4
9	581.6	18455	6.4
10	582.1	19818	6.8
11	582.6	14553	5.0
12	583.1	14475	5.0
13	594.6	11750	4.1
14	595.1	17920	6.2
15	595.6	26144	9.0
16	596.1	30437	10.5
17	596.6	35509	12.3
18	597.1	39144	13.5
19	597.6	30556	10.6
20	598.1	31551	10.9
21	598.6	22136	7.6
22	599.1	18404	6.4

#	m/z	I	I %
23	599.6	14308	4.9
24	600.1	15623	5.4
25	600.6	14205	4.9
26	601.1	18649	6.4
27	601.6	24129	8.3
28	602.1	28848	10.0
29	602.6	43191	14.9
30	603.1	56285	19.4
31	603.6	64549	22.3
32	604.1	73785	25.5
33	604.6	69322	23.9
34	605.1	59294	20.5
35	605.6	50381	17.4
36	606.1	30883	10.7
37	606.6	35103	12.1
38	607.1	34884	12.1
39	607.6	43742	15.1
40	608.1	82370	28.5
41	608.6	85393	29.5
42	609.1	138142	47.7
43	609.6	200413	69.2
44	610.1	217428	75.1
45	610.6	268391	92.7
46	611.1	289465	100.0
47	611.6	201801	69.7
48	612.1	198094	68.4
49	612.6	95433	33.0
50	613.1	65179	22.5
51	613.6	29063	10.0

Figure S22: MS-ESI spectra of complex **4** in MeOH.

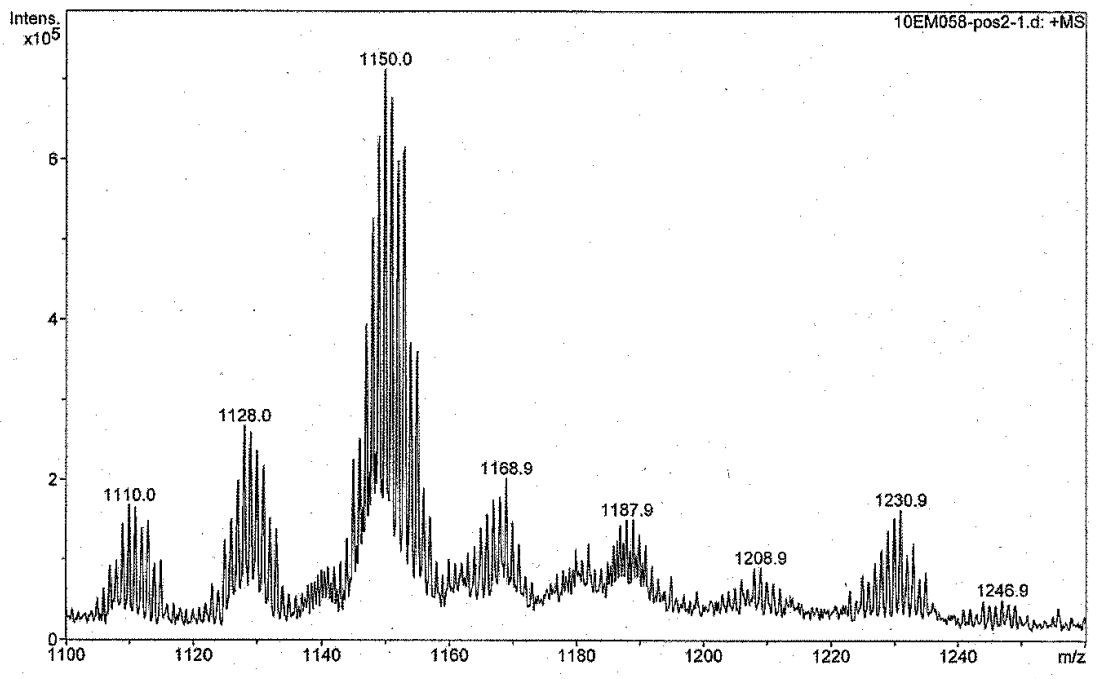

#	m/z	I	I %
1	1107.0	92326	13.0
2	1108.0	98989	13.9
3	1109.0	144085	20.2
4	1110.0	168391	23.6
5	1111.0	165641	23.2
6	1112.0	139526	19.6
7	1113.0	149071	20.9
8	1114.0	94887	13.3
9	1115.0	99327	13.9
10	1125.0	124431	17.5
11	1126.0	150790	21.2
12	1127.0	199558	28.0
13	1128.0	268069	37.6
14	1129.0	259791	36.5
15	1130.0	236374	33.2
16	1131.0	217884	30.6
17	1132.0	152330	21.4
18	1133.0	138513	19.4
19	1139.5	81007	11.4
20	1140.0	86830	12.2
21	1140.5	84792	11.9
22	1141.0	91045	12.8
23	1142.0	91502	12.8
24	1143.0	97245	13.6
25	1144.0	126882	17.8
26	1145.0	225854	31.7
27	1145.5	117096	16.4
28	1146.0	251694	35.3
29	1146.5	166252	23.3
30	1147.0	393857	55.3
31	1147.5	210634	29.6
32	1148.0	526576	73.9
33	1148.5	236459	33.2
34	1149.0	628402	88.2
35	1150.0	712619	100.0
36	1151.0	677211	95.0
37	1152.0	597861	83.9
38	1153.0	615052	86.3
39	1154.0	370587	52.0
40	1155.0	360278	50.6
41	1156.0	189809	26.6
42	1157.0	153876	21.6
43	1158.0	97638	13.7
44	1159.0	81166	11.4
45	1159.9	100407	14.1
45	1159.9	100407	14.1
46	1160.9	95135	13.4
47	1161.9	96261	13.5
48	1162.4	77712	10.9
49	1162.9	108027	15.2
50	1163.9	116300	16.3
51	1164.9	139475	19.6
52	1165.9	157228	22.1
53	1166.9	175233	24.6
54	1167.9	178900	25.1
55	1168.9	202504	28.4
56	1169.5	79263	11.1
57	1169.9	149080	20.9
58	1170.9	119843	16.8
59	1171.9	79324	11.1
60	1176.9	82980	11.6
61	1177.9	85987	12.1
62	1178.4	79698	11.2
63	1178.9	89856	12.6
64	1179.4	87813	12.3
65	1179.9	113132	15.9
66	1180.2	85515	12.0
67	1180.5	83698	11.7
68	1180.9	99035	13.9
69	1181.9	120102	16.9
70	1182.2	81705	11.5
71	1182.9	88705	12.4
72	1183.9	88917	12.5
73	1184.9	97729	13.7
74	1185.4	91822	12.9
75	1185.9	117949	16.6
76	1186.4	123987	17.4
77	1186.9	143217	20.1
78	1187.4	121451	17.0
79	1187.9	150696	21.1
80	1188.4	111837	15.7
81	1188.9	150639	21.1
82	1189.4	106330	14.9
83	1189.9	131536	18.5
84	1190.4	97086	13.6
85	1190.9	118221	16.6
86	1191.9	92765	13.0
87	1192.9	76623	10.8
88	1194.9	80392	11.3

Figure S23: UV-Vis spectroscopy of the **FTO-TiO_2-4** during the anchoring process at: 0, 1, 2, 4, 6, 8, 73 hours. Using an initial concentration of (a) 0.135 mM, (b) 0.035 mM and (c) 0.019 mM.

(a)

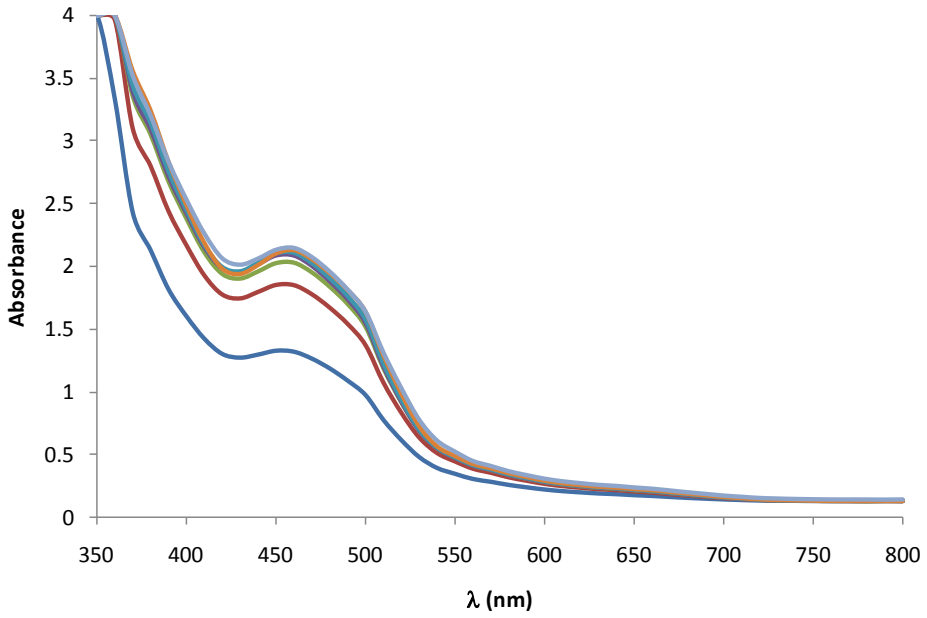

(b)

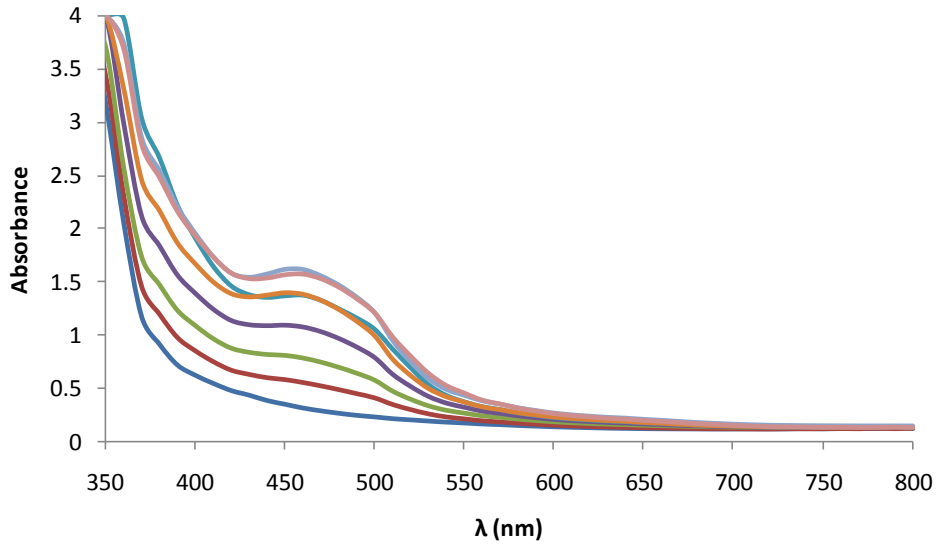

(c)

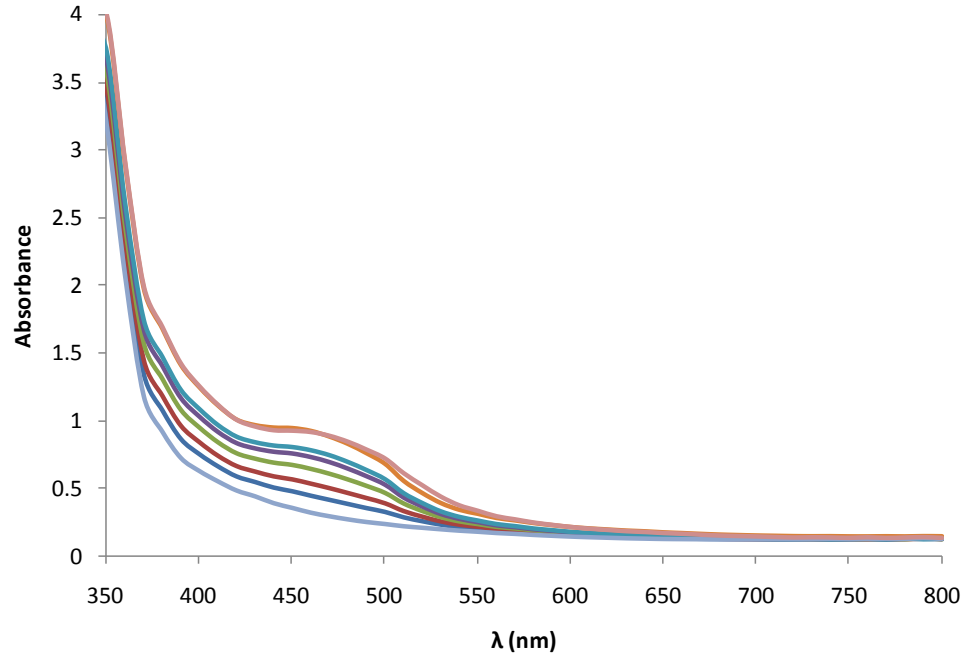

Figure S24: graphic correlation between the finale mmol anchored in the **FTO-TiO_2** and the initial complex concentration.

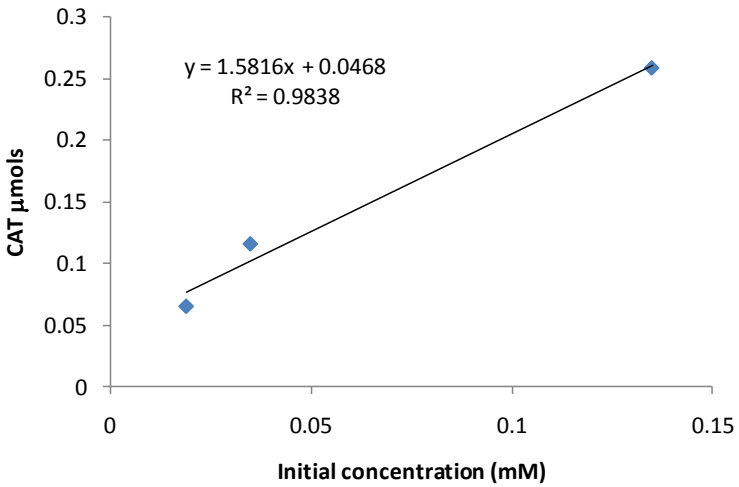

Figure S25: UV-Vis spectroscopy of the **FTO-TiO2-12**$^{2+}$ during the anchoring process at: 0, 1, 2, 4, 6, 8, 73 hours. Using an initial concentration of 0.104 mM.

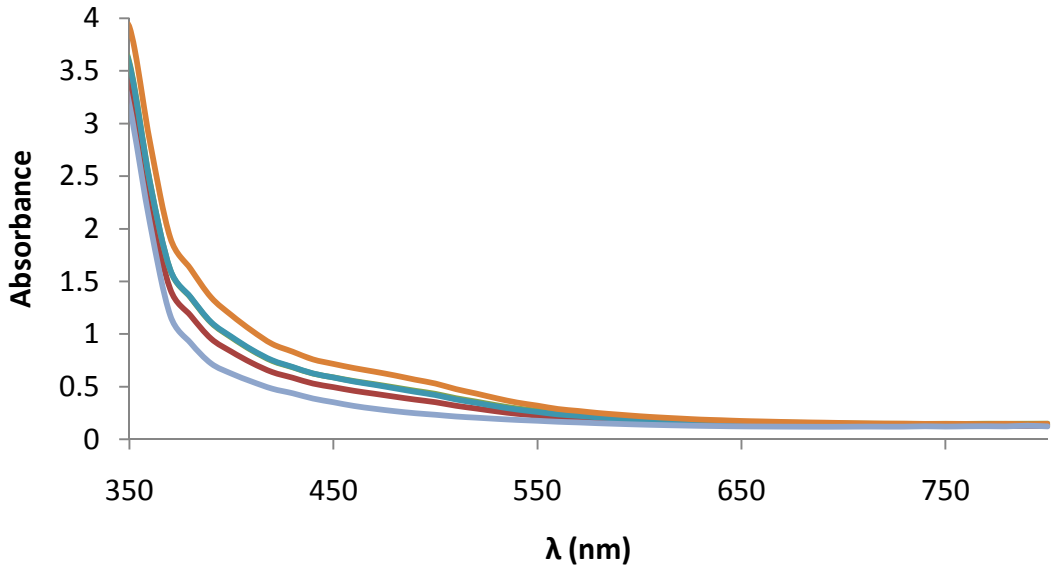

Figure S26: Example of quantification of the anchored complex in FTO-TiO_2 surface measuring the UV-vis spectra before and after the anchoring process by the Lambert-Beer law. Complex **12**$^{2+}$.

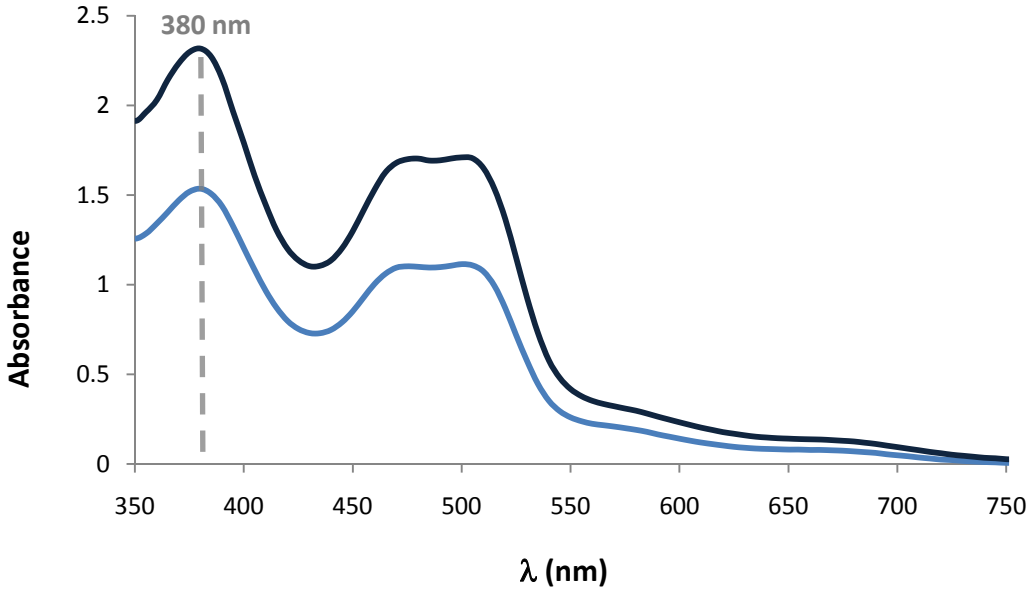

Lambert-beer equation:

$A=\varepsilon \cdot b \cdot c$

Where, A is the absorbance of the solution, ε is the molar absorptivity, b is the path length (usually 1 cm) and c is the concentration in molarity.

If,

ε = 19378.04

The volume where the anchoring process is taking place is 5 mL.

Initial absorbance = 2.32 $\xrightarrow{C_{initial} = A/\varepsilon}$ $C_{initial}$= 0.00012 M

Then at the beginning there are $5.98 \cdot 10^{-7}$ mol

final absorbance = 1.53 $\xrightarrow{C_{final} = A/\varepsilon}$ $C_{final} = 7.9251 \cdot 10^{-5}$ M

Then in the final solution there are $3.96 \cdot 10^{-7}$ mol

Anchored mol = initial mol – final mol $\longrightarrow$ anchored mol= **$2.02 \cdot 10^{-7}$ mol**

Figure S27: Manometry profile of the catalytic gases generated during the catalysis as a function of time in the system: Cat (**6^{3+}**) 1 mM/Ce 100 mM/0.1 M triflic acid with a total volume of 2 mL at 25.0 °C.

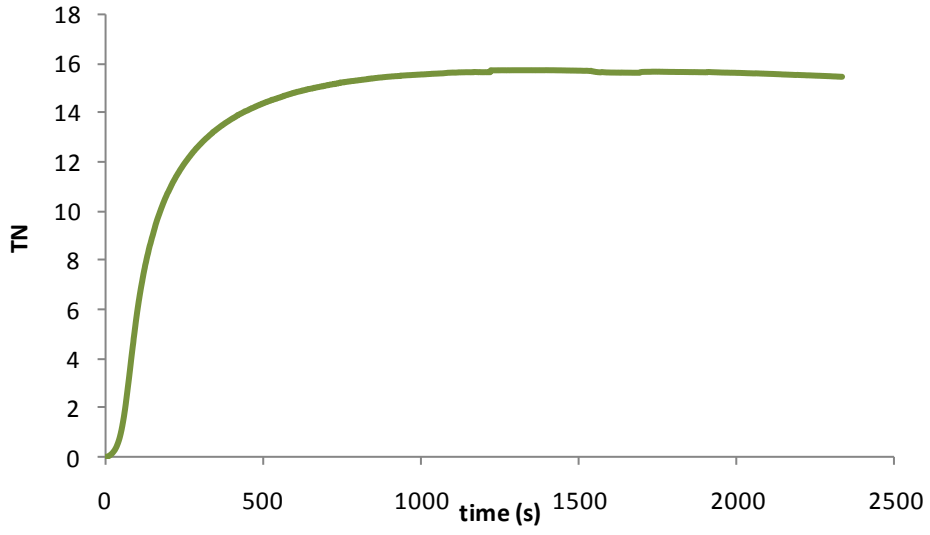

Figure S28. Blank experiments of oxygen measurement with clark electrode under catalytic conditions.

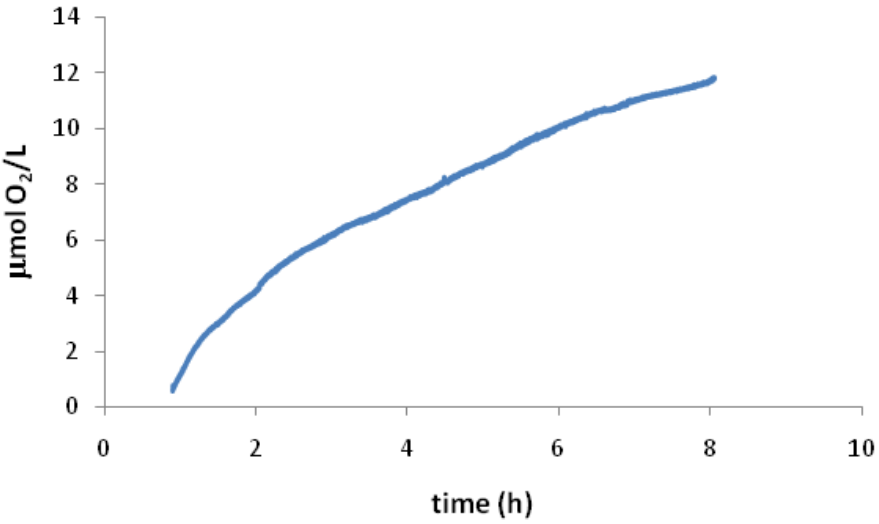

Figure S29: electrocatalytic experiments applying 1.6 V using **FTO-TiO$_2$-13^{2+}** as a working electrode. (a) coulombimetry profile during 6h. (b) oxygen measurement with clark electrode.

(a)

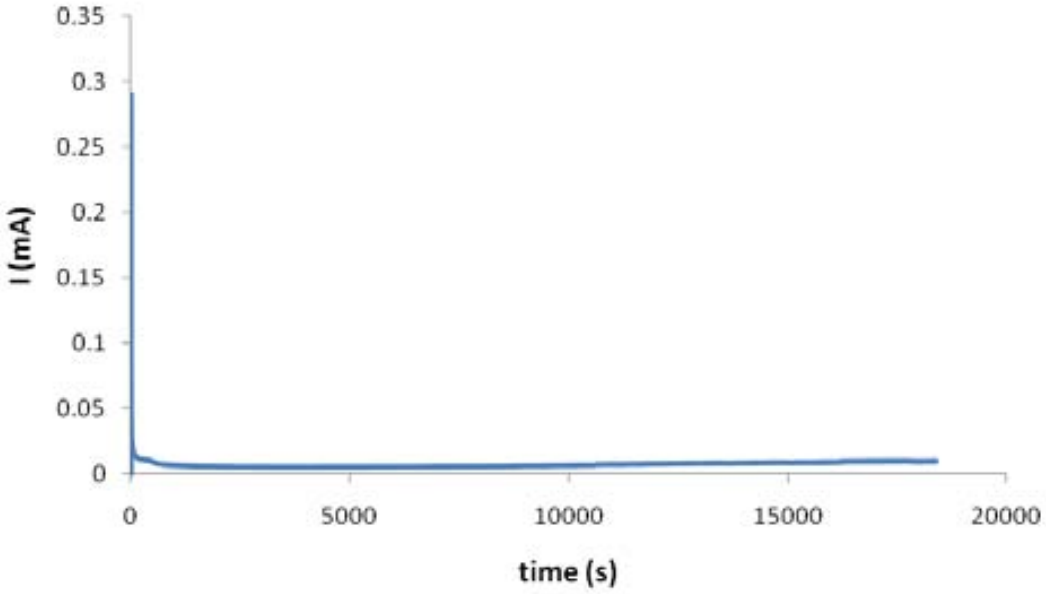

(b)

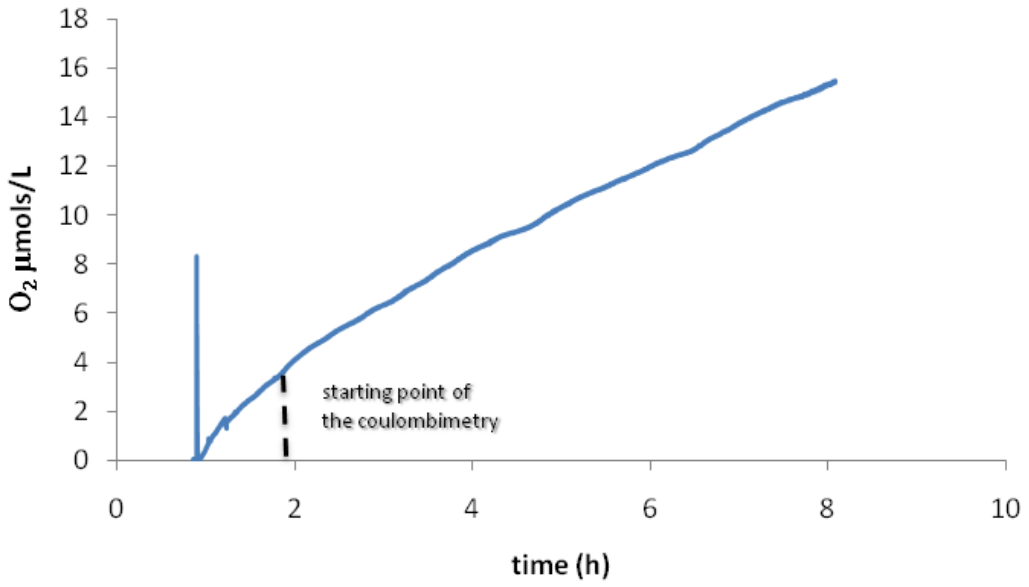

Figure S30: electrocatalytic experiments applying 1.7 V using **FTO-TiO_2-5**$^{2+}$ as a working electrode. (a) coulombimetry profile during 6h. (b) oxygen measurement with clark electrode.

(a)

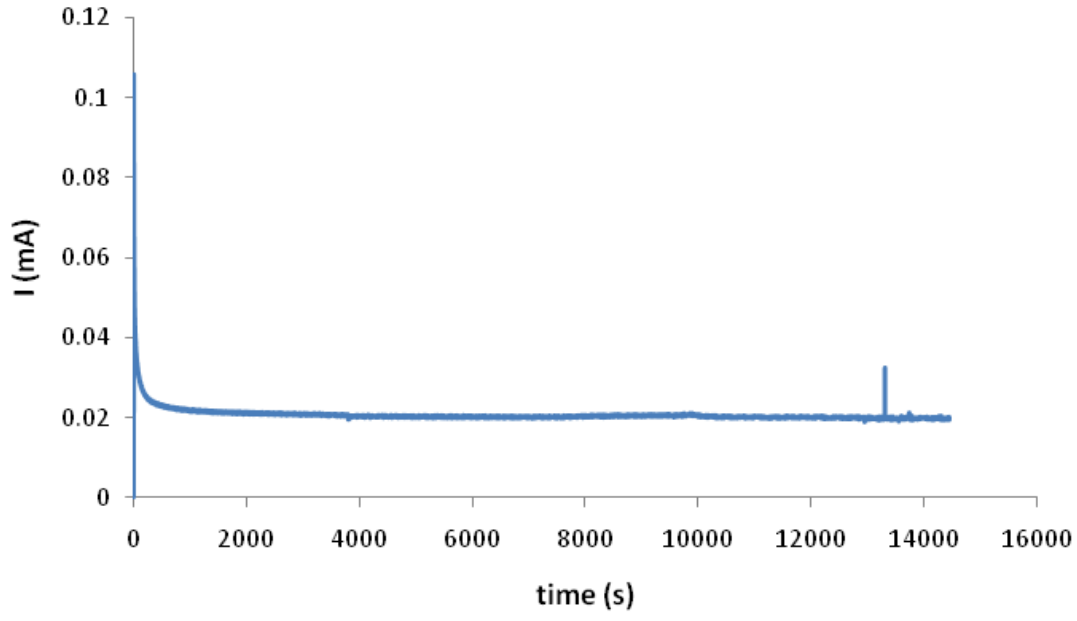

(b)

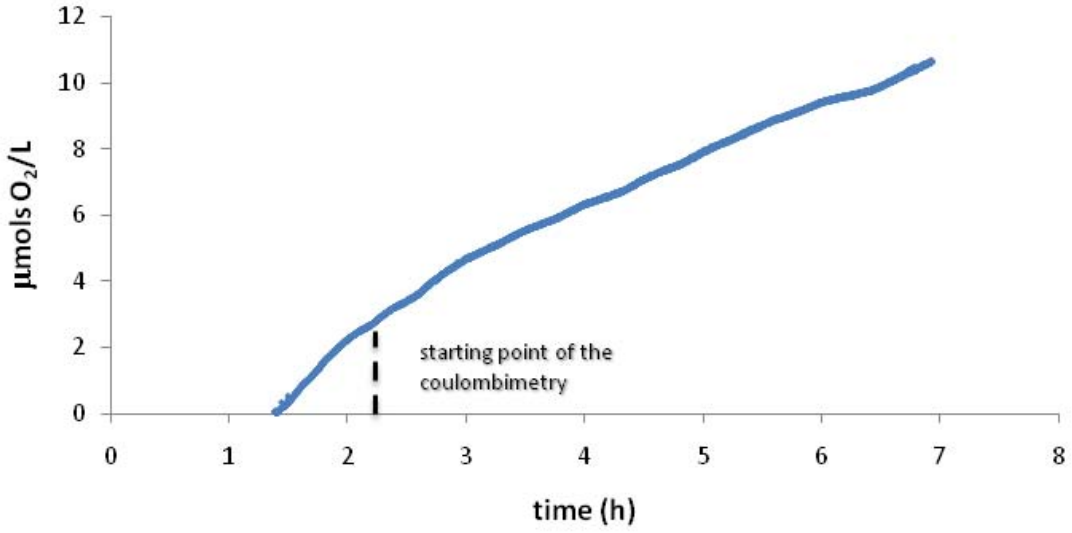

Figure S31: UV-Vis spectroscopy of the solution after the catalysis process (a) using **FTO-TiO$_2$-13^{2+}** as a working electrode, (b) using **FTO-TiO$_2$-5^{2+}** as a working electrode.

(a)

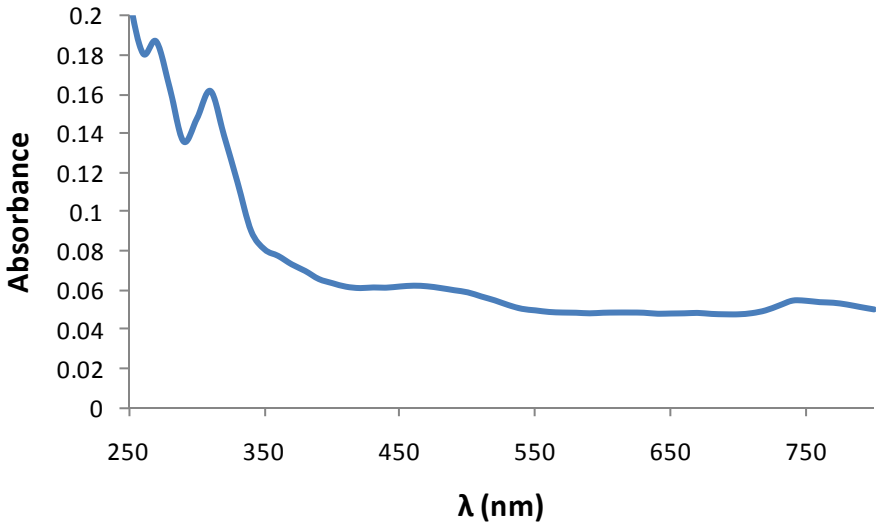

(b)

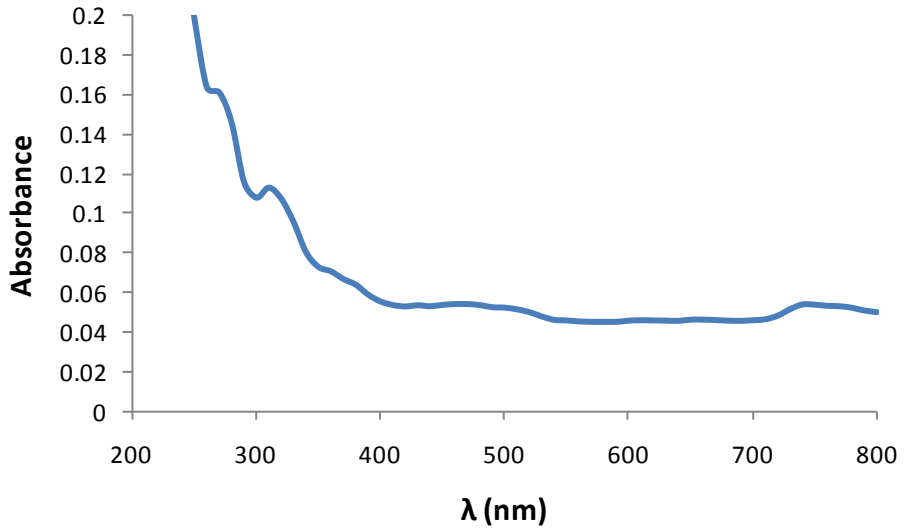

Figure S32: Temperature ramps for the calcinations films process.

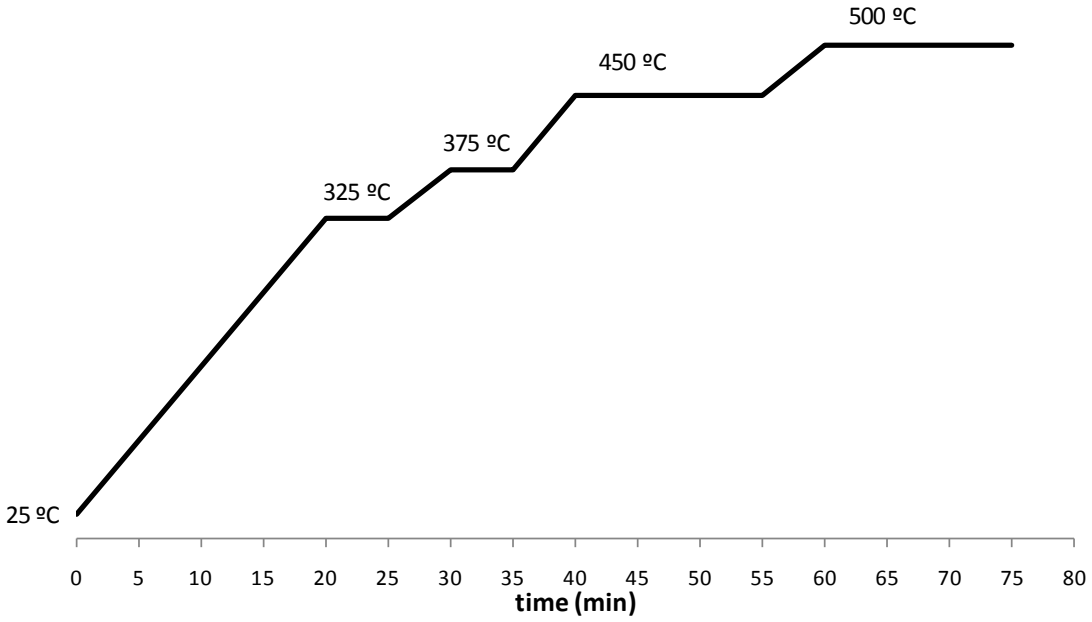

Paper E: Synthesis, Characterization and Linkage Isomerism in Mono- and Dinuclear Ruthenium Complexes Containing the New Pyrazole Based ligand Hpbl

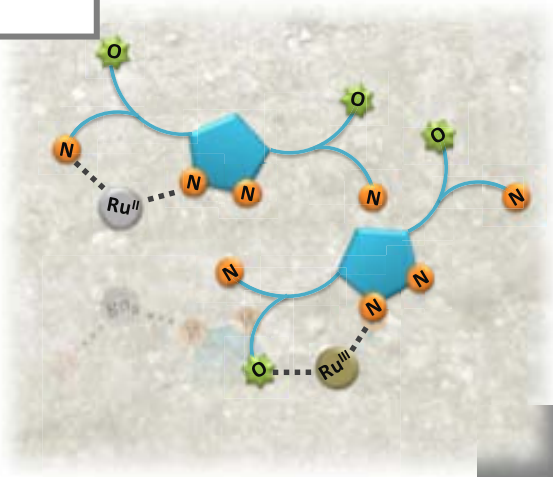

Synthesis, Characterization and Linkage Isomerism in Mono- and Dinuclear Ruthenium Complexes Containing the New Pyrazole Based ligand Hpbl

Laia Francàs,[a] Daniel Moyano,[a] Xavier Sala,[a] Jordi Benet-Buchholz,[b] Xavier Fontrodona,[c] Lluís Escriche[,a] and Antoni Llobet*[,a,b]*

[a]Departament de Química, Universitat Autònoma de Barcelona, Cerdanyola del Vallès, E-08193 Barcelona, Spain,
[b]Institute of Chemical Research of Catalonia (ICIQ), Av. Països Catalans 16, E-43007 Tarragona, Spain and [c]Serveis Tècnics de Recerca and Departament de Química, Universitat de Girona, E-17071 Girona, Spain.

lluis.escriche@uab.cat, allobet@iciq.es

Abstract

The new tetradentate bridging ligand [1,1'-(4-Methyl-1H-pyrazole-3,5-diyl)bis(1-(pyridin-2-yl)ethanol)] (Hpbl) containing a O/N mixed donor set of atoms has been synthesized and characterized by analytical and spectroscopical techniques. Inspired on the structurally related and more rigid N-donor Hbpp [3,5(bispyridyl)pyrazole] ligand, the Hpbl contains extra sp^3 carbon atoms with hydroxyl groups between the pyrazol and the pyridine groups, allowing a linkage isomerism between the pyridylic or pyrazolic nitrogen atoms and the hydroxyl oxygens. Its coordination chemistry has been studied by preparing mononuclear $[RuX(Hpbl)(trpy)]^{y+}$ (X=Cl, y=+1; X=H_2O, y=+2) and dinuclear $[Ru_2Cl_2(bpl)(trpy)_2]^+$ Ru(II) complexes. In solution all these complexes have been characterized spectroscopically (UV-vis and NMR) and electrochemically (CV). In the solid state, monocrystal X-ray diffraction analysis have been carried out for two linkage isomers of the dinuclear complex $[Ru_2(trpy)_2(pbl)Cl]^+$ and for the mononuclear [Ru(trpy)(pbl)(OH)] complex. The linkage isomerism processes for the mononuclear aqua complex has been studied as function of pH and redox potential and three different coordination environments to the Ru-OH_2/Ru-O basic structure have been identified: (1) the ruthenium metal centre coordinated by 5 nitrogen atoms of the ligands (three from the trpy and two from the Hpbl) **[Ru-N_5]**; (2) coordination to Ru through one hydroxylic oxygen an four nitrogen atoms (three from the trpy and one from the pyridyl group of Hpbl), **[Ru-ON_4(Py)]**; and (3) coordination taking place again *via* one hydroxylic oxygen and four nitrogen atoms (three from trpy but now one from the pyrazol Hpbl scaffold), **[Ru-ON_4(Pz)]**. Their combination has been used to explain the redox-dependent linkage isomerism of the dinuclear complexes observed in the solid state.

Introduction

Linkage isomerism has been used to build memory devices at the molecular level, which could provide the basis for the development of molecular electronics. [1] Transition metal complexes with ambidentate motifs, able to change their coordination due to external stimuli (such as the application of the sufficient voltage to oxidize or reduce the metal centre) are good candidates for this purpose. Different coordination environments produce different molecular properties, which allows the retention of information. Furthermore, as good memory devices, those changes must be reversible (Scheme 1). A wide number of ruthenium complexes containing sulfoxide ligands capable to carry out linkage isomerism [2] has been reported. Their dynamic behaviour is based on the higher affinity of Ru(II) and Ru(III) for S and O atoms respectively, in agreement with Pearson's theory.

Scheme 1. Schematic representation of a linkage isomerism process.

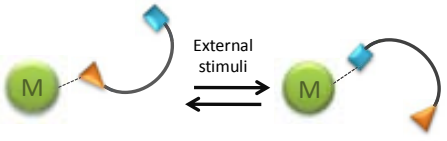

The group of Johansson and Lomoth has recently described a family of ruthenium complexes containing a modified ambidentate terpyridine [3] ligand exhibiting electron-transfer-induced linkage isomerization. The most interesting feature of these complexes is that during the isomerization process the ambidentate motif is not dissociated from the metal center (Scheme 2).

Scheme 2.

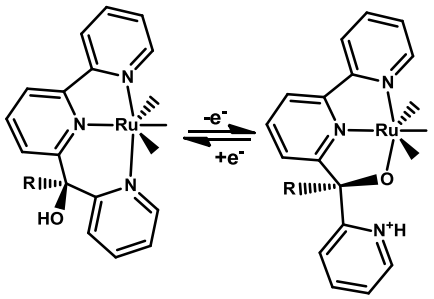

During the last three decades Ru–aqua polypyridyl complexes have been used as oxidation catalysts due to its capacity to stabilize high oxidation states. [4] This stabilization is caused by the simultaneous proton and electron extraction, which allows increasing the metal center charge at relatively low potentials (Scheme 3). Therefore, a wide range of oxidation states is accessible within a narrow potential range due to proton coupled electron transfer (PCET) and the σ and π donating nature of the oxo group formed.[5]

Scheme 3.

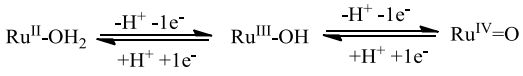

When Ru–aqua polypyridyl species are involved in oxidative catalytic cycles the metal centre continuously alters its oxidation state; typically from the initial Ru(II) to the upper Ru(III), Ru(IV) or even Ru(V), then returning to its initial oxidation state. [6] In these kind of reactions one of the most common deactivation pathways is the decomposition of the catalyst due to the instability of high oxidation states.[7] Consequently, the stabilization of all the oxidation states involved in the catalytic cycle is of paramount importance in order to guarantee the catalyst durability. Therefore, pursuing this goal and considering the literature background on memory devices, here on we report a new tetradentate bridging ligand with ambidentate motifs (Chart 1) potentially able to selectively stabilize various oxidation states through the linkage isomerism between its N and O atoms. Its coordination and isomerization chemistry is also studied by preparing their mononuclear $[RuX(Hpbl)(trpy)]^{y+}$ (X=Cl, y=+1; X=H_2O, y=+2) and dinuclear $[Ru_2Cl_2(bpl)(trpy)_2]^+$ ruthenium complexes.

Chart 1.

Hbpp

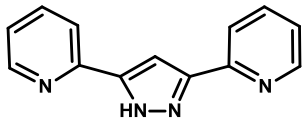

Hpbl

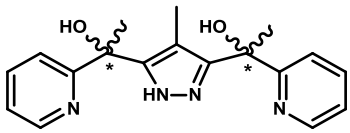

Experimental Section.

Materials. All reagents used in the present work were obtained from Sigma-Aldrich Chemical Co. and were used without further purification. Reagent grade organic solvents were obtained from SDS. $RuCl_3 \cdot 3H_2O$ was supplied by Alfa Aesar and was used as received.

Preparations. The starting complex $[RuCl_3(trpy)]$ [8] and 1'-(4-methyl-1H-pyrazole-3,5-diyl)diethanone [9] were prepared as is described in the literature. All synthetic manipulations were routinely performed under nitrogen atmosphere using Schlenck tubes and vacuum line techniques.

1,1'-(4-Methyl-1H-pyrazole-3,5-diyl)bis(1-(pyridin-2-yl)ethanol) ($Hpbl \cdot 1.5H_2O$). A sample of 0.913 mL (9.39 mmol) of 2-bromopyridine was dissolved in 100 mL of dry THF with vigorous stirring at -78ºC. Then 6.16 mL of nBuLi in hexane (1.6 M) were added dropwise with a syringe pump. After stirring the mixture during 30 minutes, 0.5 g (3.011 mmol) of 1'-(4-methyl-1H-pyrazole-3,5-diyl)diethanone dissolved in 20 mL of dry THF were added slowly with a syringe pump. The resulting mixture was stirred during 2 hours at -78 ºC and then warmed up to 0ºC, acidified with a 10% HCl aqueous solution and finally neutralized (until pH=7) with a 10% K_2CO_3 aqueous solution. During this process the colour of the

solution changes from brown to yellow and finally to orange. The resulting mixture was warmed up and extracted with successive $CHCl_3$ fractions of 100 mL until the extracted organic phase was uncolored. The collected organic phases were mixed, dried with Na_2SO_4 anhydride and evaporated until a brown oil appeared. The oil was purified by column chromatography using silica as stationary phase and ethylacetate as eluyent, and giving the desired product in the fourth fraction as a mixture of two diastereomers (A majority + B minority). Yield: 0.344 g (35%). ^{1}H NMR (360 MHz, acetonitrile-d_3) δ=8.489 (ddd, $2H_{3\text{-}9A}$, $^3J_{3\text{-}2}$=4.90 Hz, $^4J_{3\text{-}1}$=1.70 Hz , $^5J_{3\text{-}6}$=1.00 Hz), 8.483 (ddd, $2H_{3\text{-}9B}$, $^3J_{3\text{-}2}$=4.90 Hz, $^4J_{3\text{-}1}$=1.70 Hz , $^5J_{3\text{-}6}$=1.00 Hz), 7.718 (ddd, $2H_{1\text{-}11A,B}$, $^3J_{1\text{-}6}$=8.00 Hz, $^3J_{1\text{-}2}$=7.50 Hz, $^4J_{1\text{-}3}$=1.70 Hz), 7.305 (dt, $2H_{6\text{-}12A}$, $^3J_{6\text{-}1}$=8.00Hz, $^4J_{6\text{-}2,3}$= 1.30 Hz), 7.281 (dt, $2H_{6\text{-}12B}$, $^3J_{6\text{-}1}$=8.00 Hz, $^4J_{6\text{-}2,3}$= 1,00 Hz), 7.243 (ddd, $2H_{2\text{-}10B,}$ $^3J_{2\text{-}1}$=7.50 Hz, $^3J_{2\text{-}3}$=4.90 Hz, $^4J_{2\text{-}6}$=1.00 Hz), 7.241 (ddd, $2H_{2\text{-}10A,}$ $^3J_{2\text{-}1}$=7.50 Hz, $^3J_{2\text{-}3}$=4.90 Hz, $^4J_{2\text{-}6}$=1.00 Hz), 5.234 (s, $2H_{14\text{-}22B}$), 5.207 (s, $2H_{14\text{-}22A}$), 1.793 (s, $6H_{15\text{-}23B}$), 1.781 (s, $6H_{15\text{-}23A}$), 1.430 (s, $3H_{24A}$), 1.371 (s, $3H_{24B}$). ^{13}C {^{1}H} NMR (400 MHz, acetonitrile-d_3) δ=164.89 ($C_{5\text{-}7A}$), 164.84 ($C_{5\text{-}7B}$), 148.37 ($C_{3\text{-}9A}$), 148.31 ($C_{3\text{-}9B}$), 138.09 ($C_{1\text{-}11B}$), 138.09 ($C_{1\text{-}11A}$), 123.24 ($C_{2\text{-}10A,B}$), 120.99 ($C_{6\text{-}12A,B}$), 110.52 (C_{17B}), 110.33 (C_{17A}), 73.88 ($C_{13\text{-}21A}$), 73.77 ($C_{13\text{-}21B}$), 29.33 ($C_{15\text{-}23B}$), 29.29 ($C_{15\text{-}23A}$), 9.03 (C_{24A}), 8.95 (C_{24B}). ^{15}N NMR (400 MHz, acetone-d_6) δ=298.69 ($N_{4\text{-}8}$). ESI-MS (MeOH): *m/z*=324.1, 347.1 (M+Na). Elemental analysis calcd. (%) for ($C_{18}H_{23}N_4O_{2.5}$): C, 61.47; H, 6.55; N, 15.94; found: C, 61.78; H, 6.36; N, 15.80.

[Ru^{II}(Cl)(Hbpl)(trpy)](PF$_6$) [1](PF$_6$). A sample of 0.400 g (0.908 mmol) of [$RuCl_3$(trpy)] and 77 mg (1.816 mmol) of LiCl were dissolved in 40 mL of dried MeOH containing 250 µL (1.816 mmol) of NEt_3. The mixture was stirred at room temperature (RT) for 20 minutes and then 294 mg (0.908 mmol) of Hpbl were added. The resulting solution was stirred at 40ºC overnight. After that, the mixture was filtered and 2 mL of a saturated aqueous NH_4PF_6 solution and 5 mL of water were added. The volume of the resulting solution was reduced on a rotary evaporator until a precipitate appeared. After one day at 5 ºC the precipitated was filtered off. The solid was extracted with CH_2Cl_2 and the insoluble material was filtered off and discarded. The resulting solution was purified by column chromatography using neutral alumina as the solid support. The first three fractions eluted with a mixture of 140:1 (CH_2Cl_2:MeOH) were discarded and the last faction eluted with pure MeOH, corresponds to the desired product. This fraction was reduced to dryness and the brown powder obtained was dissolved in acetone and again 1 mL of a saturated aqueous NH_4PF_6 solution and 3 mL of water were added. The volume was then reduced on a rotary evaporator until a solid came out. The mixture was cooled down in the fridge for 12 h and after that, the solid obtained was filtered off, washed with cold water (3 x 5 mL) and diethyl ether (3 x 5 mL) and vacuum dried. Yield: 311 mg (41%). ^{1}H NMR (600 MHz, acetone-d_6) δ=8.731 (dd, $1H_{34A\text{ or }36A}$, $^3J_{34\text{-}35}$=8.10 Hz, $^4J_{34\text{-}36}$=0.64 Hz), 8.729 (dd, $1H_{34B\text{ or }36B}$, $^3J_{34\text{-}35}$=8.10 Hz, $^4J_{34\text{-}36}$=0.64 Hz), 8.698 (dd, $1H_{36A\text{ or }34A}$, $^3J_{36\text{-}35}$=8.10 Hz, $^4J_{36\text{-}34}$=0.64 Hz), 8.690 (dd, $1H_{36B\text{ or }36B}$, $^3J_{36\text{-}35}$=8.10 Hz, $^4J_{36\text{-}34}$=0.64 Hz), 8.64-8.60 (m, $3H_{32\text{-}43\text{-}9A,B}$), 8.386 (dd, $1H_{12A}$, $^3J_{12\text{-}11}$=5.38 Hz, $^4J_{12\text{-}10}$=1.60 Hz, $^5J_{12\text{-}9}$=0.60 Hz), 8.351 (dd, $1H_{12B}$, $^3J_{12\text{-}11}$=5.38 Hz, $^4J_{12\text{-}10}$=1.60 Hz, $^5J_{12\text{-}9}$=0.60 Hz), 8.160 (t, $1H_{35A}$, $^3J_{35\text{-}34,36}$= 8.10 Hz), 8.154 (t, $1H_{35B}$, $^3J_{35\text{-}34,36}$= 8.10 Hz), 8.143 (ddd, $1H_{3B}$, $^3J_{3\text{-}2}$=8.05 Hz, $^4J_{3\text{-}1}$=1.50 Hz, $^5J_{3\text{-}6}$= 0.46 Hz), 8.137 (ddd, $1H_{3A}$, $^3J_{3\text{-}2}$=8.05 Hz, $^4J_{3\text{-}1}$=1.50 Hz, $^5J_{3\text{-}6}$= 0.46 Hz), 8.047 (ddd, $1H_{10A}$, $^3J_{10\text{-}9}$=8.05 Hz, $^4J_{10\text{-}11}$=7.65 Hz, $^5J_{10\text{-}12}$=1.60 Hz), 8.047 (ddd, $1H_{10B}$, $^3J_{10\text{-}9}$=8.05 Hz, $^3J_{10\text{-}11}$=7.65 Hz, $^4J_{10\text{-}12}$=1.60 Hz), 8.00 (ddd, $1H_{27A,B\text{ or }42\ A,B}$, $^3J_{27\text{-}32}$=8.05 Hz, $^3J_{27\text{-}28}$=7.60Hz, $^4J_{27\text{-}29}$=1.40 Hz), 7.898 (ddd, $1H_{41B\text{ or }28B}$, $^3J_{41\text{-}40}$=8.05 Hz, $^2J_{41\text{-}42}$=7.60 Hz, $^3J_{41\text{-}43}$= 1.80 Hz), 7.897 (ddd, $1H_{41A}$, $^2J_{41\text{-}40}$=8.05 Hz, $^2J_{41\text{-}42}$=7.60 Hz, $^4J_{41\text{-}43}$= 1.80 Hz), 7.891 (d, $1H_{29A,B\text{ or }40A,B}$, under another signal), 7.786 (ddd, $1H_{40A\text{ or }29A}$, $^3J_{40\text{-}41}$=8.05 Hz, $^4J_{40\text{-}42}$=1.00 Hz, $^5J_{40\text{-}43}$=0.90 Hz), 7.768 (ddd, $1H_{40B\text{ or }29B}$, $^3J_{40\text{-}41}$=8.05 Hz, $^4J_{40\text{-}42}$=1.00 Hz, $^5J_{40\text{-}43}$=0.90 Hz), 7.633 (ddd, $1H_{11A}$, $^3J_{11\text{-}10}$=7.65 Hz, $^3J_{11\text{-}12}$=5.38 Hz, $^4J_{11\text{-}9}$=1.60 Hz), 7.624 (ddd, $1H_{11B}$, $^3J_{11\text{-}10}$=7.65 Hz, $^3J_{11\text{-}12}$=5.38 Hz, $^4J_{11\text{-}9}$=1.60 Hz), 7.612 (ddd $1H_{2A,B}$, $^3J_{2\text{-}3}$=8.05 Hz, $^3J_{2\text{-}1}$=7.20 Hz, $^4J_{2\text{-}6}$=1.55 Hz), 7.465 (ddd, $1H_{6A}$, $^3J_{6\text{-}1}$=6.10 Hz, $^4J_{6\text{-}2}$=1.55 Hz, $^5J_{6\text{-}3}$=0.46 Hz), 7.459 (ddd, $1H_{6B}$, $^3J_{6\text{-}1}$=6.10 Hz, $^4J_{6\text{-}2}$=1.55 Hz, $^5J_{6\text{-}3}$=0.46 Hz), 7.406 (ddd, $1H_{28A\text{ or }41}$, $^3J_{28\text{-}27}$=7.60 Hz, $^3J_{28\text{-}29}$=5.72 Hz, $^4J_{28\text{-}32}$=1.50 Hz), 7.406 (ddd, $1H_{28B}$, $^3J_{28\text{-}27}$=7.60 Hz, $^3J_{28\text{-}29}$=5.72 Hz, $^4J_{28\text{-}32}$=1.50 Hz), 7.363 (ddd, $1H_{42A,B\text{ or }27A,B}$, $^3J_{42\text{-}41}$=7.60 Hz, $^3J_{42\text{-}43}$=4.83 Hz, $^4J_{42\text{-}40}$=1.00 Hz), 6.749 (ddd, $1H_{1A}$, $^3J_{1\text{-}2}$=7.20 Hz, $^3J_{1\text{-}6}$=6.10 Hz, $^4J_{1\text{-}3}$=1.50 Hz), 6.747 (ddd, $1H_{1A}$, $^3J_{1\text{-}2}$=7.20 Hz, $^3J_{1\text{-}6}$=6.10 Hz, $^4J_{1\text{-}3}$=1.50 Hz), 5.988 (s, $1H_{14\text{ or }22A,B}$), 5.914 (s,

$1H_{14\ or\ 22A,B}$), 2.479 (s, $3H_{24B}$), 2.407 (s, $3H_{24A}$), 1.714 (s, $3H_{23B}$), 1.714 (s, $3H_{23A}$). ^{13}C {^{1}H} NMR (400MHz, acetone-d_6) δ=171.341 ($C_{5A,B}$), 164.280 (C_{39A} or C_{30A}), 164.232 (C_{39B} or C_{30B}), 161.192 ($C_{33A,B}$ or $C_{37A,B}$), 161.100 ($C_{33A,B}$ or $C_{37A,B}$), 160.777 (C_{7A}), 160.764 (C_{7B}), 160.490 (C_{30B} or C_{39B}), 160.475 (C_{30A} or C_{39A}), 154.645 ($C_{12A,B}$), 153.882 (C_{6A}), 153.842 (C_{6B}), 153.027 (C_{29A} or C_{40A}), 152.950 (C_{29B} or C_{40B}), 152.823 ($C_{16A,B}$), 149.235 ($C_{32A,B}$ or $C_{43A,B}$), 148.898 ($C_{20A,B}$), 138.238 ($C_{41A,B}$ or $C_{28A,B}$), 137.831 (C_{10A}), 137.797 (C_{10B}), 137.768 (C_{27A} or C_{42A}), 137.747 (C_{27B} or C_{42B}), 137.563 (C_{2A}), 137.539 (C_{2B}), 134.374 (C_{35A}), 134.327 (C_{35B}), 128.181 (C_{2A}), 128.158 (C_{2B}), 128.064 (C_{28A} or C_{41A}), 128.035 (C_{28B} or C_{41B}), 125.219 (C_{3B}), 125.154 (C_{3A}), 124.601 ($C_{43A,B}$ or $C_{32A,B}$), 124.486 ($C_{1A,B}$), 124.370 (C_{9A}), 124.344 (C_{9B}), 123.744 ($C_{34A,B}$ or $C_{36A,B}$), 123.700 (C_{42B} or C_{27B}), 123.660 (C_{42A} or C_{27A}), 123.251 (C_{36A} or C_{34A}), 123.223 (C_{36B} or C_{34B}), 121.091 (C_{40B} or C_{29B}), 121.040 (C_{40A} or C_{29A}), 114.107 (C_{17A}), 113.808 (C_{17B}), 76.860 (C_{13} or C_{21A}), 76.764 (C_{13} or C_{21B}), 36.438 (C_{23A}), 36.380 (C_{23B}), 10.734 (C_{24B}), 10.680 (C_{24A}). ^{15}N NMR (600MHz, acetone-d_6) δ=199.60 (N_{19}, $^{1}J_{N-H}$=108.24 Hz), 219.09 (N_{18}), 228.91 (N_4), 249.27 (N_8), 252.57 (N_{31} or N_{44}), 292.20 (N_{38}), 305.16 (N_{44} or N_{31}). ESI-MS (MeOH): *m/z*= 694.1 ([M-PF_6^-]$^+$). UV-vis (CH_2Cl_2) [λ_{max}, nm (ε, M^{-1} cm^{-1})]: 274 (5217), 317 (1523), 390 (1335), 487 (1278), 519 (1127), 615 (377).

[Ru^{II}(H_2O)(Hpbl)(trpy)](PF_6)$_2$ [2](PF_6)$_2$. To a solution of 0.100 g (0.1224 mmol) **[1](PF_6)**, in 40 mL of acetone:water (3:1), 5.84 mL of $AgBF_4$ 0.021 M solution were added. The mixture was stirred at RT during 2.5 h. After one night without stirring the resulting solution was filtered and 1 mL of a saturated aqueous NH_4PF_6 was added to the filtrate. The volume was then reduced on a until a solid appeared. The mixture was cooled in the fridge for 12 h and after that, the solid obtained was filtered off, washed with cold water and diethyl ether and vacuum dried. Yield: 54 mg (46%). This complex can also be obtained *in situ* by dissolving the chloro complex **1**$^+$ in aqueous media, but it cannot be isolated without the use of silver(I) salts as chlorine scavenger due to the higher insolubility of the complex [**1](PF_6)**. ^{1}H NMR (400 MHz, acetone-d_6/D_2O/CF_3SO_3D) δ=8.925 (d, $1H_{9A,B}$, $^{3}J_{9-10}$=5.80 Hz), 8.767 (td, $1H_{11B}$, $^{3}J_{11-10,12}$=8.05 Hz, $^{4}J_{11-9}$=1.60 Hz), 8.763 (td, $1H_{11A}$, $^{3}J_{11-10,12}$=8.05 Hz, $^{4}J_{11-9}$=1.60 Hz), 8.655 (d, $1H_{34A\ or\ 36A}$, $^{3}J_{34-35}$=8.05 Hz), 8.639 (d, $1H_{34B\ or\ 36B}$, $^{3}J_{34-35}$=8.05 Hz), 8.601 (d, $1H_{34B\ or\ 36B}$, $^{3}J_{36-35}$=8.05 Hz), 8.599 (d, $1H_{34A\ or\ 36A}$, $^{3}J_{36-35}$=8.05 Hz), 8.533 (d, $1H_{32A,B\ or\ 43A,B}$, $^{3}J_{32-27}$=8.00 Hz), 8.514 (d, $1H_{43A,B\ or\ 32A,B}$, $^{3}J_{43-42}$=8.00 Hz), 8.363 (d, $1H_{29B\ or\ 40B}$, $^{3}J_{29-28}$=5.70 Hz), 8.306 (d, $1H_{12B}$, $^{3}J_{12-11}$=8.05 Hz), 8.299 (d, $1H_{12A}$, $^{3}J_{12-11}$=8.05 Hz), 8.273 (d, $1H_{29A\ or\ 40A}$, $^{3}J_{29-28}$=5.70 Hz), 8.163 (ddd, $1H_{10A,B}$, $^{3}J_{10-11}$=8.05 Hz, $^{3}J_{10-9}$=5.80 Hz, $^{4}J_{10-12}$=1.10 Hz), 8.118 (t, $1H_{35A}$, $^{3}J_{35-34,36}$=8.05 Hz), 8.115 (t, $1H_{35B}$, $^{3}J_{35-34,36}$=8.05 Hz), 8.087 (dd, $1H_{40A,B\ or\ 29A,B}$, $^{3}J_{40-41}$=5.65 Hz, $^{4}J_{40-42}$= 1.40 Hz), 7.997 (dd, $1H_{3A,B}$, $^{3}J_{3-2}$=8.00 Hz, $^{4}J_{3-1}$=1.40 Hz), 7.948 (ddd, $1H_{27A,B\ or\ 42A,B}$, $^{3}J_{27-32}$=7.95 Hz, $^{3}J_{27-28}$=7.00 Hz, $^{4}J_{27-29}$=1.50 Hz), 7.934 (td, $1H_{42A,\ or\ 27A}$, $^{3}J_{42-41,43}$=8.00 Hz, $^{4}J_{42-40}$=1.40 Hz), 7.905 (td, $1H_{42B\ or\ 27B,}$, $^{3}J_{42-41,43}$=8.00 Hz, $^{4}J_{42-40}$=1.40 Hz), 7.572 (ddd, $1H_{28B\ or\ 41B,}$, $^{3}J_{28-27}$=7.00 Hz, $^{3}J_{28-29}$=5.70 Hz, $^{4}J_{28-32}$=1.20 Hz), 7.545 (ddd, $1H_{28A\ or\ 41A}$, $^{3}J_{28-27}$=7.00 Hz, $^{3}J_{28-29}$=5.70 Hz, $^{4}J_{28-32}$=1.20 Hz), 7.525 (ddd, $1H_{2A,B}$, $^{3}J_{2-3}$=8.00 Hz, $^{3}J_{2-1}$=7.40 Hz, $^{4}J_{2-6}$=1.50 Hz), 7.384 (ddd, $1H_{41A\ or\ 28A}$, $^{3}J_{41-42}$=8.00 Hz, $^{3}J_{41-40}$=5.65 Hz, $^{4}J_{41-43}$=1.10 Hz), 7.341 (d, $1H_{6A,B}$, $^{3}J_{6-1}$=6.00 Hz), 7.327 (ddd, $1H_{41B\ or\ 28B}$, $^{3}J_{41-42}$=8.00 Hz, $^{3}J_{41-40}$=5.65 Hz, $^{4}J_{41-43}$=1.10 Hz), 6.664 (ddd, $1H_{1A,B}$, $^{3}J_{1-2}$=7.40 Hz, $^{3}J_{1-6}$=6.00 Hz, $^{4}J_{1-3}$=1.40 Hz), 2.275 (s, $3H_{24B}$), 2.211 (s, $3H_{24A}$), 2.211 (s, $3H_{15B}$), 2.195 (s, $3H_{15A}$), 1.593 (s, $3H_{23B}$), 1.555 (s, $3H_{23A}$). ^{13}C {^{1}H} NMR (400 MHz, acetone-d_6/D_2O/CF_3SO_3D) δ=170.637 (C_{5B}), 170.587 (C_{5A}), 160.552 ($C_{33A,B}$ or $C_{37A,B}$), 160.480 ($C_{33A,B}$ or $C_{37A,B}$), 160.195 ($C_{30A,B}$), 159.708 ($C_{30A,B}$), 157.898 ($C_{7A,B}$), 154.676 ($C_{29A,B}$ or $C_{40A,B}$), 153.581 (C_{40B} or C_{29B}), 153.443 ($C_{40A\ or\ 29A-6A}$), 153.398 (C_{6B}), 148.798 (C_{11B}), 148.752 (C_{11A}), 144.210 ($C_{16A,B}$), 142.327 (C_{9A}), 142.286 (C_{9B}), 137.974 (C_{42B} or C_{27B}), 137.948 (C_{42A} or C_{27A}), 137.882 (C_{27B} or C_{42B}), 137.821 (C_{27A} or C_{42A}), 137.556 (C_{2A}), 137.529 (C_{2B}), 135.039 ($C_{35A,B}$), 128.231 ($C_{20A,B}$), 128.166 (C_{41A} or C_{28A}), 128.166 (C_{41B} or C_{28B}), 128.045 ($C_{28A,B}$ or $C_{41A,B}$), 127.501 ($C_{10A,B}$), 125.587 (C_{12A}), 125.476 (C_{12B}), 124.897 (C_{3B}), 124.767 (C_{3A}), 124.474 (C_{1A}), 124.767 (C_{1B}), 124.256-124.207 ($C_{32A,B\ or\ 43A,B-3A,B}$), 123.665 ($C_{34B}$ or C_{36B}), 123.621 (C_{34A} or C_{36A}), 123.103 ($C_{34A,B}$ or $C_{36A,B}$), 115.491 (C_{17A}), 115.293 (C_{17B}), 76.333 (C_{13B} or C_{21B}), 76.216 (C_{13A} or C_{21A}), 71.460 (C_{13B} or C_{21B}), 71.260 (C_{13A} or C_{21A}), 36.040 (C_{23B}), 36.850 (C_{23A}), 27.233 (C_{15B}), 27.136 (C_{15A}), 10.171 (C_{24B}), 10.132 (C_{24A}). ^{15}N NMR (600MHz, acetone-d_6/D_2O/CF_3SO_3D) δ=289.00 (N_{38}), 250.36 (N_{44}

or N_{31}), 247.22 (N_{44} or N_{31}), 225.87 (N_4), 196.62 (N_8). ESI-MS (MeOH): *m/z*= 658.2 ([M-2PF_6^--H^+]$^+$). UV-vis (pH=1, 0.1 M triflic acid aqueous solution) [λ_{max}, nm (ε, M^{-1} cm^{-1})]: 270 (5504), 310 (5449), 360 (1461), 450 (1207), 480 (1170).

[$Ru_2^{II}Cl_2$(Hpbl)(trpy)$_2$](PF_6) [3a](PF_6). To a round bottom flask charged with 20 mL of dry methanol, [Ru(trpy)Cl_3] (200 mg, 0.454 mmol), LiCl (61 mg, 1.439 mmol), Hpbl (74 mg, 228 mmol) and MeONa 0.29 M (2.4 mL, 0.685 mmol) were added. The mixture was refluxed under stirring for 24 h. Alternatively the reaction can be performed in a microwave reactor by carrying out five 10 minutes heating cycles (75^{o}C/300 W) with 5 minutes of equilibration time between cycles. The mixture was filtered and 2 mL of a saturated NH_4PF_6 aqueous solution and 5 mL of water were added to the filtrate. Then, the volume was reduced on a rotary evaporator until a precipitate appeared which, was filtered off and dried. The obtained solid was partially dissolved in hot CH_2Cl_2, and the solution was cooled down. The remaining solid precipitated was filtered off, washed with water and diethyl ether and vacuum dried. Yield: 75 mg (27%) for reflux reaction; 100 mg (36%) for microwave reaction. ESI-MS (MeOH): *m/z*= 1205.0500 ([M]$^+$).

Instrumentation and Measurements: UV-Vis spectroscopy was performed with a HP8453 spectrometer using 1 cm quartz cells. ^{1}H NMR spectroscopy was performed on a Bruker DPX 360 MHz, 400 MHz and 600 MHz in Universitat Autònoma de Barcelona magnetic resonance service (SeRMN-UAB). Samples were run in acetone-d_6, acetonitrile-d_3, D_2O with CF_3SO_3D or with NaOD with internal references (residual protons and/or tetramethylsilane or DSS respectively). Elemental analyses were performed using a Carlo Erba CHMS EA-1108 instrument provided by the Chemical Analysis Service of the Universitat Autònoma de Barcelona (CAS-UAB). ESI-MS experiments were performed on a HP298s GC-MS system from the CAS-UAB. CV experiments were performed with a PAR283 potentiostat using a three-electrode cell. A glassy carbon disk (3 mm diameter) was used as working electrode, platinum wire was used as auxiliary electrode, and a saturated sodium calomel electrode (SSCE) was used as the reference electrode. For the solutions of complexes in organic solvents, nBu_4NPF_6 was used as supporting electrolyte to yield a solution with 0.1 M ionic strength. All $E_{1/2}$ values reported here were estimated from cyclic voltammetry as the average of the oxidative and reductive peak potentials ($E_{p,a}$+$E_{p,c}$)/2 and are referred to the SSCE reference electrode. Species concentration was approximately 1 mM. For the construction of the Pourbaix diagram the following buffers were used: hydrogen phthalate/triflic acid up to pH = 4, hydrogen phthalate/sodium hydroxide for pH = 5, dihydrogenphosphate/sodium hydroxide for pH = 6, borax/triflic acid for pH = 7, hydrogen phosphate/sodium hydroxide for the pH range 8-9. Also 0.1 M triflic acid was used for pH = 1.0.

X-ray Crystal Structure Determination. Crystals of complexes **[3b](PF_6)$_2$** and **[3c](PF_6)$_2$** were obtained by slow diffusion of diethyl ether into an acetone solution containing complex **[3a](PF_6)** at room temperature. **[3b](PF_6)$_2$** crystals were obtained after 1e^- oxidation of **[3a](PF_6)** and crystals of **[3c](PF_6)$_2$** after its 2 e^- oxidation, both oxidation were caused by the atmospheric oxygen. The measured crystals were prepared under inert conditions immersed in perfluoropolyether as protecting oil for manipulation.

Data collection: Crystal structure determinations were carried out using a Bruker-Nonius diffractometer equipped with an APPEX 2 4K CCD area detector, a FR591 rotating anode with MoK_α radiation, Montel mirrors as monochromator and a Kryoflex low temperature device (T = -173 $^\circ$C). Full-sphere data collection was used with ω and φ scans. *Programs used:* Data collection APEX-2[10], data reduction Bruker Saint [11] V/.60A and absorption correction SADABS[12].

Structure Solution and Refinement: Crystal structures solutions were achieved using direct methods as implemented in SHELXTL [13] and visualized using the program XP. Missing atoms were subsequently located from difference Fourier synthesis and added to the atom list. Least-squares refinement on F^2 using all measured intensities was carried out using the program SHELXTL. All non-hydrogen atoms were refined including anisotropic displacement parameters.

Scheme 5. Complexes synthesis.

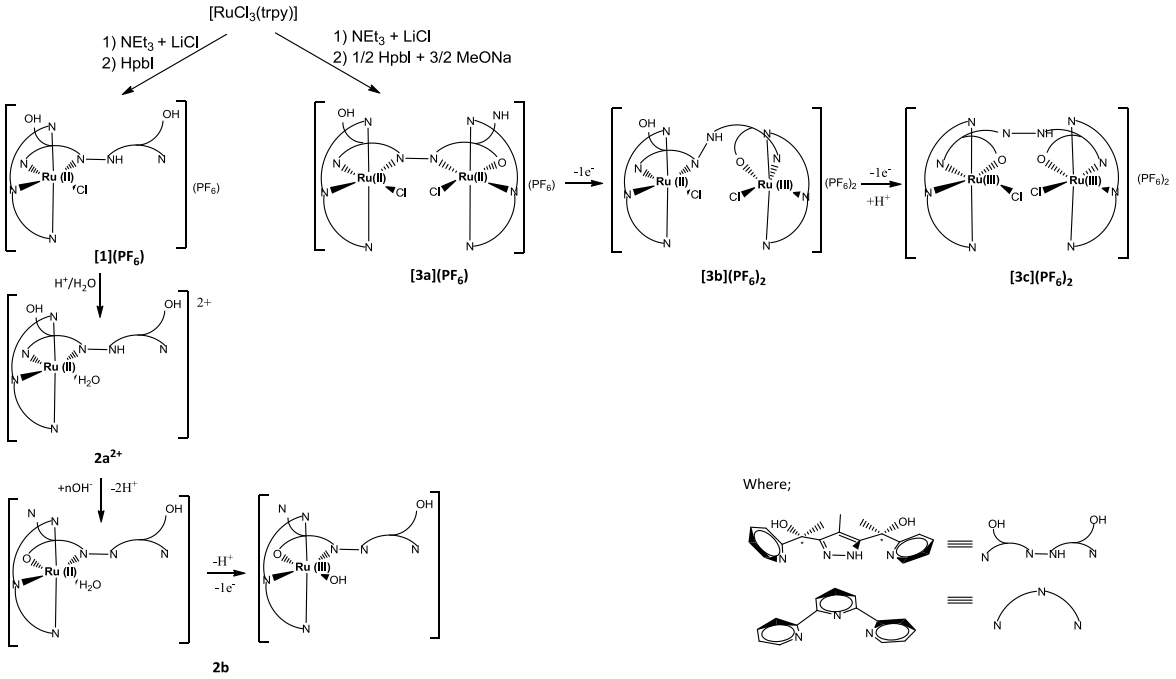

Results and discussion

Ligand and Complex Synthesis.

The synthetic strategy followed to prepare the new Hpbl ligand is depicted in Scheme 4. The synthetic procedures for steps (1) and (3) were taken from literature reports.[9a,b] Step (2), also previously described,[9c,d] was simplified by avoiding the reported unnecessary final distillation. Finally, step (4) involves the double nucleophilic attack of a pyridine lithiate derivative to the two ketone carbonyl groups, giving rise to the formation of two tertiary alcohols, which generate two chiral centres. Column chromatography of the reaction crude gave, as the last eluted fraction, the desired Hpbl ligand as a mixture of two diastereomers in a 3:1 (A:B) ratio. The new ligand was characterized by the usual analytic and spectroscopic techniques (see Figures S1 and S15).

To prepare the Ru complexes [$RuCl_3$(trpy)] was used as metal precursor. In Scheme 5 the synthetic procedure followed in the preparation of the chloro derivatives [**1**]**(PF$_6$)** and [**3a**]**(PF$_6$)**, **[3b](PF$_6$)$_2$**, **[3c](PF$_6$)$_2$** and the aqua species **2a**$^{2+}$ and **2b** has been represented. The mononuclear chloro complex **[1](PF$_6$)** was obtained by the direct reaction of equimolar amounts of Hpbl and [$RuCl_3$(trpy)] in presence of NEt_3 at 40 ºC. From the later and under acidic conditions the chloro ligand is replaced by the aqua one generating complex **2a**$^{2+}$.

Scheme 4. Schematic ligand synthesis.

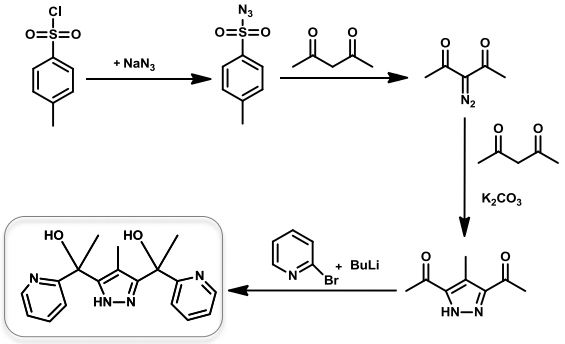

The preparation of the aqua complex **2a**$^{2+}$ has also been attempted in the presence of silver(I) ions. However, this synthetic route gave non-reproducible results, probably because of the coordinating capacity of the silver ion to the free N atoms of the Hpbl ligand. The initial ratio of the two diastereomers is maintained after ruthenium complexation but can be modified by means of a preparative alumina TLC.

The dinuclear complex **[3a](PF$_6$)** was synthesized under inert conditions in a 3:2:1 (MeONa: [$RuCl_3$(trpy)]: Hpbl) molar ratio by using two different techniques; reflux and microwave reactor as detailed in the Experimental Section. For both methodologies the purification of **3a**$^{+}$ is based on its lower solubility in hot CH_2Cl_2 with respect to the rest of by-products produced in the reaction. Complexes **3b**$^{2+}$ and **3c**$^{2+}$ can be obtained by

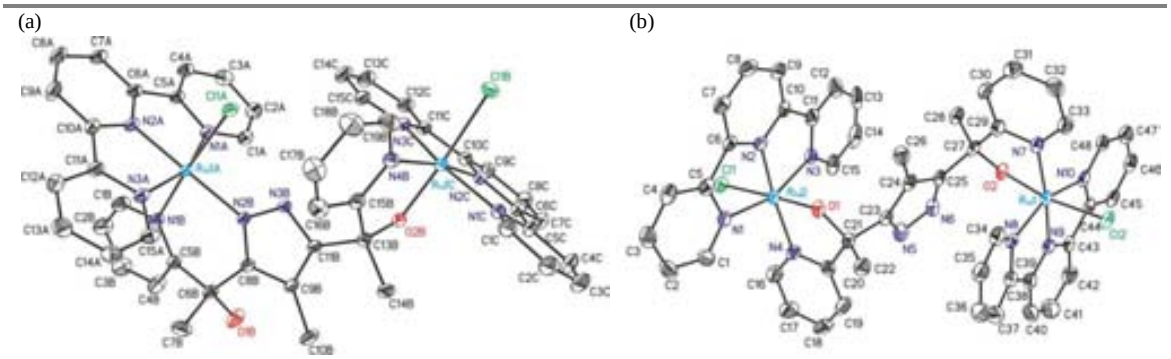

Figure 1. Ortep views (50% probability) of the cationic part of complexes **[3b](PF$_6$)$_2$** (a) and **[3c](PF$_6$)$_2$**. (b).

oxidation involving the loss of one or two electrons respectively. These complexes were obtained during the crystallization processes and they were also detected in CV.

All Ru complexes prepared in the present work were characterized by elemental analysis and spectroscopic techniques (UV-vis, MS, NMR) and their redox properties were analyzed by cyclic voltammetry (CV).

X-ray structures

Suitable crystals of complexes **2b, [3b](PF$_6$)$_2$** and **[3c](PF$_6$)$_2$** have been obtained and their structure has been studied by X-ray diffraction analysis. The crystallographic parameters for complexes **[3b](PF$_6$)** and **[3c](PF$_6$)$_2$** are reported in Table 1 and views of their cationic structures are presented in Figure 1. In these dinuclear complexes both ruthenium metal centres adopt pseudo-octahedral coordination geometries with three positions occupied by the meridional trpy ligand, two by the tetradentate Hpbl ligand and the sixth position is occupied by a chloro ligand. In the structure of complex **[3b](PF$_6$)$_2$** the two metal centres present different oxidation state Ru(II) and Ru(III), due to an oxidation process that takes place during the crystallization process. The Ru(III) centre is coordinated to the Hpbl bridging ligand through the alkoxo oxygen and the pyridine nitrogen atoms, forming a five membered ring. On the other hand, the Ru(II) metal centre is coordinated to the Hpbl ligand *via* two nitrogen atoms, one from the pyridine moiety and the other from the pyrazol scaffold. This coordination allows the formation of a six membered ring between the ruthenium metal and the Hpbl ligand. It is important to notice here that the pyrazol ring has one non-coordinated nitrogen due to the Ru(III)-O coordination.

Table 1. Crystallographic data for complexes **[3b](PF$_6$)$_2$** and **[3c](PF$_6$)$_2$.**

Complex	**[3b](PF$_6$)$_2$**	**[3c](PF$_6$)$_2$**
Empirical formula	C_{54} H_{54} Cl_2 F_{12} N_{10} $O_{4.50}$ P_2 Ru_2	C_{48} H_{44} Cl_2 F_{12} N_{10} $O_{4.50}$ P_2 Ru_2
Formula Weight	1478.05	1395.91
Temperature, K	100(2)	100(2)
Wavelength, Å	0.71073	0.71073
Crystal system	Triclinic	Triclinic
Space group	P-1	P-1
a, Å	12.5295(6)	13.2322(9)
α, deg	107.284(2)	70.027(2)
b, Å	14.6459(7)	15.2695(10)
β, deg	109.045(2)	68.822(2)
c, Å	18.2104(9)	15.8750(10)
γ, deg	96.360(2)	89.430(2)
Vol., Å^3	2935.2(2)	2787.4(3)
Z	2	2
ρ(g/cm^3)	1.672	1.663
R [I>2σ(I)]^a	0.0415	0.0543
wR	0.0981	0.1482

Another interesting fact is that the free alcohol moiety is making a hydrogen bond with an acetone molecule. The unit cell contains one molecule of the complex, two PF_6^- anions, two acetone molecules and half molecule of water. One of the acetone molecules is disordered in two positions with a ratio of 53:47. The water molecule is also disordered (50:50) being shared with the neighboring unit cell.

A 2e$^-$ oxidation process taking place while crystallizing from [**3a](PF$_6$)** leads to the formation of complex **[3c](PF$_6$)$_2$**, with both metal centers in the Ru(III) oxidation state. Their coordination to the Hpbl ligand proceeds *via* the oxygen atoms of their alkoxo groups, forming five membered rings. A free pyrazole ring can therefore be observed in the X-ray structure (Figure 1b). The asymmetric unit contains one molecule of the cationic complex, two PF_6^- anions and two and a half molecules of water.

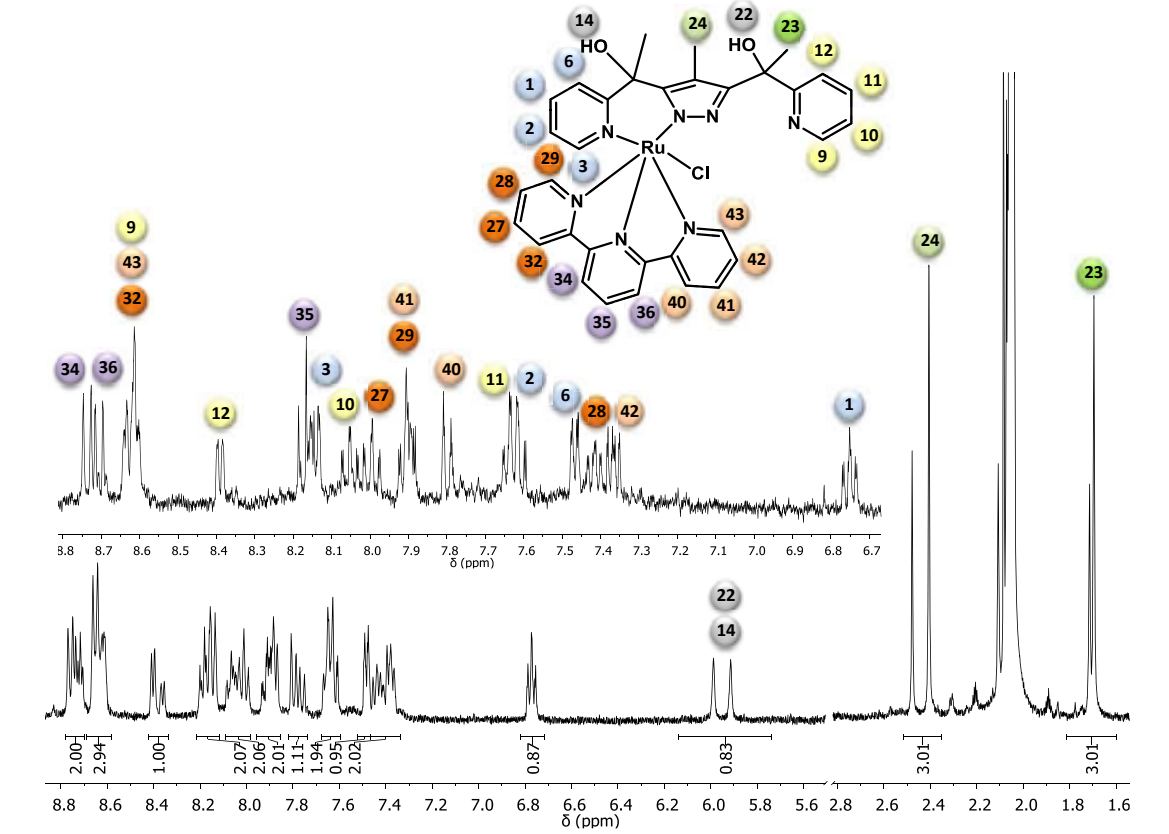

Figure 2. ^{1}H NMR spectra of complex $\mathbf{1}^{+}$ in acetone-d_6. Inset: aromatic zone of a diasteromeric enriched mixture, complex drawing and numbering scheme. Pink and orange highlighted trpy protons are indistinguishable.

The water molecules are partially disordered with and occupancy of 1:1:0.5.

Crystals of complex **2b** were obtained by slow evaporation from a mixture of acetone and NaOH basified water. However the low crystal quality only allows us to determine the connectivity of the metal centre and, therefore, its parameters and views are shown in the Supplementary Information (Figures S8 and S9). In this structure the ruthenium metal centre adopts pseudo-octahedral coordination geometry with three positions occupied by the meridional trpy ligand two by half of the tetradentate Hpbl and the final one by hydroxo or aqua groups. Here, the coordination to the Hpbl ligand occurs through the pyrazolic nitrogen and the alkoxo oxygen atom. Therefore, this structure allows observing another possible coordinative scenario in which the pyridine moiety is not coordinated to the metal centre.

NMR and UV-vis Spectroscopy

1D and 2D NMR spectroscopy allowed to structurally characterizing all the complexes in solution as well as the free Hpbl ligand (see Figure 2, Experimental Section and Figures S1-S7). In all the NMR spectra a mixture of the two diestereoisomers in a 3:1 (A:B) ratio is observed that is maintained during the complexation process.

For the free ligand all the resonances observed in the ^{1}H NMR spectrum can be unambiguously assigned based on their integrals, symmetry and multiplicity. In solution, it presents a symmetry axis bisecting the pyrazol ring. Therefore, only ^{1}H NMR resonances from one pyridine ring, one alcohol and two methyl groups, coming from the chiral centres and the central pyrazol ring, are observed (Figure S1). Furthermore, variable temperature (VT) ^{1}H NMR spectra were recorded in order to distinguish the resonances of both diastereomers taking advantage of their different temperature dependence (Figure S2). This effect allows us to distinguish when the multiplicity of a signal is caused by couplings to other protons or by two different diasteromers. The most relevant change could be observed in the 7.35 ppm signal. This resonance could be associated to a triplet at RT but it splits into two doublets (from each diasteromer) when the temperature is increased.

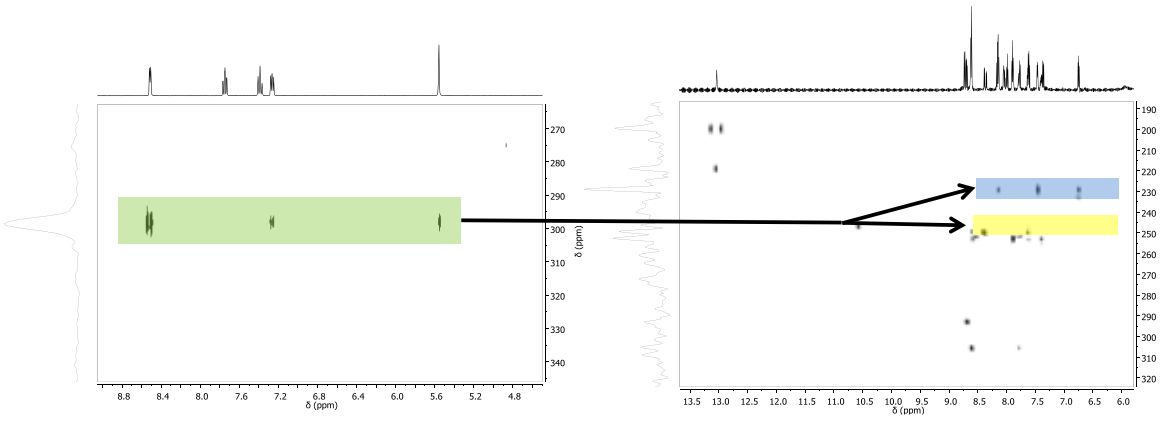

Figure 3. HMBC-N spectra for the free ligand (a) and complex $\mathbf{1}^+$(b) in acetone-d_6.

Each diastereomer of complexes $\mathbf{1}^+$ and $\mathbf{2a}^{2+}$ are non-symmetric giving one signal for each proton, carbon or nitrogen. The NMR spectra of an enriched mixture in one diastereomer, obtained after performing a preparative alumina TLC, allowed us to distinguish the signals of each diastereomer. Nevertheless, the complete assignment is not possible for the external pyridylic groups of the trpy ligand (Figure 2) that remain indistinguishable. For the chloro complex $\mathbf{1}^+$ it is important to point out that both alcohol protons can be observed. Furthermore, the low and similar ppm range at which they appear suggest that they are both not coordinated to the ruthenium metal centre. In addition, the proton from the pyrazol ring can be observed at 13 ppm. The absence of a signal at around 9 ppm is a reason to conclude that the chloro atom is occupying an *in-* disposition (the equatorial chloro ligand is oriented toward the centre of Hpbl ligand), instead of an *out-* disposition (where the chloro ligand would be oriented away from the centre of the bridging ligand). A significant downfield shift of the Hpbl proton resonances situated close to the chloro atom would be expected in the later case due to the strong deshielding effect of this ligand, as observed in related chloro-ruthenium complexes.[15] The NMR spectra for the aqua complex $\mathbf{2a}^{2+}$ were carried out in acetone-d_6 with a drop of a triflic acid D_2O solution.. Comparing the ^{1}H NMR spectra of the chloro and the aqua complexes (Figures S2a and S3a in the Supplementary information) the most shifted signals are those belonging to the non-coordinated pyridine due to its protonation in the employed acidic deuterated media.

In order to study the different species involved at different pH values, 1D and 2D NMR spectra have been performed in acidic and basic media employing a mixture of acetone-d_6, D_2O and triflic acid or acetone-d_6, D_2O, and NaOD, respectively. The ^{1}H NMR spectra indicate that at basic pH the number of involved species increase (compare Figures S4 and S5). DOSY experiments allowed us to confirm that all the involved species have similar molecular weight, according to their almost identical diffusion rate. The use of the well known $[Ru(H_2O)(bpy)(bpea)]^{2+}$ complex as internal standard in the DOSY experiments allowed us to assign all the present species as mononuclear complexes.

The presence of different nitrogen sites in the Hpbl ligand combined with their ability to perform linkage isomerism suggested the use of HMBC_N NMR experiments as a tool to study the nature of the ruthenium complexes in solution.[14] These experiences indicate that the coordination of only one ruthenium metal centre is in agreement with the loose of nitrogen symmetry observed for complex $\mathbf{1}^+$ when compared with the highly symmetric free Hpbl ligand (Figure 3). These results also allowed establishing the effect of the Ru coordination on the chemical shift of pyridilic and pyrazolic N Hpbl N atoms..

The ^{1}H NMR spectrum of complex $\mathbf{3a}^+$ presents the entire resonances as broad bands (Figure S7), fact that prevents their assignment and indicates the presence of dynamic processes. Variable temperature ^{1}H NMR experiments were run in order to modify this dynamic behaviour and improve the spectra. However, despite the shape of the signals is temperature-dependent at

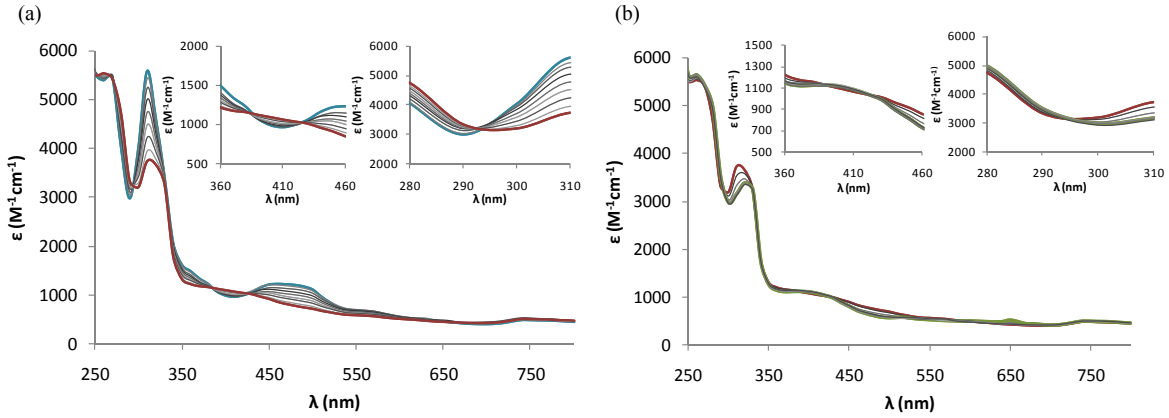

Figure 5. Titration of complex $\mathbf{2a}^{2+}$ with Ce(IV) monitored by UV-Vis spectroscopy. UV-Vis spectra colour code: Ru(II) in blue, Ru(III) in red and Ru(IV) in green. This titration was performed by 10 µL sequential additions of a 0.6 mM $Ce(NH_4)_2(NO_3)_6$ solution into 0.5 mL of 0.1 mM complex **[1](PF$_6$)** solution. Both solutions are prepared in 0.1 M CF_3COOH aqueous solution. Inset: zoom of the isosbestics points zone. (a) From Ru(II) to Ru(III); (b) From Ru(III) to Ru (IV).

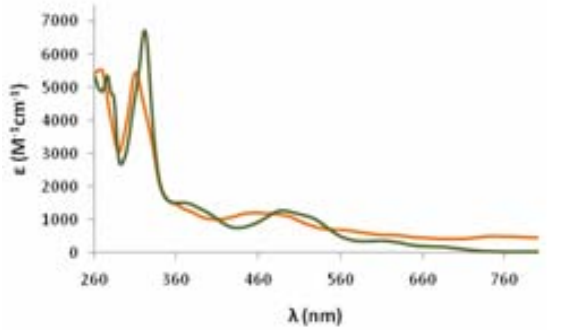

Figure 4. UV-Vis spectra for complex $\mathbf{1}^{+}$ (green) and $\mathbf{2}^{2+}$ (orange).

the studied temperature range, the ^{1}H NMR spectra was not improved enough to be assigned.

The UV-vis spectral features in solution for complexes $\mathbf{1}^{+}$ and $\mathbf{2a}^{2+}$ are listed in the experimental section. The observed absorptions agree with those published for similar complexes.[15] The spectra can be divided in three different regions: between 200 and 350 nm, in where very intense bands are observed due to intraligand π-π* transitions;[16] between 350 and 560 nm, in which there are mainly broad unsymmetrical Ru(dπ)-trpy/Hpbl(π*) metal-to-ligand charge transfer (MLCT) bands; [17] and finally the region above 560 nm in which d-d transitions are observed. Figure 4 shows the UV-vis spectra for complexes $\mathbf{1}^{+}$ and $\mathbf{2a}^{2+}$ where the different band displacement for the broad unsymmetrical Ru(dπ)-trpy/Hpbl(π*) MLCT bands is observed. The blue-shift exhibited by complex $\mathbf{2a}^{2+}$ confirms the coordination of the aqua ligand that relatively stabilize the dπ(Ru) levels and therefore gives rise to more energetic electronic transitions.

A redox titration of complex $\mathbf{2a}^{2+}$ using a Ce(IV) solution as oxidant has been carried out in order to characterize the different oxidation states. As shown in Figure 5 the redox titration generates three isosbestics points indicating a neat interconvertion between the different species, Ru(II), Ru(III) and Ru(III), Ru(IV). As can be observed, in general, as the oxidation state increase the intensity of the absorptions decreases, except for the new absortion generated at 400 nm.

Electrochemistry and linkage isomerism.

The redox properties of complexes $\mathbf{1}^{+}$, $\mathbf{2a}^{2+}$ and $\mathbf{3a}^{+}$ have been studied by cyclic voltammetry (CV). Complex $\mathbf{1}^{+}$, dissolved in dichloromethane and using 0.1 M n-Bu_4NPF_6 as electrolyte, displays one electrochemically quasi-reversible redox wave (Figure 6) at $E_{1/2}$ = 0.840 V, which is assigned to the formation of the corresponding Ru(III) complex,

$$[Ru^{II}Cl(Hbpl)(trpy)]^{+} - 1\ e^{-} \rightarrow [Ru^{III}Cl(Hbpl)(trpy)]^{2+} \quad (1)$$

As shown in Figure 6, no linkage isomerism was observed within the CV time scale, even when running the experiments at low scan rates (20 mV/s, CH_2Cl_2, 20 ^{o}C), because the ratios of [ic1]/[ia1] and [ic2]/[ia2] are not scan dependent When complex $\mathbf{1}^{+}$ is dissolved in a 0.1 M CF_3COOH pH=1 aqueous solution, the aqua complex $\mathbf{2a}^{2+}$ is generated. At high scan rates the CV of $\mathbf{2a}^{2+}$ presents two different redox

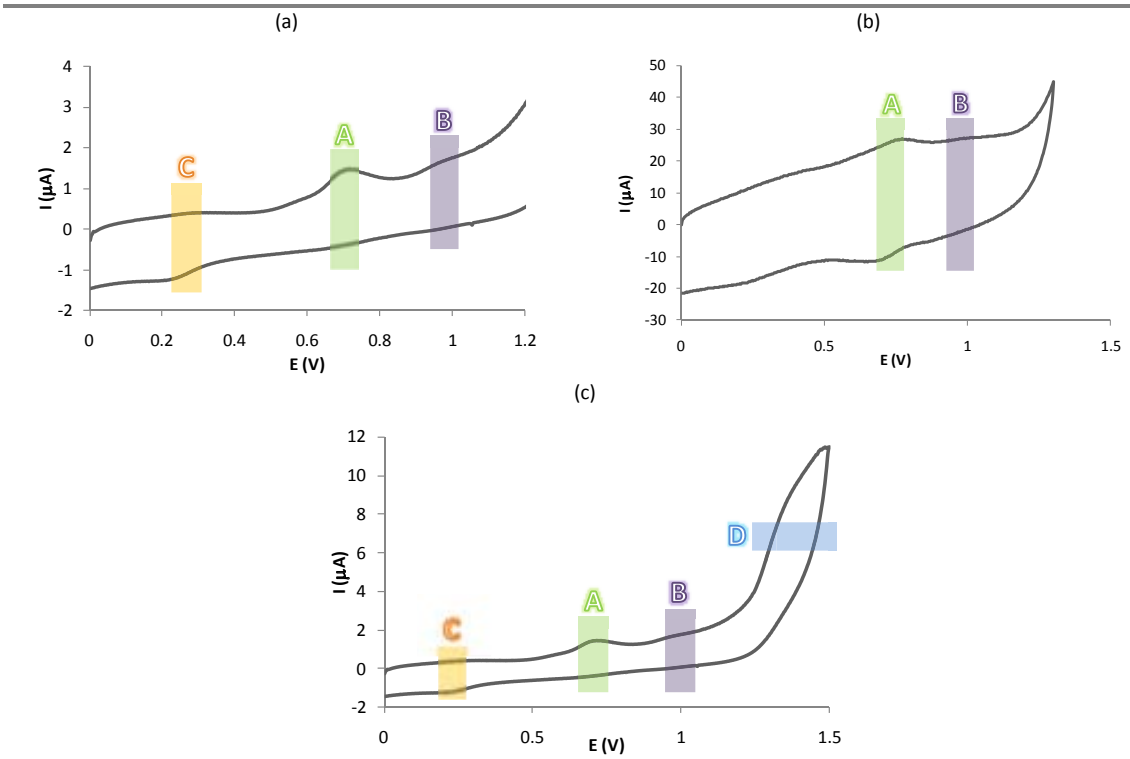

Figure 7. CV of complex $\mathbf{2a}^{2+}$ in 0.1 M CF_3COOH aqueous solution at pH=1 at different scan rates: (a) 20 mV/s, (b) 1000 mV/s and (c) 20 mV/s scanning from 0 to 1.5 V.

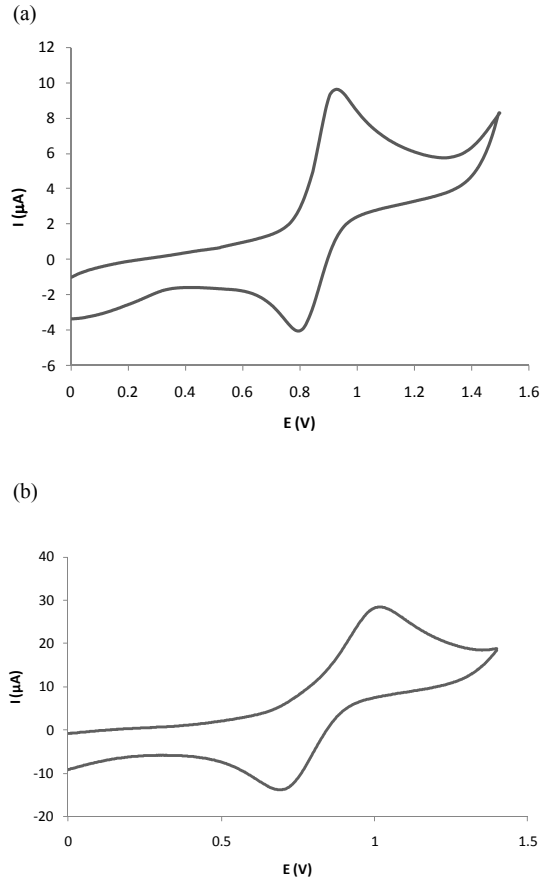

Figure 6. CV of complex $\mathbf{1}^{+}$ in CH_2Cl_2 using 0.1 M of TABH as electrolyte at different scan rates: (a) 50 mV/s and (b) 1000 mV/s.

processes (Figure 7b), the first and more intense one at $E_{1/2}$ = 0.725 V being associated to the first one electron oxidation,

$$[Ru^{II}H_2O(Hbpl)(trpy)]^{2+} - 1\ e^- \rightarrow [Ru^{III}H_2O(Hbpl)(trpy)]^{3+} \quad (2)$$

and the second and weaker one at $E_{1/2}$ = 0.932 V corresponding to the IV/III oxidation step,

$$[Ru^{III}H_2O(Hbpl)(trpy)]^{3+} - 1\ e^- \rightarrow [Ru^{IV}OH(Hbpl)(trpy)]^{3+} \quad (3)$$

Scanning up to 1.5 V (Figure 7c) we can observe a third irreversible wave (D) associated with the next oxidation step (4). This process is the responsible of oxygen evolution (5) and (6), and is typical for mononuclear Ru-aqua mononuclear complexes.[6a]

$$[Ru^{IV}OH(Hbpl)(trpy)]^{3+} - 1\ e^- \rightarrow [Ru^{V}O(Hbpl)(trpy)]^{3+} \quad (4)$$

$$[Ru^{V}O(Hbpl)(trpy)]^{3+} + H_2O \rightarrow [Ru^{III}OOH(Hbpl)(trpy)]^{3+} \quad (5)$$

$$[Ru^{III}OOH(Hbpl)(trpy)]^{3+} \rightarrow [Ru^{II}H_2O(Hbpl)(trpy)]^{2+} + O_2 \quad (6)$$

Scheme 6. Thermodynamic Cycle for the linkage isomerisation process taking place upon the electrochemical oxidation of $\mathbf{2}^{2+}$ at acidic pH (from 1 to 7) (a), and at basic pH (from 7 to 12) (a) and (b).

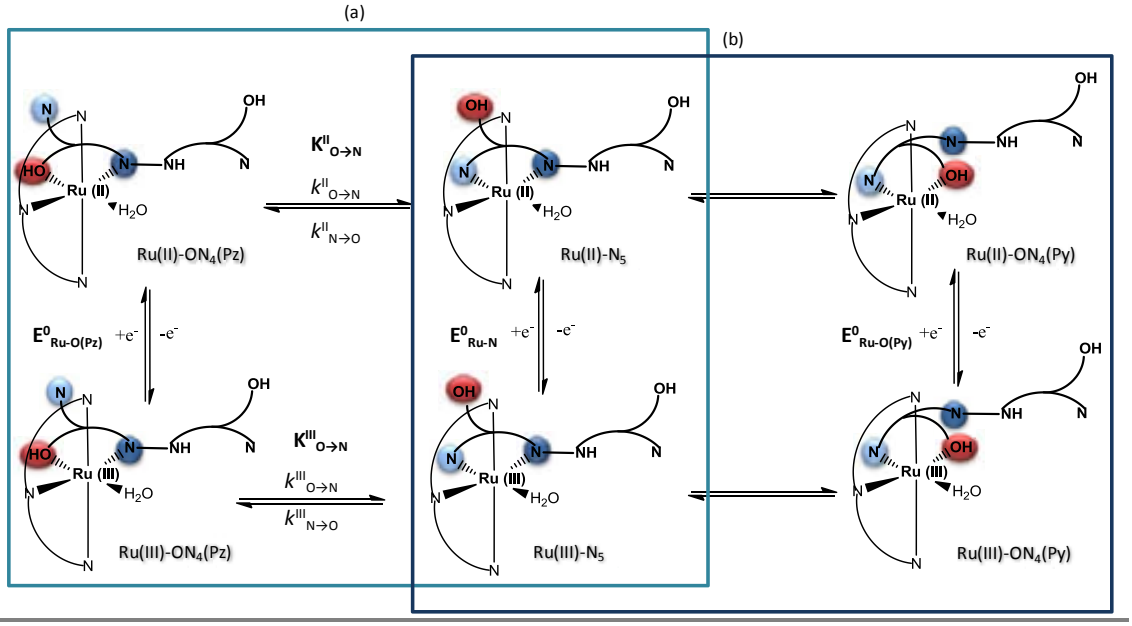

The existence of these two oxidation processes in a narrower potential range than in complex $\mathbf{1}^{+}$ is due to the presence of aqua groups that enable PCET processes.[18] Therefore, the easy access to higher oxidation states is due to fact that the simultaneous removal of electrons and protons prevents the build-up of high Coulombic charges.

The comparison of the cyclic voltammograms at fast (Figure 7b) and slow (Figure 7a) scan rates shows that the ratios of [ic1]/[ia1] and [ic2]/[ia2] are scan rate dependent. This fact points out the existence of a linkage isomerism when cycling between the Ru(II) and Ru(III) oxidation states (2) of this aqua complex. At fast scan rate scanning anodically we observe two quasi-reversible electrochemical waves (A and B), but at slow scan rates a quasi-irreversible anodic wave (A) and a quasi-irreversible cathodic wave (C) separated by about 0.5 V are observed. That confirms that the electrochemical process is associated to a chemical reaction. From now on the nomenclature of the different linkage isomers for mononuclear complexes will be as indicated in Scheme 6. Scheme 7 shows the same information for the dinuclear species. The thermodynamic cycle of this isomerisation process is represented in Scheme 6a. When the oxidation state of the metal centre is II, the ruthenium complex is coordinated to five nitrogen atoms (**Ru(II)-N_5**), three from the terpyridine ligand, and other two from the Hpbl

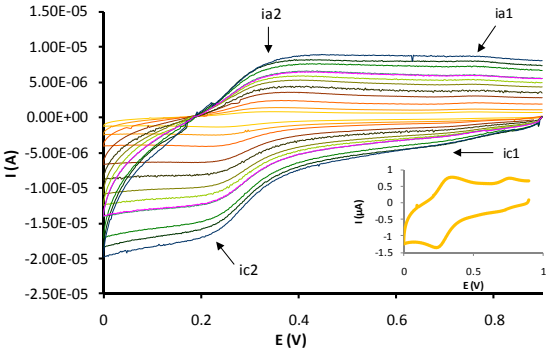

Figure 8. Cyclic voltammograms of complex $\mathbf{2a}^{2+}$ in a 0.1 M CF_3COOH aqueous solution at pH=1, scanning cathodically, and applying an initial equilibration time of 3 min. at 0.9 V. Scan rates: 20, 50, 100, 200, 300, 400, 500, 600, 700, 800, 900 and 1000 mV/s. Inset: CV at a scan rate of 20 mV/s.

Table 2. Thermodynamic and kinetic parameters for the linkage isomerisation of $\mathbf{2a}^{2+}$ determined by scan rate dependent CV (see Figure 8).

$E_{1/2}$, N (V)	0.73
$E_{1/2}$, O (V)	0.27
$K^{II}_{O->N}$	$6.7 \cdot 10^{6}$
$K^{III}_{N->O}$	8.8737
$k^{II}_{O->N}$ (s^{-1})	0.0005
$k^{II}_{N->O}$ (s^{-1})	$7.463 \cdot 10^{-11}$
$k^{III}_{O->N}$ (s^{-1})	0.03381
$k^{III}_{N->O}$ (s^{-1})	0.3

one. However, once the oxidation state III is reached, the coordination environment changes to **Ru(III)-N_4O**, where one nitrogen atom from Hpbl decoordinates and an oxygen atom from the alkoxo grup of the same ligand coordinates. This phenomenon was further corroborated by cathodically scanning from 0.9 V (Figure 8). The

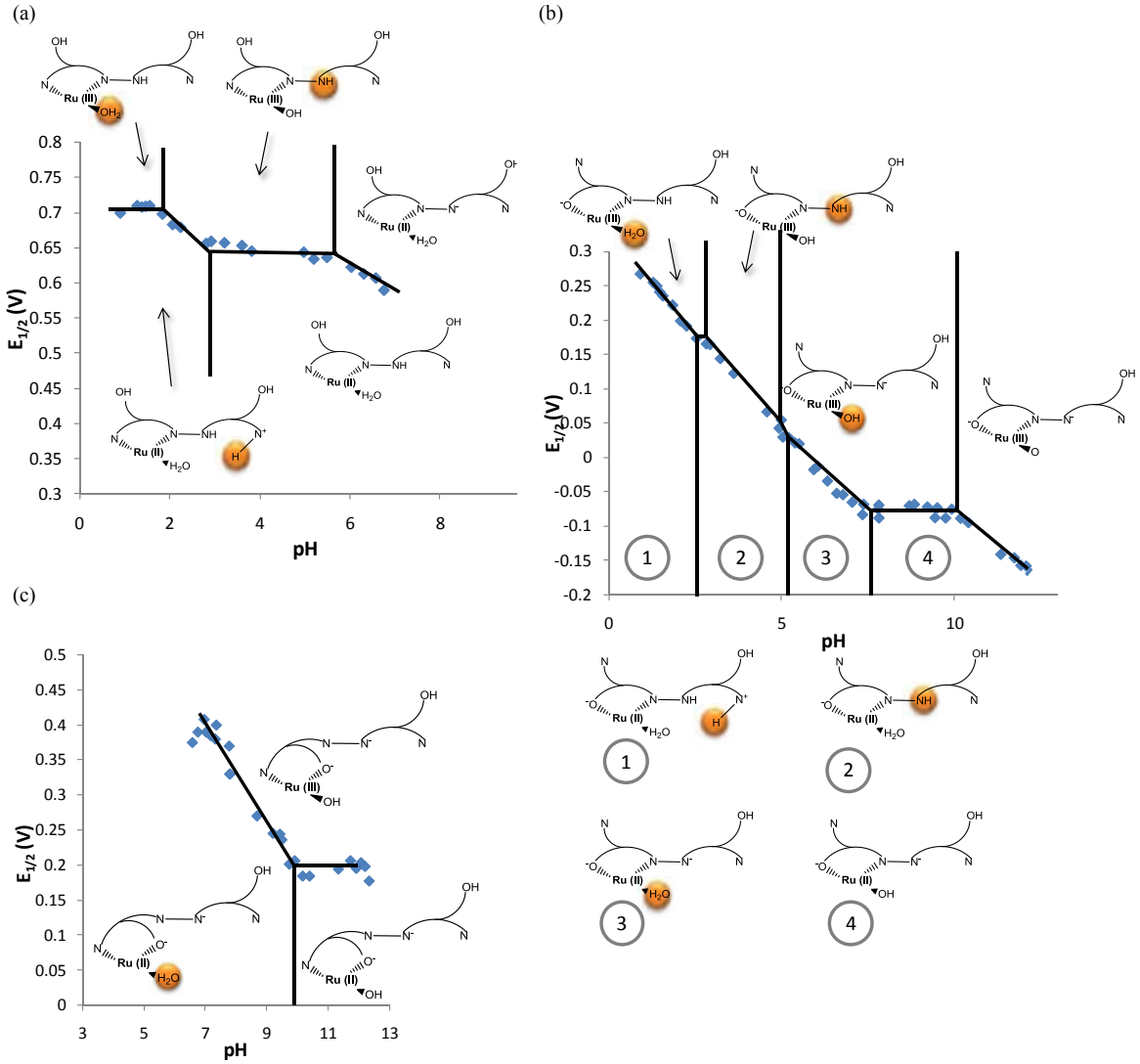

Figure 9. Pourbaix diagram for the different isomers of complex $\mathbf{2a}^{2+}$: (a) for **Ru-N$_5$** (b) **Ru-ON$_4$(Pz)** and (c) **Ru-ON$_4$(Py)**. The zones of stability of the different species are indicated by the oxidation state of the Ru metal and the degree of protonation of the aqua and Hbpl groups. The terpyridine ligand is not drawn for clarity. The proton affected in each process is indicated in orange..

ratios of [ic1]/[ia1] and [ic2]/[ia2] are strongly dependent on the scan rates and are consistent with the presence of chemical reactions coupled to the electrochemical processes as depicted in Scheme 6a.

The equilibrium constant for the Ru(III)-O/Ru(III)-N pair could be estimated at pH=1 from the cyclic voltammograms. The experiments were run from 0.90 V with an initial equilibration time of 3 min. to ensure process completeness (Figure 8). In this case, $K^{III}_{O\rightarrow N}$ could be calculated from the plot of [ic1]/[ic2] *vs.* v^{-1} and extrapolating to $v\rightarrow\infty$, which gives a value of $K^{III}_{O\rightarrow N} = 0.235$. The calculation of the equilibrium constant $K^{II}_{O\rightarrow N}$ was achieved by building the thermodynamic cycle shown in Scheme 6a, on basis of the equilibrium constant $K^{III}_{O\rightarrow N}$ and by assuming that $E^o=E_{1/2}$. The obtained value turns out to be $K^{II}_{O\rightarrow N}= 6.70\cdot10^6$.

Due to the exceedingly high stability of the O-bonded isomer, the kinetic constants (Table 2) could only be obtained by simulation with the DigiSim software[19] (Figure S18).

From these values it can be concluded that the analyzed linkage isomerism processes are slow and that the equilibrium constants agree with the Pearson's theory. Therefore, when the metal centre is in the oxidation state II (a relatively soft ion) has more affinity for the likewise softer nitrogen atom than for the harder oxygen one, a tendency that is reversed when the ruthenium oxidation state increase.

The thermodynamic stability areas of complex $\mathbf{2a}^{2+}$ with respect to pH and redox potentials have been evaluated and the corresponding Pourbaix

diagrams for all the observed isomers are shown in Figure 9. From pH 1 to pH 7 the coexistence of two different species is observed; the initial **Ru(III/II)-N_5** (Pourbaix diagram shown in Figure 9a) and the corresponding isomer **Ru(III/II)-ON_4(Pz)** (Figure 9b), obtained after successive pyridine decoordination and alkoxide coordination (Scheme 6a). The coordination environment of the later is defined by an oxygen atom from the terminal water molecule, four nitrogen atoms (three from the trpy, and one from the pyrazol group of the Hpbl ligand), and one oxygen atom (from the alkoxo group of Hpbl). While the **Ru(III/II)-N_5** species predominate in acidic media, the concentration of the **Ru(III/II)-ON_4(Pz)** isomer increase as the pH does. Once around pH = 7, a new species appears in the CV with a redox potential in between those of the **Ru(III/II)-N_5** and the **Ru(III/II)-ON_4(Pz)** isomers. Considering its $E_{1/2}$ value, the results of DOSY NMR experiments (which discard the presence of dinuclear species) [20] and the evidence of different N-decoordination patterns provided by the crystal structures, we propose here the formation of a second Ru-ON_4 species, **Ru(III/II)-ON_4(py)**, where the four coordinating nitrogen atoms are pyridylic in nature. Therefore, beside the three trpy N atoms, the linkage isomerism between the pyrazolic and the pyridylic nitrogens of Hpbl should take place (Scheme 6b). This **Ru(III/II)-ON_4(py)** species becomes more and more important as pH increase (Figure 9c).

Most of the pKa values, extrapolated from the Pourbaix diagrams, are similar to those described in the literature for similar polypyridylic ruthenium complexes.[15] The estimated pKa value for the Ru(II)-H_2O/Ru(II)-OH (pKa≈8) and Ru(III)-OH/Ru(III)-O (pKa≈10) for the **Ru(III/II)-ON_4(Pz)** isomer are much lower than the expected ones for this kind of complexes (pKa≈10 and pKa≈12, respectively). This decrease could be caused by the stabilization of the Ru(III)-O species though massive hydrogen bonding from OH^- and/or H_2O molecules that including the alkoxo moiety. An example of the OH^- hydrogen bond bridging both entities is displayed in Figure 10.

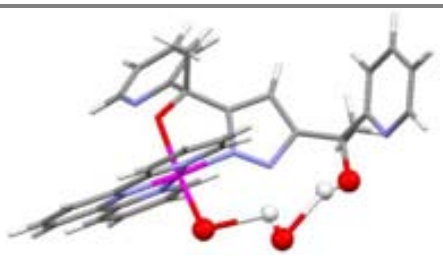

Figure 10. Mercury draw of the calculated structure of **[Ru^{III}-ON_4(Pz)-OH ·OH].** Hydrogen bonding between the Ru-OH and the alcohol group of the Hpbl.

The electrochemical behaviour of the dinuclear complex **3a**$^+$ has been studied in CH_2Cl_2 by cyclic voltammetry. The recorded voltammograms show the presence of three redox processes which are direction- and scan rate-dependent (Figure 11). When scanning anodically (Figures 11a and 11b), two different waves with very different behaviour appear. The first one [(A) in Figure 11a and 11b], at $E_{1/2}$ = 0.048 V, corresponds to a quasi-reversible redox process with an [ic]/[ia] ratio independent of the scan rate. This wave corresponds to the N_5-Ru(II)—**Ru(III/II)-ON_4(Pz)** part of complex **3a**$^+$ and it doesn't present linkage isomerism at the time scale of the CV (7).

N_5-Ru(II)—**Ru(II)-ON_4(Pz)** -1e^- ->
N_5-Ru(II)—**Ru(III)-ON_4(Pz)** (7)

On the other hand, the [ic]/[ia] of the second redox process [(B) in Figures 11a and 11b], is strongly scan rate dependent and corresponds to the **Ru(III/II)-N_5**—Ru(III)-ON_4(Pz) part of complex **3a**$^+$, which presents linkage isomerism promoted by the redox process (8).

N_5-Ru(II)—Ru(III)-ON_4(Pz) -1e^- ->
N_5-Ru(III)—Ru(III)-ON_4(Pz) (8)

As can be observed in Figure 11a the isomer generated after linkage isomerism of the **Ru(III/II)-N_5**—Ru(III)-ON_4(Pz) subunit presents a slightly different redox potential [(C) in Figure 11a] than that of N_5-Ru(II)—**Ru(III/II)-ON_4(Pz)** [(A) in Figure 11a]. This can only be rationalized assuming the generation of a **Ru(III)-ON_4(Py)** —Ru(III)-ON_4(Pz) subunit upon oxidation where now the pyridine, instead of the pyrazole of the Hpbl ligand is coordinated to the metal centre.

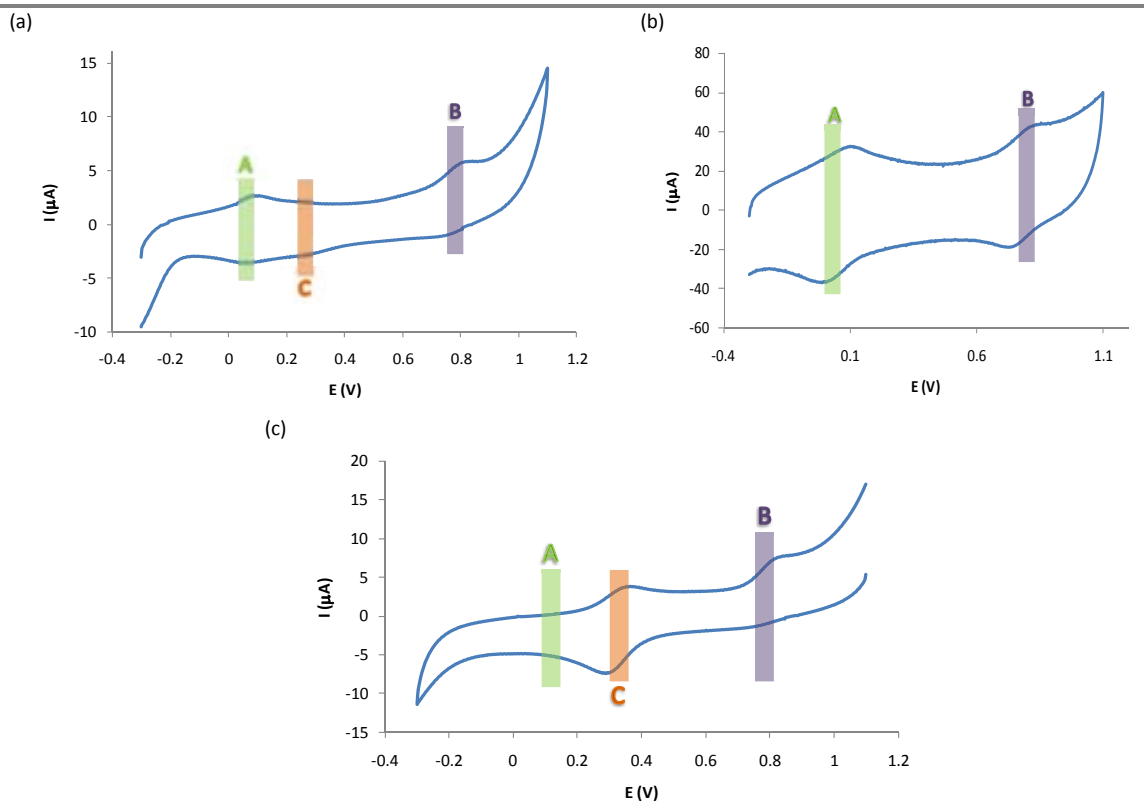

Figure 11. Cyclic voltammograms of complex $\mathbf{3a}^{+}$ (CH_2Cl_2, 0.1 M TABH as electrolyte) at different scan rates and scanning directions: (a) 40 mV/s anodically scanning (b) 700 mV/s anodically scanning (c) 50 mV/s scanning cathodically.

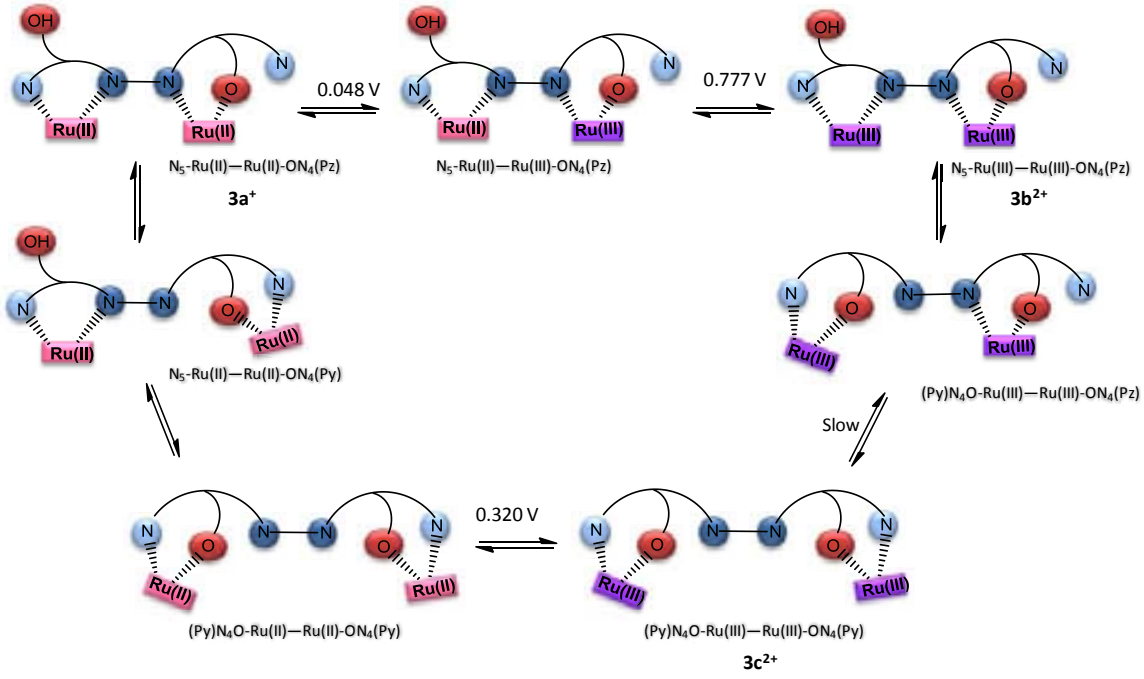

N_5-Ru(III)—Ru(III)-ON_4(Pz) ->
(Py)N_4O-Ru(III)—Ru(III)-ON_4(Pz) (9)

This fact is in agreement with the observed coordination environment of **[3b]$(PF_6)_2$ N_5-Ru(II)—Ru(III)-ON_4(Py)** in the obtained crystal structure (Figure 1a), where the oxidized metal centre is coordinated by the pyridylic nitrogen atom. Another isomer is then generated when both metal centres are oxidized to Ru(III) resulting in the replacement of the pyrazolic nitrogen by the pyridylic one (10).

(Py)N_4O-Ru(III)—**Ru(III)-ON_4(Pz)** ->
(Py)N_4O-Ru(III)—**Ru(III)-ON_4(Py)** (10)

Confirmation for the presence of this new isomer comes from two different points; (a) the X-ray structure of [**3c**]**$(PF_6)_2$** (Figure 1b) which shows a **(Py)N_4O-Ru(III)—Ru(III)-ON_4(Py)** arrangement of the metal centres and (b) the displacement of wave (B) to the same redox potential of wave (C) when scanning cathodically with a 3 min. equilibration time (Figure 11c). Therefore, this new coordination environment is favoured for the Ru(III) oxidation state but its formation is a slow process that can only be observed when spending long times at the Ru(III) potential (Scheme 7).

Conclusions

A new tetradentate bridging ligand containing ambidentate O/N motifs has been designed and synthesized in order to assist/stabilize the necessary cycling between intermediates of different oxidation states when performing redox oxidative catalysis. The coordination chemistry of this ligand to one and two ruthenium metal centres has been thoroughly studied and the redox- and pH-dependent linkage isomerism processes occurring has been identified both in the solid state (X-ray) and in solution (CV). The application of these new complexes in different biologically and technologically relevant catalytic oxidation processes is currently under development in our laboratories.

Acknowledgements

Support form SOLAR-H2 (EU 212508) and MEC (CTQ2010-21497 and Consolider Ingenio 2010 CSD2006-0003) are gratefully acknowledged. LF is grateful for the award of doctoral grant from UAB.

References

[1] (a) Wagenknecht, P. S.; Ford, P. C. *Coord. Chem. Rev.* **2011**, *255*, 591-616. (b) Jurow, M.; Schuckman, A. E.; Batteas, J. D.; Drain, C. M. *Coord. Chem. Rev.* **2010**, *254*, 2297-2310. (c) Ceroni, P. *Electrochemistry of functional supramolecular systems*; Wiley: Hoboken N.J., **2010**. (d) De Salvo, B.; Molas, G.; Perniola, L.; Jahan, C.; Buckley, J.; Jalaguier, E.; Gely, M. In *ECS Transactions*; Vienna, Austria, **2009**; 151-162. (e) Akita, M.; Koike, T. *Dalton Trans.* **2008**, 3523. (f) Nishihara, H.; Kanaizuka, K.; Nishimori, Y.; Yamanoi, Y. *Coord. Chem. Rev.* **2007**, *251*, 2674-2687. (g) Baranoff, E.; Collin, J.; Furusho, J.; Furusho, Y.; Laemmel, A.; Sauvage, J. *Inorg. Chem.* **2002**, *41*, 1215-1222. (h) Ballardini, R.; Balzani, V.; Credi, A.; Gandolfi, M. T.; Venturi, M. *Int. J. Photoenerg.* **2001**, *3*, 63-77. (i) Ashton, Peter R.; Ballardini, Roberto; Balzani, Vincenzo; Credi, Alberto; Dress, Klaus Ruprecht; Ishow, Elena; Kleverlaan, Cornelis J.; Kocian, Oldrich; Preece, Jon A.; Spencer, Neil; Stoddart, J. Fraser; Venturi, Margherita; Wenger, Sabine *Chem. Eur. J.* **2000**, *6*, 3558-3574.

[2] (a) Hamaguchi, T.; Ujimoto, K.; Ando, I. *Inorg. Chem.* **2007**, *46*, 10455-10457. (b) Rachford, A. A.; Rack, J. J. *J. Am. Chem. Soc.* **2006**, *128*, 14318-14324. (c) Butcher,, D. P.; Rachford, A. A.; Petersen, J. L.; Rack, J. J. *Inorg. Chem.* **2006**, *45*, 9178-9180. (d) Sens, C.; Rodríguez, M.; Romero, I.; Llobet, A.; Parella, T.; Sullivan, B. P.; Benet-Buchholz, J. *Inorg. Chem.* **2003**, *42*, 2040-2048.

[3] (a) Johansson, O.; Johannissen, L.; Lomoth, R. *Chem.-Eur. J.* **2009**, *15*, 1195-1204. (b) Johansson, O.; Lomoth, R. *Inorg. Chem.* **2008**, *47*, 5531-5533. (c) Johansson, O.; Lomoth, R. *Chem. Commun.* **2005**, 1578.

[4] (a) Serrano, I.; López, M. I.; Ferrer, I.; Poater, A.; Parella, T.; Fontrodona, X.; Solà, M.; Llobet, A.; Rodríguez, M.; Romero, I. *Inorg. Chem.* **2011**, DOI: 10.1021/ic200053f. (b) Prades, A.; Peris, E.; Albrecht, M. *Organometallics* **2011**.(c) Roeser, S.; Farràs, P.; Bozoglian, F.; Martínez-Belmonte, M.; Benet-Buchholz, J.; Llobet, A. *ChemSusChem* 2011, *4*, 197-207.(d) Tada, M.; Muratsugu, S.; Kinoshita, M.; Sasaki, T.; Iwasawa, Y. *J. Am. Chem. Soc.* **2010**, *132*, 713-724. (e) Dakkach, M.; López, M. I.; Romero, I.; Rodríguez, M.; Atlamsani, A.; Parella, T.; Fontrodona, X.; Llobet, A. *Inorg. Chem.* **2010**, *49*, 7072-7079.(f) Benet-Buchholz, J.; Comba, P.; Llobet, A.; Roeser, S.; Vadivelu, P.; Wiesner, S. *Dalton Trans.* **2010**, *39*, 3315.(g) Jiang, G.; Chen, J.; Thu, H.; Huang, J.; Zhu, N.; Che, C. *Angew. Chem. Int. Ed.* **2008**, *47*, 6638-6642.(h) Sala, X.; Santana, N.; Serrano, I.; Plantalech, E.; Romero, I.; Rodríguez, M.; Llobet, A.; Jansat, S.; Gómez, M.; Fontrodona, X. Eur. J. *Inorg. Chem.* **2007**, 5207-5214. (i) Serrano, I.; Sala, X.; Plantalech, E.; Rodríguez, M.; Romero, I.; Jansat, S.; Gómez, M.; Parella, T.; Stoeckli-Evans, H.; Solans, X.; Font-Bardia, M.; Vidjayacoumar, B.; Llobet, A. *Inorg. Chem.* **2007**, *46*, 5381-5389.(j) Rodríguez, M.; Romero, I.; Sens, C.; Llobet, A. *J. Mol. Catal. A-Chem.* **2006**, *251*, 215-220. (k) Punniyamurthy, T.; Velusamy, S.; Iqbal, J. *Chem. Rev.* **2005**, *105*, 2329-2364. (l) Catalano, V. J.; Heck, R. A.;

Immoos, C. E.; Öhman, A.; Hill, M. G. *Inorg. Chem*. **1998**, *37*, 2150-2157. (m) Sens, C.; Romero, I.; Rodríguez, M.; Llobet, A.; Parella, T.; Benet-Buchholz, J. *J. Am. Chem. Soc.* **2004**, *126*, 7798-7799. (n) Rodríguez, M. *Electrochim. Acta* **2003**, *48*, 1047-1054. (o) Marmion, M. E.; Takeuchi, K. J. *J. Am. Chem. Soc.* **1988**, *110*, 1472-1480. (p) Marmion, M. E.; Takeuchi, K. J. *J. Am. Chem. Soc.* **1986**, *108*, 510-511.

[5] (a) Meyer, T. J.; Huynh, M. H. V. *Inorg. Chem.* **2003**, *42*, 8140-8160. (b) Dovletoglou, A.; Adeyemi, S. A.; Meyer, T. J. *Inorg. Chem.* **1996**, *35*, 4120-4127. (c) Suen, H. F.; Wilson, S. W.; Pomerantz, M.; Walsh, J. L. *Inorg. Chem.* **1989**, *28*, 786-791. (d) Roecker, L.; Kutner, W.; Gilbert, J. A.; Simmons, M.; Murray, R. W.; Meyer, T. J. *Inorg. Chem.* **1985**, *24*, 3784-3791. (e) Takeuchi, K. J.; Thompson, M. S.; Pipes, D. W.; Meyer, T. J. *Inorg. Chem.* **1984**, *23*, 1845-1851. (f) Binstead, R. A.; Moyer, B. A.; Samuels, G. J.; Meyer, T. J. *J. Am. Chem. Soc.* **1981**, *103*, 2897-2899. (g) Moyer, B. A.; Meyer, T. J. *Inorg. Chem.* **1981**, *20*, 436-444. (h) Moyer, B. A.; Meyer, T. J. *J. Am. Chem. Soc.* **1978**, *100*, 3601-3603.

[6] (a) Concepcion, J. J.; Tsai, M.; Muckerman, J. T.; Meyer, T. J. *J. Am. Chem. Soc.* **2010**, *132*, 1545-1557. (b) Bozoglian, F.; Romain, S.; Ertem, M. Z.; Todorova, T. K.; Sens, C.; Mola, J.; Rodríguez, M.; Romero, I.; Benet-Buchholz, J.; Fontrodona, X.; Cramer, C. J.; Gagliardi, L.; Llobet, A. *J. Am. Chem. Soc.* **2009**, *131*, 15176-15187. (c) Cape, J. L.; Siems, W. F.; Hurst, J. K. *Inorg. Chem.* **2009**, *48*, 8729-8735. (d) Nunes, G.; Alexiou, A.; Toma, H. *J. Catal.* **2008**, *260*, 188-192. (e) Cape, J. L.; Hurst, J. K. *J. Am. Chem. Soc.* **2008**, *130*, 827-829. (f) Hurst, J. *Coord. Chem. Rev.* **2005**, *249*, 313-328. (g) Bennett, S.; Brown, S. M.; Conole, G.; Kessler, M.; Rowling, S.; Sinn, E.; Woodward, S. *J. Chem. Soc., Dalton Trans.* **1995**, *367*.

[7] (a) Francàs, L.; Sala, X.; Escudero-Adán, E.; Benet-Buchholz, J.; Escriche, L.; Llobet, A. *Inorg. Chem.* **2011**, *50*, 2771-2781. (b) Francàs, L.; Sala, X.; Benet-Buchholz, J.; Escriche, L.; Llobet, A. *ChemSusChem* 2009, *2*, 321-329.

[8] Sullivan, B.P.; Calvert, J.M.; Meyer, T. J. *Inorg.Chem.* **1980**, *19*, 1404.

[9] (a) Sachse, A.; Penkova, L.; Noël, G.; Dechert, S.; Varzatskii, O.; Fritsky, I.; Meyer, F. *Synthesis* **2008**, 800-806. (b) Ghosh, A.; Bischoff, A.; Cappiello, J. *Eur. J. Org. Chem.* **2003**, 821-832. (c) Meth-Cohn, O.; Vuorinen, E.; Modro, T. A. *J. Org. Chem.* **1989**, *54*, 4822-4827. (d) Wulfman, D. *Tetrahedron* **1976**, *32*, 1257-1265.

[10] Data collection with APEX II versions v1.0-22, v2009.1-0 and v2009.1-02. Bruker (2007). Bruker AXS Inc., Madison, Wisconsin, USA.

[11] Data reduction with Bruker SAINT versions V.2.10(2003), V/.60A and V7.60A. Bruker (2007). Bruker AXS Inc., Madison, Wisconsin, USA.

[12] SADABS: V.2.10(2003); V2008 and V2008/1 Bruker (2001). Bruker AXS Inc., Madison, Wisconsin, USA. Blessing, Acta Cryst. (1995) A51 33-38.

[13] Sheldrick, G.M. *Acta Cryst*. **2008** A64, 112-122. SHELXTL versions V6.12 and 6.14.

[14] Pérez-Trujillo, M.; Nolis, P.; Parella, T. *Org. Lett.* **2007**, *9*, 29-32.

[15] Sens, C.; Rodríguez, M.; Romero, I.; Llobet, A.; Parella, T.; Benet-Buchholz, J. *Inorg. Chem.* **2003**, *42*, 8385-8394.

[16] (a) Hu, Y.-Z.; Xiang, Q.; Thummel, R. P. *Inorg. Chem*. **2002**, *41*, 3423. (b) Brown, D.; Muranjan, S.; Jang, Y.; Thummel, R. *Org. Lett*. **2002**, *4*, 1253. (c) Wu, F.; Thummel, R. P. *Inorg. Chim. Acta* **2002**, *327*, 26. (d) Juris, A.; Prodi, L.; Harriman, A.; Ziessel, R.; Hissler, M.; El-Ghayoury, A.; Wu, F.; Riesgo, E. C.; Thummel, R. P. *Inorg. Chem*. **2000**, *39*, 3590. (e) Wu, F.; Riesgo, E. C.; Thummel, R. P.; Juris, A.; Hissler, M.; El-Ghayoury, A.; Ziessel, R. *Tet. Lett*. **1999**, *40*, 7311.

[17] (a) Rodríguez, M.; Romero, I.; Llobet, A.; Deronzier, A.; Biner, M.; Parella, T.; Stoeckli-Evans, H. *Inorg. Chem*. **2001**, 40, 4150. (b) Barkawi, K.; Llobet, A.; Meyer, T. J. *J. Am. Chem. Soc*. **1988**, *110*, 7751. (c) *Llobet, A. Inorg. Chim. Acta* **1994**, *221*, 125-131.

[18] Huynh, M. H. V.; Meyer, T. J. *Chem. Rev.*, **2007**, *107*, 5004–5064.

[19] DigiSim for Windows 95. Version 3.05. File type: CV. Bioanalytical Systems.

[20] (a) Llobet, A.; Curry, M. E.; Evans, H. T.; Meyer, T. J. *Inorg. Chem.* **1989**, *28*, 3131-3137. (b) Burchfield, D. E.; Richman, R. M. *Inorg. Chem.* **1985**, *24*, 852-857.

SUPPLEMENTARY INFORMATION FOR:

Synthesis, Characterization and Linkage Isomerism in Mono- and Dinuclear Ruthenium Complexes Containing the New Pyrazole Based ligand Hpbl

Laia Francas,[a] Daniel Moyano,[a] Xavi Sala,[a] Jordi Benet-Buchholz,[b] Xavier Fontrodona,[c] Antoni Llobet[a,b]* and Lluis Escriche[a]*

[a]Departament de Química, Universitat Autònoma de Barcelona, Cerdanyola del Vallès, E-08193 Barcelona, Spain; [b]Catalan Institute of Chemical Research (ICIQ), Av. Països Catalans 16, E-43007 Tarragona, Spain; and [c]Serveis Tècnics de Recerca and Departament de Química, Universitat de Girona, E-17071 Girona, Spain.

lluis.escriche@uab.cat, allobet@iciq.es

Figure S1. 1D and 2D NMR spectra (360 MHz, 298 K, acetonitrile-d_3) for ligand HPBL: (a) ^{1}H-NMR, (b) COSY, (c) ^{13}C{^{1}H}-NMR, (d) HSQC NMR, (e) HMBC NMR (f) HMBC_N NMR

(a)

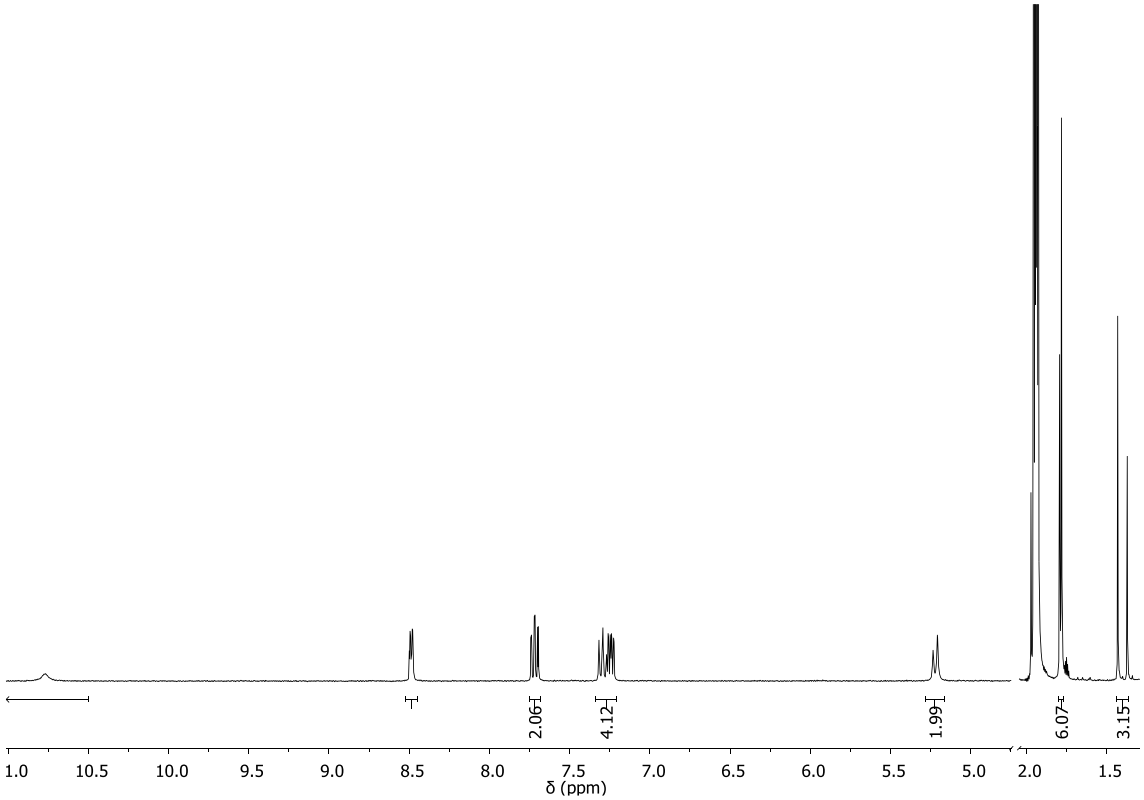

(b)

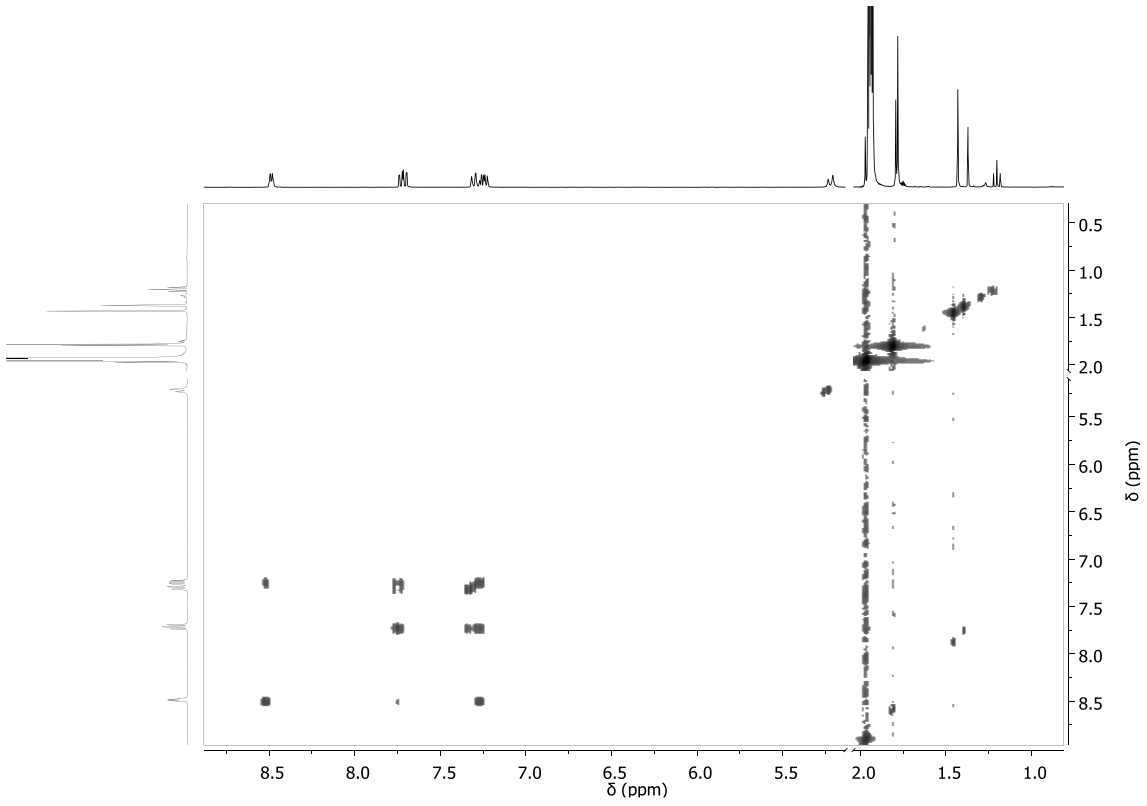

(c)

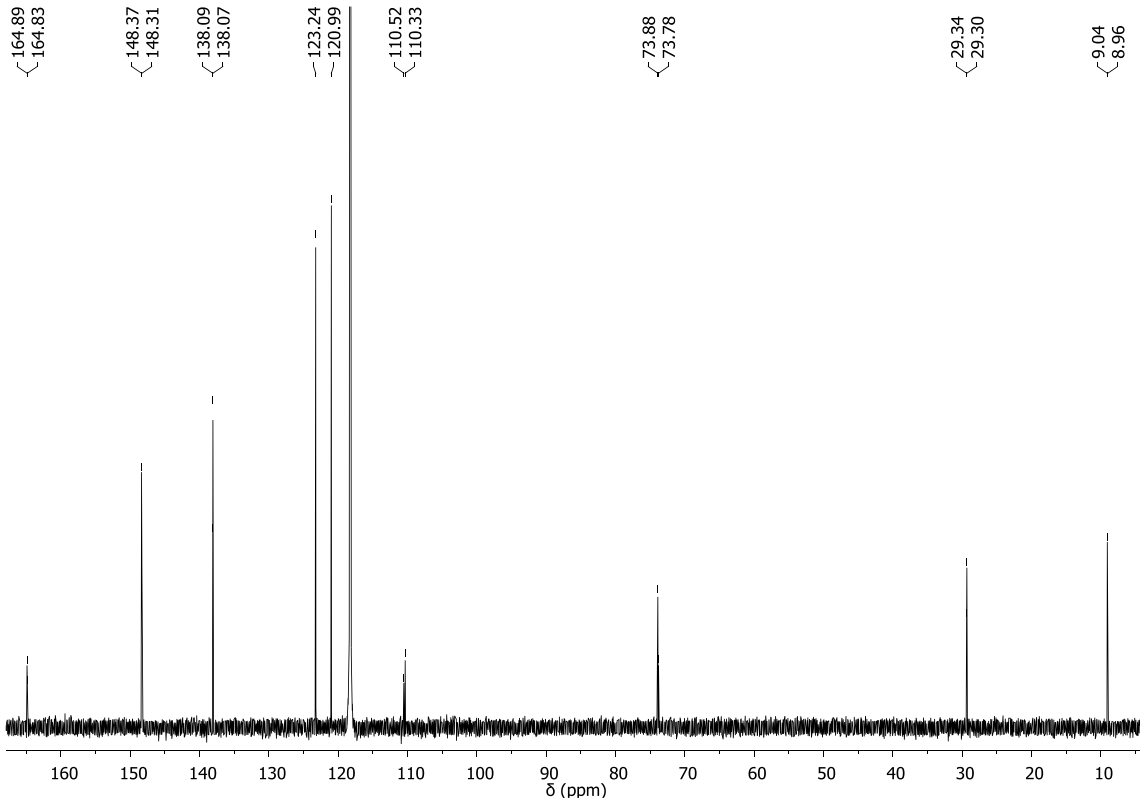
164.89
164.83
148.37
148.31
138.09
138.07
123.24
120.99
110.52
110.33
73.88
73.78
29.34
29.30
9.04
8.96
160 150 140 130 120 110 100 90 80 70 60 50 40 30 20 10
δ (ppm)

(d)

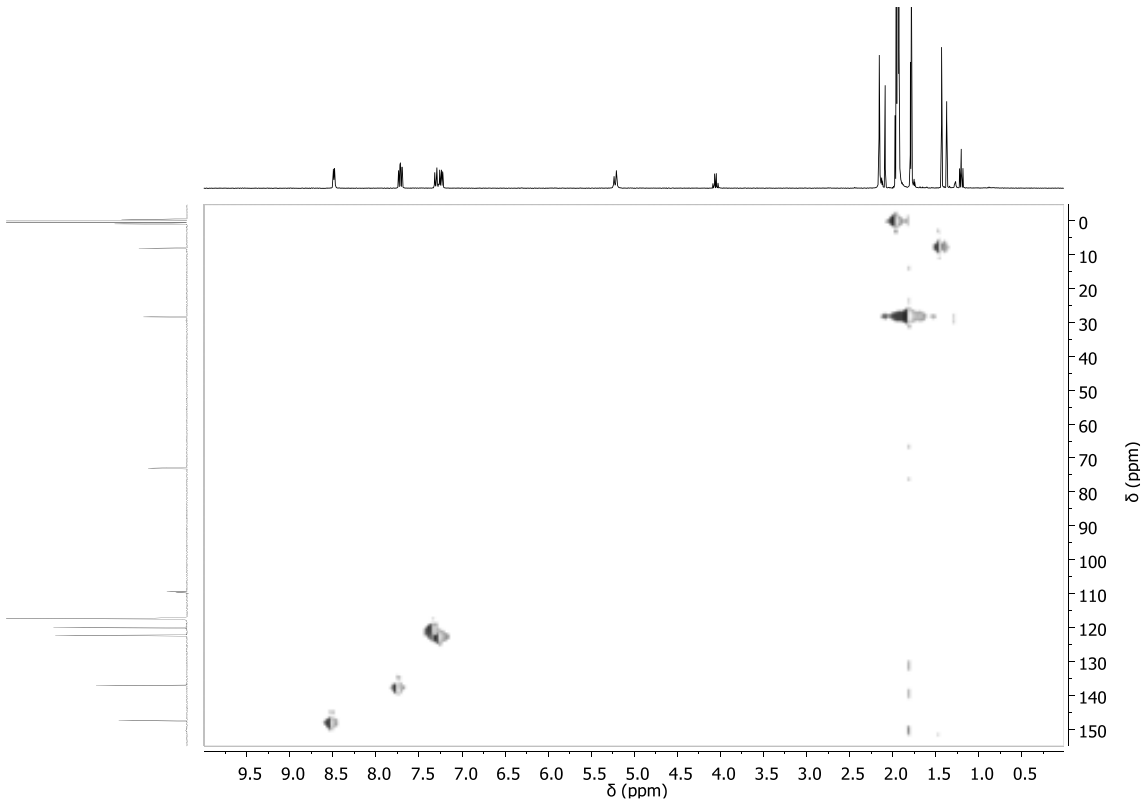
0 10 20 30 40 50 60 70 80 90 100 110 120 130 140 150
δ (ppm)
9.5 9.0 8.5 8.0 7.5 7.0 6.5 6.0 5.5 5.0 4.5 4.0 3.5 3.0 2.5 2.0 1.5 1.0 0.5
δ (ppm)

(e)

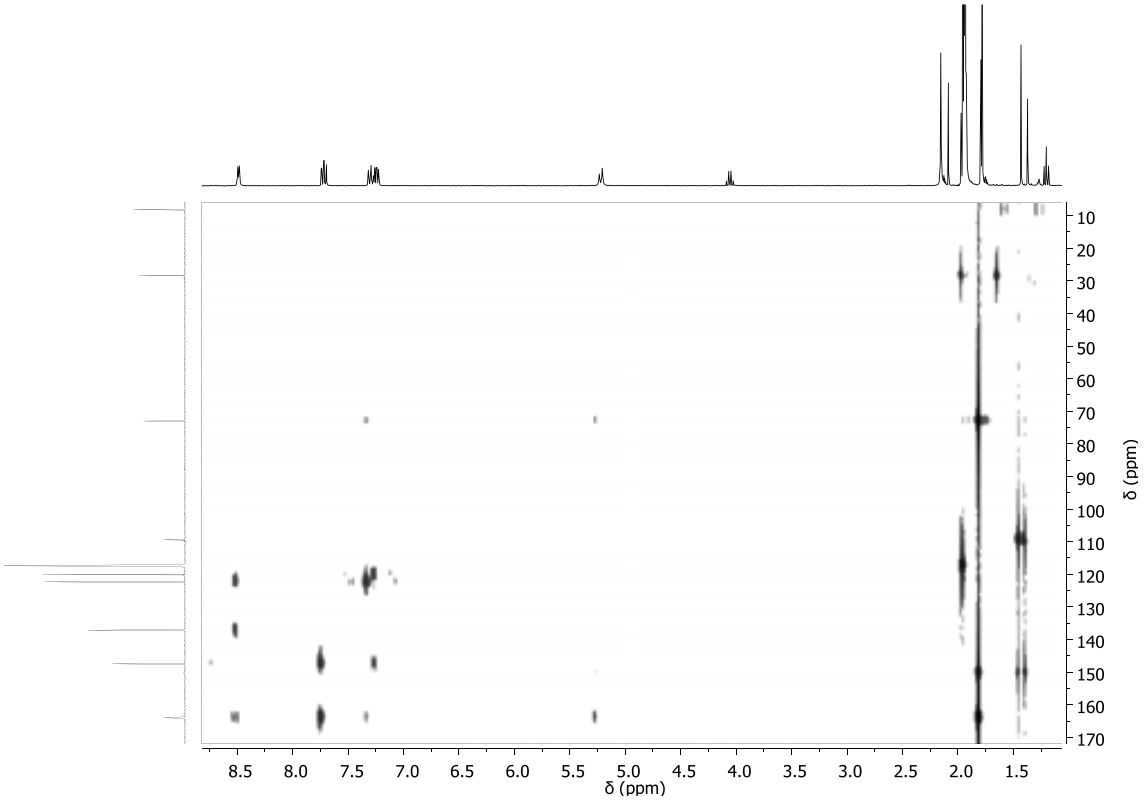
10
20
30
40
50
60
70
80
90
100
110
120
130
140
150
160
170
δ (ppm)
8.5
8.0
7.5
7.0
6.5
6.0
5.5
5.0
4.5
4.0
3.5
3.0
2.5
2.0
1.5
δ (ppm)

(f)

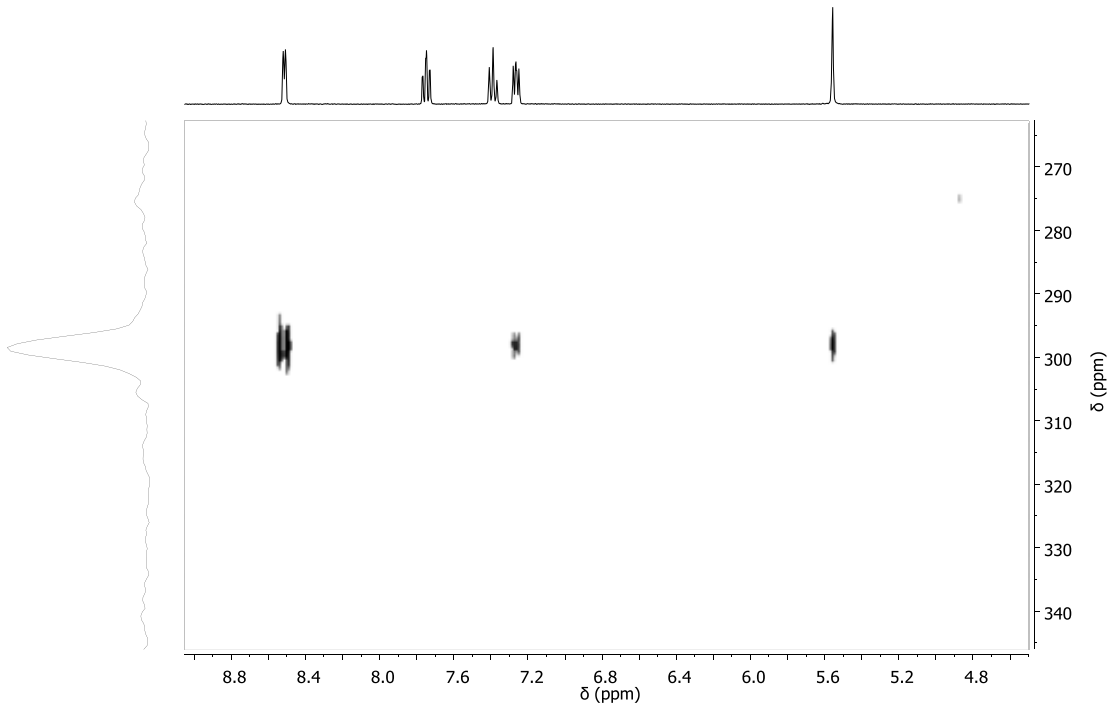
270
280
290
300
310
320
330
340
δ (ppm)
8.8
8.4
8.0
7.6
7.2
6.8
6.4
6.0
5.6
5.2
4.8
δ (ppm)

Figure S2: ^{1}H-NMR spectra for the aromatic part of the Hpbl ligand at different temperatures (400 MHz, acetonitrile-d_3).

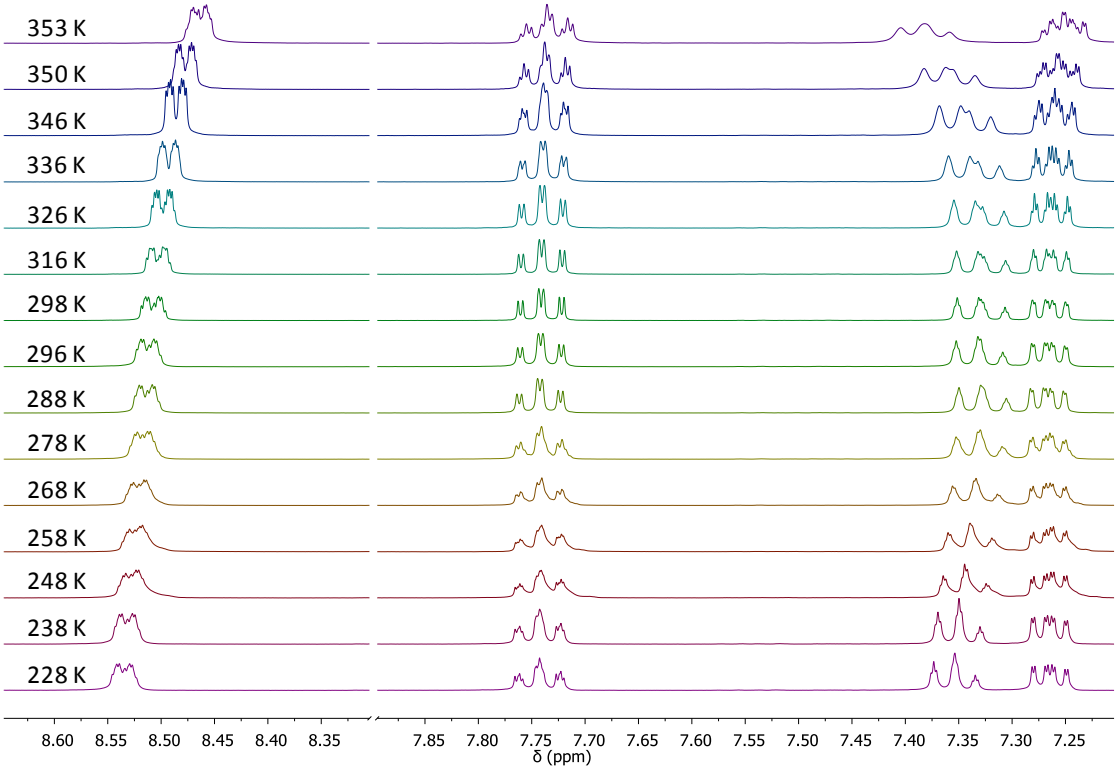

Figure S3. 1D and 2D NMR spectra (400 MHz, 298 K, acetone-d_6) for complex $\mathbf{1}^{+}$: (a) ^{1}H-NMR, (b) COSY, (c) ^{13}C{^{1}H}-NMR, (d) HSQC NMR, (e) aromatic zone HSQC NMR (f) HMBC NMR (g) aromatic zone HMBC NMR (h) HMBC-N NMR.

(a)

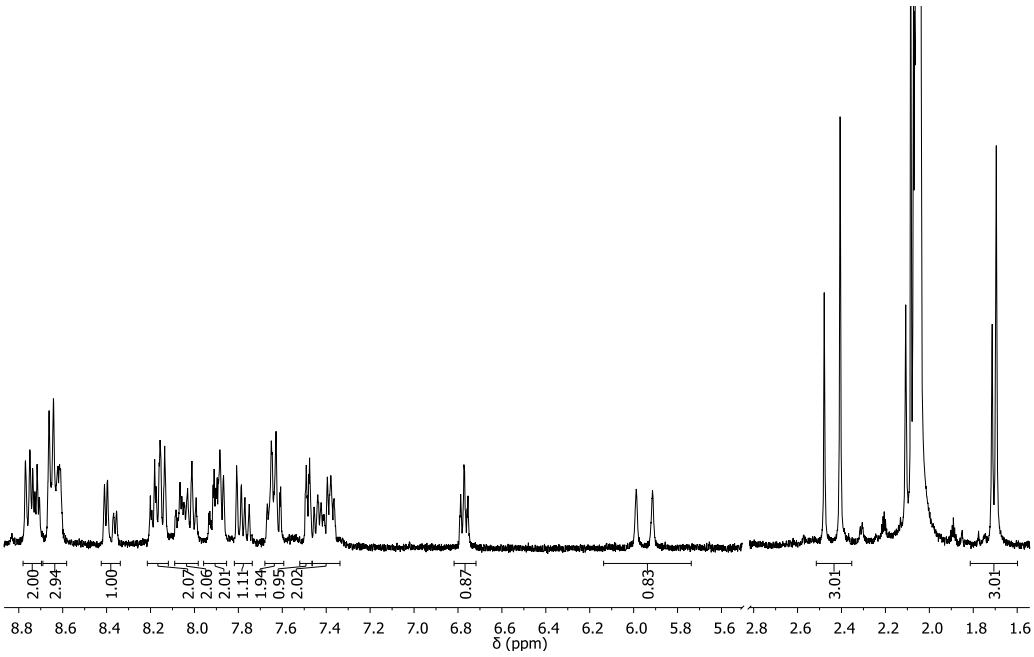

(b)

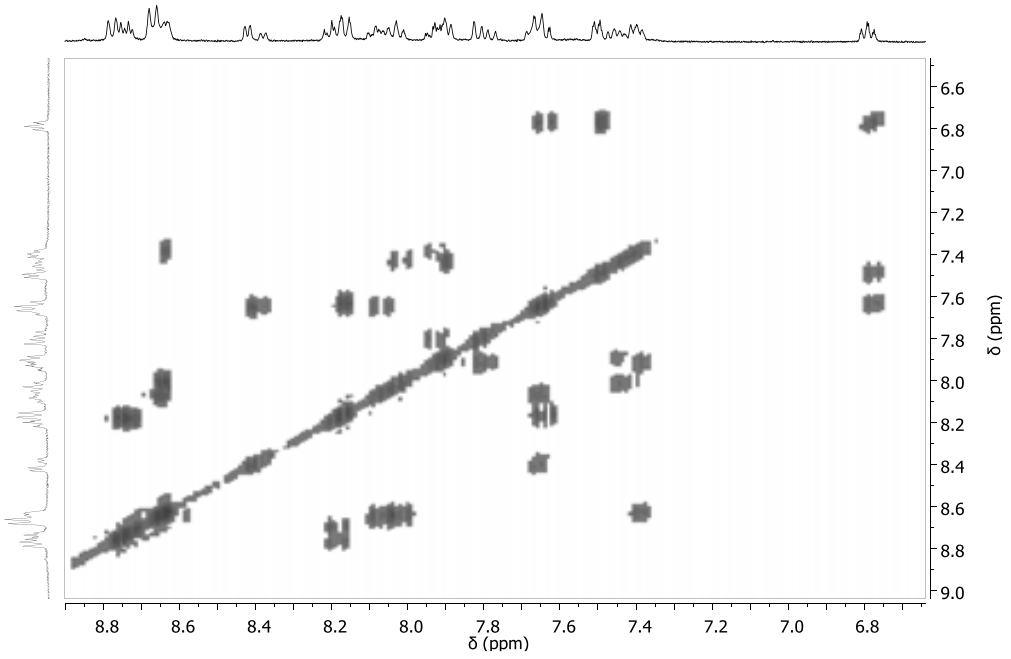
6.6
6.8
7.0
7.2
7.4
7.6
7.8
8.0
8.2
8.4
8.6
8.8
9.0
δ (ppm)
8.8
8.6
8.4
8.2
8.0
7.8
7.6
7.4
7.2
7.0
6.8
δ (ppm)

(c)

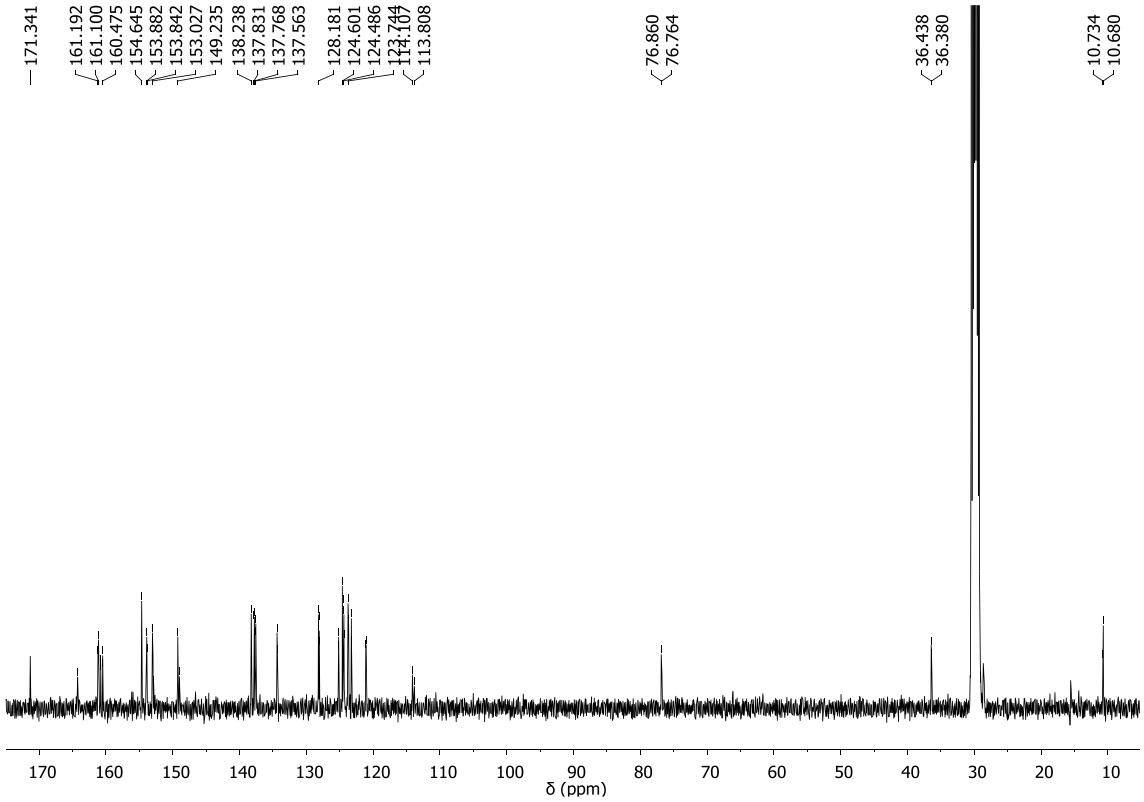
171.341
161.192
161.100
160.475
154.645
153.882
153.842
153.027
149.235
138.238
137.831
137.768
137.563
128.181
124.601
124.486
123.744
114.107
113.808
76.860
76.764
36.438
36.380
10.734
10.680
170
160
150
140
130
120
110
100
90
80
70
60
50
40
30
20
10
δ (ppm)

(d)

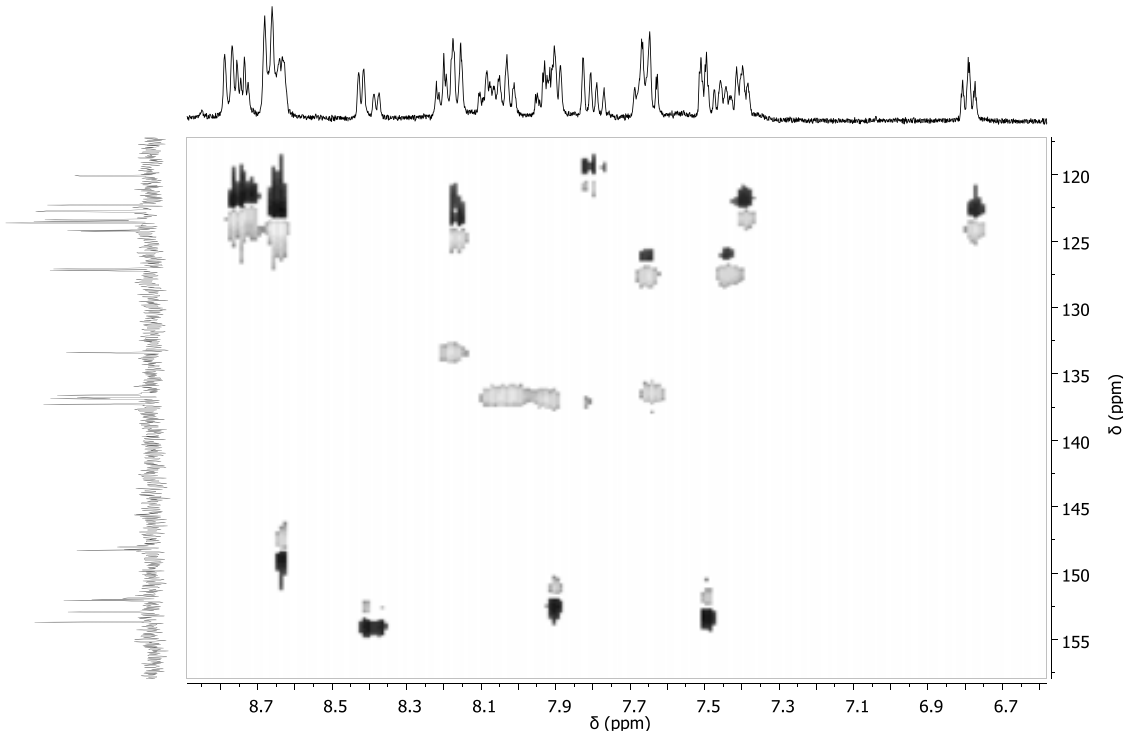
120
125
130
135
140
145
150
155
δ (ppm)
8.7
8.5
8.3
8.1
7.9
7.7
7.5
7.3
7.1
6.9
6.7
δ (ppm)

(e)

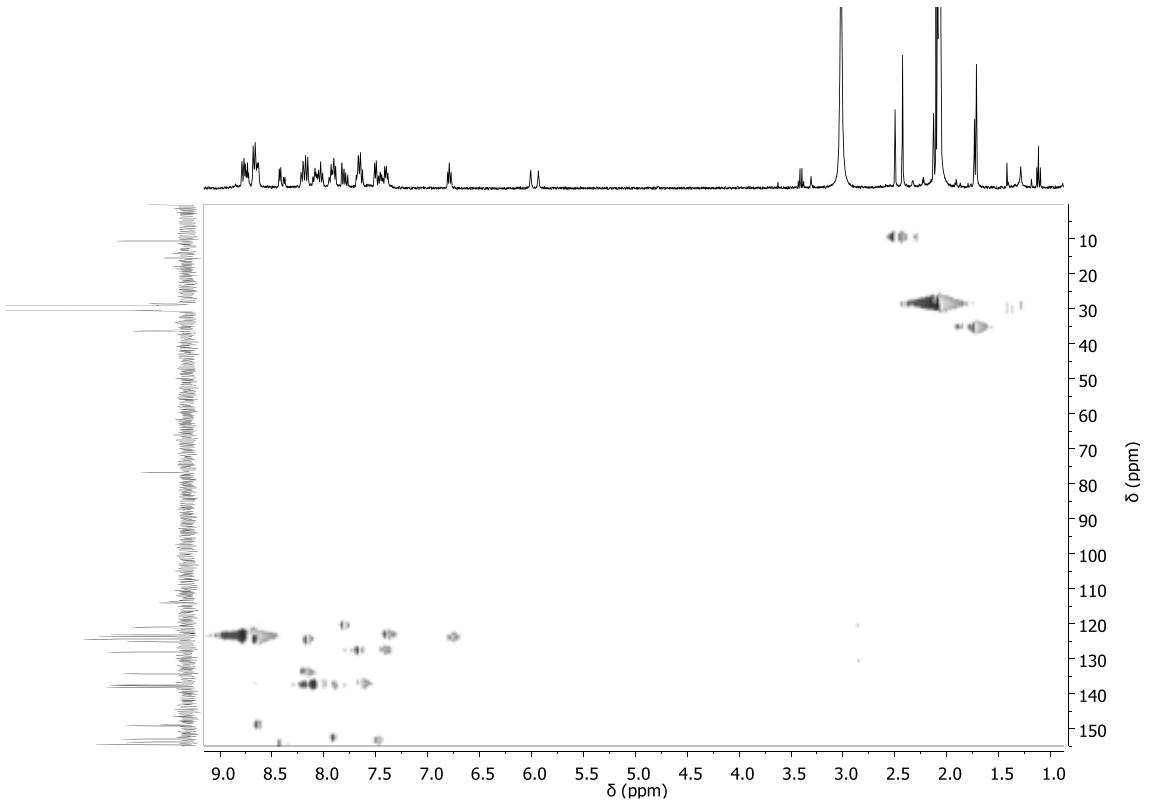
10
20
30
40
50
60
70
80
90
100
110
120
130
140
150
δ (ppm)
9.0
8.5
8.0
7.5
7.0
6.5
6.0
5.5
5.0
4.5
4.0
3.5
3.0
2.5
2.0
1.5
1.0
δ (ppm)

(f)

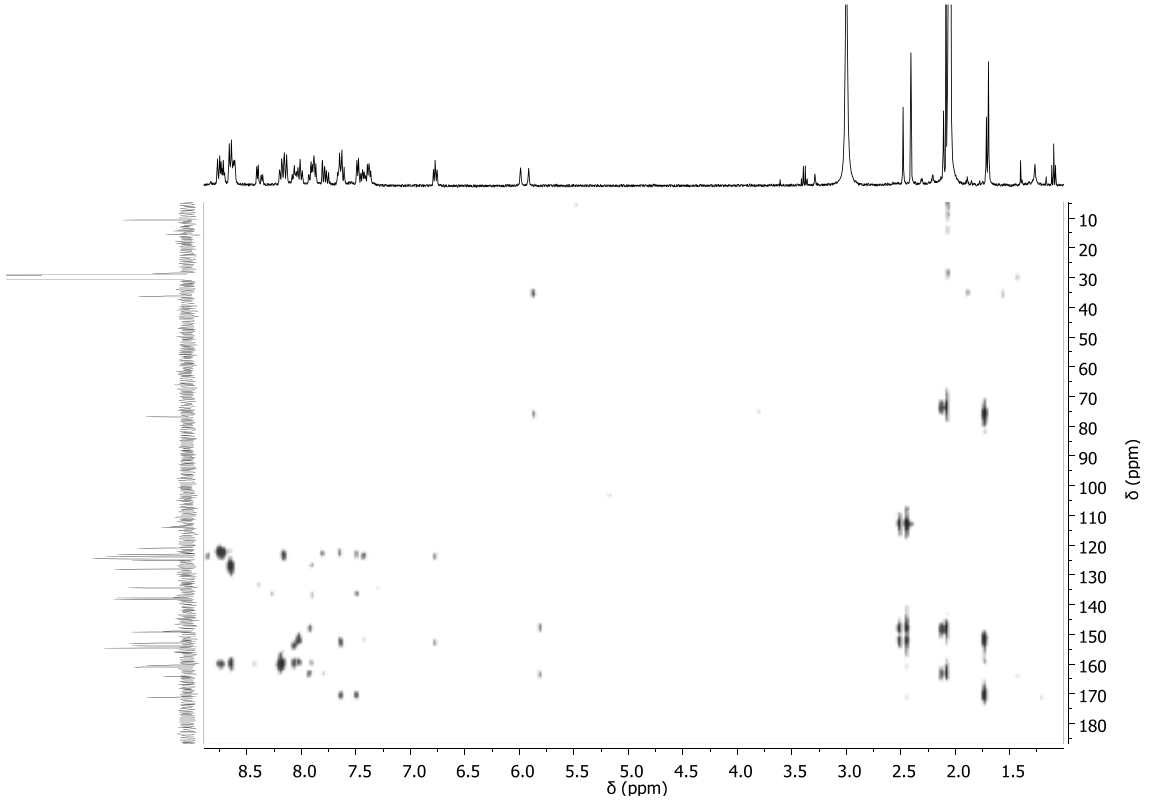
10
20
30
40
50
60
70
80
90
100
110
120
130
140
150
160
170
180
δ (ppm)
8.5 8.0 7.5 7.0 6.5 6.0 5.5 5.0 4.5 4.0 3.5 3.0 2.5 2.0 1.5
δ (ppm)

(g)

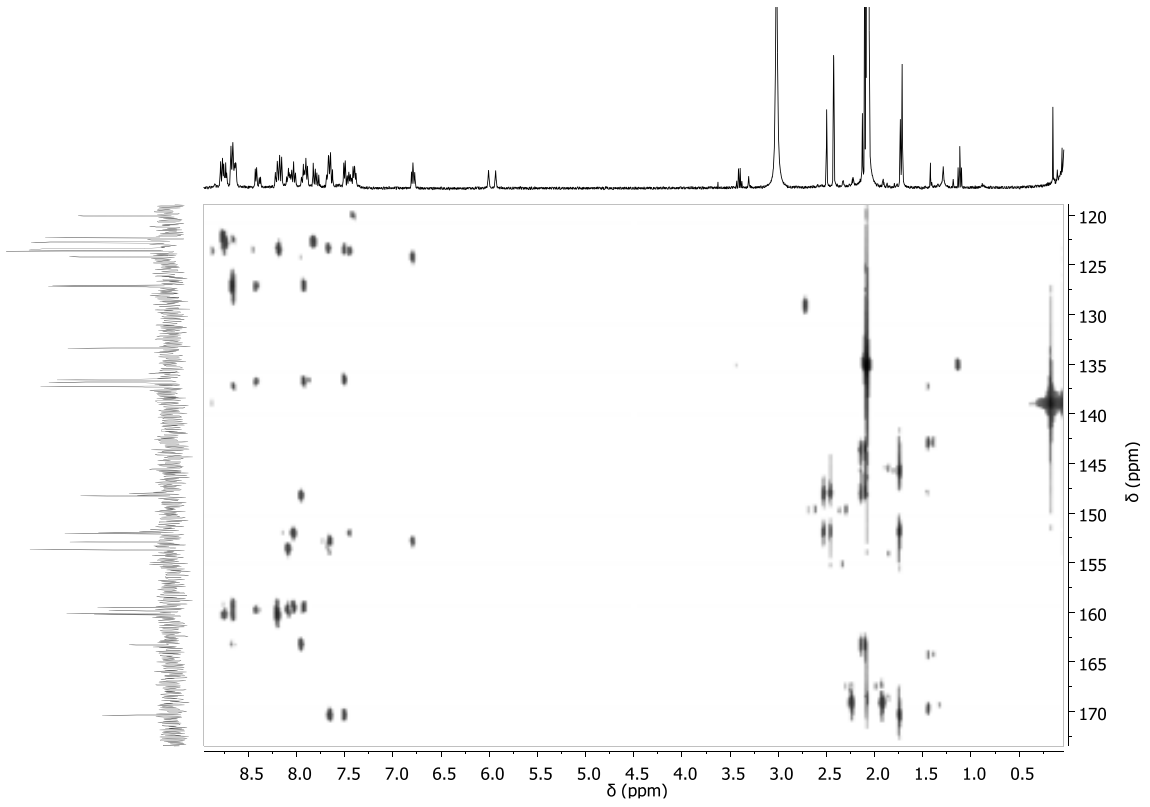
120
125
130
135
140
145
150
155
160
165
170
δ (ppm)
8.5 8.0 7.5 7.0 6.5 6.0 5.5 5.0 4.5 4.0 3.5 3.0 2.5 2.0 1.5 1.0 0.5
δ (ppm)

(h)

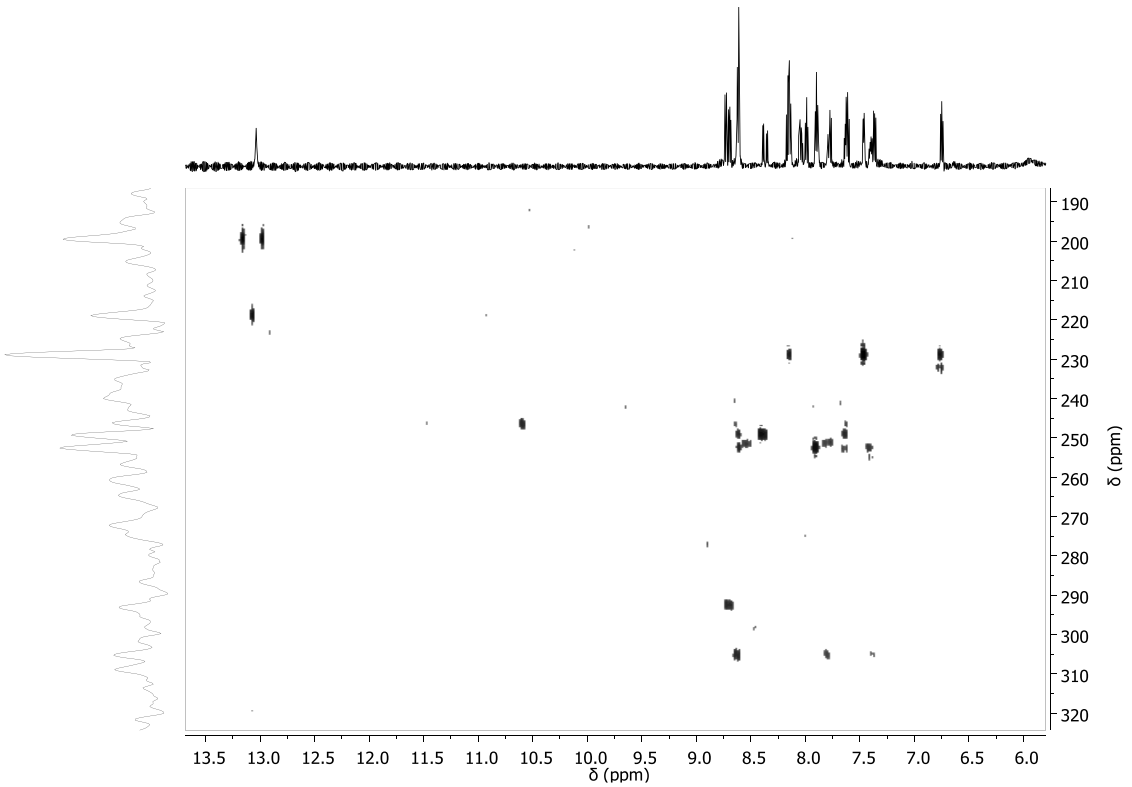

Figure S4. 1D and 2D NMR spectra (400 MHz or 600 MHz, 298 K, acetone-d_6/D_2O/CF_3SO_3D) for complex **2a**$^{2+}$: (a) ^{1}H-NMR, (b) COSY, (c) ^{13}C{^{1}H}-NMR, (d) HSQC NMR, (e) aromatic zone HSQC NMR (f) HMBC-N

(a)

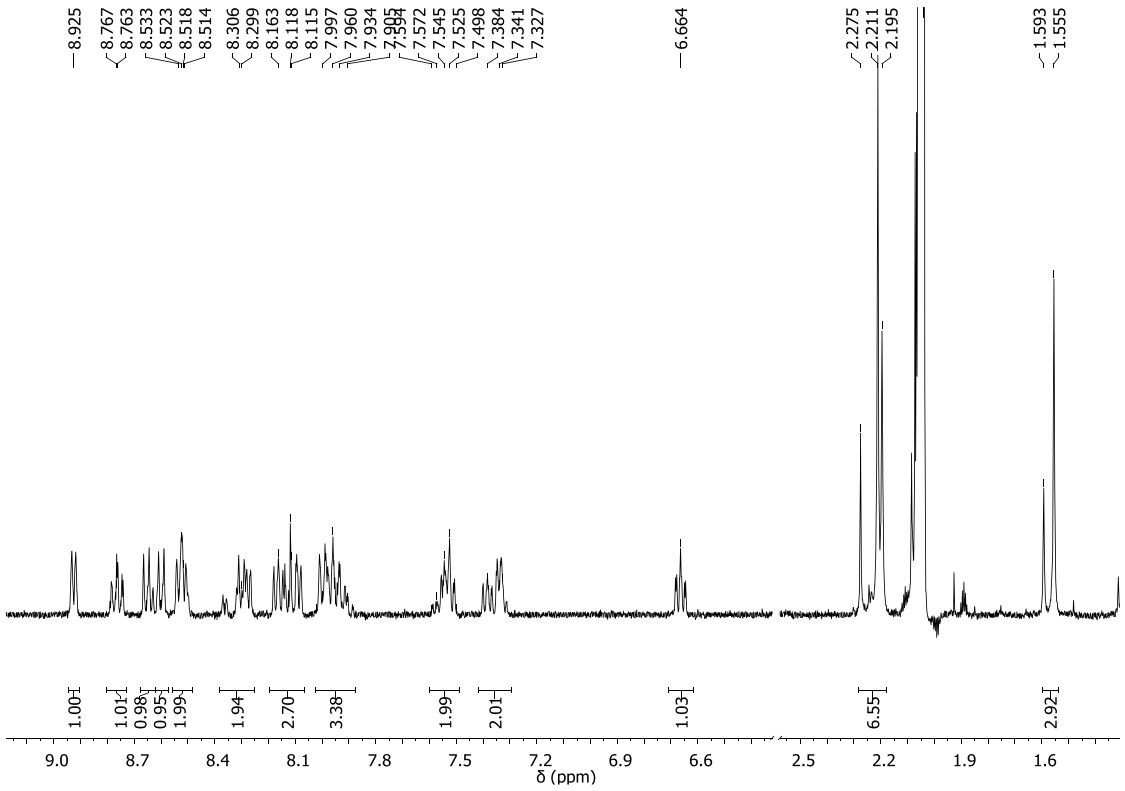

(b)

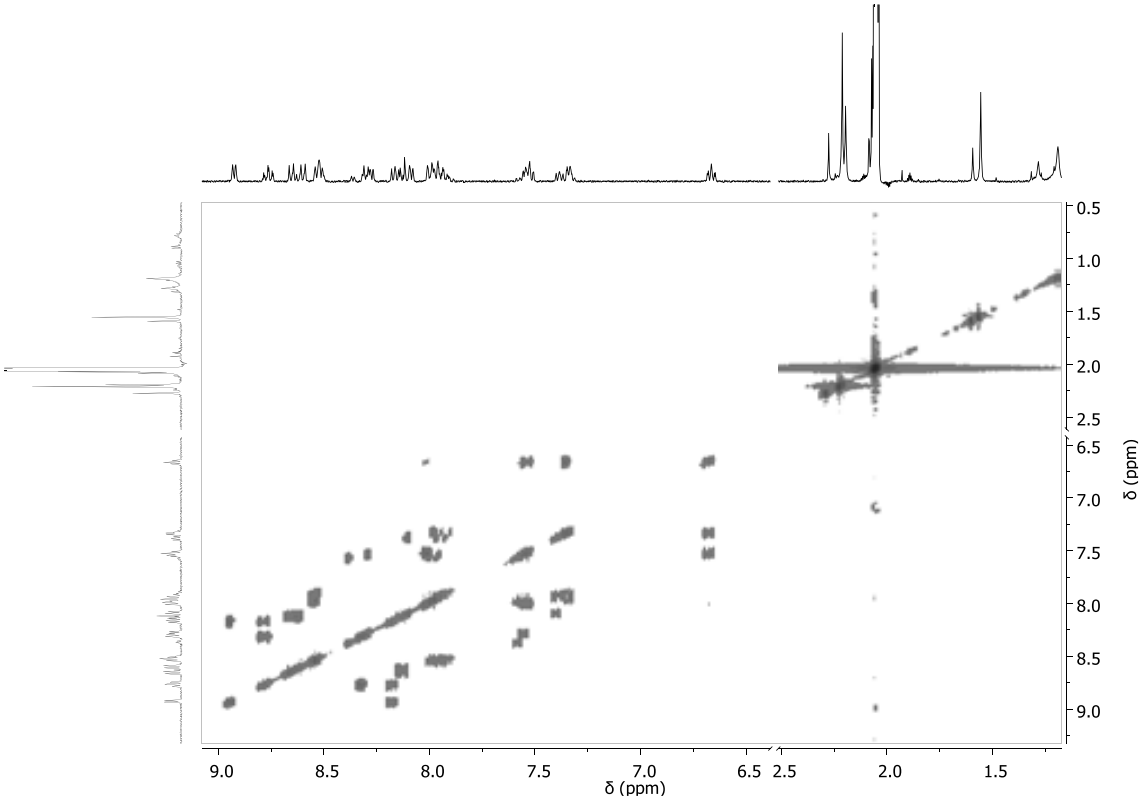
0.5
1.0
1.5
2.0
2.5
6.5
7.0
7.5
8.0
8.5
9.0
δ (ppm)
9.0
8.5
8.0
7.5
7.0
6.5
2.5
2.0
1.5
δ (ppm)

(c)

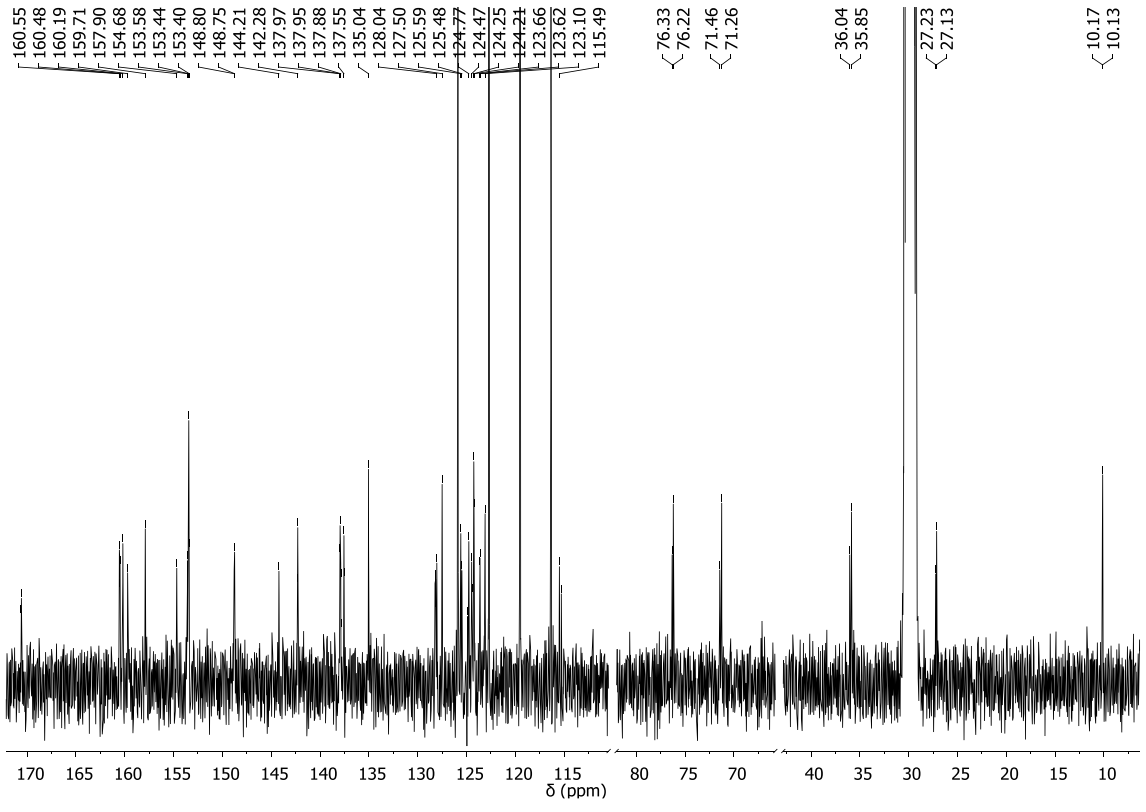
160.55
160.48
160.19
159.71
157.90
154.68
153.58
153.44
153.40
148.80
148.75
144.21
142.28
137.97
137.95
137.88
137.55
135.04
128.04
127.50
125.59
125.48
124.77
124.47
124.25
124.21
123.66
123.62
123.10
115.49
76.33
76.22
71.46
71.26
36.04
35.85
27.23
27.13
10.17
10.13
170
165
160
155
150
145
140
135
130
125
120
115
80
75
70
40
35
30
25
20
15
10
δ (ppm)

(d)

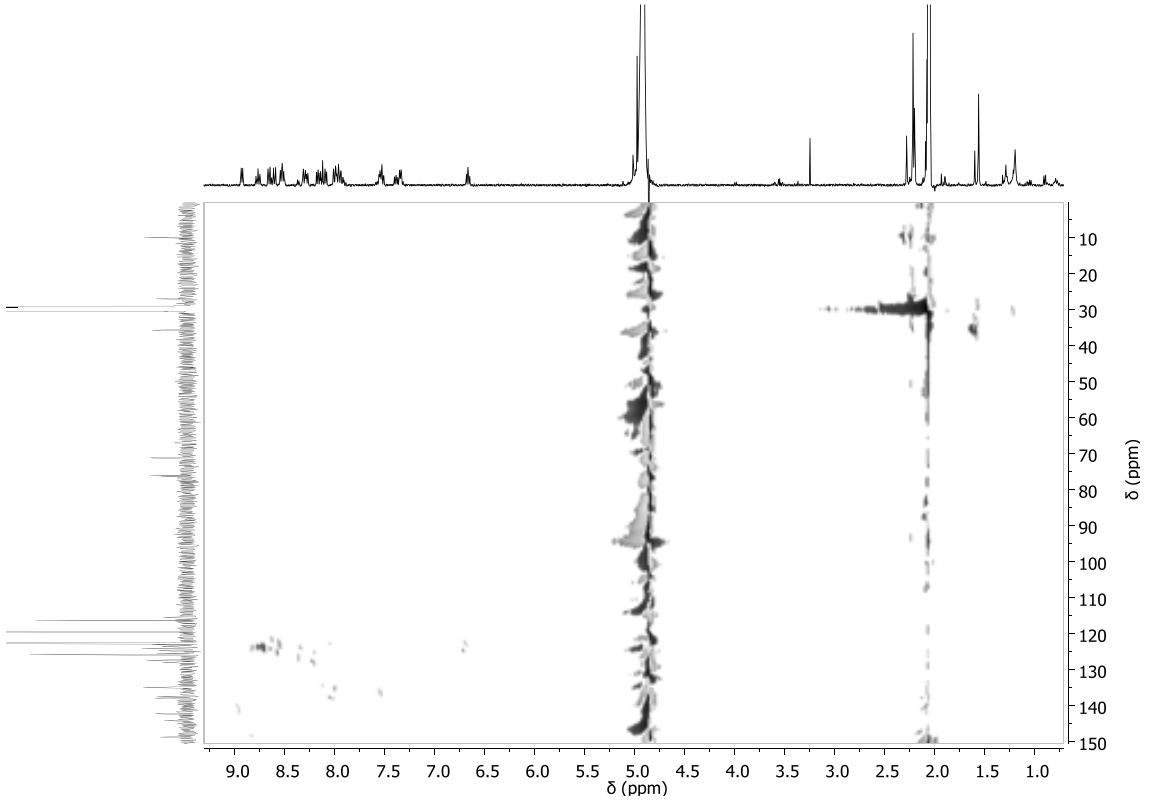
10
20
30
40
50
60
70
80
90
100
110
120
130
140
150
δ (ppm)
9.0
8.5
8.0
7.5
7.0
6.5
6.0
5.5
5.0
4.5
4.0
3.5
3.0
2.5
2.0
1.5
1.0
δ (ppm)

(e)

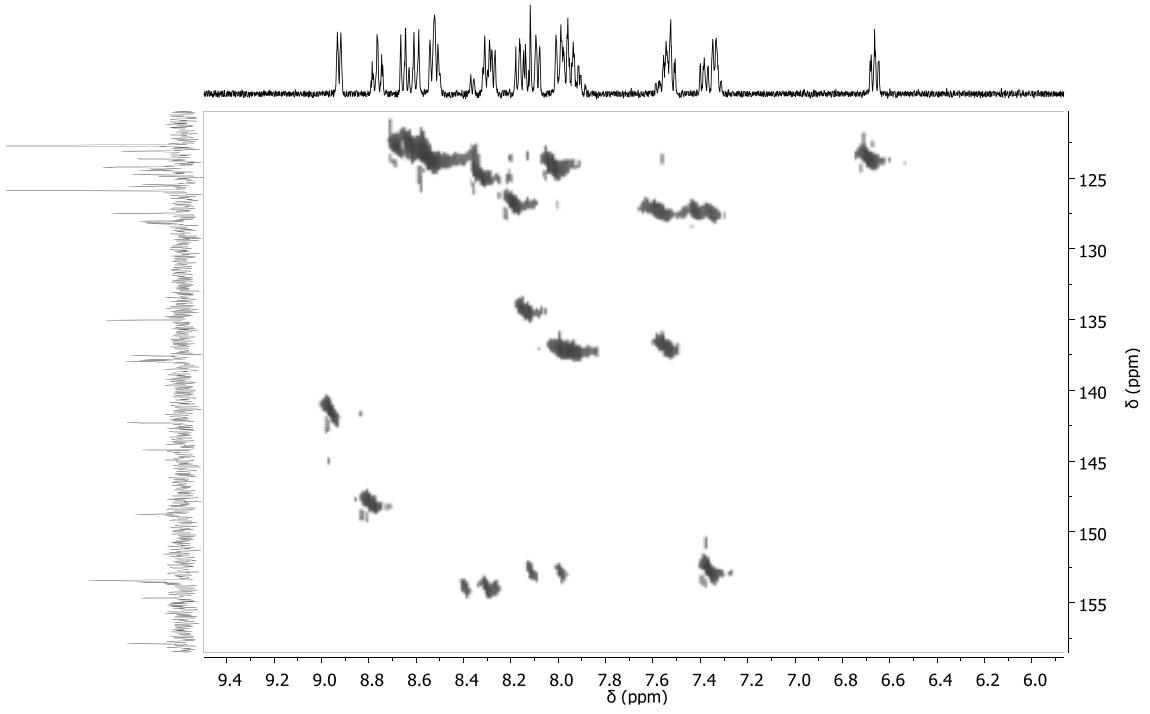
125
130
135
140
145
150
155
δ (ppm)
9.4
9.2
9.0
8.8
8.6
8.4
8.2
8.0
7.8
7.6
7.4
7.2
7.0
6.8
6.6
6.4
6.2
6.0
δ (ppm)

(f)

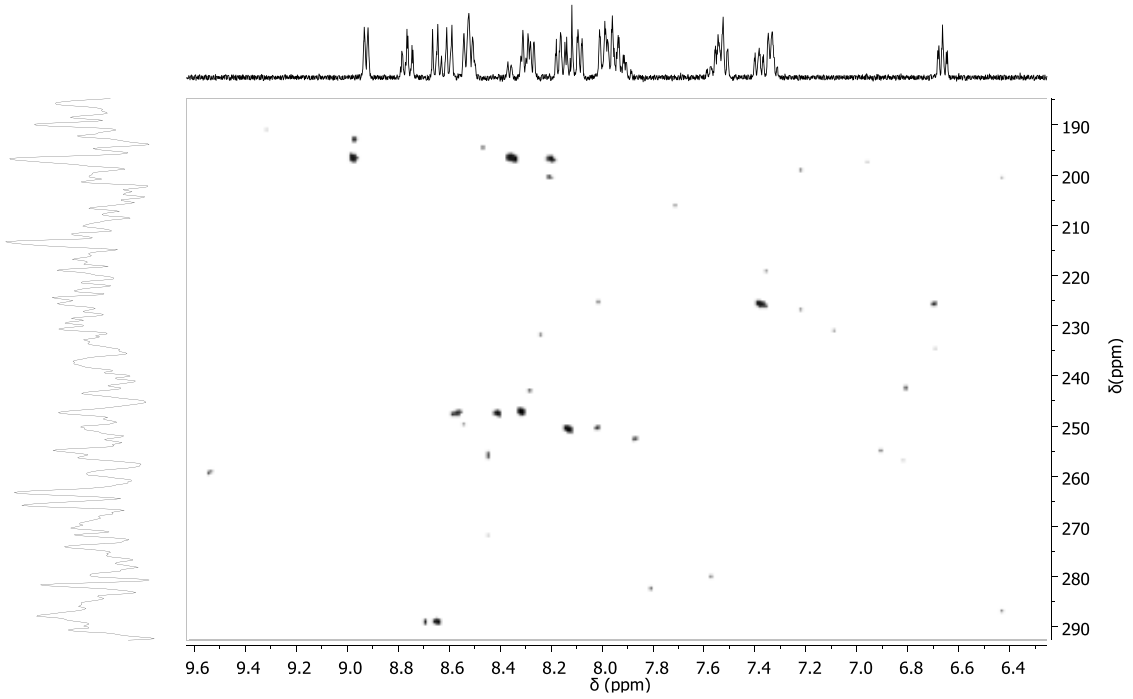

Figure S5. 1D and 2D NMR spectra (400 MHz or 600 MHz, 298 K, acetone-d_6/D_2O/NaOD) for complex **2a**$^+$: (a) ^{1}H-NMR, (b) COSY, (c) $^{13}C\{^1H\}$-NMR, (d) HSQC NMR, (e) HMBC-N NMR, (f) DOSY NMR.

(a)

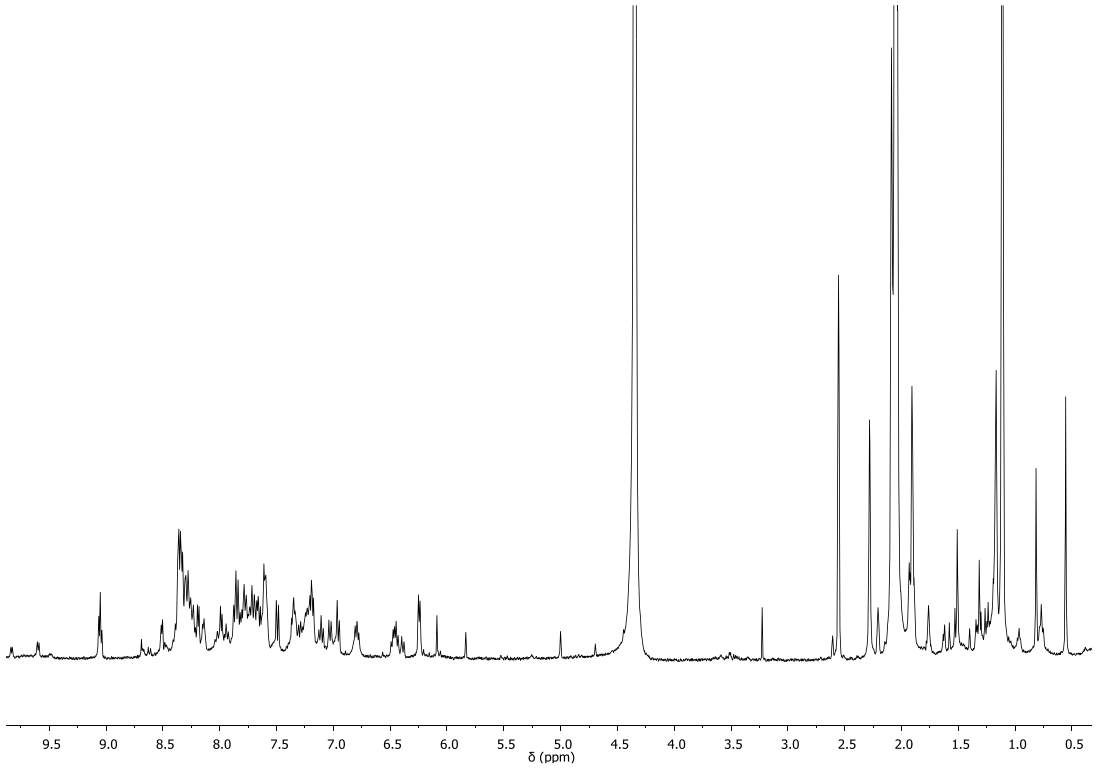

(b)

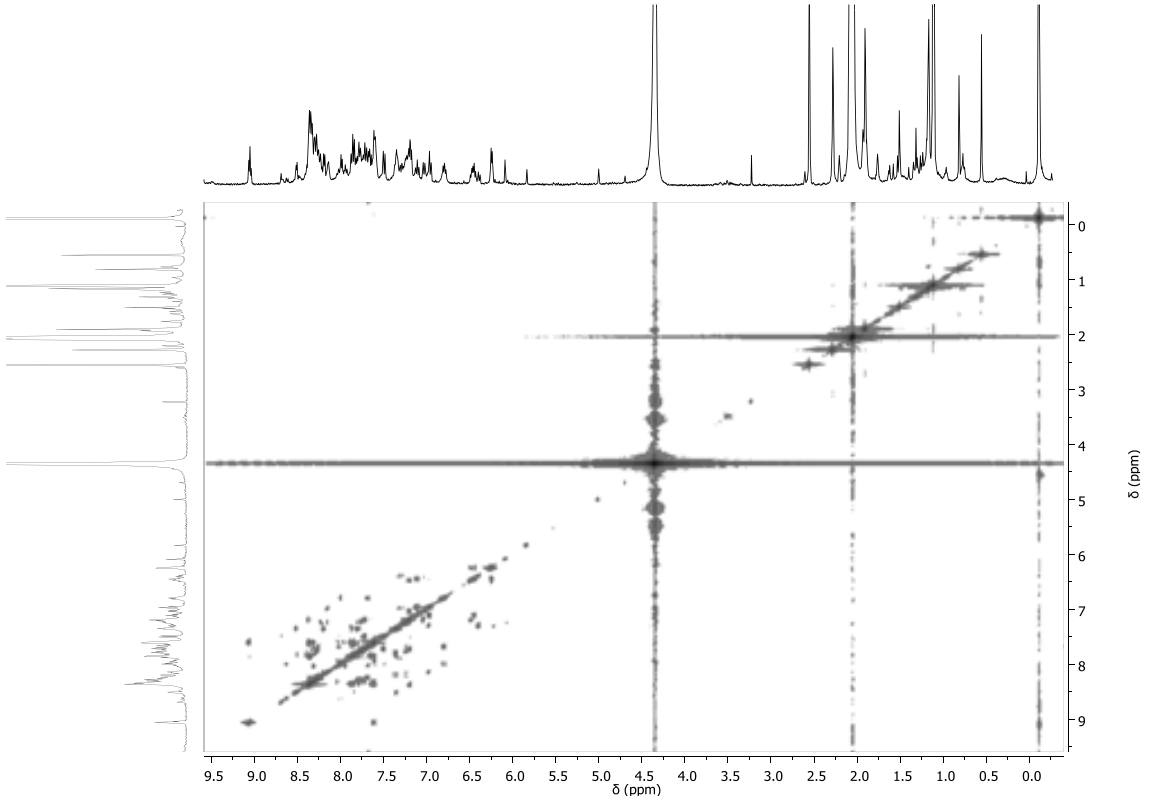
0
1
2
3
4
5
6
7
8
9
δ (ppm)
9.5 9.0 8.5 8.0 7.5 7.0 6.5 6.0 5.5 5.0 4.5 4.0 3.5 3.0 2.5 2.0 1.5 1.0 0.5 0.0
δ (ppm)

(c)

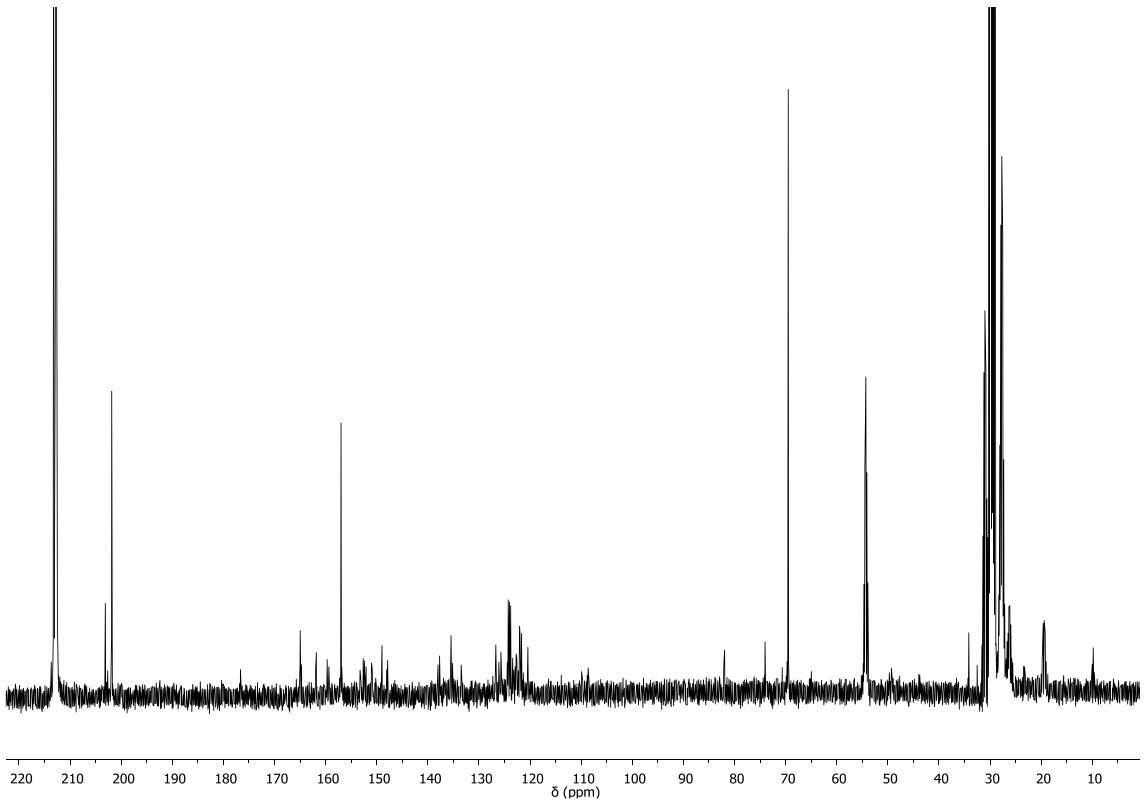
220 210 200 190 180 170 160 150 140 130 120 110 100 90 80 70 60 50 40 30 20 10
δ (ppm)

(d)

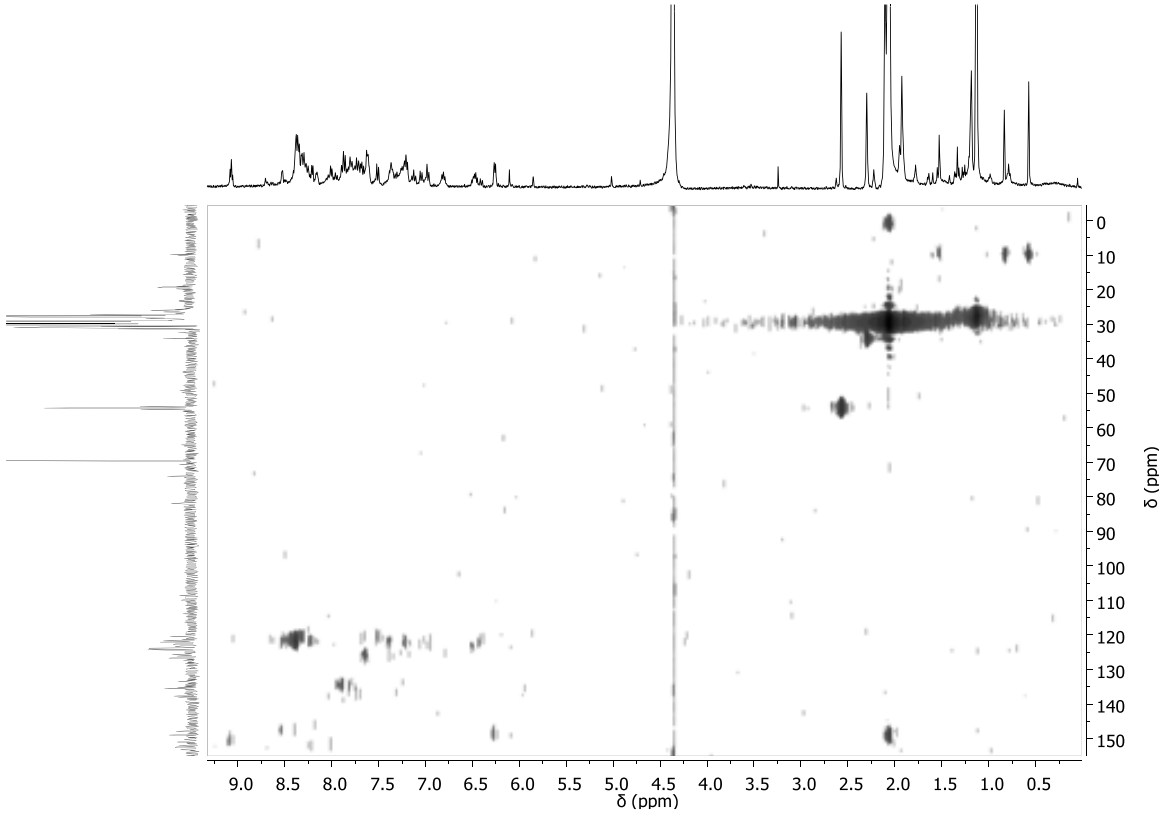
0
10
20
30
40
50
60
70
80
90
100
110
120
130
140
150
δ (ppm)
9.0 8.5 8.0 7.5 7.0 6.5 6.0 5.5 5.0 4.5 4.0 3.5 3.0 2.5 2.0 1.5 1.0 0.5
δ (ppm)

(e)

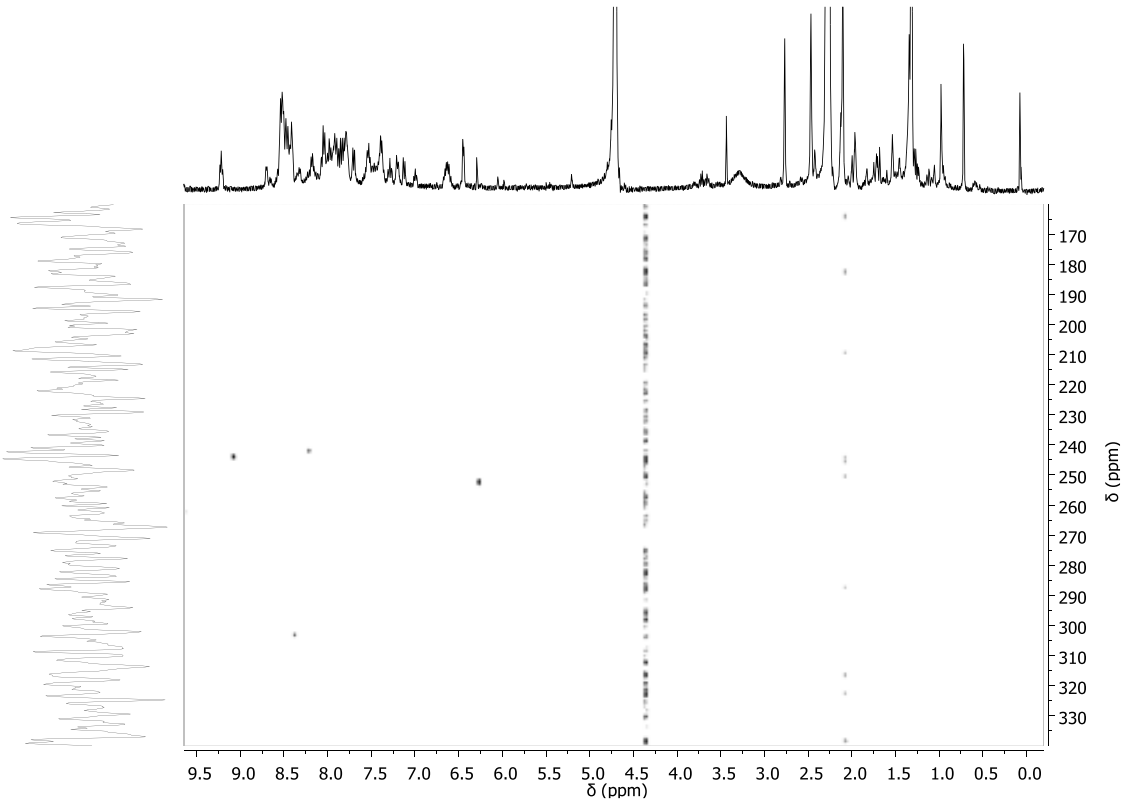
170
180
190
200
210
220
230
240
250
260
270
280
290
300
310
320
330
δ (ppm)
9.5 9.0 8.5 8.0 7.5 7.0 6.5 6.0 5.5 5.0 4.5 4.0 3.5 3.0 2.5 2.0 1.5 1.0 0.5 0.0
δ (ppm)

(f)

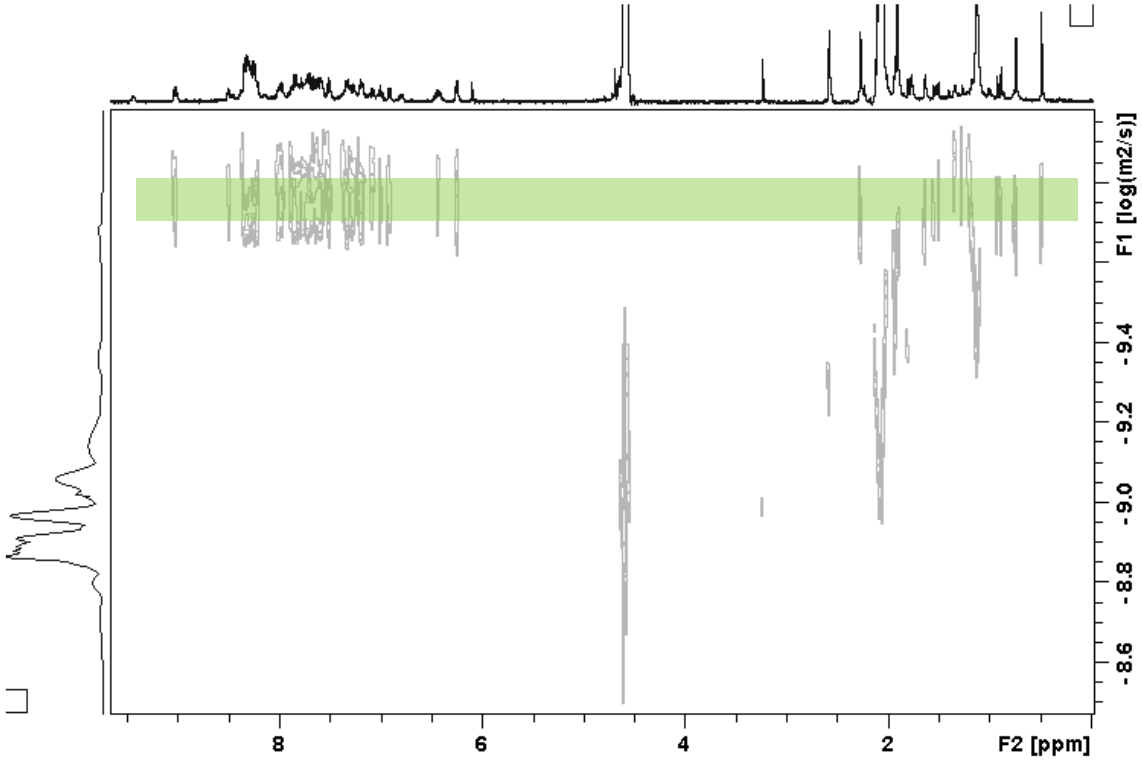

Figure S6. DOSY NMR experiment for complex **2a**$^{2+}$ (400 MHz or 600 MHz, 298 K, acetone-d_6/D_2O/NaOD) using $[RuH_2O(bpy)(bpea)]^{2+}$ as internal patron.

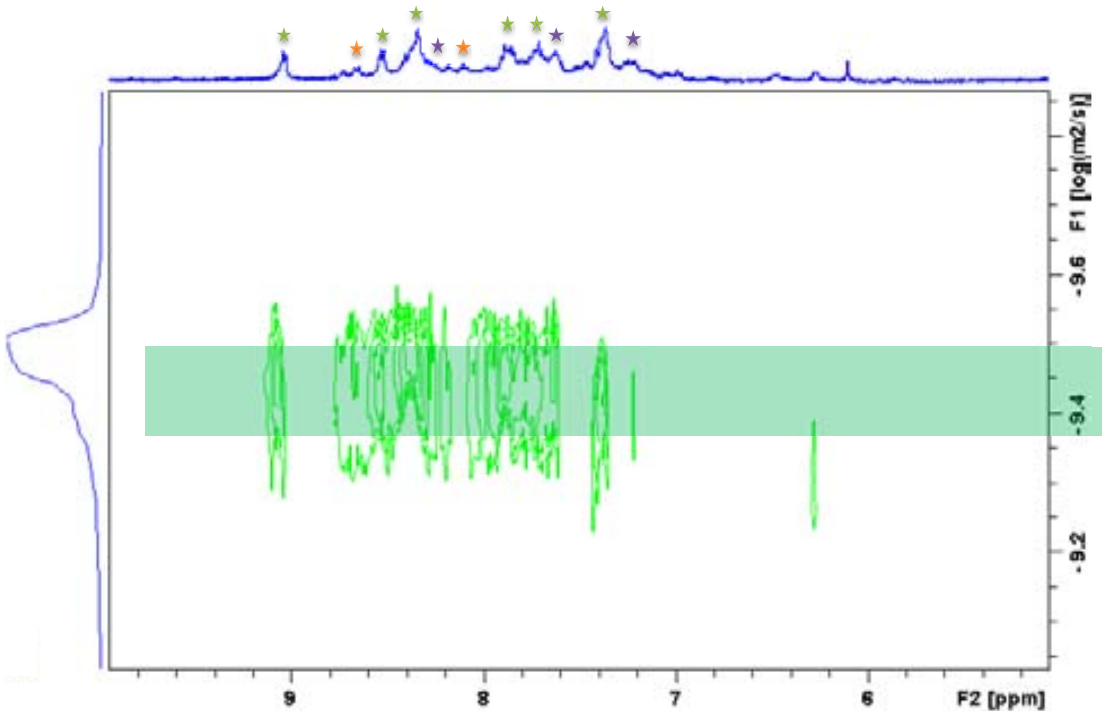

Figure S7: ^{1}H-NMR spectra for the aromatic part of the Hpbl ligand at different temperatures (400 MHz, acetone-d_6): (a) T=298 K (b) cooling down and (c) warming up.

(a)

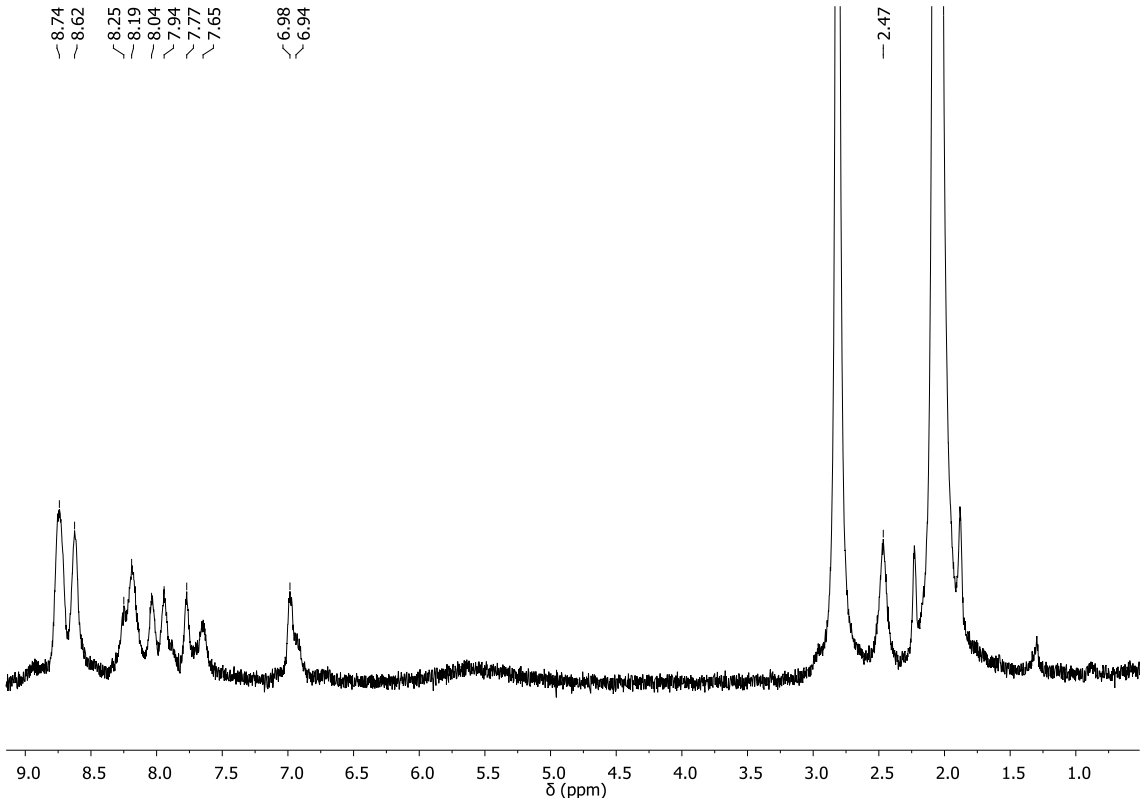

(b)

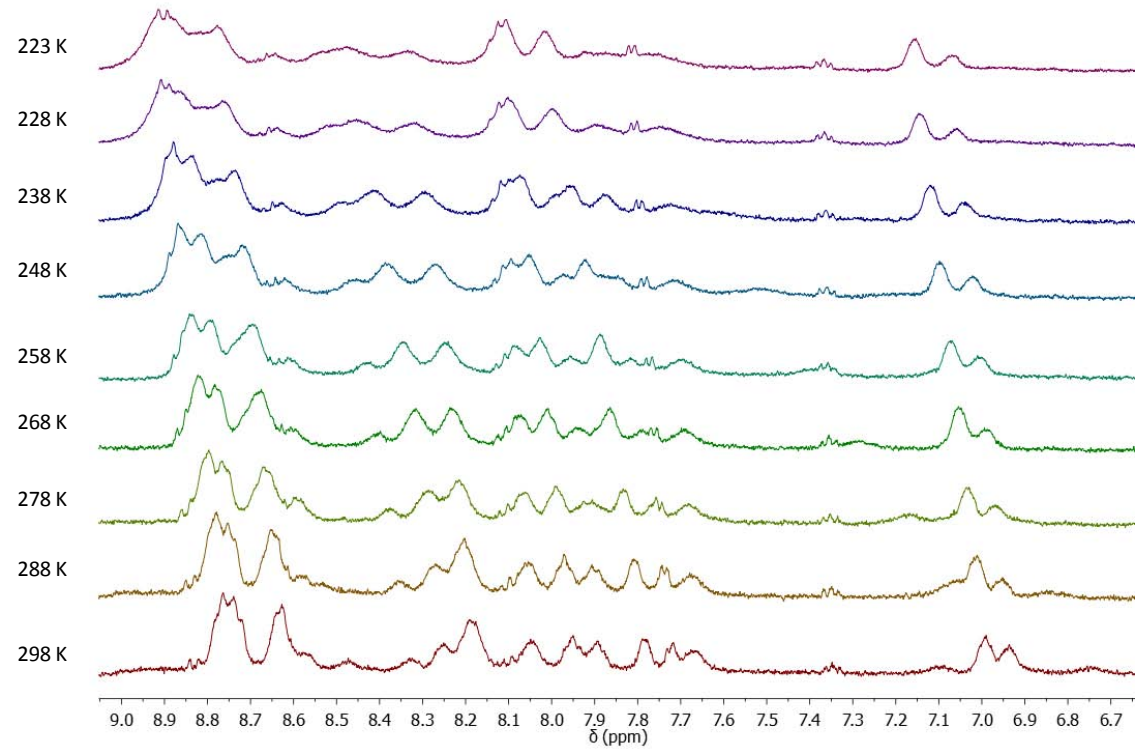

(c)

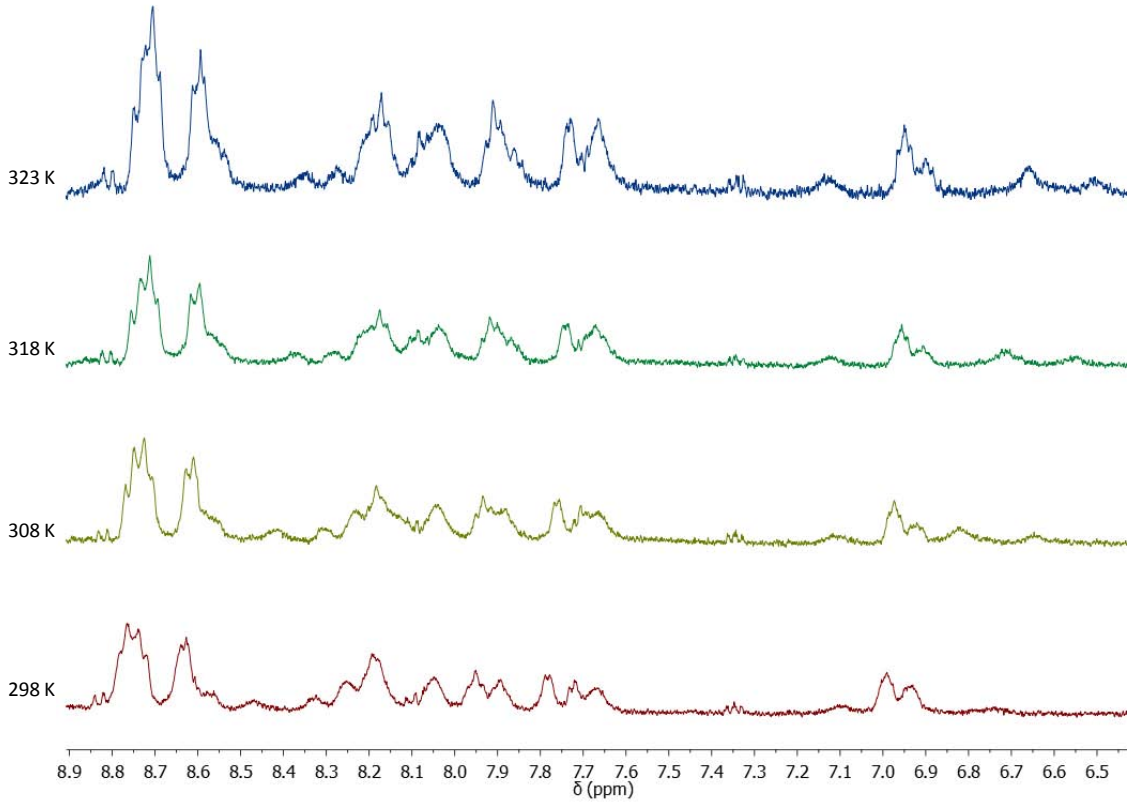

Figure S8: . Crystallographic Data for Complex $\mathbf{2^{2+}}$

Empirical formula	'C33 H31 N7 O3 Ru
Formula Weight	674.72
Temperature, K	300(2)
Wavelength, Å	0.71073
Crystal system	Triclinic
Space group	P-1
a, Å	8.091(14)
α, deg	93.16(3)
b, Å	12.96(2)
β, deg	97.72(3)
c, Å	16.97(3)
γ, deg	101.49(3)
Vol., $Å^3$	1722(5)
Z	2
ρ(g/cm^3)	1.301
R [$I>2\sigma(I)$]$^{\alpha}$	0.1452
wR	0.3134

$$R = \sum[F_0 - F_c]/\sum F_0 \qquad \mathrm{wR} = \left[\sum\left(w(F_0^2 - F_c^2)^2\right)/\sum(wF_0^4)\right]^{1/2}$$

Figure S9: Mercury™ ellipsoid plot (50% probability) for complex **2b**. Color codes: Ru, pink; Cl, green; N, blue; O, red; the hydrogen atoms are not shown for clarity.

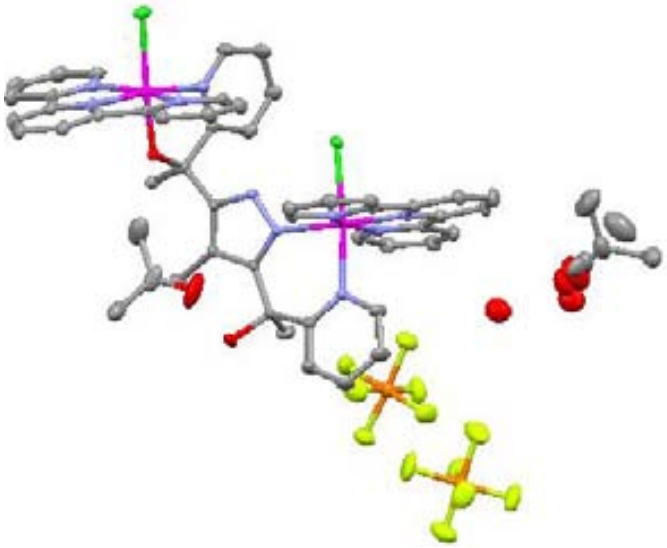

Figure S10: Cyclic voltammogram of complex $\mathbf{2a}^{2+}$ in aqueous solution 0.1 M CF_3COOH at scan rate of (a) 20-50-100-200-300-400-500-600-700-800-900-1000 mV/s and (b) 20 mV/s vs SSCE using carbon electrode from ocp to 0.9 V.

(a)

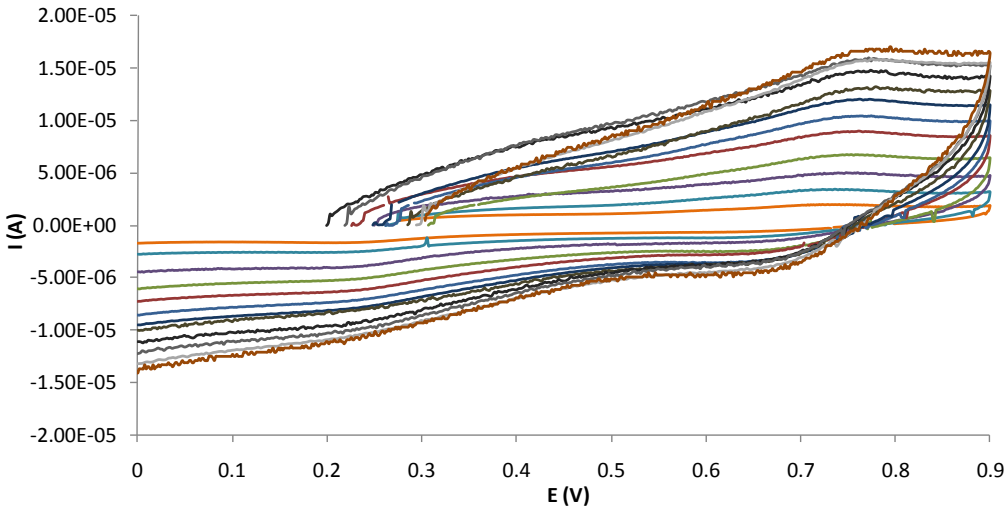

(b)

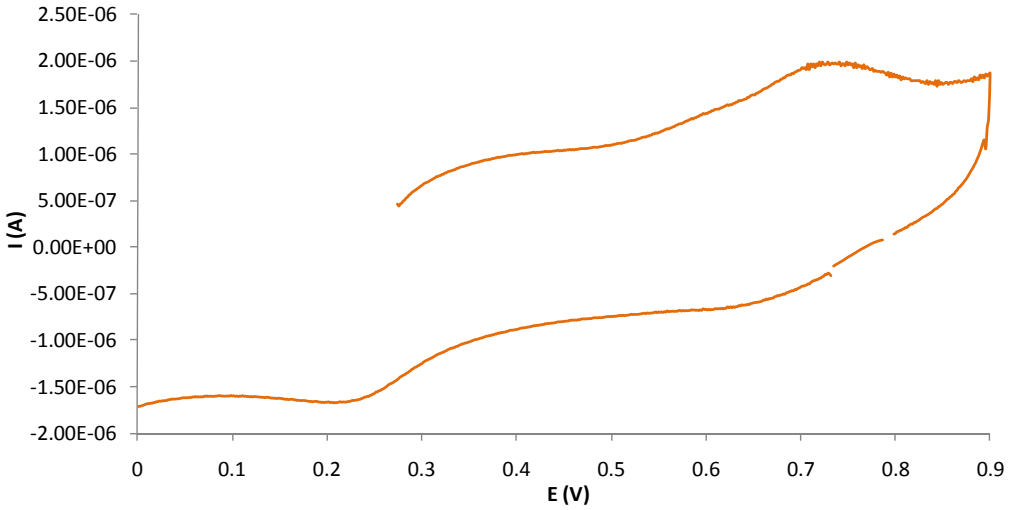

Figure S11: Cyclic voltammogram of complex **2a**$^{2+}$ in aqueous solution pH=8buffer at scan rate of (a) 100 mV/s scanning anodically (b) 900 mV/s scanning anodically (c) 100 mV/s scanning cathodically with 3 minutes of equilibration time (d) 900 mV/s scanning cathodically with 3 minutes of equilibration time. The oxidation transitions are indicated in green line for isomer [Ru-ON$_4$(Pz)], orange line [Ru-ON$_4$(Py)] and purple line [Ru-N$_5$].

(a)

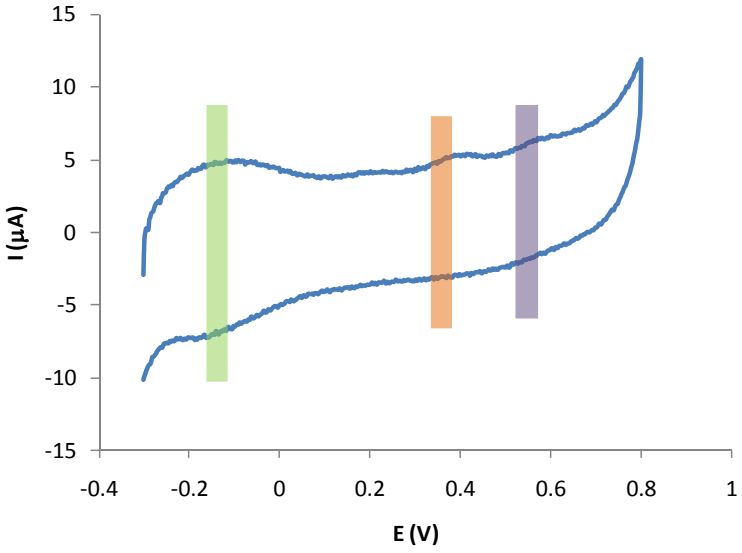

(b)

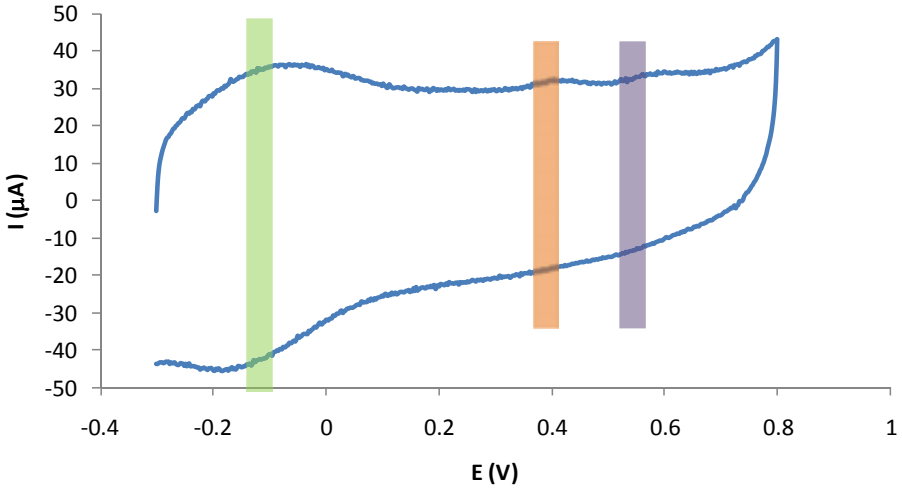
50
40
30
20
10
0
-10
-20
-30
-40
-50
I (µA)
-0.4
-0.2
0
0.2
0.4
0.6
0.8
1
E (V)

(c)

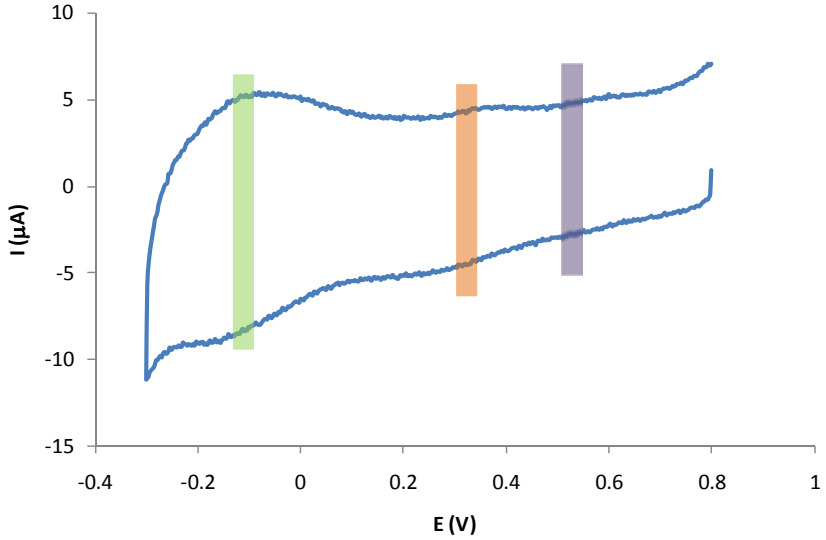
10
5
0
-5
-10
-15
I (µA)
-0.4
-0.2
0
0.2
0.4
0.6
0.8
1
E (V)

(d)

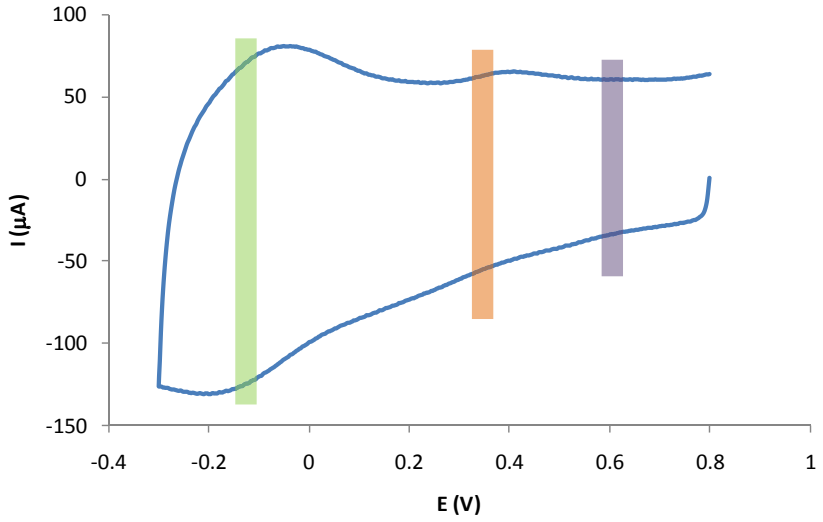
100
50
0
-50
-100
-150
I (µA)
-0.4
-0.2
0
0.2
0.4
0.6
0.8
1
E (V)

Figure S12: Cyclic voltammogram of complex **2a**$^{2+}$ in aqueous solution pH=12 buffer at scan rate of (a) 100 mV/s scanning anodically (b) 900 mV/s scanning anodically (c) 100 mV/s scanning cathodically with 3 minutes of equilibration time (d) 900 mV/s scanning cathodically with 3 minutes of equilibration time. The oxidation transitions are indicated in green line for isomer [Ru-ON$_4$(Pz)] and orange line [Ru-ON$_4$(Py)].

(a)

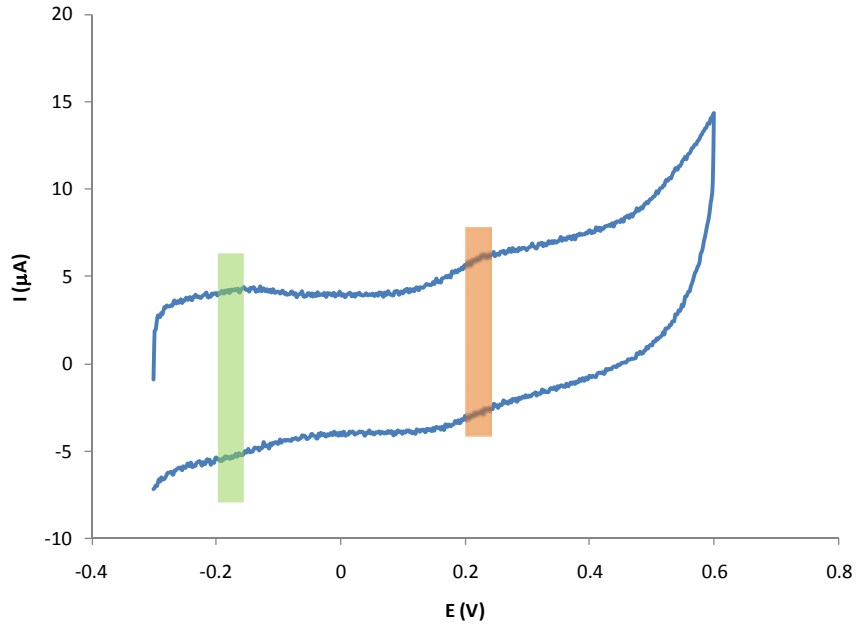

(b)

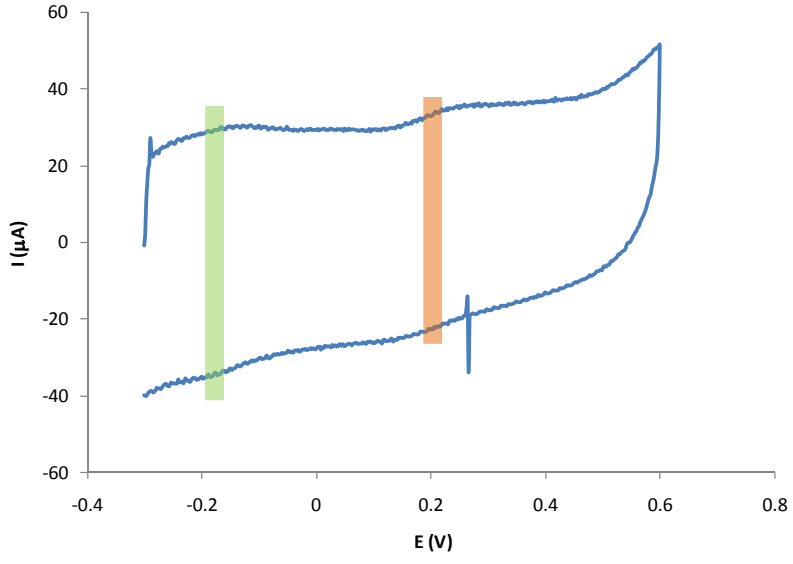

(c)

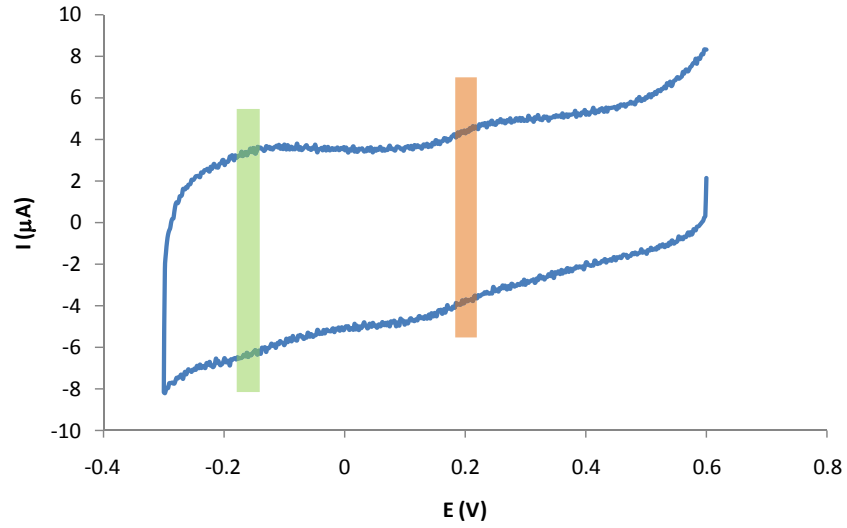

(d)

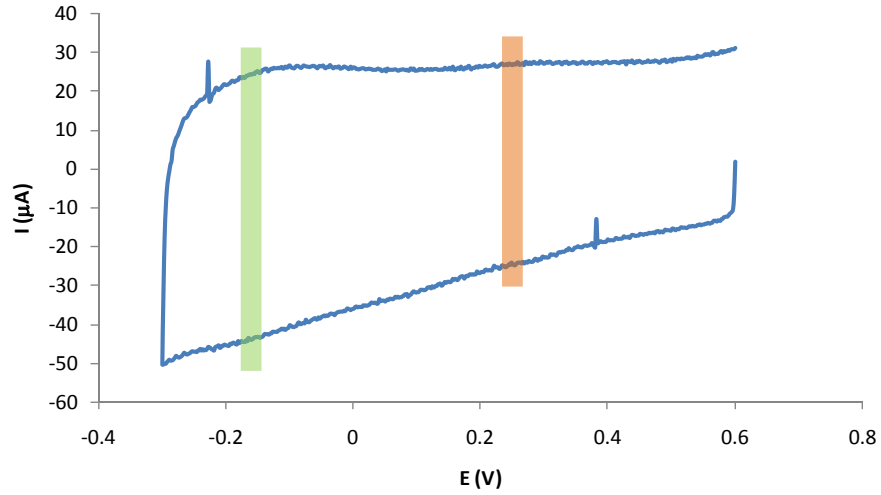

Figure S13: Plot of ic1/ic2 vs. ν-1, plus its linear fitting extrapolating ν→∞ to obtain $K^{III}_{O\rightarrow N}$ for complex **2a**$^{2+}$.

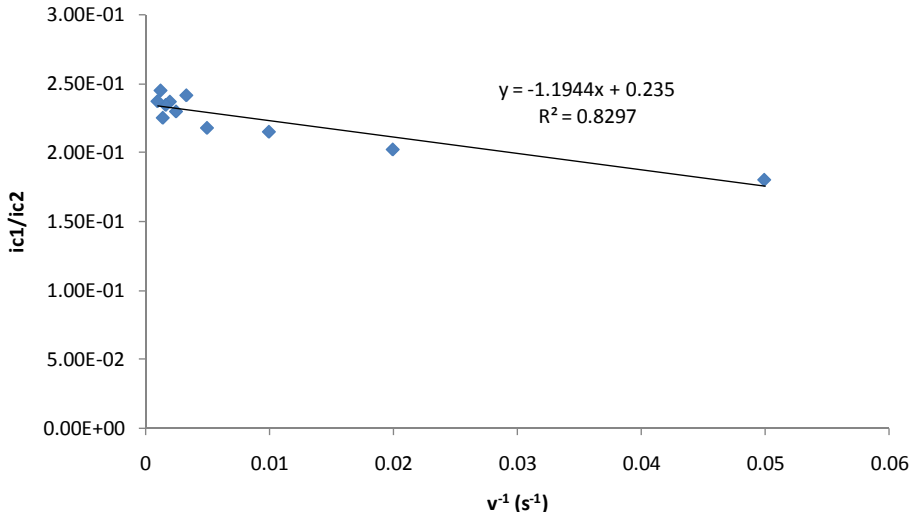

Figure S14:

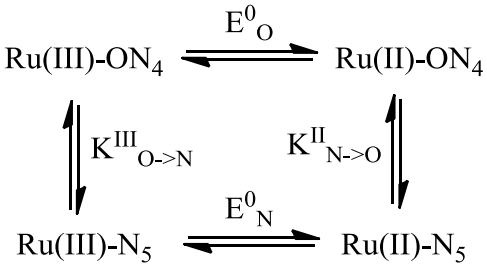

$$\Delta G^0_O = \Delta G^0(K^{II}_{N->O}) + \Delta G0(K^{III}_{O->N}) + \Delta G^0_N$$

$$\Delta G^0 = -RTlnK;\ \Delta G^0 = -nFE^0$$
$$(R=8.314\ J\cdot K^{-1}\cdot mol^{-1};\ F=96485\ C\cdot mol^{-1})$$

Figure S15: MS-ESI spectra of Ligand Hpbl.

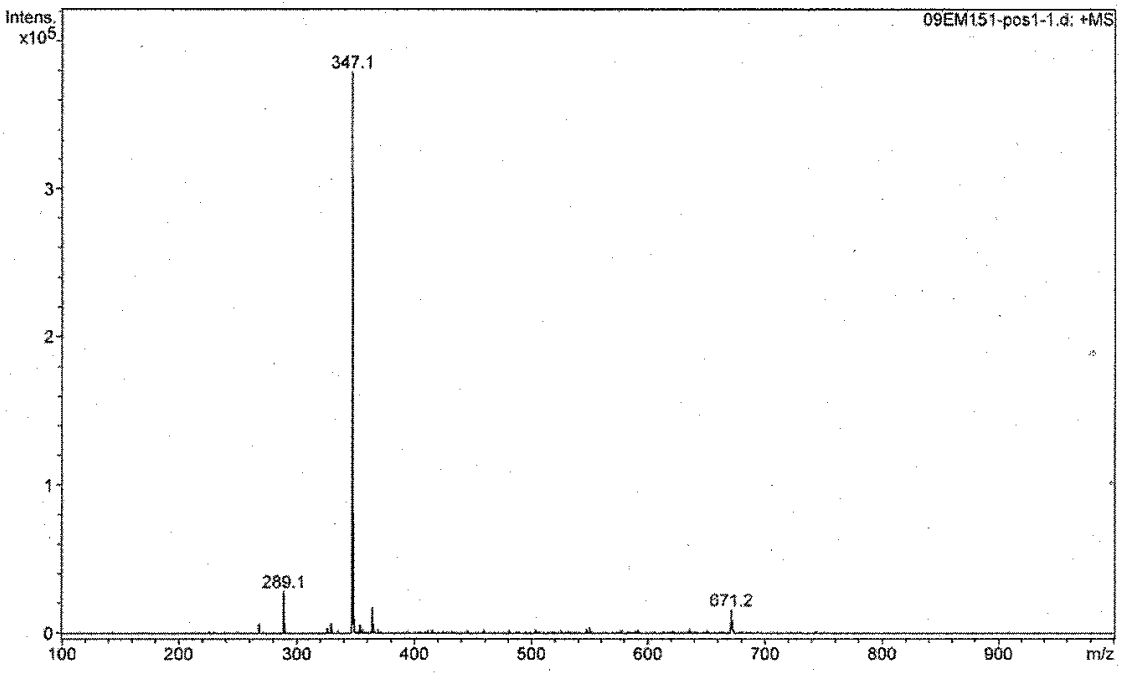

#	m/z	I	I %
1	268.2	6005	1.6
2	289.1	27843	7.4
3	290.0	7173	1.9
4	329.1	6141	1.6
5	347.1	378621	100.0
6	348.1	80935	21.4
7	349.1	9295	2.5
8	353.9	5287	1.4
9	364.3	17362	4.6
10	365.3	5457	1.4
11	550.2	3869	1.0
12	671.2	15361	4.1
13	672.3	8548	2.3

Figure S16: MS-ESI spectra of complex $\mathbf{1}^{+}$ in MeOH.

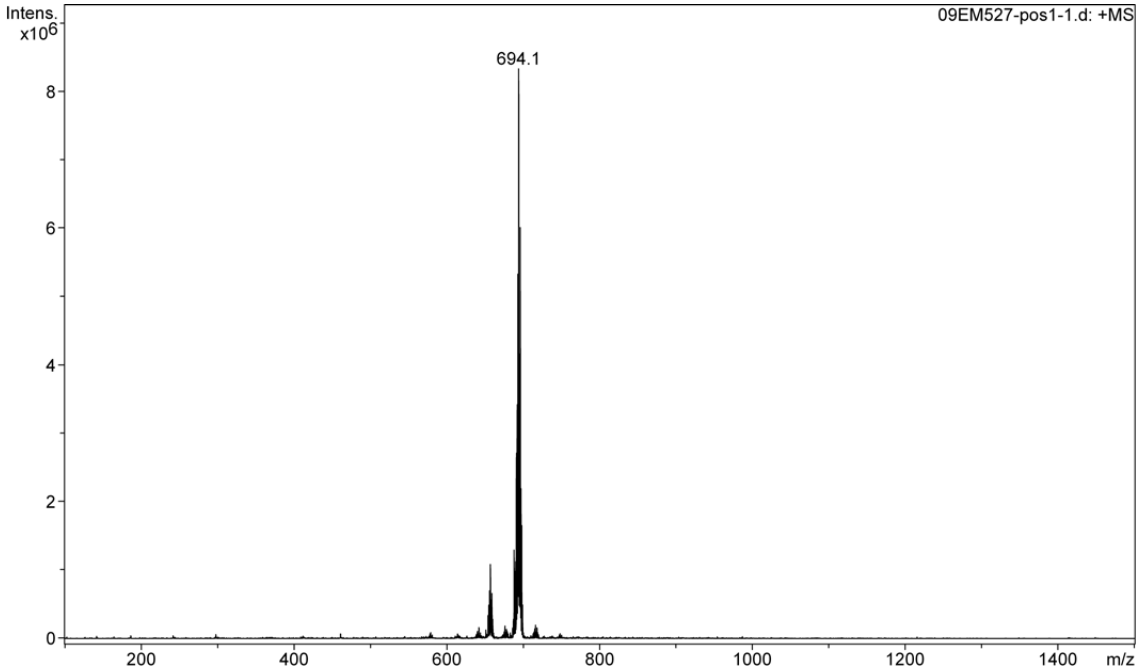

#	m/z	I	I %
1	579.1	85960	1.0
2	640.2	103048	1.2
3	642.2	157828	1.9
4	651.2	123016	1.5
5	654.2	336841	4.0
6	655.2	490276	5.9
7	656.2	697986	8.4
8	657.2	1080730	13.0
9	658.2	563532	6.8
10	659.2	657517	7.9
11	660.2	279224	3.4
12	675.2	97404	1.2
13	676.2	180675	2.2
14	677.1	88483	1.1
15	678.1	130599	1.6
16	679.1	98099	1.2
17	683.2	80692	1.0
18	686.2	154461	1.9
19	687.2	283378	3.4
20	688.2	1293649	15.5
21	689.2	979872	11.8
22	690.2	1120032	13.4
23	691.1	2709816	32.5
24	692.2	3422659	41.1
25	693.2	5323208	63.9
26	694.1	8328491	100.0
27	695.1	4154602	49.9
28	696.1	6004354	72.1
29	697.1	2192950	26.3
30	698.1	1652415	19.8
31	699.1	488040	5.9
32	700.1	79457	1.0
33	714.1	93250	1.1
34	715.1	138707	1.7
35	716.2	193581	2.3
36	717.1	91554	1.1
37	718.1	155774	1.9
38	719.1	86031	1.0

Figure S17: Exact MS-ESI spectra of complex **3a**$^{+}$ in MeOH. (a) Experimental. (b) Theorical.

(a)

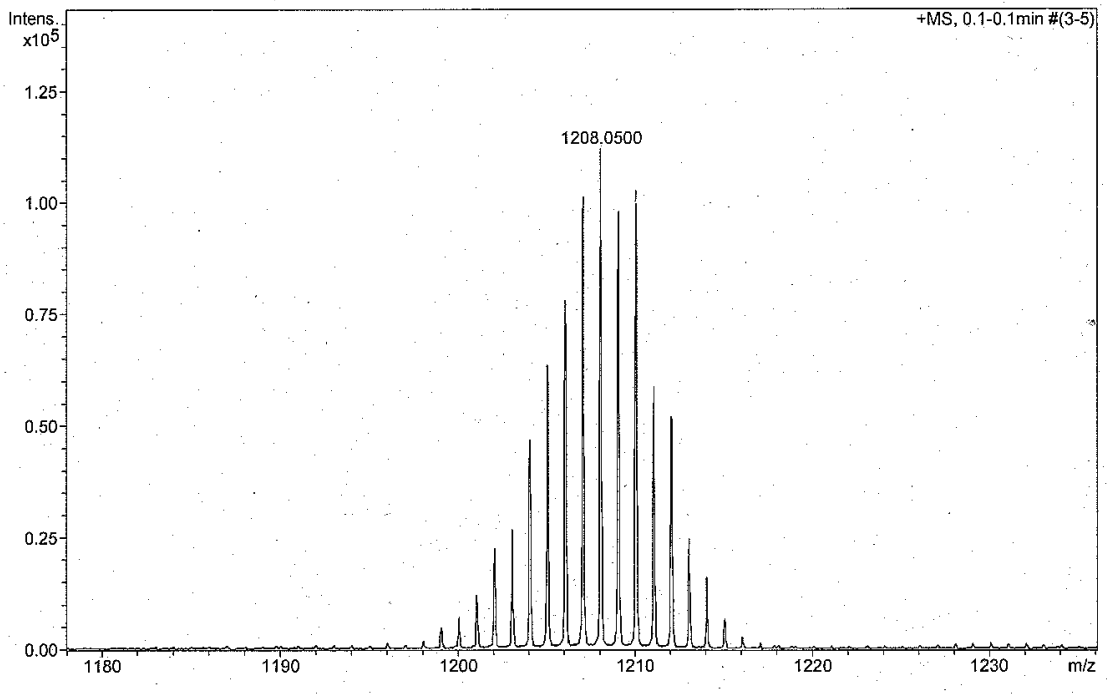

#	m/z	I	I %
1	1198.0544	2021	1.8
2	1199.0537	5023	4.5
3	1200.0537	7459	6.7
4	1201.0531	12169	10.9
5	1202.0507	22769	20.3
6	1203.0523	26917	24.0
7	1204.0516	47023	41.9
8	1205.0507	63791	56.9
9	1206.0506	78100	69.6
10	1207.0504	101216	90.3
11	1208.0500	112137	100.0
12	1209.0507	98004	87.4
13	1210.0492	102851	91.7
14	1211.0492	58859	52.5
15	1212.0502	52263	46.6
16	1213.0482	25013	22.3
17	1214.0472	16323	14.6
18	1215.0485	7060	6.3
19	1216.0505	2347	2.1

(b)

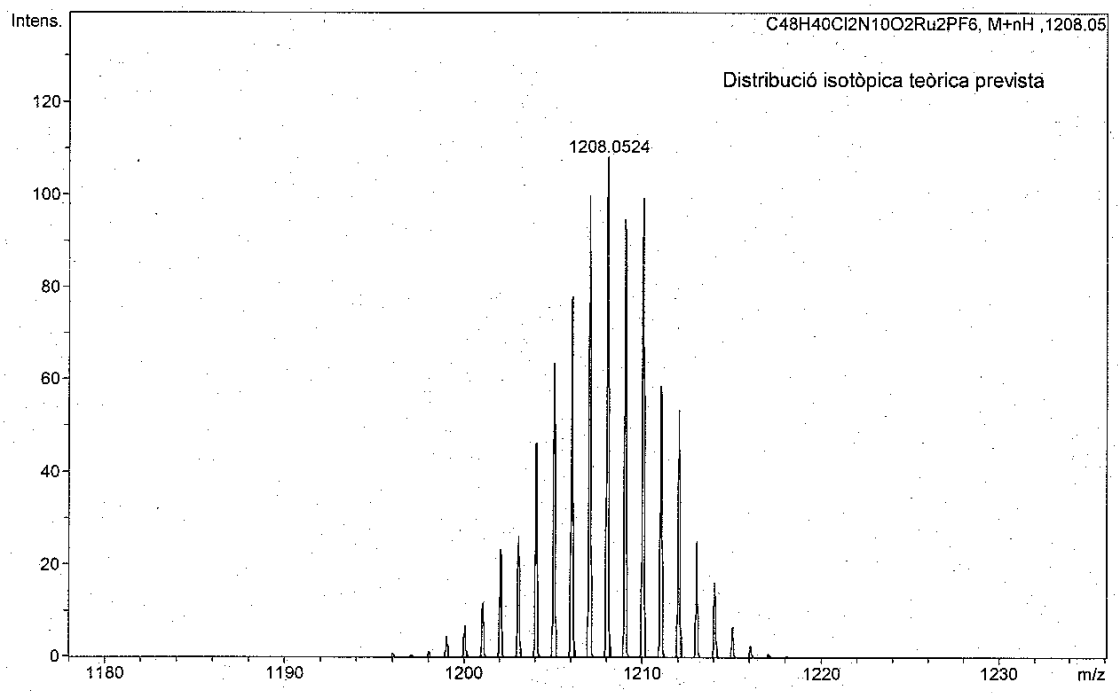

#	m/z	I	I %
1	1196.0579	1	0.8
2	1197.0613	0	0.4
3	1198.0562	1	1.1
4	1199.0566	4	4.2
5	1200.0561	6	6.2
6	1201.0560	11	11.1
7	1202.0553	22	21.8
8	1203.0549	25	24.6
9	1204.0543	43	43.2
10	1205.0540	59	58.9
11	1206.0531	72	72.3
12	1207.0530	92	92.5
13	1208.0524	100	100.0
14	1209.0527	88	87.7
15	1210.0522	92	92.1
16	1211.0531	55	54.7
17	1212.0520	50	49.9
18	1213.0535	23	23.4
19	1214.0520	15	15.2
20	1215.0533	6	6.1
21	1216.0524	2	2.4
22	1217.0534	1	0.8

S18. Cyclic voltammograms of 0.08 mM **2a**$^{2+}$ at pH=1. (a) scanning cathodically from 0.9 to 0 with 3 min. of equilibration time at 20 mV/s, (b) scanning anodically from 0 to 0.9 at 20 mV/s, (a) scanning cathodically from 0.9 to 0 with 3 min. of equilibration time at 100 mV/s, (b) scanning anodically from 0 to 0.9 at 100, mV/s.

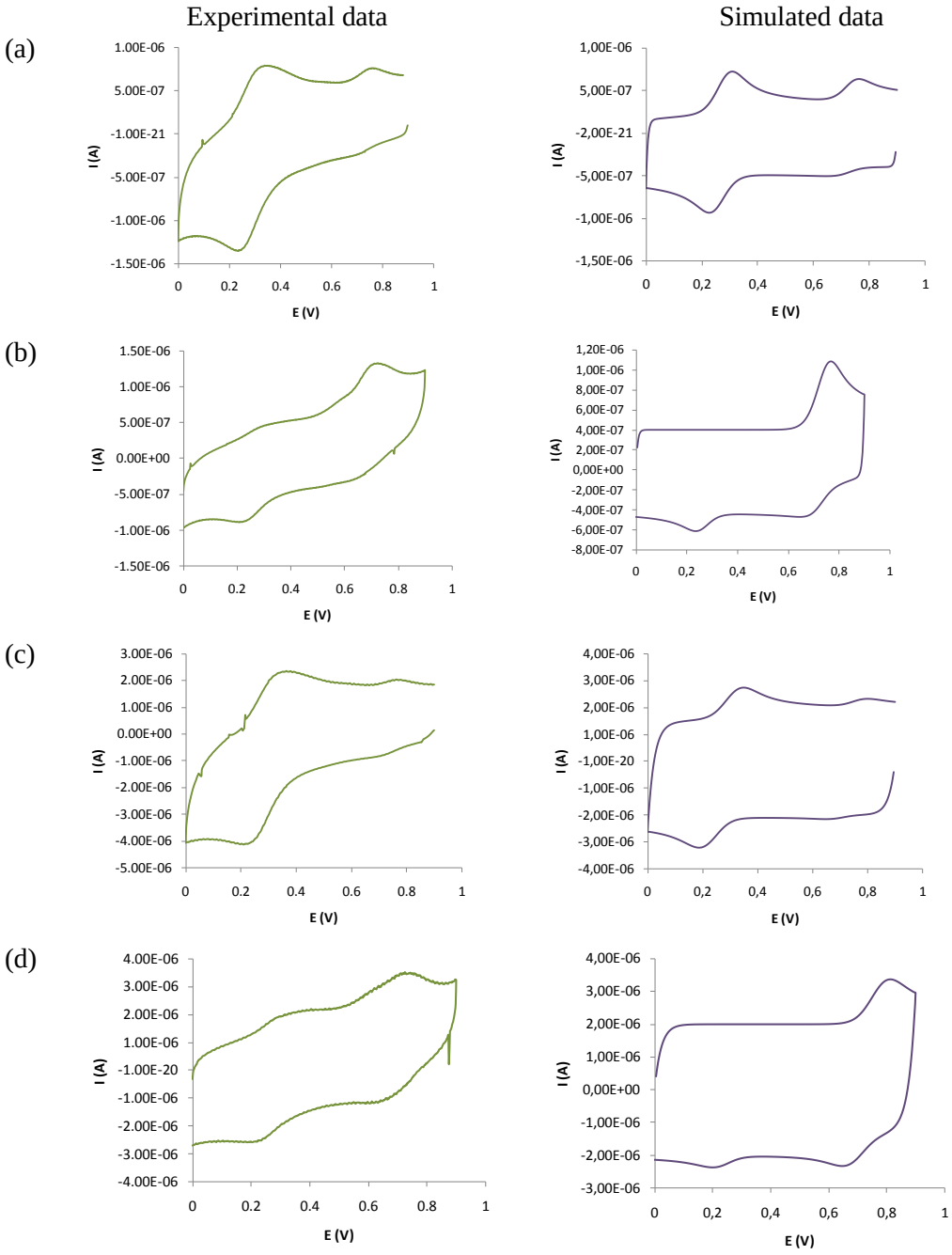

Simulation parameters:

Source program: DigiSim 3.03

File type: CV

Mechanism: ECEC

[1E] Ru3N + 1e = Ru2N

[1C] Ru3N = Ru3O

[2E] Ru3O + 1e = Ru2O

[2C] Ru2O = Ru2N

Experimental parameters:

T (K) = 298.2 K

Ru (Ohms) = 10000

CdI (F) = 2E-005

Cycles = 1

Electrode geometry = planar

Diffusion = semi-infinite

Pre-equilibrium = enabled

Charge transfer parameters:

E0[1] (V)= 0.725

alpha [1E]= 0.5

Ks[1E] (cm/s):10000

E0[2E] (V)= 0.26

alpha [2E]= 0.5

Ks[2E] (cm/s):10000